Mechanics and Materials Issues in Processing and Flexibility of Soft Contact Lenses

by

Lisa Jan Tegeler

Submitted to the Department of Mechanical Engineering
in partial fulfillment of the requirements for the degree of

Master of Science in Mechanical Engineering

at the

MASSACHUSETTS INSTITUTE OF TECHNOLOGY

May 1995

Author .....
Department of Mechanical Engineering
May 23, 1995

Certified by .....
Mary C. Boyce
Associate Professor of Mechanical Engineering
Thesis Supervisor

Accepted by .....
Ain A. Sonin
Chairman, Departmental Committee on Graduate Students

Mechanics and Materials Issues in Processing and Flexibility of Soft Contact Lenses

by

Lisa Jan Tegeler

Submitted to the Department of Mechanical Engineering
on May 23, 1995, in partial fulufillment of the
requirements for the degree of
Master of Science in Mechanical Engineering

Abstract

Three issues pertaining to the processing and design of hydrogel contact lenses were studied and modeled using finite element techniques. First, two possible causes of lens shape distortion due to crosslinking processing parameters were examined. The effects of nonuniform swelling coefficient and/or elastic modulus distributions were modeled. It was found that nonuniform through-thickness and radial variation of swelling coefficient by $\pm 10\%$ caused significant shape distortion in lenses manufactured from a material that is first crosslinked to a rigid state and then hydrated, a material which expands by approximately 40% during hydration. However, such material property distribution caused little shape distortion in lenses crosslinked in an already-hydrated state, which contract $\approx 7\%$ during crosslinking.

The shape distortion effects of sequential crosslinking history were also modeled. It was shown that if sequential crosslinking occurs during processing, the accompanying volume shrinkage acting against the shape constraint of a rigid mold can lead to large internal stresses in the lens material. Such residual stresses, if locked in during processing, will redistribute to relieve themselves when the lens is removed from the mold, resulting in large shape distortion, even when the overall material volume contraction is small. The internal stresses and resulting distorted lens shapes due to several patterns of sequential crosslinking history were examined.

Next, the lens design issue of the relationship of lens flexibility to cross sectional thickness profile was examined. The pinching of a lens, as if between a thumb and index finger, was simulated, and the force-displacement response recorded. Actual and blank lens geometries were used in pinching simulations, and their stiffness responses were related to the thickness profile of various lens regions. It was found that the thickness of the outer lens region was significant in determining the stiffness at very slight deformations, while the thickness of the lens region between the center and the edge (the lenticular region) had greater influence on lens stiffness at larger deformations.

Finally, modeling of lens placement on the eye was performed. First, modeling issues were discussed, with a focus on capturing the mechanical behavior and influence of the tear layer between the eye surface and the contact lens. A model of the tear layer as a nearly incompressible solid which was free to slide between the eye and the lens but that was constrained to remain in contact with both was arrived at, and a solution in which the lens and the tear were in equilibrium on the eye was found. Due to the level of difficulty of using such a model, a second model without a tear layer was tested, and the placement of several lenses of varying geometries was simulated. It was found that both internal stress state and lens/eye interface pressure were influenced by the curvature and the thickness profile of the lens. In general, lenses with a steep bearing induced negative interface pressure at the lens center, and positive pressure at the edge, while flat-fitting lenses created positive central interface pressure, and negative pressure at the lens edge.

Applications to lens and process design of all three issues studied were presented.

Thesis supervisor: Mary C. Boyce

Title: Associate Professor of Mechanical Engineering

Acknowledgments

There are so many people and things that I am grateful for, and I'd like to mention some of them here.

Thanks to CIBA Vision for sponsoring this project with funding and technical support. I also want to thank Dr. Peter Hagman for lending his advice and experience to this research. I am very grateful to have had the opportunity to work on this project. I have learned a lot from it, and I have really enjoyed it, and it wouldn't have been possible without their support.

One of the things I am most grateful for, not just in the context of my thesis or of graduate school, but in the context of my life, is having had the chance to get to know Professor Mary Boyce. She has always been supportive and understanding of me, academically, by generously sharing her experience and knowledge whenever I needed some insight, professionally, by listening to my numerous and sometimes painful interviewing experiences, and by lending her well-grounded perspective to my situation, and personally, by just understanding when things weren't going so well and by sharing her faith that they would get better. Working with her has made the past two years something I will always treasure.

I want to thank some of the friends I have known in the past couple or more years for the happiness they have given me. Debbie DeMania has been a source of inspiration through graduate school. I have a lot of admiration for the way she remains undaunted by imposing situations, and keeps and shares her sense of humor. My roommate, Rita Gupta was a joy to live with. She was always frank and easy to be with, and was an enthusiastic confidante. Kathryn Fricks was another terrific roommate. She made our home a comfortable and welcoming place just by being in it. I also very much appreciate her good sense and caring when I was short on the sense part.

Thanks too to some of my older friends. I'm really glad Matt Marjanovic is still around. It was fun going through MIT the first time together, and it's been fun the second time. I'm happy for the good time we have spent. Hoang Tran is an old friend,

and a new one who I have just recently come to know more. I appreciate his caring and his not-too-serious view of himself. Seeing him always makes me feel good about myself and everyone else. That's a pretty neat gift. Thanks, Hoang.

I also want to acknowledge Tony Mona Hechanova, PhD. I consider myself very lucky to have had him in my life and to have been a part of his. I am so appreciative of his loving and generous nature. Another PhD, Scott Johnson, has made my past two years a lot of fun. Scott has shared with me a point of view I don't think I would have ever seen otherwise. I am also very grateful for his generous offerings of compassionate and wise advice.

Thanks to my dad for really taking pride in the stuff I've been doing at MIT. I am so glad that he has a real love for mechanical things, and that we can share it together. Thanks to my mom for always caring about me.

I also want to thank MIT as a whole, my much-loved home for the past six years. I haven't always been comfortable and happy at MIT, but I have always felt that I belonged, and that I had a place here. A sense of belonging is a feeling that doesn't come easily, and I am very appreciative of the fact that I found it here.

I want to thank my dear friend Chris Lerch. Chris has been an amazing part of my life for the past nine months, and getting to know him over that time has made my life intense, and exciting, and wonderfully satisfying. I am so grateful to him for his caring and his trust in me. Knowing that I can always share all my emotions and ideas with him has made and continues to make him a very treasured part of my life. Thank you, Chris.

Contents

1 Introduction of Contact Lens Processing and Design Issues 16

2 Modeling of Processing of Hydrogel Contact Lenses 19

2.1 Lens Distortion Due to Nonuniform Material Property Distribution . 20

2.1.1 Thermally-induced shape distortion of "bi-metal" bodies . . . 21

2.1.2 Material and Mesh Characteristics 22

2.1.3 Uniform Lens Swelling Simulations 23

2.1.4 Nonuniform Lens Swelling Simulations 29

2.1.5 Nonuniform lens simulation cases 29

2.1.6 Results of Nonuniform lens simulations 31

2.1.7 Conclusions from Material Property Distribution Distortion Simulations 36

2.2 Lens Shape Distortion Effects due to Sequential Crosslinking History 37

2.2.1 Related Experimental and Modeling Work 37

2.2.2 Sequential Crosslinking Simulations 42

2.2.3 Conclusions of Sequential Crosslinking Simulations 67

2.3 Conclusions of Lens Processing Simulations 67

3 Lens Flexibility 69

3.1 Finite Element Model 70

3.2 Simulation Cases 74

3.3 Results of Simulations with Actual Lens Geometries 75

3.4 Results of Simulations with Uniform Thickness Lens Blanks 84

3.5 Results of Simulations with Step-Variable Thickness Lens Blanks . . . 84
3.6 Conclusions of Lens Flexibility Simulations 89

4 Modeling of Lens Fit on the Eye 92
4.1 Lens Fit Modeling Issues 96
4.1.1 Eye Model 96
4.1.2 Lens Model 96
4.1.3 Tear Model 97
4.1.4 Loading History 107
4.1.5 Tear Layer Element type 116
4.1.6 Summary of Tear Modeling Issues 116
4.1.7 A Test: No Tear Layer 118
4.2 Lens Placement Simulations with Varying Lens Geometries 129
4.2.1 Finite Element Model 129
4.2.2 Lens Geometries Modeled 131
4.2.3 Results of Lens Placement Simulations 134
4.3 Conclusions of Lens Placement Simulations 165

5 Conclusions and Future Extensions of Contact Lens Processing and Design Modeling 169

A Example Input Deck for Lens Placement Simulations 174

List of Figures

2-1 Unhydrated mesh used for swelling simulations. 23

2-2 Three sections of a lens 24

2-3 Initial values of radii of curvature of unhydrated lens regions. 24

2-4 Initial values of radii of curvature of swelled lens regions for shrinking simulation. 25

2-5 Final node points and measurement of overall lens dimensions. 26

2-6 Four patterns of nonuniform swelling coefficient and/or modulus distribution tested 30

2-7 Simulation of lens with different swelling coefficient in upper and lower layers. (case 1, $\alpha_0 = 0.344$) 32

2-8 Simulation of lens with different swelling coefficient and elastic modulus in upper and lower layers. (case 2, $\alpha_0 = 0.344$) 33

2-9 Simulation of lens with different swelling coefficient in upper and lower layers of edge region. (case 3, $\alpha_0 = 0.344$) 33

2-10 Simulation of lens with different swelling coefficient in edge region. (case 4, $\alpha_0 = 0.344$) 34

2-11 Simulation of lens with different swelling coefficient in upper and lower layers. (case 1, $\alpha_0 = -0.0725$) 35

2-12 Simulation of lens with different swelling coefficient in upper and lower layers of edge region. (case 3, $\alpha_0 = -0.0725$) 35

2-13 Simulation of lens with different swelling coefficient in edge region. (case 4, $\alpha_0 = -0.0725$) 36

2-14 Photograph of curled lens 38

2-15 Axisymmetric mesh used for constrained shrinking simulation 44
2-16 Constrained mesh before and after central shrinkage 46
2-17 Stress in 1 direction after simultaneous shrinkage in single-material lens 47
2-18 Stress in 3 direction after simultaneous shrinkage in single-material lens 48
2-19 Stress in 2 direction after simultaneous shrinkage in single-material lens 48
2-20 Stress in 1 direction after central shrinkage in dual stiffness lens . . . 49
2-21 Stress in 1 direction after central shrinkage in single stiffness lens . . 50
2-22 Stress in 3 direction after central shrinkage in dual stiffness lens . . . 50
2-23 Stress in 3 direction after central shrinkage in single stiffness lens . . 51
2-24 Stress in 2 direction after central shrinkage in dual stiffness lens . . . 51
2-25 Stress in 2 direction after central shrinkage in single stiffness lens . . 52
2-26 Strain in 1 direction after central shrinkage in dual stiffness lens . . . 53
2-27 Strain in 1 direction after central shrinkage in single stiffness lens . . 54
2-28 Strain in 2 direction after central shrinkage in dual stiffness lens . . . 54
2-29 Strain in 2 direction after central shrinkage in single stiffness lens . . 55
2-30 Strain in 3 direction after central shrinkage in dual stiffness lens . . . 55
2-31 Strain in 3 direction after central shrinkage in single stiffness lens . . 56
2-32 Mesh used for 3-dimensional unconstrained simulations 58
2-33 Shrinking in small central oval-shaped region 58
2-34 Shrinking in large central oval-shaped region 59
2-35 Shrinking in strip through center 59
2-36 Axisymmetric shrinking in central region 60
2-37 Locations of cross sections taken for Figures 1-38 to 1-40 61
2-38 Deformed cross section shape for small oval-shaped shrinking region . 61
2-39 Deformed cross section shape for large oval-shaped shrinking region . 62
2-40 Deformed cross section shape for central strip shrinking region 62
2-41 Geometry of flat lens blanks used for simulations of a proposed laboratory experiment to evaluate the degree of sequential crosslinking. . 63
2-42 Typical mesh used in blank lens experiment simulations 64
2-43 Final shapes produced by 16mm diameter blank simulations 65

2-44 Final shapes produced by 8mm diameter blank simulations 65
2-45 Final shapes produced by two and four-layer 16mm diameter blank simulations 66

3-1 Loading of lens 71
3-2 Undeformed mesh 71
3-3 Early deformation, top view 72
3-4 Intermediate deformation, top view 72
3-5 Final deformation, top view 72
3-6 Early deformation, angle view 73
3-7 Intermediate deformation, angle view 73
3-8 Final deformation, angle view 73
3-9 Three sections of a lens 75
3-10 F88 series force-displacement 77
3-11 F88 series thickness profile 77
3-12 G88 series force-displacement 78
3-13 G88 series thickness profile 78
3-14 H88 series force-displacement 79
3-15 H88 series thickness profile 79
3-16 I85 series force-displacement 80
3-17 I85 series thickness profile 80
3-18 Force-displacement for F88, H88, and I85 lenses 81
3-19 Thickness profile of F88, H88, and I85 lenses 81
3-20 Force-displacement of "/1" series lenses 82
3-21 Thickness profile of "/1" series lenses 82
3-22 Force-displacement of "/2" series lenses 83
3-23 Thickness profile of "/2" series lenses 83
3-24 Force-displacement of 8.5mm radius blanks of varying thickness . . . 85
3-25 Force-displacement of 0.09mm thickness of varying basecurve radius . 85
3-26 Stiffness vs. thickness of constant-thickness blanks 86

3-27 Force-displacement of blanks with step variable thickness 87
3-28 Stiffness vs. thickness of blanks with step variable thickness 90
3-29 Stiffness vs. thickness of F88/1, G88/1, H88/1, and H88/2 lens geometries 90

4-1 Geometry of the eye model 97
4-2 I85/1 lens mesh used for placement simulations 98
4-3 Model of tear as a thin sheath surrounding an incompressible liquid . 100
4-4 Buckling of the sheath as the lens is lowered onto the tear. The displacement shown has been magnified by a factor of 10 100
4-5 Interface pressure between lens and sheath near center of lens 101
4-6 Thickening of tear layer at cornea/sclera junction to relieve hydrostatic tension 102
4-7 Solid tear attached to underside of lens 103
4-8 Master (lower surface of lens) and slave (upper surface of tear) surfaces. Once contact is established between the two surfaces, nodes of the slave surface may not separate from the master surface. 106
4-9 Step by step procedure for placing lens on tear 109
4-10 Digging into the tear by the lens when all displacements were released simultaneously 110
4-11 Separation of the tear from lens when lens displacements were released before tear/lens contact was established at lens edge. 111
4-12 Position of redundant surfaces introduced to prevent digging-in and tear/lens separation 112
4-13 Large hydrostatic tension in tear layer at equilibrium state 113
4-14 Lens in equilibrium on 50μm tear layer. The lower figure shows an enlargement of the cornea/sclera junction region, and the upper figure includes the undeformed lens mesh. 114
4-15 Pressure Distribution at tear/eye interface for lens in equilibrium on 50μm tear layer 115

4-16 Tear layer thickness distribution when lens was in equilibrium on 50μm tear layer 115
4-17 Four eye geometries tested for use in no-tear simulations. The lower plot shows a blow-up of the cornea/sclera junction zone. 120
4-18 Initial and final configuration of lens I85/1 placed on eye geometry 4 121
4-19 S11 stress distribution in lower layer of lens elements when lens is placed on 4 eye geometries with no tear, and when a 50μm tear layer is present 122
4-20 S11 stress distribution in upper layer of lens elements when lens is placed on 4 eye geometries with no tear, and when a 50μm tear layer is present 122
4-21 S22 stress distribution in lower layer of lens elements when lens is placed on 4 eye geometries with no tear, and when a 50μm tear layer is present 123
4-22 S22 stress distribution in upper layer of lens elements when lens is placed on 4 eye geometries with no tear, and when a 50μm tear layer is present 123
4-23 S33 stress distribution in lower layer of lens elements when lens is placed on 4 eye geometries with no tear, and when a 50μm tear layer is present 124
4-24 S33 stress distribution in upper layer of lens elements when lens is placed on 4 eye geometries with no tear, and when a 50μm tear layer is present 125
4-25 Lens/eye interface pressure distribution when lens is placed on 4 eye geometries with no tear, and when a 50μm tear layer is present 126
4-26 Interface pressure and $\frac{2tS33}{r}$ when lens is placed on the eye with a 50μm tear layer 127
4-27 Interface pressure and $\frac{2tS33}{r}$ when lens is placed on eye4 without a tear layer 127

4-28 Typical finite element model for simulating the placement of various lens geometries on a rigid eye 130
4-29 Geometry of the eye4 eye surface. All dimensions are in mm. 130
4-30 The six circular arcs that compose the N83 and N85 lenses. 132
4-31 Thickness profiles of the N83a, N83b, N83c, and N85b lenses 133
4-32 Cross sections of the N83b and N85b lenses 133
4-33 Initial and final configurations of G88/1 lens placed on eye with no tear layer 137
4-34 S11 stress distribution in lower layer of lens elements for F88/1, G88/1, H88/1, and I85/1 lens placement simulations 137
4-35 S11 stress distribution in upper layer of lens elements for F88/1, G88/1, H88/1, and I85/1 lens placement simulations 138
4-36 S33 stress distribution in lower layer of lens elements for F88/1, G88/1, H88/1, and I85/1 lens placement simulations 139
4-37 S33 stress distribution in upper layer of lens elements for F88/1, G88/1, H88/1, and I85/1 lens placement simulations 140
4-38 Free body diagram which illustrates the forces needed to cause lenses with flat (a) and steep (b) bearing to conform to the eye. 141
4-39 Interface pressure distributions for F88/1, G88/1, H88/1, and I85/1 lens placement simulations 142
4-40 $\frac{S33(2t)}{r}$ distribution in lower element layer for F88/1, G88/1, H88/1, and I85/1 lens placement simulations 142
4-41 $\frac{S33(2t)}{r}$ distribution in upper element layer for F88/1, G88/1, H88/1, and I85/1 lens placement simulations 143
4-42 Initial and final configurations of N83b lens placed on eye with no tear layer 144
4-43 S11 stress distribution in lower layer of lens elements for N83a, N83b, N83c, and N85b lens placement simulations 145
4-44 S11 stress distribution in upper layer of lens elements for N83a, N83b, N83c, and N85b lens placement simulations 145

4-45 S33 stress distribution in lower layer of lens elements for N83a, N83b, N83c, and N85b lens placement simulations 146
4-46 S33 stress distribution in upper layer of lens elements for N83a, N83b, N83c, and N85b lens placement simulations 147
4-47 Interface pressure distributions for N83a, N83b, N83c, and N85b lens placement simulations 148
4-48 $\frac{S33(2t)}{r}$ distribution in lower element layer for N83a, N83b, N83c, and N85b lens placement simulations 148
4-49 $\frac{S33(2t)}{r}$ distribution in upper element layer for N83a, N83b, N83c, and N85b lens placement simulations 149
4-50 Initial and final configurations of Martin and Holden blank geometry M3 placed on eye with no tear layer 150
4-51 S11 stress distribution in lower layer of lens elements for M1, M2, and M3 lens placement simulations 151
4-52 S11 stress distribution in upper layer of lens elements for M1, M2, and M3 lens placement simulations 151
4-53 S33 stress distribution in lower layer of lens elements for M1, M2, and M3 lens placement simulations 152
4-54 S33 stress distribution in upper layer of lens elements for M1, M2, and M3 lens placement simulations 153
4-55 Interface pressure distributions for M1, M2, and M3 lens placement simulations 154
4-56 $\frac{S33(2t)}{r}$ distribution in lower element layer for M1, M2, and M3 lens placement simulations 154
4-57 $\frac{S33(2t)}{r}$ distribution in upper element layer for M1, M2, and M3 lens placement simulations 155
4-58 Initial and final configurations of Martin and Holden blank geometry M5 placed on eye with no tear layer 156
4-59 S11 stress distribution in lower layer of lens elements for M1, M4, and M5 lens placement simulations 157

4-60 S11 stress distribution in upper layer of lens elements for M1, M4, and M5 lens placement simulations 157
4-61 S33 stress distribution in lower layer of lens elements for M1, M4, and M5 lens placement simulations 159
4-62 S33 stress distribution in upper layer of lens elements for M1, M4, and M5 lens placement simulations 159
4-63 Interface pressure distributions for M1, M4, and M5 lens placement simulations 160
4-64 $\frac{S33(2t)}{r}$ distribution in lower element layer for M1, M4, and M5 lens placement simulations 160
4-65 $\frac{S33(2t)}{r}$ distribution in upper element layer for M1, M4, and M5 lens placement simulations 161
4-66 Initial and final configurations of Fatt lens geometry placed on spherical eye with no tear layer 163
4-67 S11 stress distribution in lower and upper layer of lens elements for placement simulations of a spherical lens on a spherical eye 164
4-68 S33 stress distribution in lower and upper layer of lens elements for placement simulations of a spherical lens on a spherical eye 164
4-69 Interface pressure and $\frac{S33(2t)}{r}$ distributions for placement simulations of a spherical lens on a spherical eye 165

List of Tables

2.1 Overall lens dimensions obtained in uniform lens simulations. 27

2.2 Average radii of curvature obtained in uniform lens simulations. . . . 28

3.1 Initial and Final stiffnesses of variable-thickness blanks 87

4.1 Lens blank geometries used in the experimental study by Fatt 93

4.2 Summary of tear modeling issues 117

4.3 Approximate interface pressures measured by Martin and Holden, and central interface pressures obtained in simulations 162

Chapter 1

Introduction of Contact Lens Processing and Design Issues

Contact lenses are becoming an increasingly popular method of vision correction, and current advances in the technology, such as the improvement of extended wear lenses, the introduction of disposable lenses, and new, less expensive manufacturing methods will continue to increase the demand for contact lenses. In spite of the recent growth in contact lens technology, a large part of the knowledge of contact lens design and processing issues has been gathered empirically by a trial and error approach. The purpose of this work was to develop a predictive tool to provide information about the mechanical behavior of contact lenses that can augment and aid in the design of experimental studies. Due to the complex and varied geometry of contact lenses, the finite element method was chosen as a modeling technique for this work. Three basic issues of contact lens mechanics are explored: 1) the crosslinking of hydrogel materials directly into a lens shape as a form of processing soft contact lenses, 2) the relationship of lens thickness profile to overall lens flexibility, and 3) the relationship between lens geometry and lens fit on the eye.

In Chapter 2, possible causes of shape distortion of hydrogel contact lenses due to processing are discussed. First, the effects of uneven spatial material property distribution (elastic modulus and coefficient of expansion) on the final lens shape are examined. Next, the effects of sequential crosslinking (where the lens material is

transformed from a liquid to solid state with a spatial time history rather than simultaneously throughout the lens) are explored. Shape distortion due to the residual stresses resulting from sequential crosslinking are examined for varying patterns of crosslinking history. While the simulations performed in this chapter use the properties of actual materials that are currently being tested, the simulation technique can be modified to model lens production with new materials and crosslinking methods as they are discovered and developed. Therefore, our techniques can be used to identify and understand a material's potential sensitivity to certain processing conditions and histories.

Chapter 4 focuses on one issue of lens design: how the thickness profiles of lenses are related to their flexibility. In this chapter, the pinching of contact lenses, such as between a thumb and index finger, is simulated, and the resulting force-displacement responses are compared to the lens geometries. While such pinching is not a typical mode of deformation when a lens is worn on the eye, this pinching test provides information about the flexibility of the lens as a whole, which can be used to compare the relative flexibilities of various lens geometries, and to determine which lens geometry characteristics contribute most significantly to which characteristics of lens mechanical behavior. In practice, optometrists often use a pinch test to assess a lens' potential performance.

The final issue of contact lens mechanics explored in this study is the issue of lens fit on the eye. The details of lens fit will determine how well the lens moves over the eye surface in response to lid pressure, and how comfortable it is to wear. In this chapter, significant attention was paid to the role of the tear layer, and a number of practical issues involved with modeling the behavior of the tear layer were discussed. Next, results obtained from models with and without a tear layer were compared, and finally, the placement of several actual and blank lens geometries onto an eye surface without a tear layer was simulated. The internal lens stress state and the lens/eye interface pressure distributions were then related to lens thickness and curvature. The use of these simulations in understanding the mechanics of lens fit and thus in the design of lens geometries is then discussed.

In the final chapter, conclusions drawn from this work are presented, and possible extensions of it are suggested.

Chapter 2

Modeling of Processing of Hydrogel Contact Lenses

The first goal of this work was to discover possible causes of shape distortion of soft contact lenses due to processing. Soft contact lens material consists of a sparse polymer matrix that contains microscopic molecular "voids" or pathways into which water molecules may be introduced, i.e. it is a water-permeable polymer called a hydrogel material. Prior to the placement of a lens on the eye, the lens material must be in this fully hydrated state in order to allow oxygen transfer to the cornea. Two types of lens materials were studied: one which was hydrated after lens processing, and one with which lenses were produced in an already hydrated state.

To manufacture lenses with the first type of material, the lens material, which is initially in a liquid state, is placed into a matched mold which is transparent to UV radiation. Once in the mold, the material is crosslinked with UV radiation to form a relatively rigid solid lens. The lens is then removed from the mold and placed in a water solution for hydration. During hydration, the lens expands in volume by 25-100%, depending on the material, and transforms from a rigid to a rubbery-like hydrogel state, where the water essentially acts like a plasticizer in the polymer, lowering its T_g (glass transition temperature), putting it in the rubber state. When lenses are made with the second type of material, the liquid polymer material is again placed into a matched mold and crosslinked with UV radiation. In this case, the

polymer contains a significant amount of water, and, after crosslinking, the material is in the rubbery state since it is already fully hydrated. During this process, the lens material experiences a slight volume decrease, on the order of 7%.

Lenses processed from both types of materials have been found to demonstrate shape distortions once in the fully hydrated state due to small changes in processing parameters. Two different types of simulations were performed to investigate the potential causes of distortion in both lens materials. In the first set of simulations, shape distortion due to nonuniform material property distribution as a result of processing was investigated. In the second set of simulations, lens distortion due to sequential crosslinking history effects were explored.

2.1 Lens Distortion Due to Nonuniform Material Property Distribution

The first set of simulations focused on the possible effects on lens shape of uneven material property distribution that might arise during curing. It was hypothesized that inhomogeneous property distribution may arise during a crosslinking process if the material were not uniformly crosslinked. For example, if the radiation were coming from one side of the mold, the material closest to that side might have a higher crosslink density, which would, in turn, result in different mechanical properties. (e.g. modulus and/or coefficient of swelling)

Since the lens material undergoes both a volume change and a stiffening during curing, simulations were performed in which both the expansion factor and the stiffness of the material were varied in different lens regions. Two groups of simulations were performed. The first was to verify that lenses with uniform expansion coefficient and elastic modulus would cure without distortion. In these simulations, constant properties were assigned to all regions of the lens. The expansion coefficient and elastic modulus were varied between trials, but in each simulation, the lens had uniform properties. In the second set of simulations, the effect of nonuniform expansion coeffi-

cient and elastic modulus on the final shape were examined. In these simulations, the spatial distribution of expansion coefficient and modulus were varied within a single lens. In addition, the magnitude of variation of these properties from reference values was adjusted.

2.1.1 Thermally-induced shape distortion of "bi-metal" bodies

A commonly-observed defect in hydrogel soft contact lenses made by crosslinking to a rigid state and then hydrating is a "lifting up" of the edge region upon hydration. It was hypothesized that a swelling coefficient and modulus distribution that varied through the thickness of the lens would result in this type of shape distortion, which is similar to the thermally-induced bending of a flat bimetallic strip composed of two materials with mis-matched thermal expansion coefficients. [1] When such a strip is heated, the two materials attempt to expand by different amounts, inducing opposing stresses in the two metals. The offset of the midplane of each material from the plane where the stress acts (the interface) produces a moment in the body which results in a bending of the strip. When both strip materials have the same thickness $h/2$, the curvature of one of metals, ρ_1, is given by:

$$\frac{1}{\rho_1} = \frac{3(\alpha_2 - \alpha_1)T}{(1 + \frac{E_1}{E_2})h} \tag{2.1}$$

The amount of curvature present in the strip after heating is a function of the difference in expansion coefficients of the two materials, $\alpha_2 - \alpha_1$, the ratio of their elastic moduli, E_2/E_1, and the total temperature change, T. The same principle causes curling of a bimetallic disk, but will result in a different final shape. An initially flat disk will have a parabolic cross section if heated by a small amount, but, when the disk is heated by a larger amout, higher order geometry effects become influential, and the deformed shape will no longer be parabolic. In a disk with an initially spherical midplane, the effect of the initial curvature results in a deformed shape that is not parabolic, but that is described by a more complicated function,

even when the amount of heating is small. [12]

2.1.2 Material and Mesh Characteristics

In this section the characteristics of the model used to explore distortion due to nonuniform material property distribution are described. The lens material was modeled as linear elastic with an elastic modulus that varied between 1.2 MPa (modulus of fully-hydrated material) and 1.2GPa (the modulus when the material is in its rigid state.) The Poisson ratio was set to 0.49 since the material is nearly incompressible. Because both lens materials were initially isotropic, we modeled the volume change that each undergoes as a thermal expansion with linear coefficient of expansion, α, set to correspond to the expansion or contraction of each material. For the material with the two-step processing, α refers to the swelling that occurs when the lens is hydrated and changes from its rigid to its rubbery state. For the second material, α corresponds to the small shrinkage that accompanies crosslinking. The swelling coefficient, α, is defined as

$$\alpha = \ln \frac{l_{\text{swelled}}}{l_{\text{unswelled}}} \tag{2.2}$$

where l is a given linear dimension of the lens (center thickness, diameter, etc.) For the first material, α ranged from .2 to .7 which correspond to a strain of 22.1% to 101.4%, respectively. For the second material, α was set to -0.0725 (-7% strain.) The degree of completion of the volume change process was represented by a temperature change, with 0° corresponding to the initial state, and 1° representing the final state.

The mesh used for the simulations is shown in Figure 2-1. It consisted of two rows, each with 24 8-node axisymmetric elements (CAX8H, parabolic displacement interpolation, linear pressure interpolation). One node on the central axis was fixed in translation and rotation. The other nodes on the axis were allowed vertical motion and rotation, but were constrained horizontally to remain on the central axis. These displacement boundary conditions prevented rigid body motion, but allowed through-thickness straining along the central axis.

The initial geometry of the mesh is that of an undistorted -3 diopter lens. The

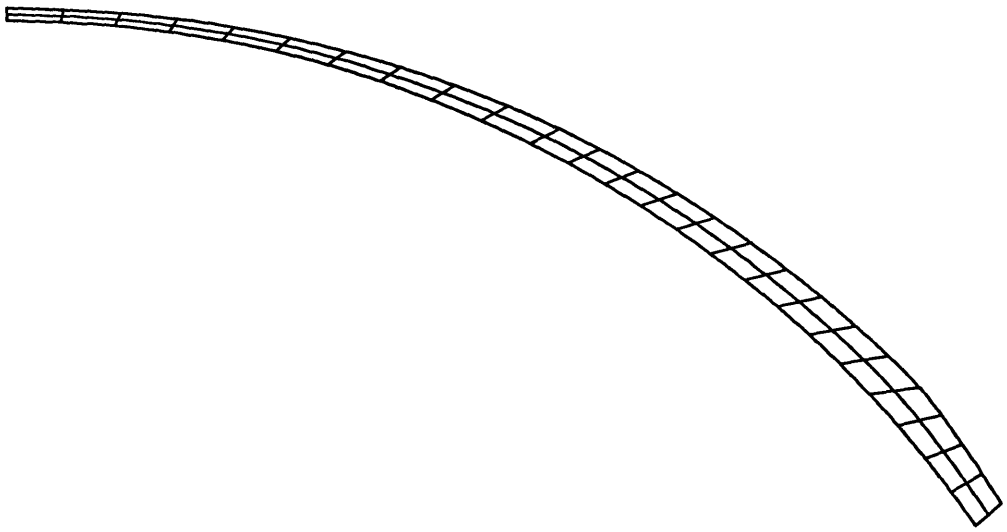

Figure 2-1: Unhydrated mesh used for swelling simulations.

upper surface is constructed of three circular arcs of varying radii of curvature and diameter. Each arc corresponds to one of three lens regions, termed the optical zone, the lenticular zone, and the edge region. (see Figure 2-2) The lower surface, called the basecurve, is made of a single circular arc. The diameter of the lens is 11.05mm, and the thickness varies from 0.071mm at the center to 0.23mm at the thickest part near the outer edge. The geometry of the lens is shown in Figure 2-3.

2.1.3 Uniform Lens Swelling Simulations

The swelling of lenses with uniform material property distribution was first simulated in order to confirm that these lenses would swell uniformly. Five simulations were performed using uniform lenses. For the first three tests, the assigned elastic modulus was 1.2GPa, and the assigned swelling coefficients were 0.2367, 0.344, and 0.6931. A fourth test was run with $\alpha = 0.344$ but with a much more compliant elastic modulus (E = 1.2MPa.) Since the results produced by this trial were identical to those

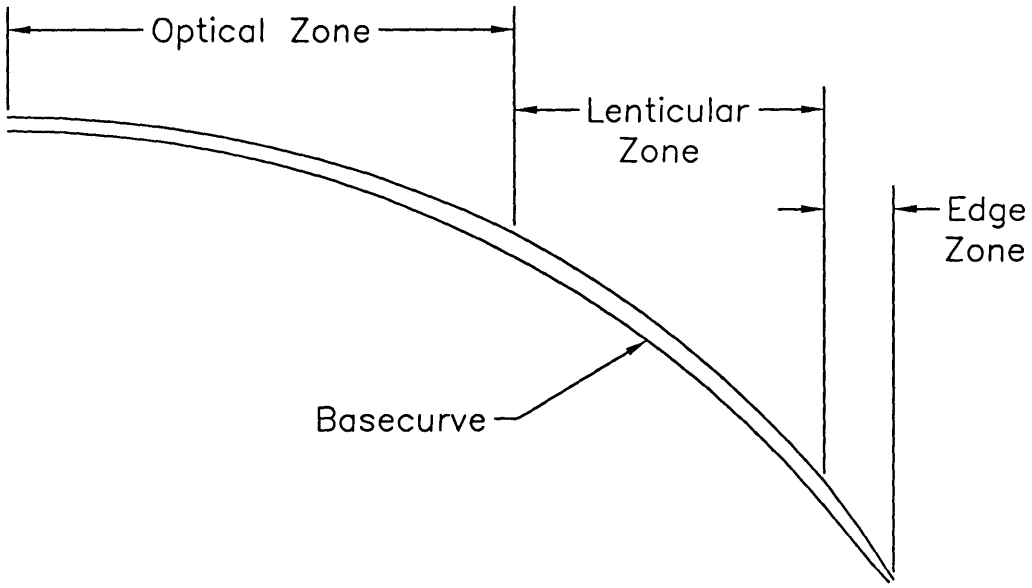

Figure 2-2: Three sections of a lens

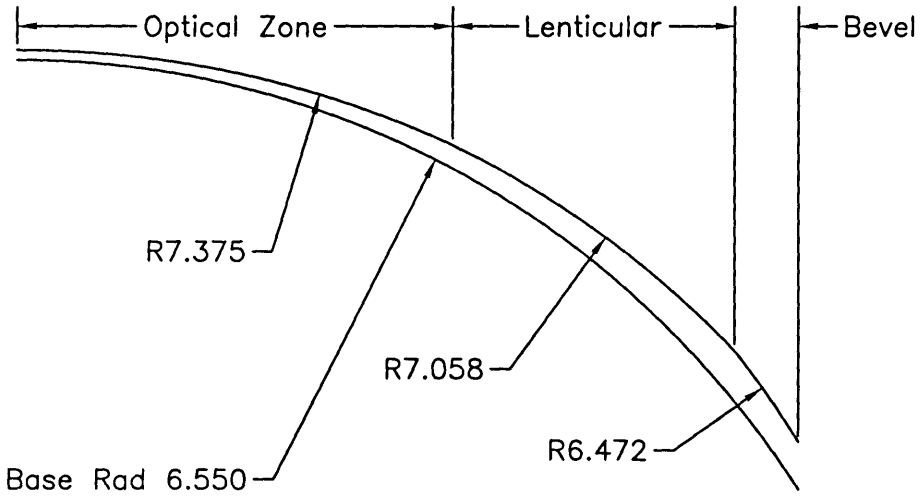

Figure 2-3: Initial values of radii of curvature of unhydrated lens regions.

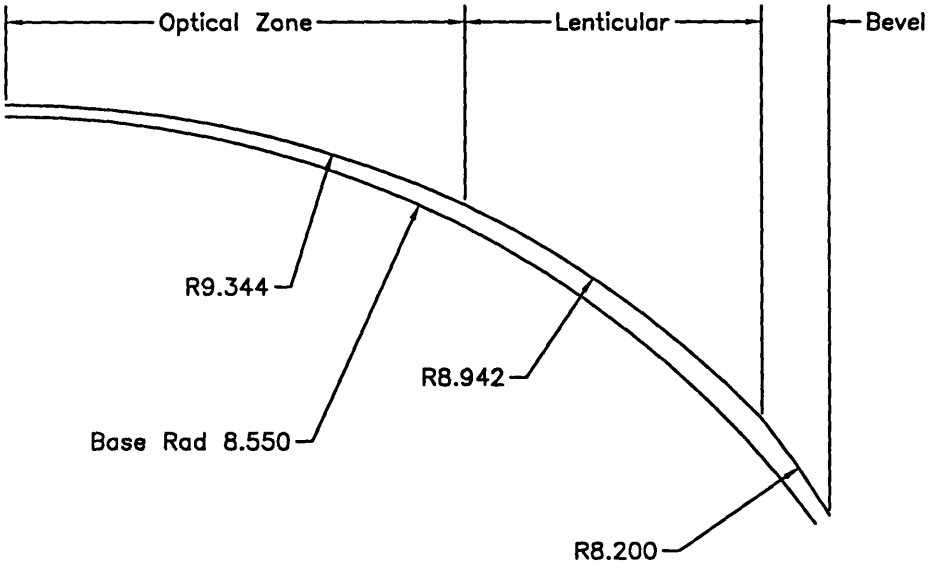

Figure 2-4: Initial values of radii of curvature of swelled lens regions for shrinking simulation.

obtained using the same swelling coefficient with the stiffer elastic modulus, this was the only uniform lens simulation performed with the lower modulus. The final test was a shrinking simulation. The initial mesh geometry was obtained from drawings of a hydrated -3 dpt lens. (see Figure 2-4) For this simulation the swelling coefficient was specified to be -0.344, and the modulus to be 1.2GPa.

Measurement of Hydrated Lens Dimensions

Figure 2-5 shows the final node points of the upper and lower surfaces produced by a typical simulation. The center thickness, lens height, and lens diameter were measured as shown.

The radius of curvature was measured separately for the four different regions: the optical zone, the lenticular zone, and the edge region on the upper surface, and the basecurve on the lower surface. The radius of curvature of each region was found by fitting a circle in the least-squares sense to the nodes within each region. Because

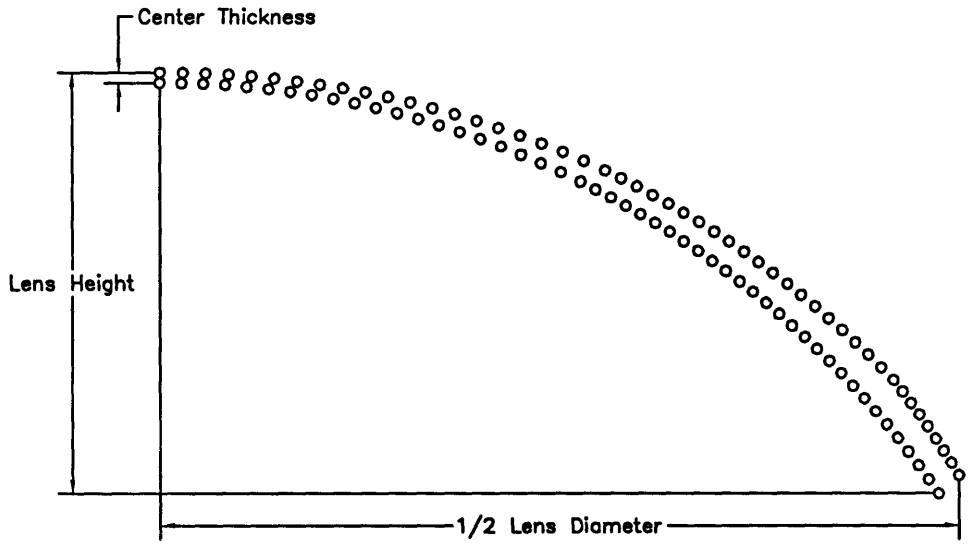

Figure 2-5: Final node points and measurement of overall lens dimensions.

of symmetry, the center of each circle was constrained to lie on the central axis of the lens. The radius of the calculated circle was then taken to be the local radius of curvature of the region.

Results of Uniform Lens Simulations

The results of the uniform lens simulations are presented in Tables 2.1 and 2.2. It was found that in all cases, both the linear dimensions of center thickness, lens height, and lens diameter (Table 2.1) as well as the local radii of curvature of the optical, lenticular, edge, and basecurve regions (Table 2.2) swelled by a factor of e^{α}, just as a single element would. Therefore, it can be expected that if the swelling coefficient and elastic modulus are constant throughout the lens, no shape distortion will occur. The magnitudes of the swelling coefficient and modulus have no effect on the final shape.

Swelling Coefficient,α	Dimension	Final Value	Initial Value	Final/ Initial	e^{α}
0.2367					1.267
	cen. thick.	0.090	0.071	1.27	
	Lens Height	3.66	2.89	1.27	
	Lens Dia/2	7.00	5.53	1.27	
0.344 (E=1.2GPa)					1.41
	cen. thick.	0.10	0.071	1.41	
	Lens Height	4.08	2.89	1.41	
	Lens Dia/2	7.79	5.53	1.41	
0.344 (E=1.2MPa)					1.41
	cen. thick.	0.10	0.071	1.41	
	Lens Height	4.08	2.89	1.41	
	Lens Dia/2	7.79	5.53	1.41	
0.6931					2.00
	cen. thick.	0.142	0.071	2.0	
	Lens Height	5.78	2.89	2.0	
	Lens Dia/2	11.05	5.53	2.0	
-0.344					0.71
	cen. thick.	0.071	0.10	0.71	
	Lens Height	2.54	3.58	0.71	
	Lens Dia/2	4.96	7.00	0.71	

Table 2.1: Overall lens dimensions obtained in uniform lens simulations.

Swelling Coefficient,α	Radius	Final Dimension	Initial Dimension	Final/ Initial	e^{α}
0.2367					1.267
	Base	8.169	6.550	1.25	
	Optical	9.308	7.375	1.26	
	Lenticular	8.680	7.058	1.23	
	Bevel	9.041	6.472	1.40	
0.344					1.41
	Base	9.283	6.550	1.42	
	Optical	10.375	7.375	1.41	
	Lenticular	10.149	7.058	1.44	
	Bevel	9.586	6.472	1.48	
0.6931					2.00
	Base	15.757	6.550	2.41	
	Optical	14.737	7.375	2.00	
	Lenticular	14.125	7.058	2.00	
	Bevel	10.203	6.472	1.58	
-0.344					0.71
	Base	5.972	8.550	0.70	
	Optical	6.604	9.344	0.71	
	Lenticular	5.161	8.942	0.58	
	Bevel	7.643	8.200	0.93	

Table 2.2: Average radii of curvature obtained in uniform lens simulations.

2.1.4 Nonuniform Lens Swelling Simulations

The simulations in this section were designed to test the shape distortion effects of nonuniform material properties within a lens by varying both the spatial distribution of swelling coefficient and elastic modulus as well as the magnitude of variation of these two quantities.

2.1.5 Nonuniform lens simulation cases

The mesh and displacement boundary conditions used for these simulations were the same as those used previously for the uniform lens simulations. The Poisson ratio was again 0.49. In all cases, the elastic modulus and swelling coefficient were modified from reference values of E_0 and α_0, respectively. To simulate the hydration of the lenses made with the two-step material, α_0 was set to 0.344 (41% expansion.) To simulate the shrinkage that occurs during crosslinking of the one-step material, α_0 was set to -0.0725 (7% shrinkage.) For both materials, E_0 was set to 1.2 GPa.

Figure 2-6 illustrates the spatial distributions and magnitude variation of E and α of four cases tested.

In case 1, the swelling coefficient varied from the reference value by mesh layer, with the magnitude of α higher than α_0 on the lower layer, and lower than α_0 on the upper layer. Three trials were run with this distribution pattern, for the first two, $\alpha_0 = 0.344$, and in the third, $\alpha_0 = -0.0725$ In the first trial, the lower layer elements were assigned $\alpha = 1.05\alpha_0$ and the upper elements $\alpha = 0.95\alpha_0$. In the second and third trials, the swelling coefficient varied by $\pm 10\%$ between layers: $\alpha = 1.10\alpha_0$ on the lower layer, and $\alpha = 0.90\alpha_0$ on the upper layer.

In case 2, the spatial distribution of material properties was again divided by layer, but this time both the swelling coefficient and elastic modulus were varied by $\pm 10\%$ simultaneously. i.e. on the lower layer, $\alpha = 1.10\alpha_0$, $E = 1.10E_0$, and on the upper layer, $\alpha = 0.90\alpha_0$, $E = 0.90E_0$. α_0 was set to 0.344.

In case 3, the swelling coefficient was varied only in the edge region. Again, three trials were run, the first two with $\alpha_0 = 0.344$, and third with, $\alpha_0 = -0.0725$ In the

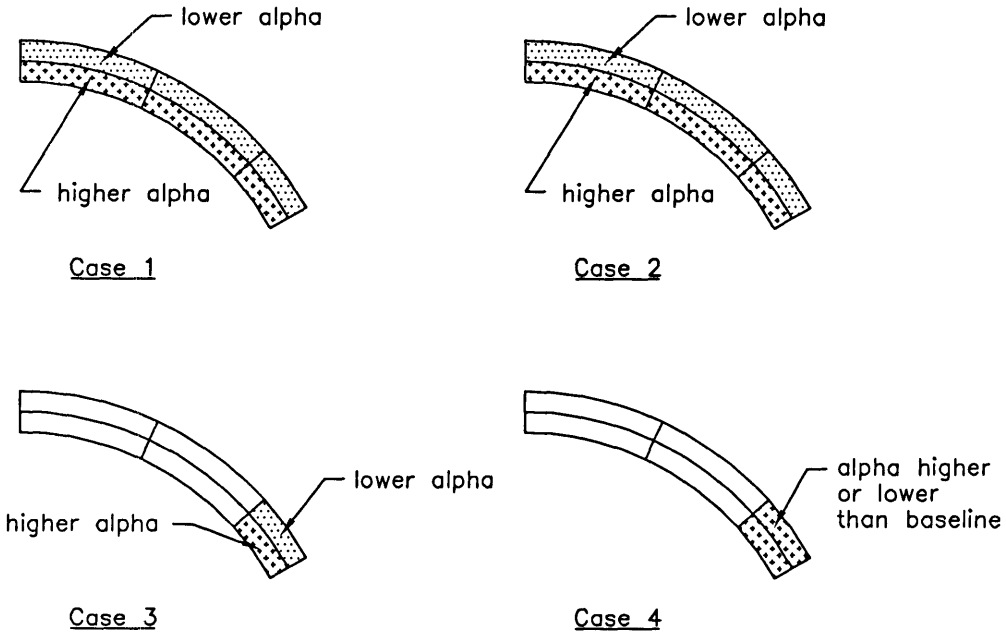

Figure 2-6: Four patterns of nonuniform swelling coefficient and/or modulus distribution tested

first trial, elements in the lower layer of the edge region were assigned $\alpha = 1.05\alpha_0$, and those in the upper layer of the edge region were assigned $\alpha = 0.95\alpha_0$. For the second and third trials, the lower layer of the edge region was assigned $\alpha = 1.05\alpha_0$, and the upper layer of the edge region was assigned $\alpha = 0.95\alpha_0$. For all three trials, the elements in both layers of the optical and lenticular regions were assigned the reference swelling coefficient value, α_0.

In case 4, the same modified swelling coefficient was assigned to elements in both layers of the edge region, and α_0 was assigned to all elements in the optical and lenticular regions. Four trials were run, with $\alpha_0 = 0.344$ in the first two, and $\alpha_0 = -0.0725$ in the second two. In the first and third trials the swelling coefficient in the edge region was $1.10\alpha_0$, and in the second and fourth, the edge region swelling coefficient was $0.90\alpha_0$.

2.1.6 Results of Nonuniform lens simulations

The final lens shapes produced by these simulations are illustrated in Figures 2-7 to 2-13, which show the upper and lower surfaces of the hydrated lenses. In all figures, the hydrated shape of a uniform lens ($\alpha = \alpha_0$, $E = E_0$) is included for reference. The drawing in the lower left hand corner indicates the nature of swelling coefficient and modulus modification for each case. The Figures 2-7 to 2-10 show the results of simulations with the two-step material ($\alpha_0 = 0.344$) and Figures 2-11 to 2-13 illustrate the results of the simulations with the one-step material ($\alpha_0 = -0.0725$.)

In Figure 2-7, the shape distortion due to swelling coefficient variation by layer is illustrated. (case 1) There is noticeable curling up in the edge region that increases as the magnitude of swelling coefficient variation between layers increases. This type of shape distortion is similar to that of the bimetallic disk, whose axisymmetric geometry lead to a parabolic shape after heating.

The distortion when both E and α were modified simultaneously is shown in Figure 2-8. The shape from the $\pm 10\%$ variation of α alone (from case 1) is also included. The nearly identical shapes of the two nonuniform lenses illustrate that variation of the elastic modulus through the lens thickness by 20% has almost no

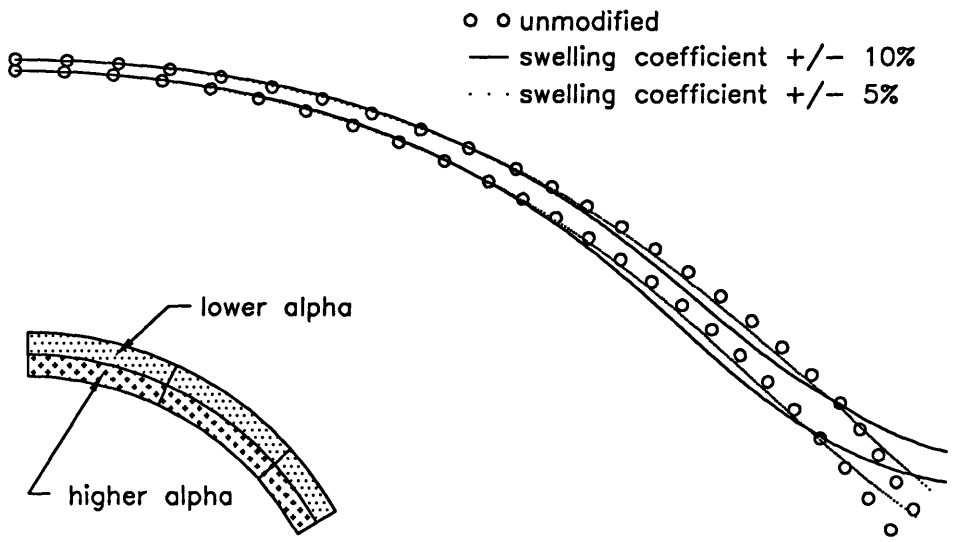

Figure 2-7: Simulation of lens with different swelling coefficient in upper and lower layers. (case 1, $\alpha_0 = 0.344$)

effect on the swelled shape. This result is compatible with the effect of modulus on a bimetallic strip given by equation 2.1. The elastic moduli of the two metals appears in equation 2.1 only as a ratio added to unity. For small differences in elastic modulus, the factor $(1 + \frac{E_2}{E_1})$ will vary only slightly from 2. In contrast, small differences in swelling coefficient have a much stronger effect on curvature since the difference between α_1 and α_2 is included directly as a factor in 2.1.

Figure 2-9 shows the hydrated shape of case 3 when the swelling coefficient varied by layer in the edge region only. Here again there is an increase in the amount of distortion with an increasing difference in swelling coefficient between the two layers. In this case distortion is only noticeable in the edge region, where the swelling coefficient variation was present. The central portions of the lens demonstrated no hydration distortion.

However, such localized distortion is not observed in case 4, when both layers of the edge region had the same modified swelling coefficient. (Figure 2-10) Here the magnitude of the deviation from the uniformly swelled shape is much greater in the

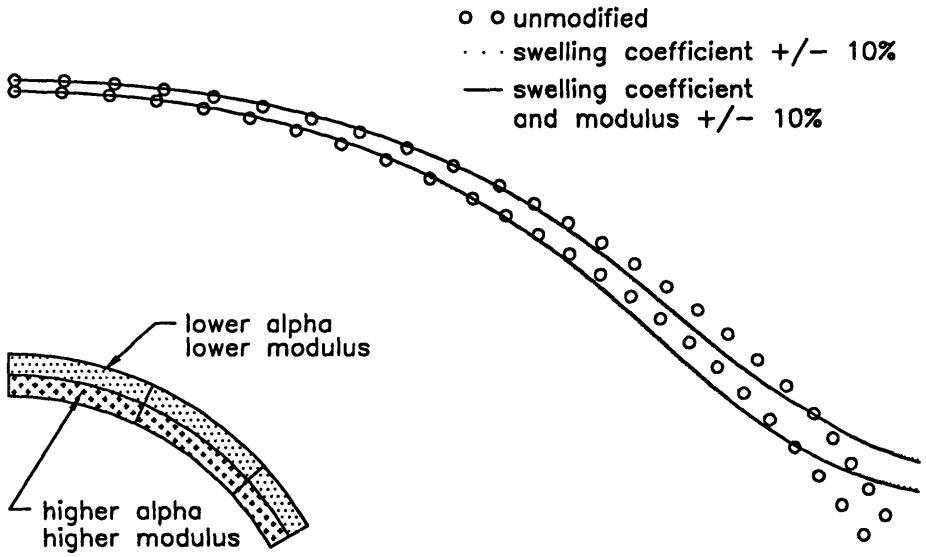

Figure 2-8: Simulation of lens with different swelling coefficient and elastic modulus in upper and lower layers. (case 2, $\alpha_0 = 0.344$)

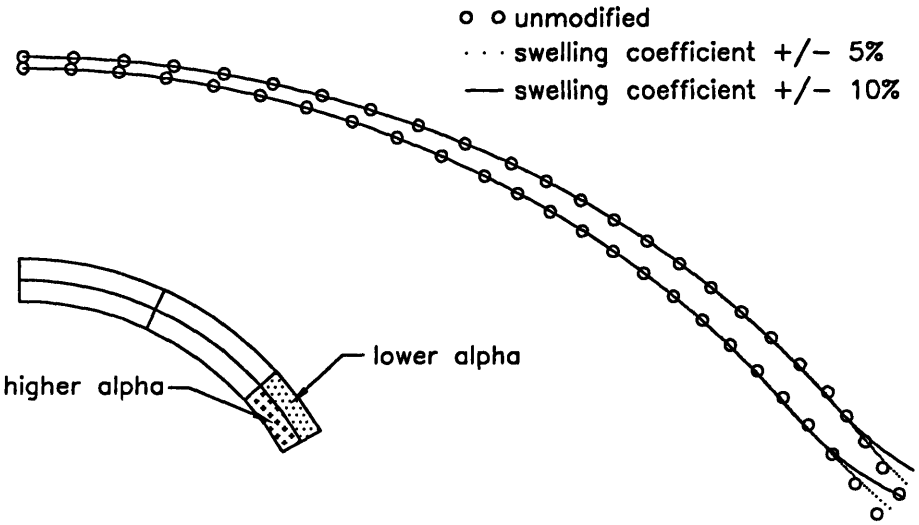

Figure 2-9: Simulation of lens with different swelling coefficient in upper and lower layers of edge region. (case 3, $\alpha_0 = 0.344$)

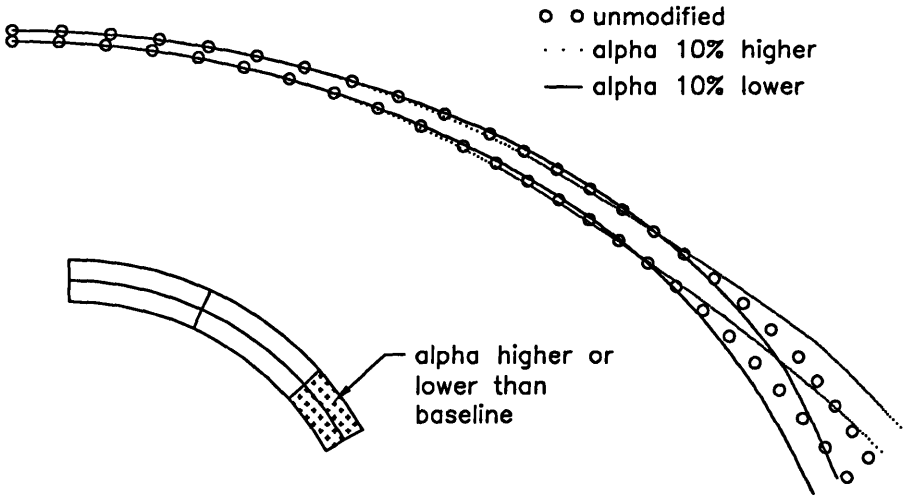

Figure 2-10: Simulation of lens with different swelling coefficient in edge region. (case 4, $\alpha_0 = 0.344$)

edge region than it was in case 3. Also, the region of noticeable distortion extends inward much further toward the center of the lens. This difference is probably due to the fact that in case 4, the overall volume of the edge region increased more (when $\alpha = 1.10\alpha_0$) or less (when $\alpha = 0.90\alpha_0$) than the rest of the lens, while in case 3, the addition volume expansion of the lower layer was compensated by the lower degree of expansion in the upper layer. This balancing of the higher and lower swelling coefficients allowed the shape distortion in case 3 to be contained within a more localized area than it was in case 4.

When α_0 was assigned the smaller value of -0.0725 there are similar distortion tendencies in the final lens shapes, (Figures 2-11 to 2-13) but the magnitude of distortion is much smaller than it is in the corresponding distribution cases with higher α_0.

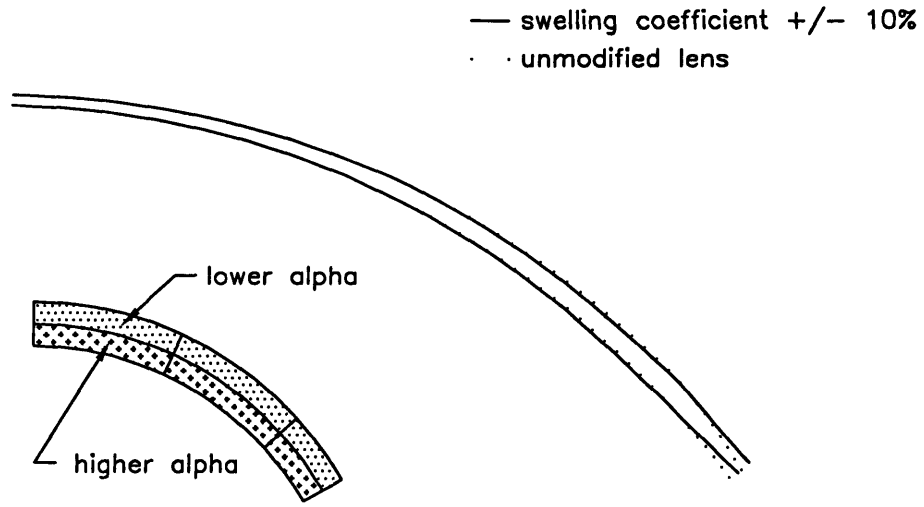

Figure 2-11: Simulation of lens with different swelling coefficient in upper and lower layers. (case 1, $\alpha_0 = -0.0725$)

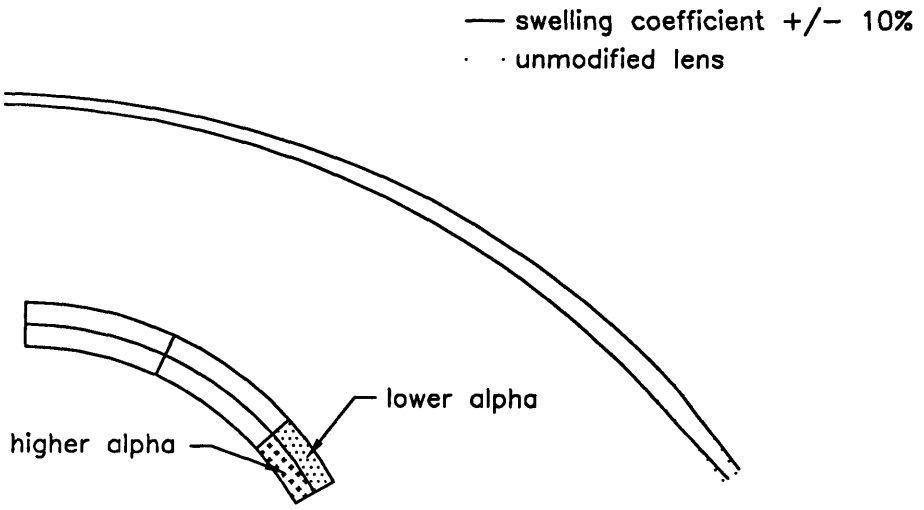

Figure 2-12: Simulation of lens with different swelling coefficient in upper and lower layers of edge region. (case 3, $\alpha_0 = -0.0725$)

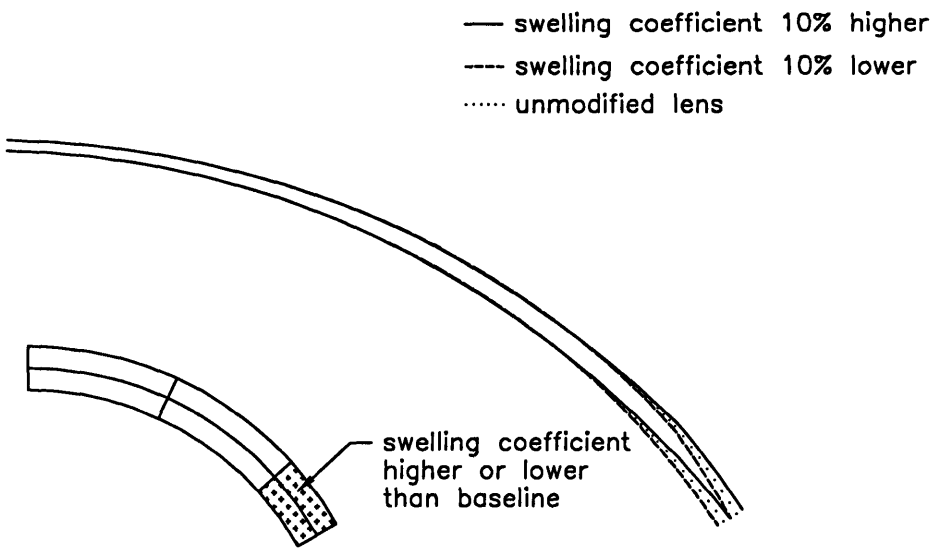

Figure 2-13: Simulation of lens with different swelling coefficient in edge region. (case 4, $\alpha_0 = -0.0725$)

2.1.7 Conclusions from Material Property Distribution Distortion Simulations

The results of these simulations suggest several important properties about lens shape before and after curing. The uniform lens simulations demonstrated that lenses with constant swelling coefficient will shrink or expand without distortion, as one would expect, regardless of the magnitude of the swelling coefficient or elastic modulus. The nonuniform lens simulations in which the swelling coefficient was varied by $\pm 10\%$ from a baseline of $\alpha_0 = 0.344$ illustrated that such a swelling coefficient variation will cause large shape distortion. However, when both the modulus and swelling coefficient were varied by $\pm 10\%$ simultaneously, the resulting lens shapes were nearly identical to those produced by varying swelling coefficient alone, illustrating that the modulus variation had little effect on shape distortion. It was also found that the shape of the edge region was very sensitive to swelling coefficient variation both when the variation occurred throughout the lens, and also when the variation was confined to the edge region. Finally, the simulations run with a very low reference swelling

coefficient ($\alpha_0 = -0.0725$) demonstrated that it is the magnitude of the variation of the swelling coefficient rather than the relative percentage of variation that influences shape distortion.

2.2 Lens Shape Distortion Effects due to Sequential Crosslinking History

In this section, effects of sequential crosslinking on lens shape are examined. These effects are most relevant to lenses formed in the already-hydrated state, which experience a volume contraction of 7% upon crosslinking. The results of the previous section demonstrate that when the overall amount of volume change experienced by a lens during processing is small, variation in the magnitude of the swelling coefficient within the lens of $\pm 10\%$ has only a minor shape distortion effect. (See Figure 2-11. Here $\alpha_0 = -0.0725$.) However, in the laboratory, it was found that shapes of lenses formed in the already-hydrated state ($\alpha_0 = -0.0725$) deviated greatly from the mold shape, in some cases completely curling back on themselves. (See photograph in Figure 2-14.) Therefore, it was decided that the distortion observed in these lenses was not due to local swelling coefficient variation as hypothesized in the previous section. Instead, the idea was investigated that if crosslinking occurred sequentially in various regions of the lens rather than simultaneously throughout the whole lens, internal stresses may be created as regions of the lens attempted to shrink while being restrained by the rigid mold. These stresses might then be locked in as the crosslinking process continued. Upon removal from the mold, these stresses would redistribute to relieve themselves, and attain an equilibrium state, resulting in severe lens distortion.

2.2.1 Related Experimental and Modeling Work

Several experiments and simulations have been performed to measure the effects of constraints on polymers during crosslinking. In this section the work of two authors is described and related to the hydrogel contact lens crosslinking problem: a constrained

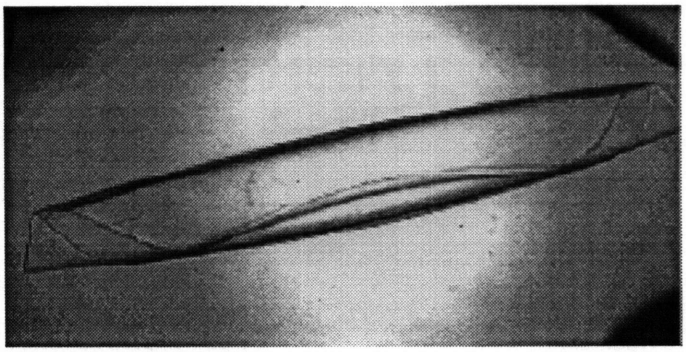

Figure 2-14: Photograph of curled lens

crosslinking simulation by Termonia, [10] and experimental work by Plepys and Farris. [8]

Termonia modeled the crosslinking of elastomers in a state of strain and measured the amount of "permanent set" that remained after the strain constraint had been removed. His modeling involved four steps. In the first step, a square section of a 2-dimensional isotropic polymer lattice was crosslinked at a given percentage, α, of the available crosslinking sites. ($\alpha = 0.33$ or 0.50) In the second step, the partially crosslinked polymer was stretched uniaxially to a given draw ratio [1] that ranged from 2 to 6. In the third step, the remaining crosslinking sites were reacted with their nearest neighbors until the external stress required to maintain the prescribed strain increased by a few percent. In the fourth step, the externally applied constraint was released, and the network was allowed to relax to equilibrium. This final equilibrium state was referred to as the "state of ease."

Termonia found that the macroscopic shape of the polymer in the state of ease was not the same as the original shape prior to crosslinking. He measured this "permanent set" as the ratio of the length of the sample in the state of ease to the initial length. He found that the amount of permanent set increased with increasing draw ratio and with decreasing molecular weight. Of the cases tested, the maximum permanent set measured was approximately 1.8 when the molecular weight was 18, the draw ratio

[1] draw ratio=$\frac{\text{stretched length}}{\text{initial length}}$

was four, and the percentage of crosslinking formed prior to straining (α) was 33%.

Termonia's simulation is similar to the sequential crosslinking process that might occur during the forming of contact lenses. The liquid lens material from which lenses are made is initially a homogeneous polymer, which has the same randomness of crosslinking site distribution as the uncrosslinked polymer network in the simulation. The key characteristic modeled in the simulation was the presence of two stages of crosslinking: one in the initial geometry, and the other in a strained geometry. In the simulation this process occurred in three separate steps, with the straining imposed by an externally applied boundary displacement. In the lens, the crosslinking and straining would occur simultaneously, since the straining is induced by the shrinkage of the polymer that takes place as a result of crosslinking. However, if the crosslinking in the lens did not occur instantaneously, there would be some links formed earlier than others. These earlier links would cause shrinkage, which, coupled with the rigid constraint provided by the mold, would impose strains on those regions of material that had not yet crosslinked. Therefore, the same basic sequence of crosslinking, straining, and crosslinking would be present in the lens, though not in the discrete steps of the simulation.

In the Termonia simulation, the polymer reached its state of ease when the forces on the boundary used to impose the strain were removed. In the state of ease, a final shape different than the initial shape was maintained by the links formed when the material was in its strained configuration. The same phenomenon would occur in the lens, when the forces imposed by the mold were removed, resulting in a final lens shape different from both the initial mold shape and a shape that reflected a uniform 7% shrinkage. One major difference between the simulation and the lens is a directionality constraint imposed on the molecules in the simulation. For computational purposes, the molecules were constrained to move in the vertical direction only. This constraint prevented a shearing-type distortion and resulted in a final shape that closely resembled the initial shape, but that was rectangular rather than square. In the lens, this type of constraint would not be imposed, allowing shape distortion to occur in any direction, and also to occur differentially through the lens

thickness, which could lead to vastly different initial and final shapes.

Experimental work has also been done to determine the internal stresses developed in epoxies cured under mechanical constraint. Plepys and Farris performed a number of experiments to measure these stresses. In [8], they describe a technique for providing a three-dimensional constraint of an epoxy resin during cure and for measuring the internal stresses developed. In this experiment, the liquid resin material was placed in a stainless steel cylinder 6" in length, 3/8" in diameter, with a wall thickness of 0.035". The tube was placed in an environmental chamber and subjected to a heating schedule for curing. The epoxy was first cured isothermally for several hours at a temperature below the glass transition temperature (T_g). The material was then heated to a temperature above T_g, and then slowly cooled to room temperature. Stresses in the epoxy were determined throughout the curing process by measuring the longitudinal and hoop strains on the tube with strain gauges, and then calculating the stress in the epoxy required to impose these measured strains on the tube.

The stresses that develop within a constrained epoxy depend on several factors. One is the amount of volume change experienced by the material. For the epoxies tested by Plepys and Farris, volume change comes from two sources[11]:1) volume contraction due to the formation of chemical crosslinks, and 2) thermally-induced expansion and contraction. The internal stresses developed also depend upon the modulus and Poisson ratio of the material, both of which change during curing. Initially, when the epoxy is in a liquid state, it has a tensile modulus of essentially zero and a Poisson ratio of 0.5. During the isothermal cure, the epoxy begins to gel, and the tensile modulus becomes finite, but the material remains nearly incompressible, with a Poisson ratio of almost 0.5. As the epoxy is heated above T_g, the tensile modulus continues to increase while the Poisson ratio remains near 0.5. When the samples are cooled to room temperature, below T_g, the epoxy is in a glassy state, at which time it has a very high tensile modulus, and is no longer incompressible, with a Poisson ratio of ≈ 0.33.

Plepys and Farris found that the experimental stresses measured were compatible

with the above property changes. During the isothermal curing stage, the internal stresses started at zero, but continuously increased, reaching a level of $\approx$ 8MPa tension by the end of the isothermal curing. The observed increase in stress was due to the three dimensional mechanical constraint preventing contraction due to crosslinking. The increasing modulus during the process acted to amplify the stress levels induced from the constraint. It is interesting to note that the stress level reached during isothermal cure under three dimensional constraint was nearly 100 times greater than that reached in another experiment in which the epoxy was constrained in one dimension only. This is due to the fact that the three dimensional constraint prevented volume contraction, while the one dimensional constraint allowed straining in the two unconstrained directions. The incompressible behavior of the material at this stage resulted in large stresses in the three dimensionally constrained case.

As the temperature was increased, they observed that the internal stresses became compressive, due to the thermal expansion of the material during this stage. Finally, when the epoxy was cooled back to room temperature, the thermal contraction of the material caused internal tensile stress that reached a level of $\approx$ 25MPa by the end of the cooling stage.

The crosslinking of hydrogel contact lens material is analogous to the curing of epoxies, but is also different from the experiment of Plepys and Farris in several ways. First, the crosslinking of contact lens material is caused by UV radiation, in contrast to the thermally-activated curing process of the epoxy used by Plepys and Farris. Therefore, thermal expansion and contraction does not contribute significantly to the volume change of the lens material. The second major difference is that the glass transition temperature of the hydrated lens material is below room temperature, so that at room temperature, it is in a rubbery state and therefore has a much lower modulus than the epoxy did at the same temperature. The T_g of the epoxies tested ranged from $65 - 80°C$, so these materials were in their glassy state at room temperature.

However, the similarities between the two processes allow us to draw a relevant conclusion about hydrogel contact lens processing via irradiation from the results

of the epoxy curing experiment. The first step of the epoxy curing process is very similar to the entire curing process of lens material in four ways: 1) The first step of epoxy curing is isothermal, so no thermally-induced volume change takes place. 2) The epoxy material starts as a liquid and gels to a rubbery state, just as the lens material does. (note that the Poisson ratio of both the liquid and rubbery states is ≈ 0.5 for both materials.) 3) The epoxy material undergoes a volume shrinkage of $\approx 5\%$ due to the formation of chemical crosslinks; the lens material shrinks $\approx 7\%$ during crosslinking. 4) The rigid mold used for contact lens forming provides a three dimensional constraint just as the steel tube did in the epoxy experiment. Therefore, it can be expected that internal stresses would develop during lens curing just as happened in the isothermal stage of epoxy curing. As in the experiment, the internal stresses would be caused by rigid restraint acting against volume contraction and increasing material modulus.

2.2.2 Sequential Crosslinking Simulations

Three types of simulations were performed to investigate the effects of sequential crosslinking on contact lens curing. In the first type, the internal stresses and strains induced in a partially cured lens restrained by a rigid mold are examined. In these simulations, an axisymmetric mesh of a hydrated lens was confined between rigid surfaces whose shape exactly matched that of the initial lens geometry. A central region of the lens was then shrunk by 7% in order to simulate the first part of a crosslinking process that began in the center of the lens.[2] As shrinkage of the central region occurred, the lens was not allowed to distort freely, but was constrained by the rigid mold surfaces. This constraint produced stresses within the lens in its final, partially shrunken state. These stresses were similar to ones that might be locked during a sequential crosslinking process as the remainder of the lens crosslinks. Upon release from the mold, the residual stresses would produce a distortion in the lens shape.

[2]In the irradiation process being simulated, the UV source was centrally located.

The second set of simulations was performed to determine the nature of lens shape distortion that such residual stresses might cause. Here, a three-dimensional mesh was shrunk in central regions of varying shape and size. This time the lens was not constrained, so that the free distorted shape could be examined. This simulation represented an idealized model in which a crosslinking process occurs in two steps. First, the lens center crosslinks and shrinks, causing internal stresses; then, the rest of the lens crosslinks, locking in the stresses created during the first step. If this lens were then released from the mold, its relaxed shape due to these internal residual stresses would be represented by the shape produced in these simulations.

The third set of simulations modeled a laboratory experiment that could be performed to isolate and test for the occurrence of sequential crosslinking and its associated effects. In these simulations, flat, cylindrical disks of several geometries were assigned varying swelling coefficient distribution patterns to simulate different crosslinking histories. The meshes were axisymmetric and were not constrained by mold surfaces so that distorted shapes could be observed.

Constrained Axisymmetric Shrinking Simulations

The first set of simulations was performed to observe the development of internal stresses as a lens sequentially crosslinks and transforms from a fully liquid state to a rubbery solid one. The stresses produced in this process are a result of the shrinking and stiffening that accompanies crosslinking, and the restraining force supplied by the rigid mold surfaces. The model is first described - the geometry, material, and mesh used - followed by the loading conditions. Then, results from two simulations are presented, and the effects of material properties on the residual stress and strain state produced in the lens from sequential crosslinking are examined.

Model for Constrained Crosslinking Simulations The mesh used for these simulations is shown in Figure 2-15. The lens geometry is the same axisymmetric hydrated -3 Dpt lens used in the previous section (Figure 2-1.) As before, two rows of 49 8-node CAX8H elements were used. However, the boundary conditions on

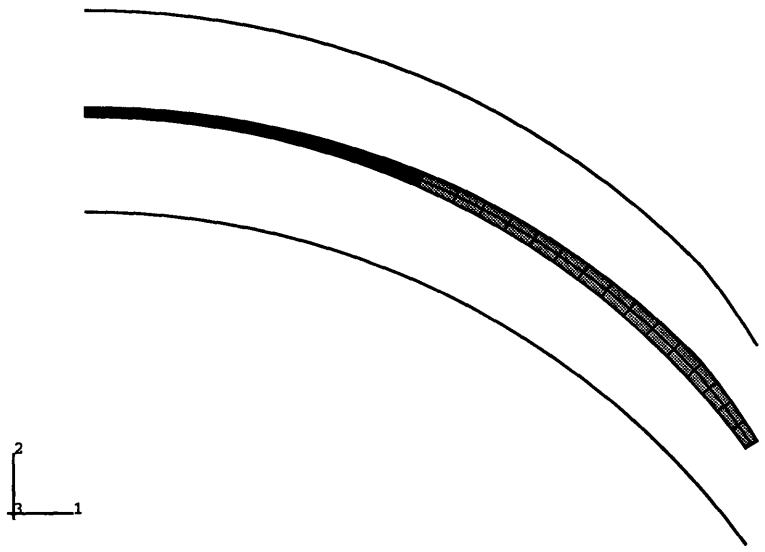

Figure 2-15: Axisymmetric mesh used for constrained shrinking simulation

the central axis were slightly different - all nodes on the axis were prevented from horizontal displacement, but vertical displacement was permitted at all nodes. Rigid body motion was prevented by the presence of the mold surfaces, modeled by the arcs above and below the lens shown in Figure 2-15. These arcs are rigid surfaces which exactly match the shape of the upper and lower lens surfaces, and represent the rigid mold halves. The motion of these surfaces was completely prescribed - first to move vertically into contact with the lens, and then to remain fixed in both translation and rotation. These surfaces were in contact with the lens during the simulation of crosslinking, but here are shown displaced for clarity. Therefore, the model configuration just after the mold surfaces were moved into contact with the lens represented liquid lens material completely filling a rigid mold. Contact between the lens and mold surfaces was monitored with parabolic rigid surface interface elements (IRS22A) located on the upper and lower surfaces of the lens.

All the material for the simulations was modeled as linear elastic, however, the elastic modulus, E, and swelling coefficient, α, were varied in certain regions of the lens to represent material in different stages of crosslinking. Fully crosslinked material was assigned a modulus of 2MPa, while partially crosslinked material was assigned a more compliant modulus of only .5MPa. Likewise, material that was modeled as

shrinking the full 7% was assigned a swelling coefficient of -0.0725, and the non-shrinking material was assigned $\alpha = 0$. A Poisson ratio of 0.49 was used for all materials, since the polymer is nearly incompressible in both its liquid and fully crosslinked, rubbery states.

The crosslinking process itself is difficult to simulate because it is a continuous process that gradually alters both the stiffness and swelling coefficient of the lens material. Therefore, the magnitude and distribution of the internal stresses developed depends on the rate and sequence in which the crosslinking takes place throughout the lens. In order to simplify this complex process, the lens was arbitrarily divided into two sections, and only the first part of the crosslinking process was simulated. The elements at the center of the lens (shown in dark gray in Figure 2-15) represent the material that crosslinks completely in the early part of UV exposure, because of higher radiation intensity, closer proximity to the UV lamp, etc. The outer mesh elements are modeled as material that crosslinks after the center material has solidified. (The light gray elements in Figure 2-15.)

Two loading conditions were prescribed to consider two crosslinking scenarios. The first was designed to show the stress state in the lens after the central region had completely shrunk and stiffened, while the outer region had only partially stiffened (dual-stiffness scenario.) Therefore the central material was assigned $\alpha = -0.0725$ and $E = 2$MPa. The outer material was assumed to not shrink at all, and only to partially stiffen during the first part of crosslinking, so it was assigned $\alpha = 0$ and $E = 0.5$MPa. The second loading condition was designed to approximate the stress state in the lens after only the material in the central region had shrunk, but after all the material had completely stiffened (single-stiffness scenario.) Therefore the inner material was assigned $\alpha = -0.0725$ and $E = 2$MPa, and the outer was assigned $\alpha = 0$ and $E = 2$MPa. Note that both simulations neglect any changes in the stress distribution due to shrinkage of the outer material. For comparison, a third simulation was run to find the stress state in a lens in which crosslinking occurs simultaneously everywhere (single material scenario.) For this simulation, only one, fully crosslinking material was modeled. All elements were assigned $\alpha = -0.0725$ and

Figure 2-16: Constrained mesh before and after central shrinkage

$E = 2\text{MPa}$.

Results of Constrained Axisymmetric Crosslinking Simulations Figures 2-16 to 2-31 present the results of the simulations. In Figure 2-16, the final shape of the partially crosslinked lens is superposed on the initial shape. There is only a slight contraction noticeable at the outer edge of the lens, where the lens was free to slide between the mold surfaces. This figure is valid for both sequential simulations (dual-stiffness and single-stiffness) since the amount of overall lens shrinkage was the same for these two cases.

In Figures 2-17 to 2-31, the coordinate directions for the stress and strain contours are aligned with each element. The 1 direction points tangentially along the lens contour, the 2 direction points through the lens thickness, and the 3 direction points circumferentially around the lens. The directions are aligned with each element, and therefore vary in space from element to element.

Figures 2-17 to 2-19 show the stress distributions produced in the simulation of

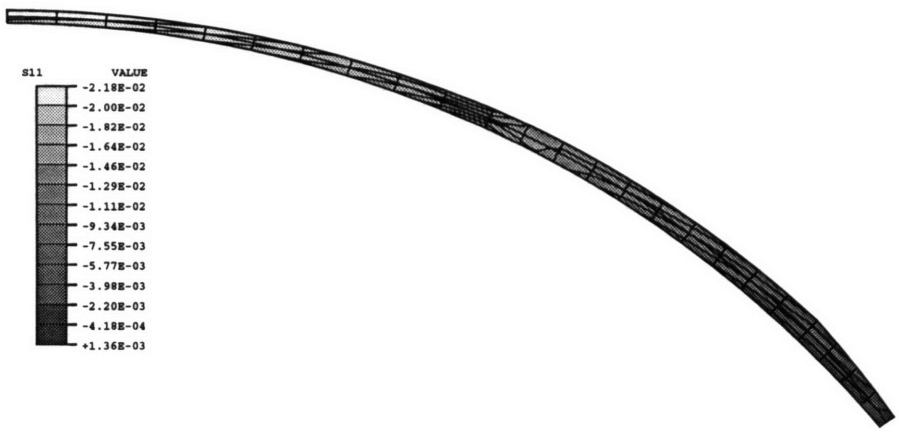

Figure 2-17: Stress in 1 direction after simultaneous shrinkage in single-material lens

a single-material lens of modulus 2MPa crosslinking simultaneously throughout its geometry. Figure 2-17 shows the stress in the 1 direction. Nearly the entire lens is in compression, with values ranging from approximately 1kPa at the outer edge to approximately 23kPa at the center. The stress in the 3 direction, the "hoop stress," is shown in Figure 2-18. In this direction, the stress is compressive in the center of the lens, and tensile at the outer edge. Figure 2-19 shows the stress state in the through-thickness 2 direction. In this direction, there is less clear separation between regions of tensile and compressive stress. The stress throughout most of the lens is nearly constant and falls between approximately $\pm$4kPa.

Figures 2-20 to 2-25 show the stress distributions that arise in the simulations of the sequential crosslinking processes. Figures 2-20 (dual stiffness) and 2-21 (single stiffness) show the internal stress oriented in the 1 direction. The stress is tensile through most of the lens, and that the greatest tensile stress is located in the central portion of the lens. This stress is caused by the thicker, unshrunken outer lens material resisting the contraction of the inner material. This tensile stress is not present in the simultaneously crosslinked lens, (Figure 2-17) where the stress state in the 1 direction is almost all compressive. The hoop stresses produced in the sequential simulations are shown in Figures 2-22 (dual stiffness) and 2-23 (single stiffness.) Again, the

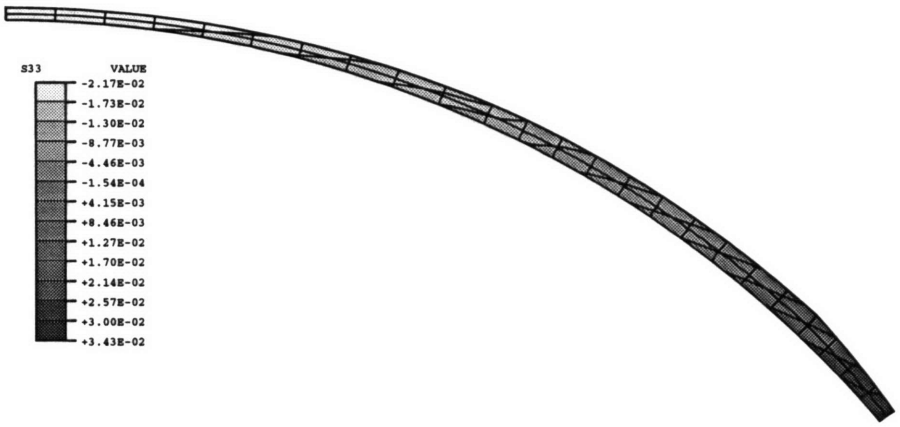

Figure 2-18: Stress in 3 direction after simultaneous shrinkage in single-material lens

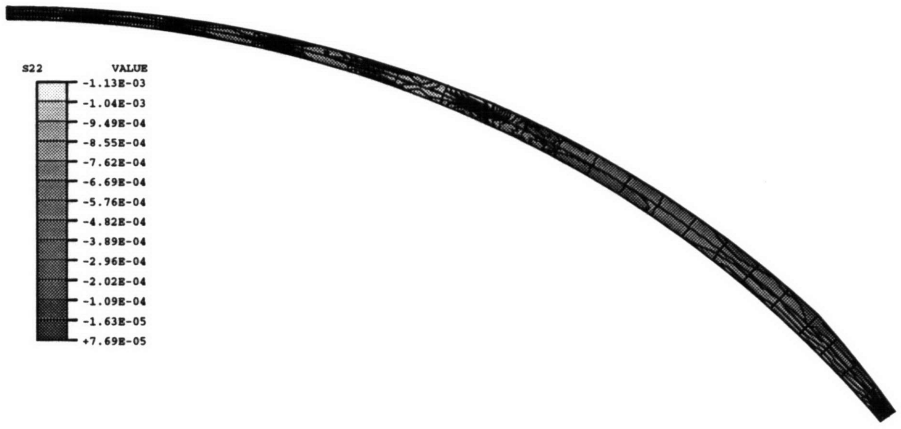

Figure 2-19: Stress in 2 direction after simultaneous shrinkage in single-material lens

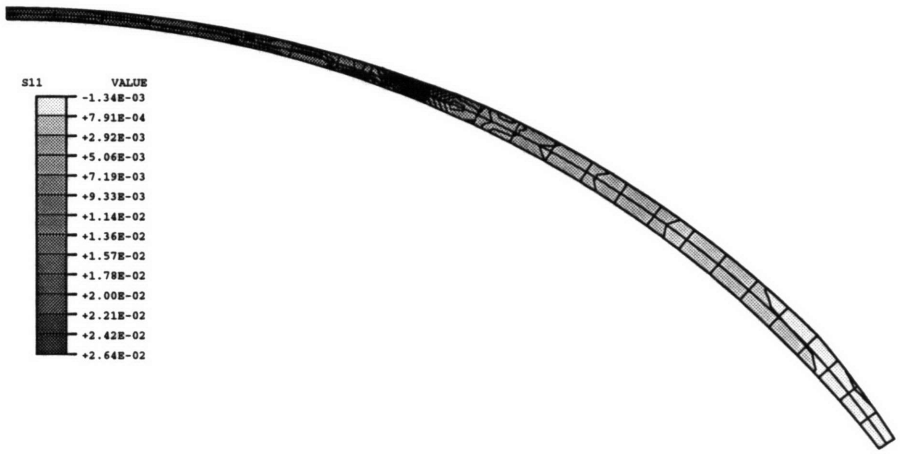

Figure 2-20: Stress in 1 direction after central shrinkage in dual stiffness lens

stress varies along the radius, with tensile stresses toward the center of the lens, and very low circumferential compressive stress at the outer edges. The decrease in hoop stress at the outer edge is due to the fact that at the edge, there is more material to accommodate the central shrinkage, so the amount of strain is less than it is toward the center. In addition, the edge material is farther away from the central shrinking region, so most of the strain compensation occurs in the middle of the lens, leaving the outer edge less affected by the imposed strain at the center. This distribution of the hoop stress - tensile in the center and compressive at the edges - is exactly opposite to that of the simultaneously crosslinked lens, (Figure 2-18) where the central region was in compression and the outer edge was under tension. Figures 2-24 and 2-25 show the stress in the 2 direction. These distributions are similar to that of the simultaneously crosslinked lens shown in Figure 2-19. The magnitude of the through-thickness stress is quite low, and is fairly constant throughout the lens.

In all three coordinate directions, the magnitude of the stress in the sequential simulation in which both materials had $E = 2$MPa (single stiffness) is approximately 4 times as great as the stress produced in the simulation in which the outer material modulus was 0.5MPa, and the inner material modulus was 2MPa. (dual stiffness) This result was expected since the central shrinkage imposed a strain on the lens,

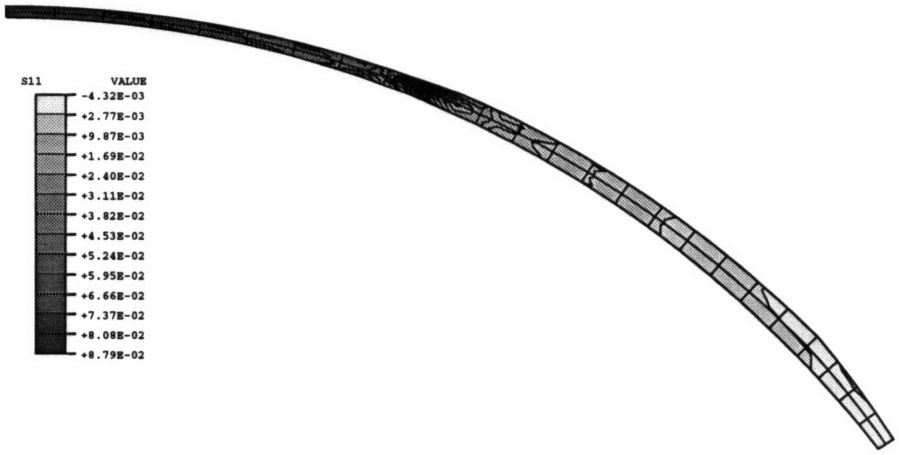

Figure 2-21: Stress in 1 direction after central shrinkage in single stiffness lens

Figure 2-22: Stress in 3 direction after central shrinkage in dual stiffness lens

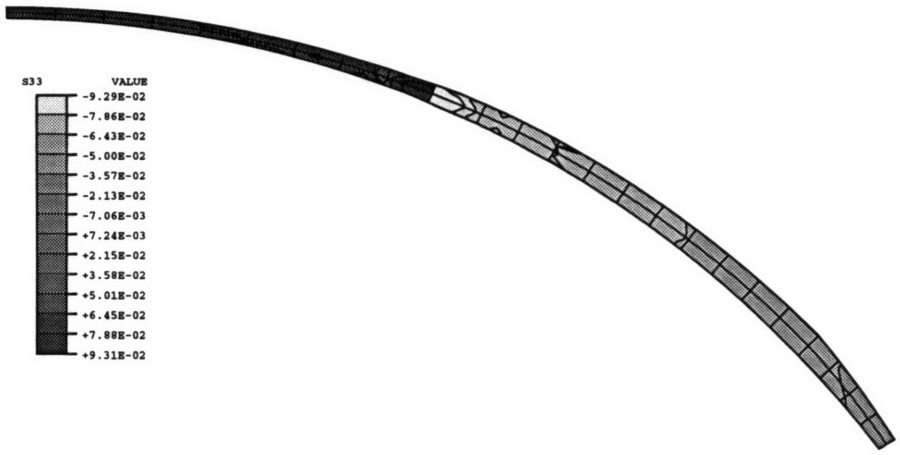

Figure 2-23: Stress in 3 direction after central shrinkage in single stiffness lens

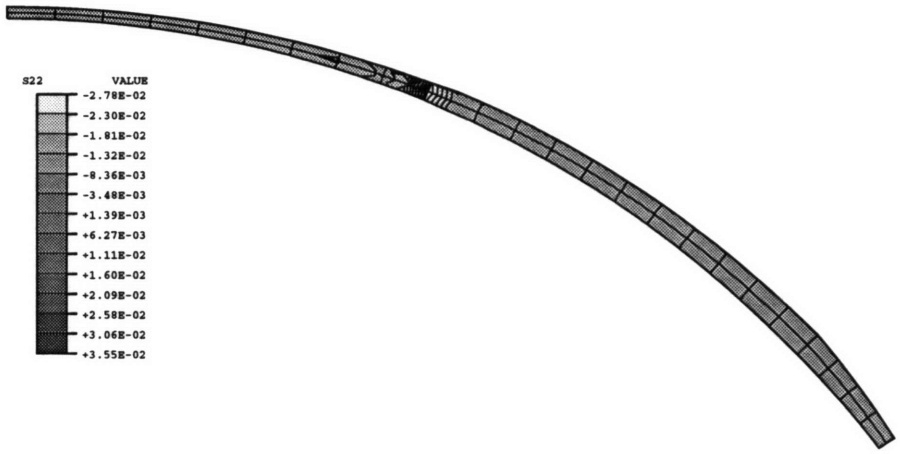

Figure 2-24: Stress in 2 direction after central shrinkage in dual stiffness lens

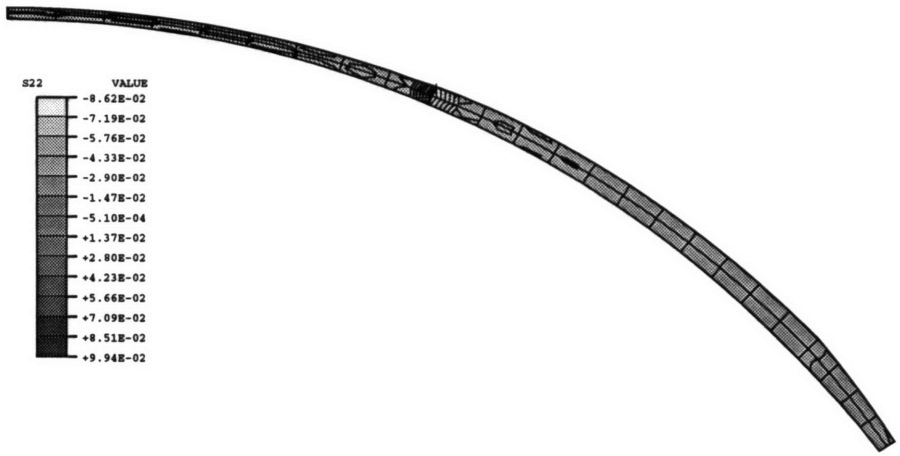

Figure 2-25: Stress in 2 direction after central shrinkage in single stiffness lens

which caused higher stresses in the stiffer material. Another feature common to all the stress contours of the sequential crosslinking simulations is a high stress gradient at the interface between the shrinking and non-shrinking material due to the discontinuity in the material behavior at that point. Since this material discontinuity is not present in the simultaneous crosslinking simulations, this gradient does not appear in the resulting stress distributions.

Figures 2-26 to 2-31 show the strain distributions resulting from the two sequential crosslinking simulations, corresponding to the stress distributions in Figures 2-20 to 2-25. Figures 2-26 and 2-27 present the strains in the 1 direction for the dual-stiffness and single-stiffness shrinking simulations. The effect of the stiffer outer material can be observed by comparing the strain at the lens centers. In the dual-stiffness lens, the 1 direction strain is approximately -0.0626, while the corresponding strain in the single-material lens is only -0.045, due to the greater resistance to shrinkage provided by the stiffer outer material in the second lens. When the central strains in the 2 direction are compared, (Figures 2-28 and 2-29) the opposite result is found. The through-thickness strain in the dual-stiffness lens is only -0.0861 while it is -0.12 in the single-stiffness lens. This difference is due to the Poisson effect and the large Poisson ratio (0.49) which causes greater 2 direction contraction in the lens that

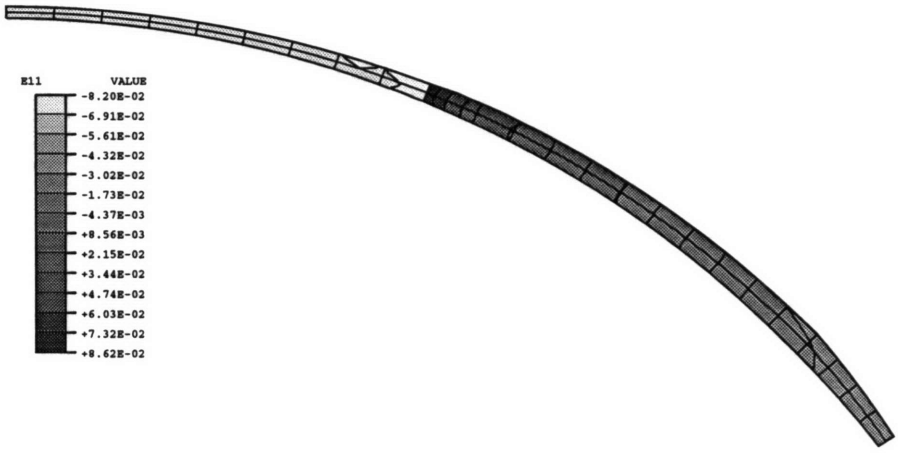

Figure 2-26: Strain in 1 direction after central shrinkage in dual stiffness lens

experiences less 1-direction contraction. Figures 2-30 and 2-31 show the strain in the 3 direction (hoop strain.) Here the magnitude of contraction is consistently greater at all locations in the dual-stiffness lens which has a softer outer portion than in the single-stiffness lens.

The two sequential crosslinking simulations shown here were meant to model the results of two phenomena that might occur in a sequential crosslinking process 1) the locking in of stress, or 2) the locking in of strain. The dual-stiffness simulation yields the stresses shown in Figures 2-20, 2-22, and 2-24, which are the ones that would be present as residual stress if the crosslinking of the outer material locked in stresses. Since these stresses were produced when the outer material had a low modulus, their magnitude would be relatively low in comparison to the stiffness of the outer material once it fully crosslinked and reached its 2MPa modulus. Therefore, the shape distortion upon unloading would be rather small since the outer material would have stiffened and therefore could easily resist distortion from this relatively low level of stress.

The single-stiffness simulation was meant to show residual stresses that would be trapped in the fully crosslinked lens if strains were locked in during the crosslinking of the outer material. In effect, this simulation is a continuation of the dual-stiffness

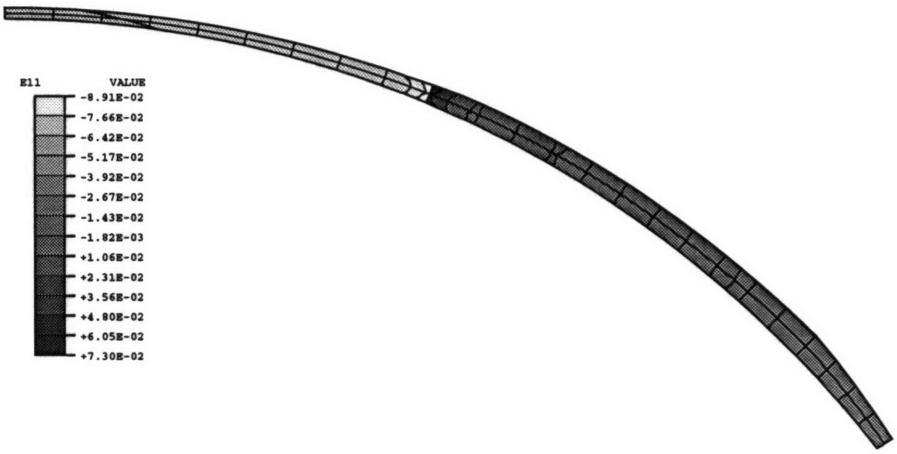

Figure 2-27: Strain in 1 direction after central shrinkage in single stiffness lens

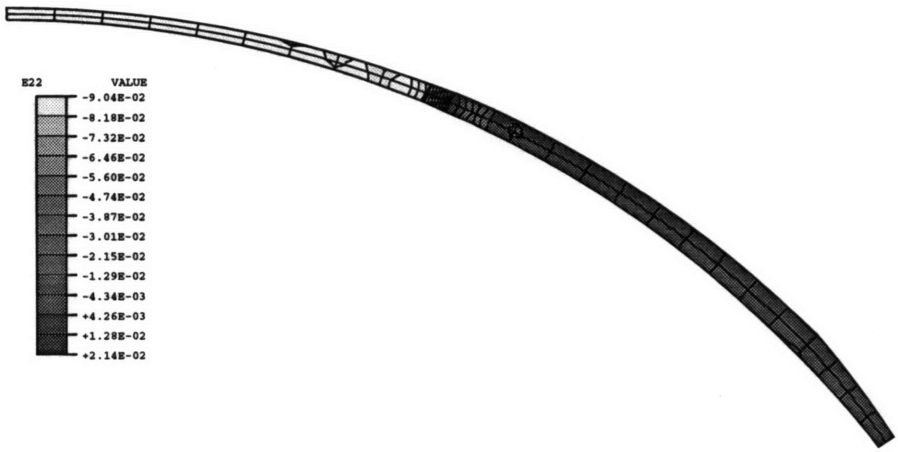

Figure 2-28: Strain in 2 direction after central shrinkage in dual stiffness lens

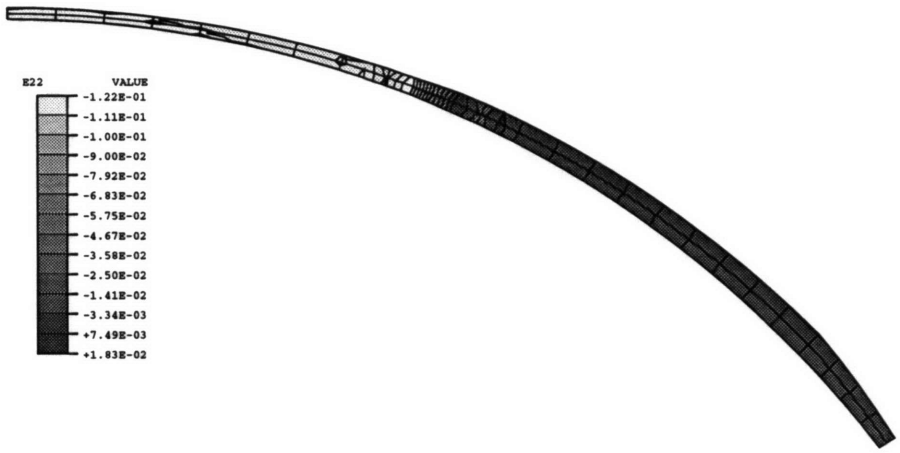

Figure 2-29: Strain in 2 direction after central shrinkage in single stiffness lens

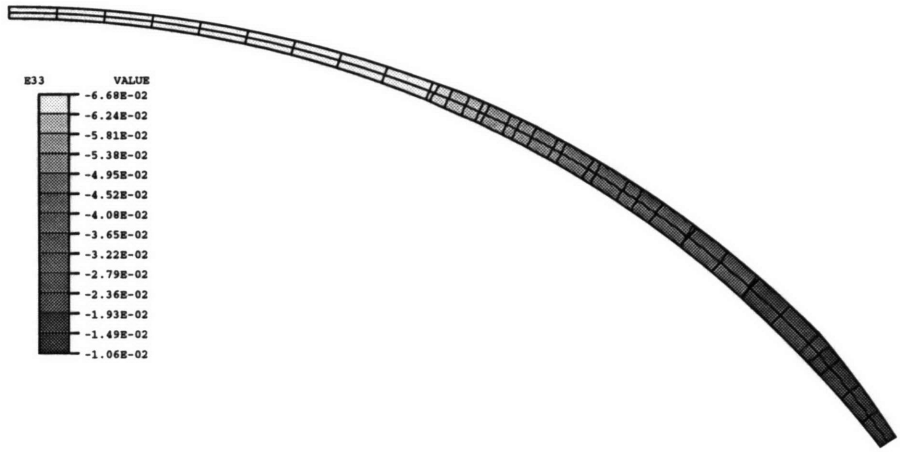

Figure 2-30: Strain in 3 direction after central shrinkage in dual stiffness lens

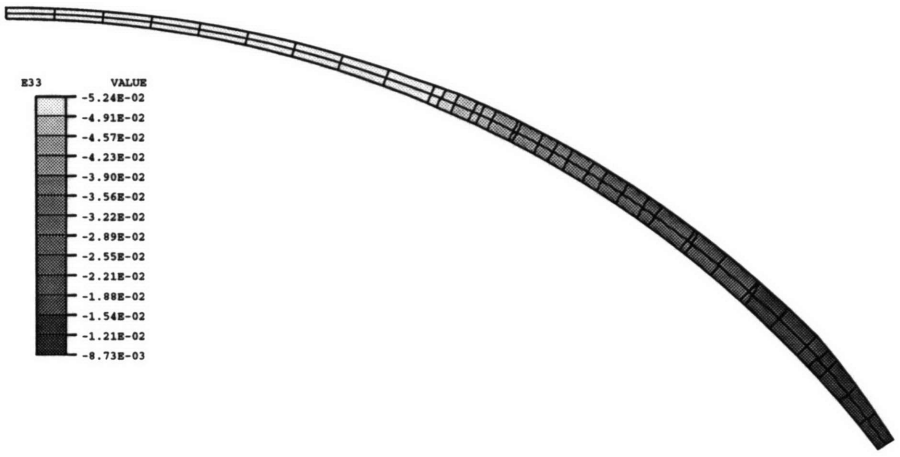

Figure 2-31: Strain in 3 direction after central shrinkage in single stiffness lens

scenario, stiffening the outer material while holding it in the position it reached after the central shrinkage and stiffening occurred. The scenario produced much higher stresses, since stress rises proportionately with modulus at a given strain. This locking in of strains would yield larger distortions than the locking in of stresses modeled in the first scenario since the final residual stresses would be much higher relative to the final stiffness of the lens material.

The stresses depicted in Figures 2-20 to 2-25 represent stresses that may be locked in during a sequential crosslinking process, and that would be present in a final, fully crosslinked lens as internal residual stresses. These stress distributions may cause distortion of the lens upon removal from the mold, which could result in curling of the lens. In the next section simulations are described that are designed to predict the distorted shape of such lenses after removal from the mold.

Three-Dimensional Unconstrained Simulations

This second set of simulations was designed to illustrate the lens shape distortion due to the sequential crosslinking modeled above. For simplicity, only the case in which strains are locked into the material are simulated. (The single-stiffness scenario above, in which both inner and outer elements have a fully-stiffened modulus.) As before,

only the central lens material shrunk by 7% ($\alpha = -0.0725$) while the outer region did not shrink at all. Several simulations were performed with varying nonaxisymmetric swelling coefficient spatial distributions to observe the effect of the geometry of the central shrinking region on the distorted lens shape. The distortions predicted by this model are inaccurate in the respect that the outer lens regions did not experience any shrinkage. However, the simulation does capture the effect of residual stresses similar to those shown in Figures 2-21, 2-23, and 2-25 caused by locking in strain during sequential crosslinking of a constrained lens. This effect of residual stresses on final shape is very large compared to that of the neglected shrinking of the outer material.

3-Dimensional Model for Unconstrained Simulations The mesh for the unconstrained crosslinking simulations is shown in Figure 2-32. Its thickness profile and curvature geometry are axisymmetric, and are the same as those of the -3 dpt hydrated lens used in the previous simulations. Here however, a three-dimensional mesh was used so that non-axisymmetric swelling patterns could be studied. The elements used were 20-node biquadratic bricks (C3D20.) One node on the central axis was fixed in translation in all three coordinate directions, while the other axis nodes were constrained to vertical motion only. In addition, symmetry was specified about the 1-2 and 2-3 planes along the two planar edges. Nonlinear geometric analysis was used in order to accurately model the large shape change. The lens material was modeled as in the constrained simulations as linear elastic ($E = 2$MPa) and nearly incompressible (Poisson ratio=0.49)

Four patterns of swelling coefficient distribution were tested. (See Figures 2-33 to 2-36.) The darker elements were assigned a swelling coefficient of -0.0725 and the lighter elements were assigned $\alpha = 0$. The oblong shapes of the patterns in Figures 2-33 to 2-35 represent a possible crosslink sequence caused by a UV lamp with a filament having a directional orientation. For reference, an axisymmetric swelling coefficient distribution shown in Figure 2-36 was also tested.

The lens was constrained at the nodes on its central vertical axis to prevent free-body motion. One node was pinned, and the others were restricted to motion in the

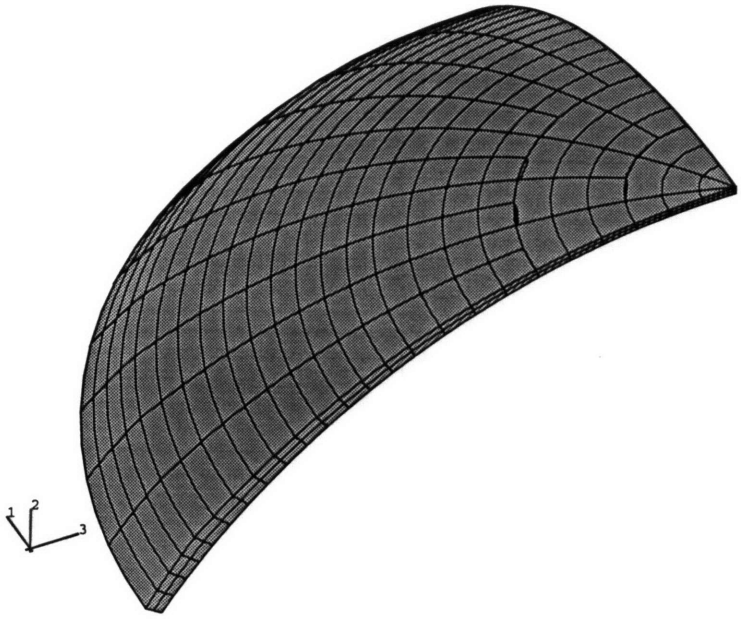

Figure 2-32: Mesh used for 3-dimensional unconstrained simulations

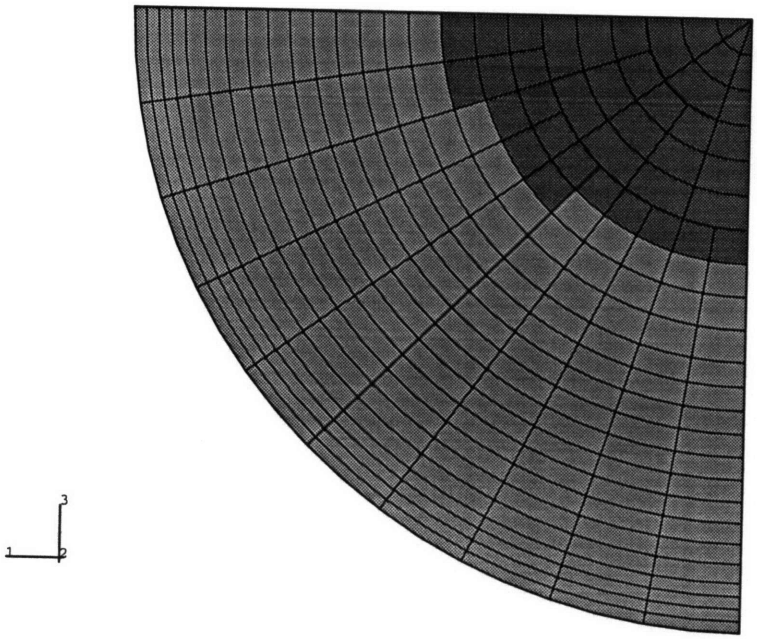

Figure 2-33: Shrinking in small central oval-shaped region

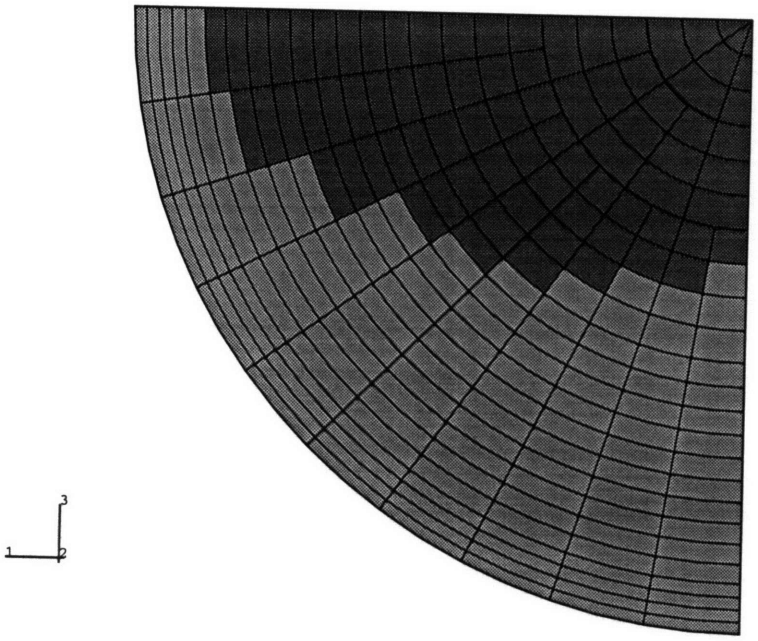

Figure 2-34: Shrinking in large central oval-shaped region

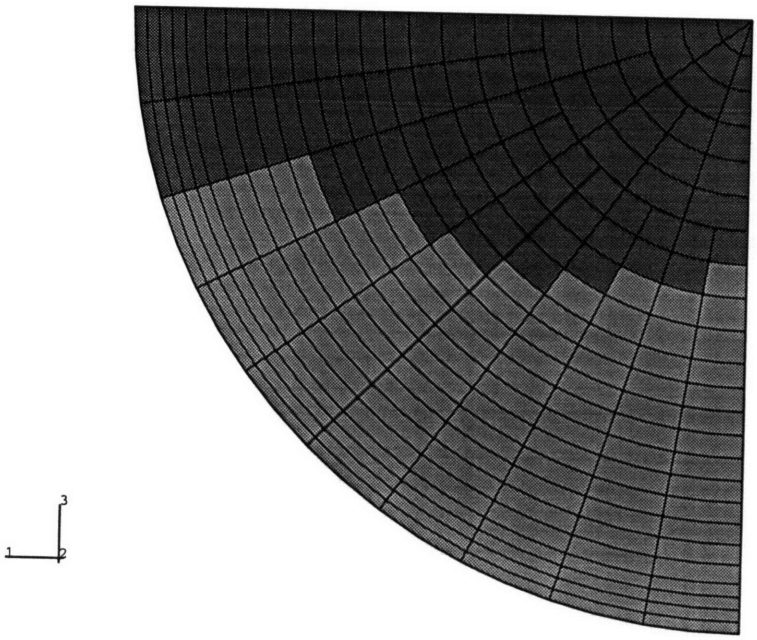

Figure 2-35: Shrinking in strip through center

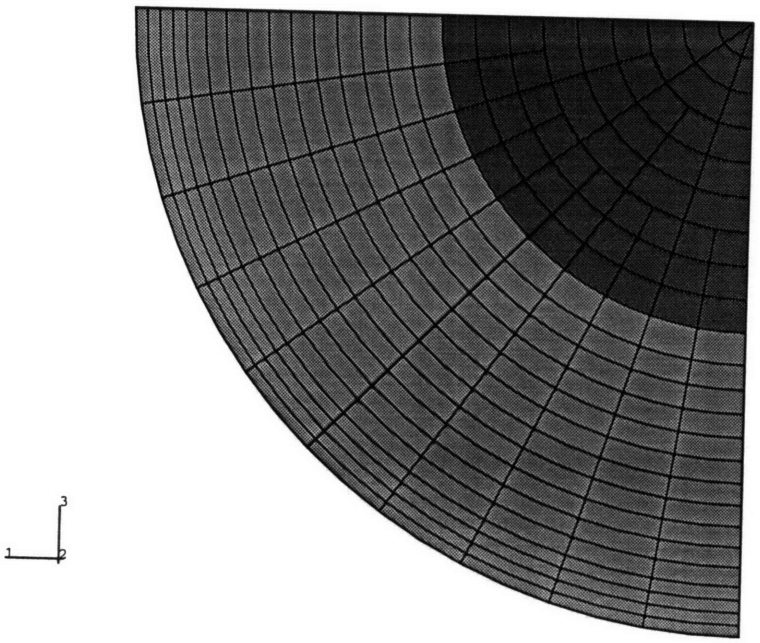

Figure 2-36: Axisymmetric shrinking in central region

through-thickness direction only.

Results of 3-Dimensional Unconstrained Simulations Results of these simulations are presented in Figures 2-38 to 2-40. The four solid lines in each figure represent the midplane lens profile at four different angular cross sections. (See Figure 2-37) For reference, the shape produced by simultaneous shrinking is shown as a dotted line, and that produced by the axisymmetric central shrinking of the lens shown in Figure 2-36 is shown as a dashed line.

The results of the axisymmetric shrinking simulation, demonstrate that such a central shrinkage would yield a lens shape with a significantly flatter central region than that produced by uniform shrinkage. However, the cross-sectional shape would be axisymmetric for both cases. When non-axisymmetric shrinkage histories are specified, variation is produced in the cross-sectional shape around the lens. In particular, the large oval-shaped pattern shown in Figure 2-34 produced the greatest cross-sectional variation. In addition, the lenses with larger shrinking regions (the large oval and

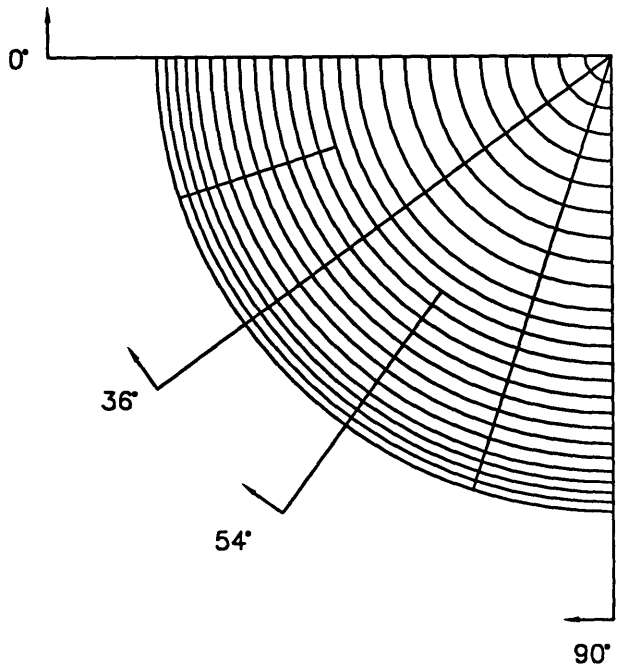

Figure 2-37: Locations of cross sections taken for Figures 1-38 to 1-40

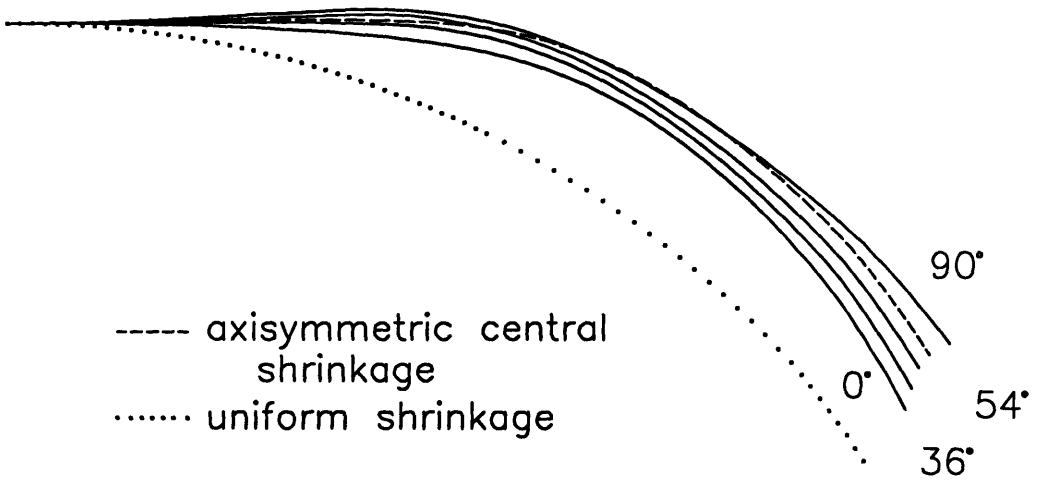

Figure 2-38: Deformed cross section shape for small oval-shaped shrinking region

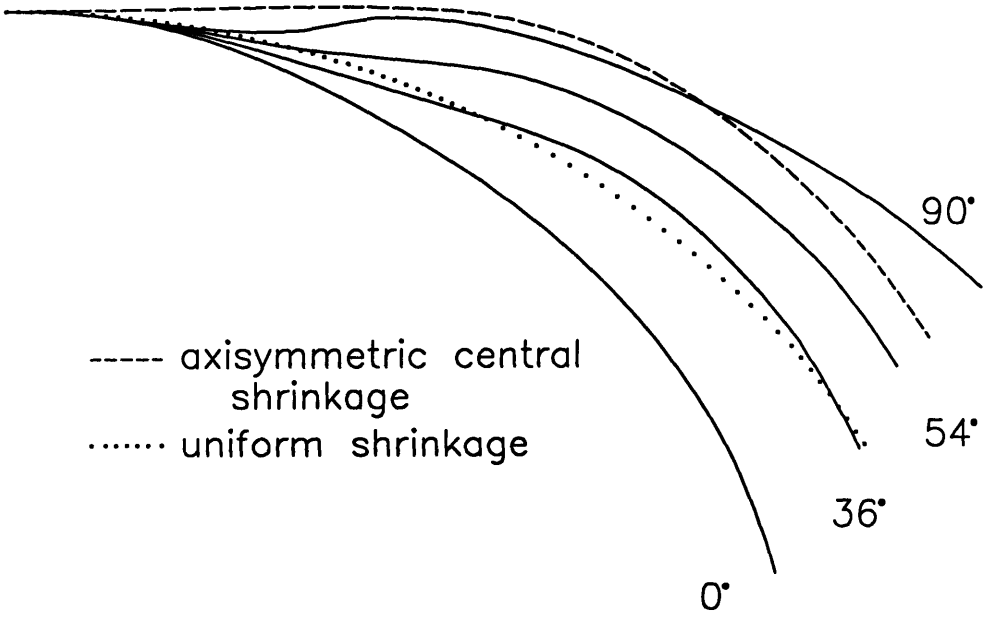

Figure 2-39: Deformed cross section shape for large oval-shaped shrinking region

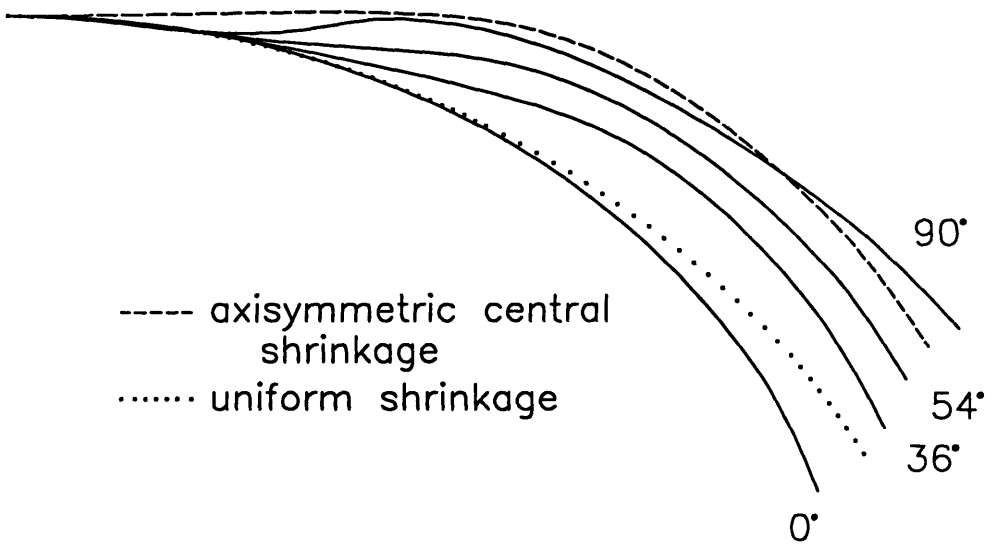

Figure 2-40: Deformed cross section shape for central strip shrinking region

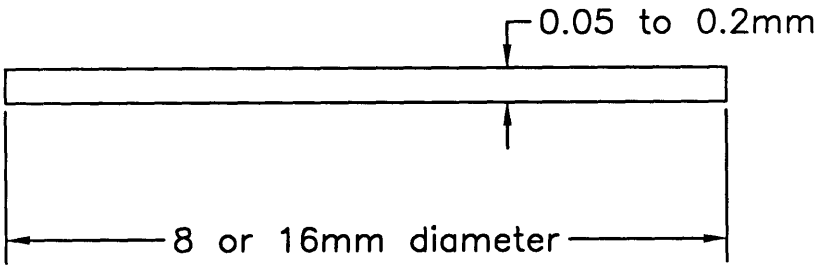

Figure 2-41: Geometry of flat lens blanks used for simulations of a proposed laboratory experiment to evaluate the degree of sequential crosslinking.

strip shown in Figures 2-34 and 2-35 there is not only a central flattening like that produced by the symmetric distribution, but there is also a curling in at the 0° cross section below the profile of the uniform lens. This dual action of curling in along one axis and flattening out on the perpendicular axis is also observed in the actual folded lens (see photograph in Figure 2-14.)

Simulations of blank lens sequential crosslinking experiments

This set of simulations demonstrates a simple experiment that could be performed in the laboratory to assess the degree and nature of crosslinking history. The blank geometry used in these simulations was a flat, cylindrical disk with dimensions similar to those of a contact lens. (See Figure 2-41) The mold for such a blank would be easy to produce, and the flat initial shape would facilitate comparison of various distorted lens shapes. A typical mesh used in these simulations is shown in Figure 2-42. It is axisymmetric and is composed of two or four element layers, each containing 24 quadratic CAX8 elements. As before, the nodes on the central axis were constrained to vertical motion only.

Two groups of simulations were performed to simulate two possible through-thickness crosslinking histories. For the first group, six 2-layer meshes were used. The blanks had thicknesses of 0.1, 0.2, and 0.3mm, and diameters of 8 and 16mm. The upper layer of each blank was shrunk by 7%, and the lower layer was not shrunk

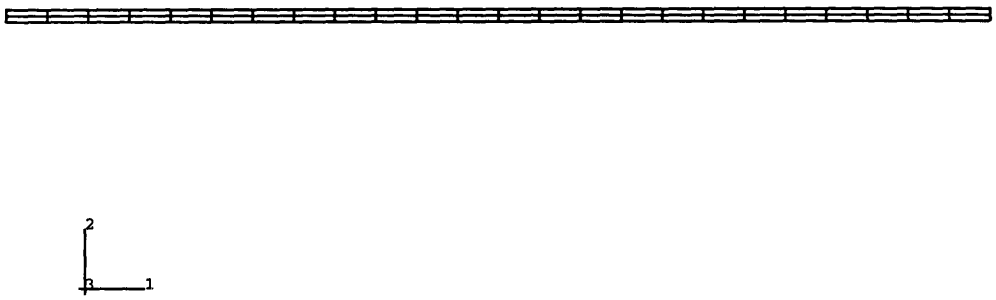

Figure 2-42: Typical mesh used in blank lens experiment simulations

at all.

The final shapes of the 16mm blanks are shown in Figure 2-43, and those of the 8mm blanks are shown in Figure 2-44. For both diameters, the thinnest blank curls sharply at the outer edge while remaining flat in the center, and the thickest blank curls more gently through a greater portion of the blank radius. In addition, the thicker blank geometry results in a greater lifting up. While the same trends are present in both the 8mm and 16mm blanks, the effect of thickness is more pronounced in the 16mm simulation.

For the second simulation group, swelling coefficients were distributed by absolute distance from the upper surface rather than by thickness percentage. Two 16mm diameter meshes were used of these simulations. The first had a total thickness of 0.1mm, and was composed of two layers, each 0.05mm thick. The second mesh was 0.2mm thick, and was composed of four 0.05mm thick layers. The two-layer blank was shrunk by 7% in the upper layer and by 5% in the lower. The four-layer blank was shrunk by 7% in the top layer, 5% in the second, 3% in the third, and 1% in the lowermost layer. The shrinking of this four-layer blank simulated a crosslinking history with a more refined through-thickness gradation.

The shapes produced by these simulations are shown in Figure 2-45. This time, the sharpness of the curling is similar for both blanks, but, as before, the thicker blank lifts up more than the thinner one.

This type of laboratory experiment using simple geometries could serve as a di-

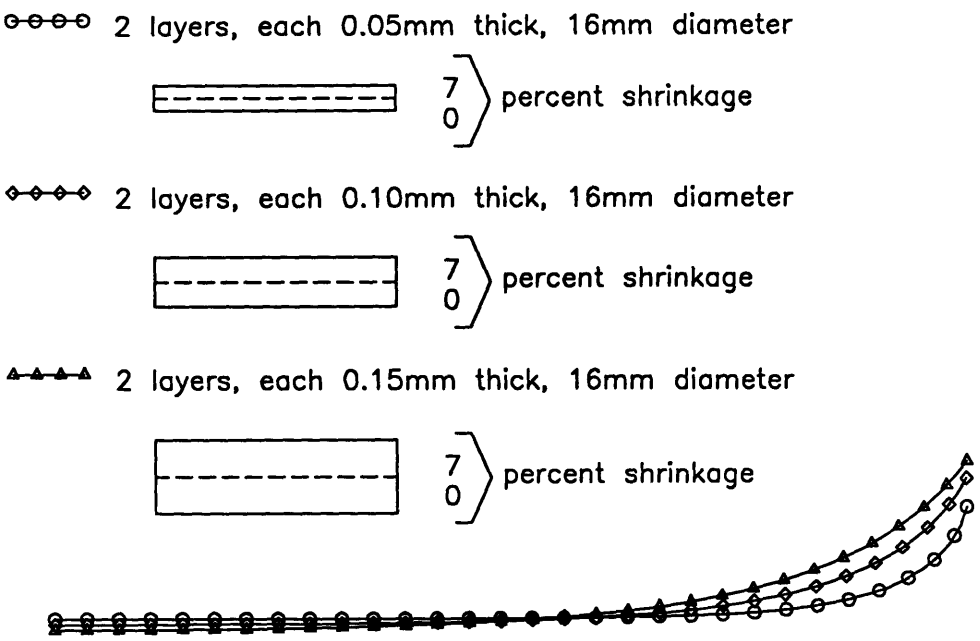

Figure 2-43: Final shapes produced by 16mm diameter blank simulations

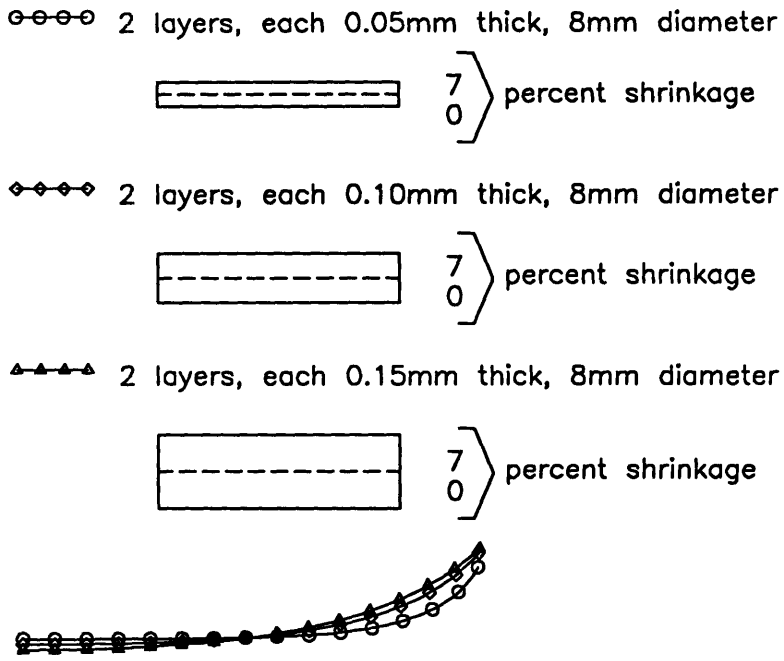

Figure 2-44: Final shapes produced by 8mm diameter blank simulations

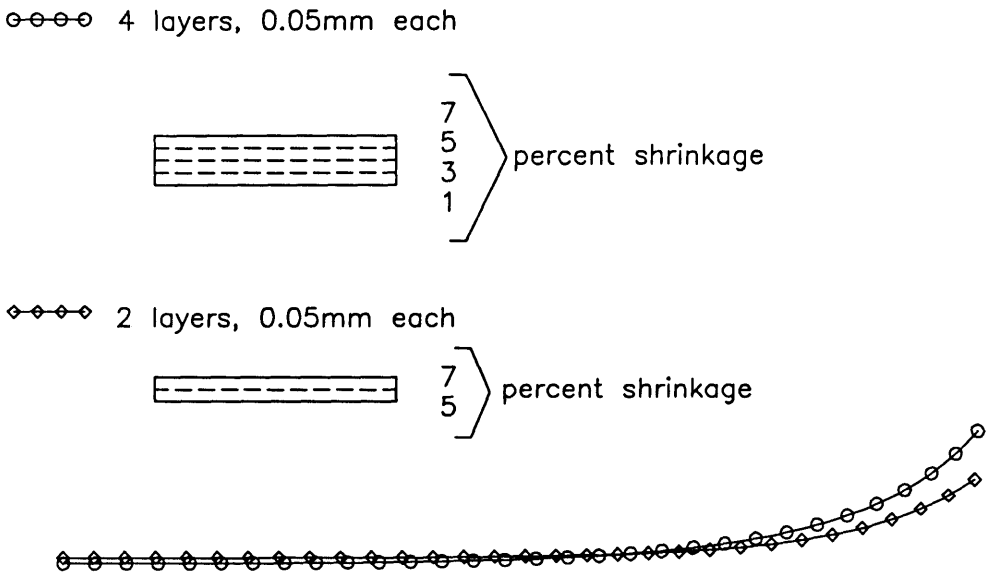

Figure 2-45: Final shapes produced by two and four-layer 16mm diameter blank simulations

agnostic tool to provide a measure of sequential crosslinking. In a typical set of experiments, crosslinking parameters such as the intensity, wavelength, and exposure time of UV radiation could be parametrically varied, and the resulting blank shapes compared to those obtained from simulations such as these in order to determine the effects of processing parameters on crosslinking history. With such an approach, these parameters could be optimized for given lens thicknesses such that lens distortion was minimized and processing was fast.

2.2.3 Conclusions of Sequential Crosslinking Simulations

The constrained and unconstrained sequential crosslinking simulations illustrate results that a non-simultaneous crosslinking process may cause. The constrained simulations demonstrate the development of internal stresses due to the combination of time dependent material shrinkage and the constraining of the lens by the rigid mold. The unconstrained simulations demonstrate the shape distortion effect of such residual stress on the lens upon release from the mold.

While the simulations did not predict curled lens shapes as extreme as those experimentally observed, they do indicate tendencies similar to those experienced in the laboratory. One important effect that this study did not consider is the role of random variations in geometry or material properties that could work in conjunction with the effects illustrated here to trigger a geometric instability. In a lens with no internal residual stresses, such random variation would have little effect on the overall lens shape. However, if residual stresses due to sequential crosslinking were present, these minor variations could lead to buckling of the shell structure and cause a curling up of the lens.

2.3 Conclusions of Lens Processing Simulations

In this chapter two possible causes of lens shape distortion during forming were investigated. The first was spatial variation of material property in a fully crosslinked lens. It was found that with large enough baseline swelling coefficient, variation in swelling

coefficient on the order of $\pm 10\%$ can have a significant effect on final lens shape. However, $\pm 10\%$ variation of modulus has almost no effect. In addition, the magnitude of the shape distortion increases with the baseline magnitude of the swelling coefficient. When the baseline swelling coefficient is small (≈ 0.07) little shape distortion is produced by spatial variation of swelling coefficient by $\pm 10\%$.

The second shape distortion effect investigated was sequential crosslinking history. It was illustrated that if lenses crosslink sequentially in space rather than simultaneously, significant internal stresses can be created. If these stresses are locked in as the crosslinking process progresses, large shape distortion can appear in the lenses. Note that this distortion can occur even when the swelling coefficient is small, unlike distortion due to uneven swelling coefficient distribution. A test with simple blank lens geometries such as the one simulated, could be used to identify the nature of sequential crosslinking history, and, through experimental parametric variation of processing parameters, could be used to minimize or eliminate such shape distortion effects.

Chapter 3

Lens Flexibility

The focus the next two chapters shifts from lens processing issues to lens design issues. In particular, the lens characteristics that determine its fit on the eye are examined. A lens that fits properly on the eye does not remain fixed, but moves with respect to the cornea due to lid pressure and eye motion. This motion pumps fresh tears under and through the hydrogel lens which allows oxygen delivery to the cornea. The tear flow that accompanies lens motion also aids in the elimination of debris that may be trapped under the lens [9].However, excessive lens motion can cause discomfort and reduced vision for the wearer [7].

A number of clinical tests have been developed to determine the quality of fit of the lens on the eye. These include measuring the amount of lag the lens demonstrates when the patient looks up and down or side to side. The relative ease with which the lens is moved from the cornea by applying pressure to the lower lid is also regarded as a reproducible, though subjective, measure of lens fit [13].The outcome of tests such as these is affected by the geometry of the lens, however, the relationships between the lens' geometry and its fit are not well-understood. The goal of this work was to examine how specific lens geometry characteristics affect the lens' overall mechanical response. This mechanical information can then be used to correlate a lens' geometric characteristics to its motion properties on the eye.

In this chapter, the mechanics of the lens itself are examined, independent of its interaction with the eye. It has been reported that an experienced optometrist can

obtain a "feel" of a lens by pinching it between his or her fingers, and then predict how the lens will fit based on this pinch test. This lens pinching was simulated in order to determine the information it provides to the optometrist and which features of the lens geometry determine its mechanical response during a pinch test. Of particular interest is the sensitivity of the pinch test to both subtle and not so subtle changes in lens geometry.

3.1 Finite Element Model

A schematic of the lens pinching modeled in this chapter is shown in Figure 3-1. By measuring the force required to flex the lens, it is possible to determine the stiffness an optometrist would feel by squeezing a real lens. A typical mesh used in these simulations is shown in Figure 3.1. It is made of 8-node quadratic shell elements (S8R) and has an axisymmetric cross section. Due to the symmetry of the lens geometry and of the loading, only one quarter of the lens was modeled. The centermost lens node was constrained to remain on the central axis, but motion was permitted in the 2 direction. Symmetry was specified about the 1-2 and 2-3 planar lens edges. Pinching the lens was simulated by imposing a 3mm displacement in the negative 1 direction on the the outermost edge node. (see Figure 3-1) Figures 3-3 to 3-8 illustrate the progression of the deformed lens shape through the loading process.

A linear elastic, nearly incompressible material model was again used for the lens material. (E = 2MPa, Poisson ratio=0.49) To check the validity of using the linear elastic material model, the strain contours of a fully-deformed lens were examined. It was found that all elements experienced less than 30% strain. In experimental stress/strain material data supplied by the contact lens manufacturer, it was observed that the lens material demonstrated linear behavior to approximately 35% strain. A number of simulations were also performed with a modulus of 0.66 and 0.14 MPa, and it was found that the stiffness response of the lens scaled linearly with modulus, as expected.

Nonlinear geometrical analysis was used in the simulations due to the large change

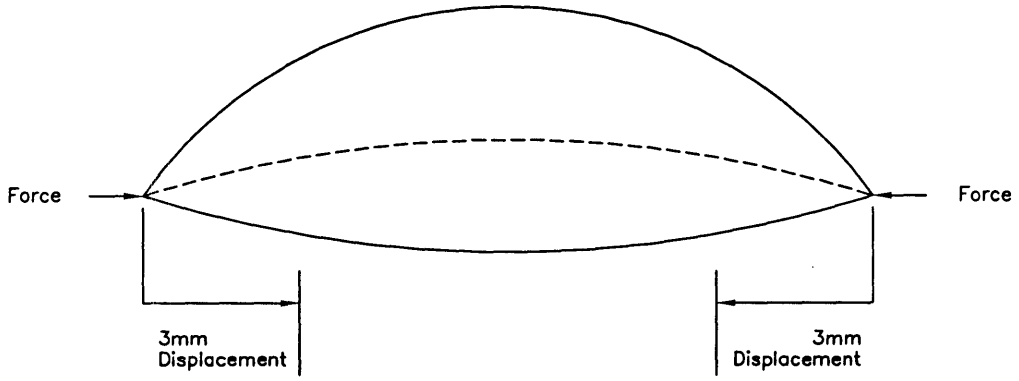

Figure 3-1: Loading of lens

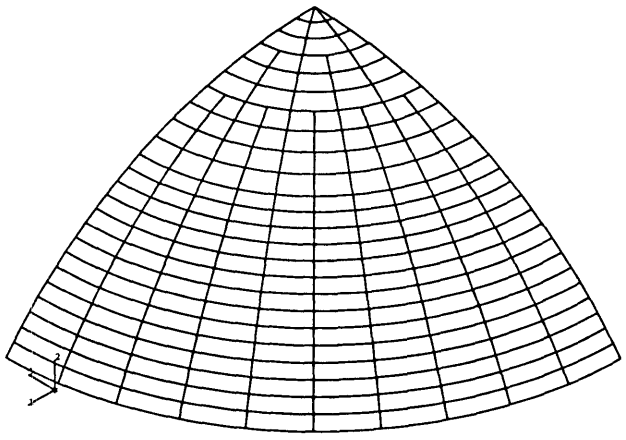

Figure 3-2: Undeformed mesh

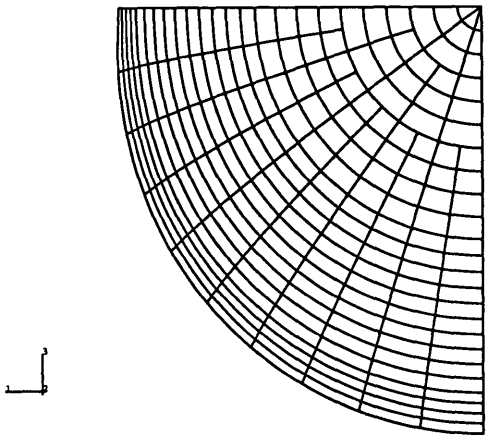

Figure 3-3: Early deformation, top view

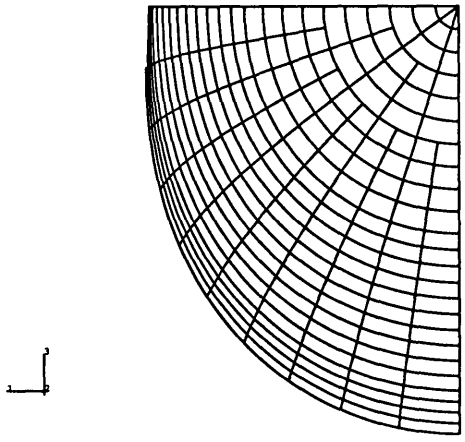

Figure 3-4: Intermediate deformation, top view

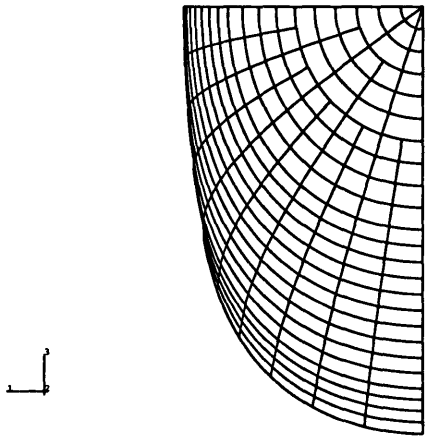

Figure 3-5: Final deformation, top view

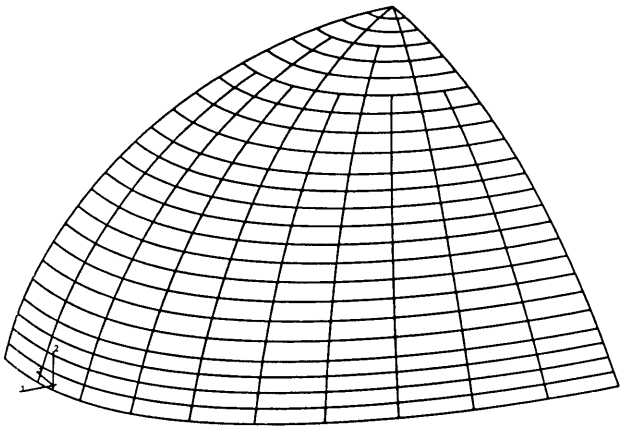

Figure 3-6: Early deformation, angle view

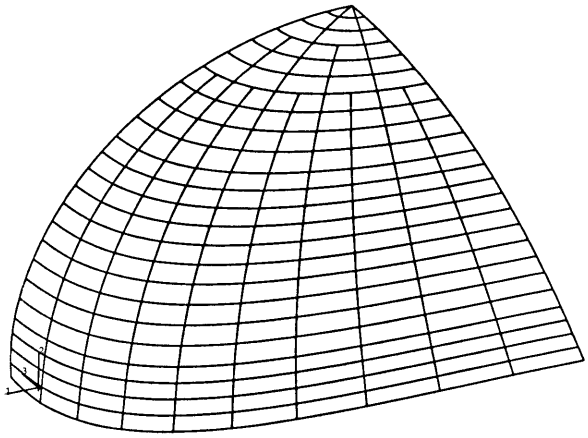

Figure 3-7: Intermediate deformation, angle view

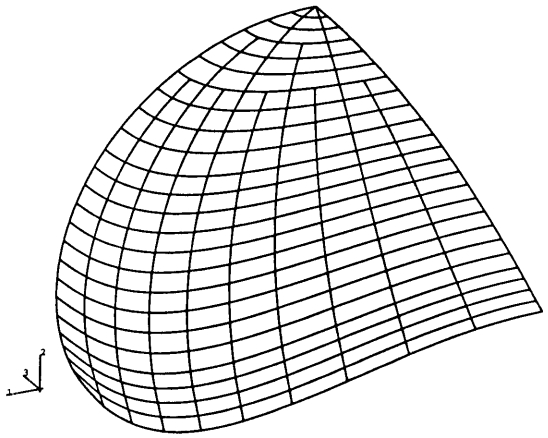

Figure 3-8: Final deformation, angle view

in lens shape that would occur during loading. These changes alter the curvature distribution of the lens shell and therefore influence its flexibility.

3.2 Simulation Cases

Three sets of lens geometries were modeled. First, four families of actual lens geometries were tested (labelled F88, G88, H88, and I85.) The thickness profiles of these lenses are shown in Figures 3-11, 3-13, 3-15, and 3-17. The edge design of the lens was the same within each family, but varied between families. The lenses all had one of four center thicknesses, (approximately 0.09, 0.011, 0.13, or 0.15mm) and all lenses within one family had a different center thickness. The radius of curvature of the lens surface that contacts the eye was 8.8mm for the F88 G88 and H88 lenses, and 8.5mm for the I85 lenses.

Next, a set of blank lens shapes which had constant thickness and radius of curvature were tested. A series of simulations was run in which both the thickness and radius of curvature were adjusted independently in order to determine the effect of each of these parameters on the lens stiffness response. Five thicknesses were tested that spanned the range of the central thicknesses of the actual lenses. (0.08, 0.90, 0.10, 0.125, and 0.13mm) These lenses all had a radius of curvature of 8.5mm. Three more blanks with a radii of curvature of 8.5, 8.65, and 8.8mm, respectively, were tested. These three blanks had a constant thickness of 0.90mm. Again, the values of radius of curvature tested spanned the range of curvatures of the actual lenses.

Finally, a second set of blank geometries was tested to determine the influence on stiffness of the thickness of the individual optical, lenticular, and edge regions. (see Figure 3-9) Three blank geometries were tested in this set, each with a thickness of 0.125mm in one region (optical, lenticular, or edge) and a thickness of 0.1mm in the two remaining regions. In these blanks, diameters of the optical, lenticular, and edge regions were 6.65, 12.26, and 14.0mm, respectively. The radius of curvature of all three of these blanks was 8.5mm.

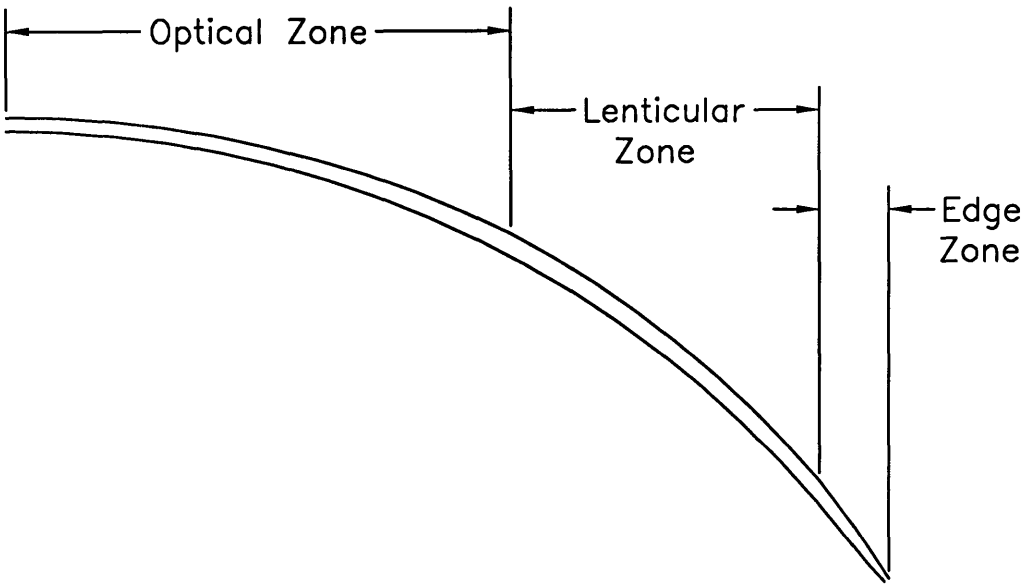

Figure 3-9: Three sections of a lens

3.3 Results of Simulations with Actual Lens Geometries

Figures 3-10 to 3-23 show the results of the simulations of actual lens geometries, cross plotted in two ways to best depict the effects of various thickness profiles. Two graphs are shown for each grouping. The first represents the overall stiffness of the lens, where the horizontal displacement of the outermost edge node is plotted against the reaction force at that node. The second graph shows the thickness profile of each lens. In the second graph, the perpendicular distance to the central axis is plotted on the horizontal axis, and the thickness, which is measured perpendicular to the basecurve radius, is plotted on the vertical axis.

In Figures 3-10 to 3-17, lenses are grouped by family. As mentioned above, the thickness profiles of the optical and lenticular lens regions vary within a family, however, the edge regions of all lenses in a family are nearly identical. In each case, the

stiffness increases with increasing overall lens thickness. Figures 3-18 to 3-23 plot the same data as Figures 3-10 to 3-17, but these graphs compare lenses from different families that have approximately the same center thickness. In all three cases, the H88 lenses provide a stiffer response than the F88 and I85 lenses. This corresponds to additional thickness in the lenticular region of the H88 lenses. Figures 3-20 and 3-22 show that the G88 lenses are more compliant than the F88 and I85 lenses. This is reasonable since the G88 lenses have a much thinner lenticular region than the other lenses. It is interesting to note that for a given center thickness, the optical zone geometry of lenses from different families is nearly identical. Therefore, differences in stiffness response between lenses having the same center thickness are due entirely to variations in the lenticular and edge regions.

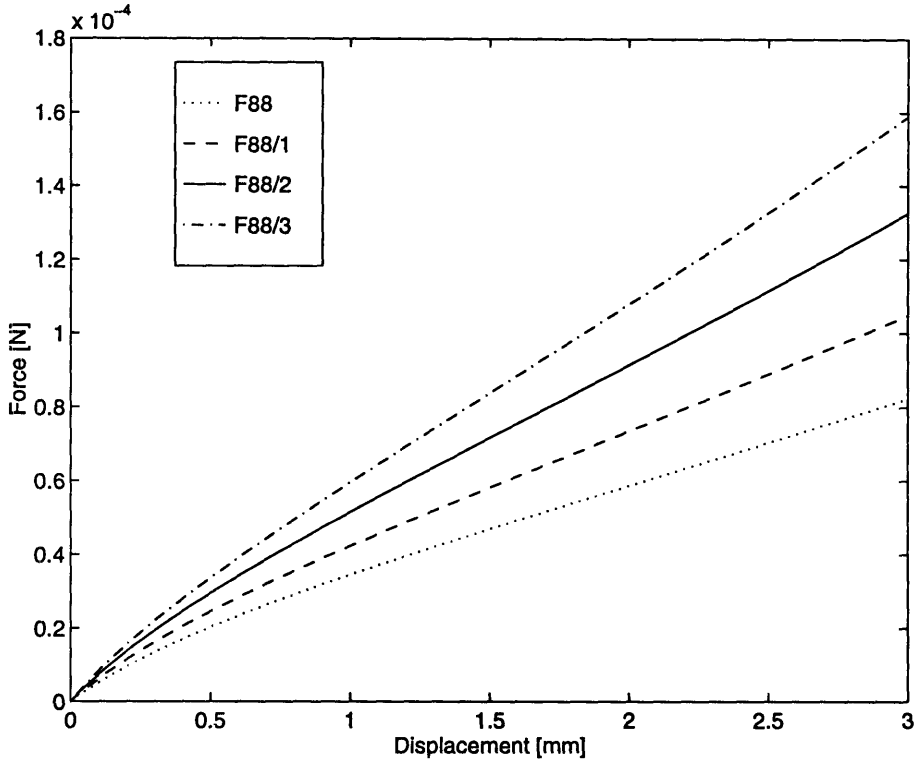

Figure 3-10: F88 series force-displacement

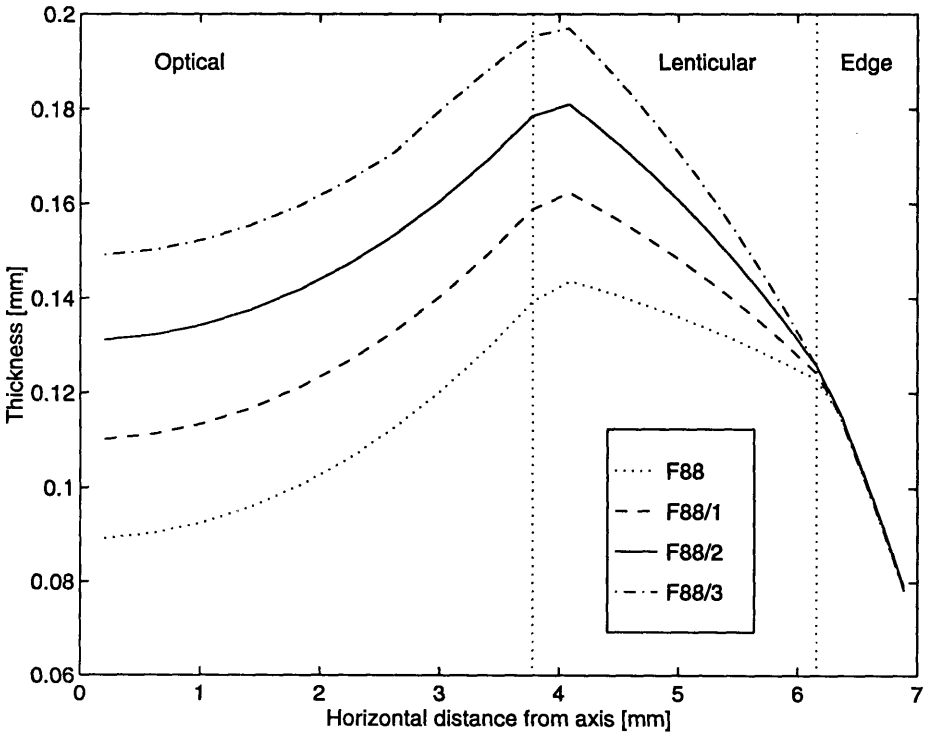

Figure 3-11: F88 series thickness profile

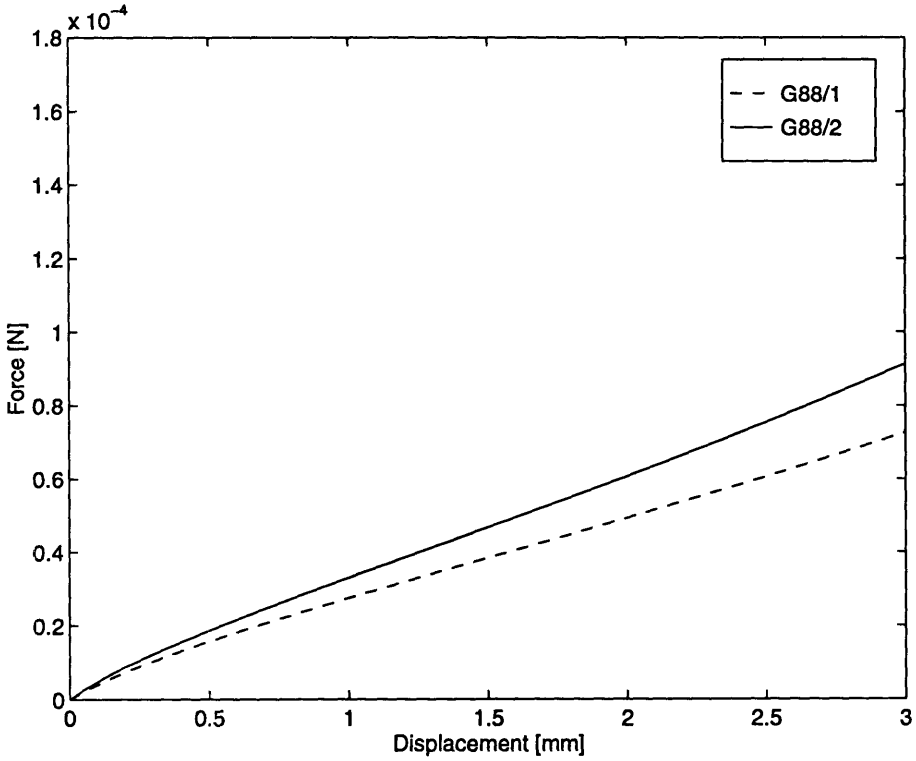

Figure 3-12: G88 series force-displacement

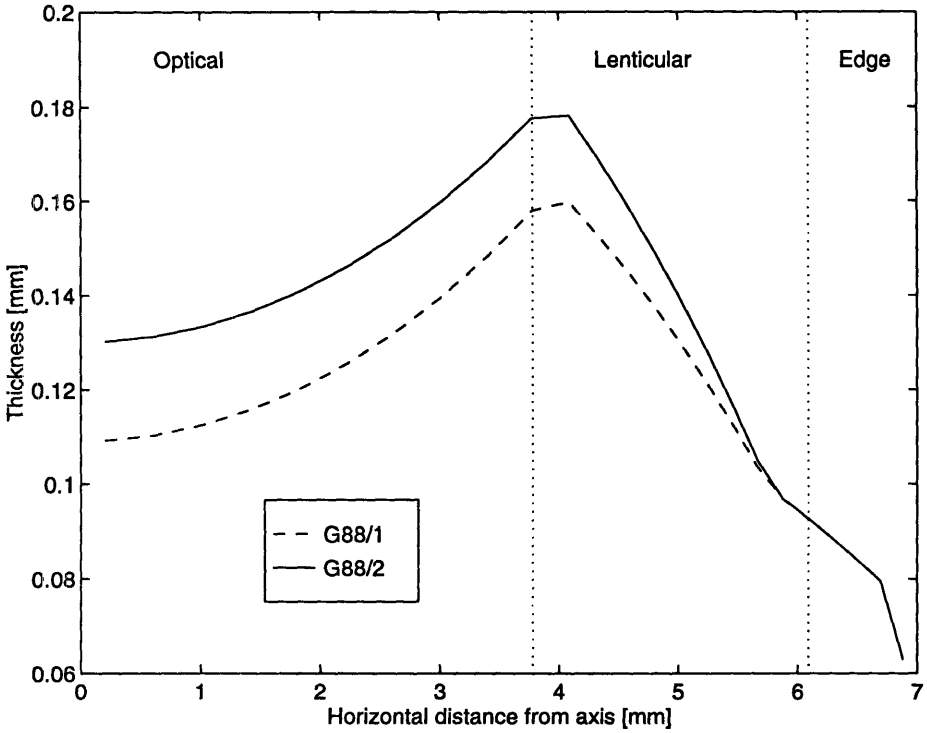

Figure 3-13: G88 series thickness profile

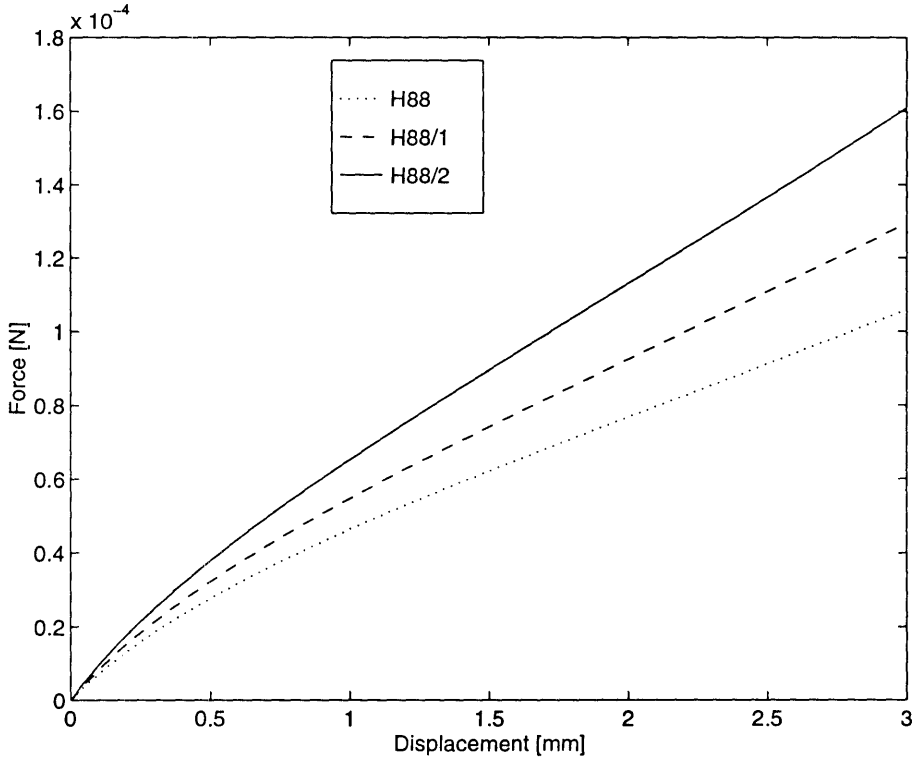

Figure 3-14: H88 series force-displacement

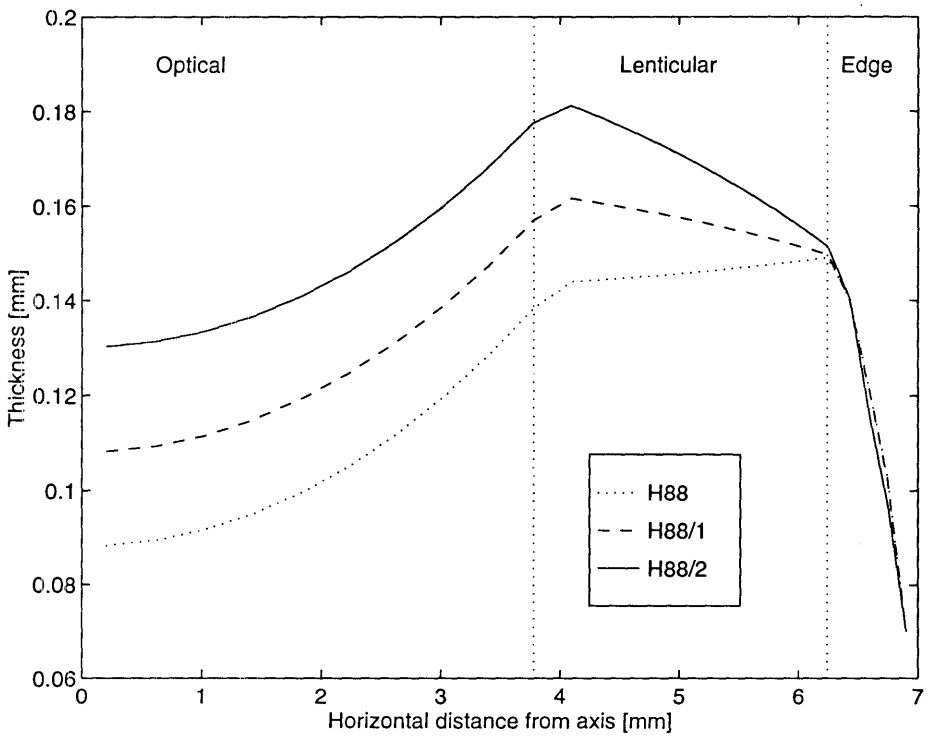

Figure 3-15: H88 series thickness profile

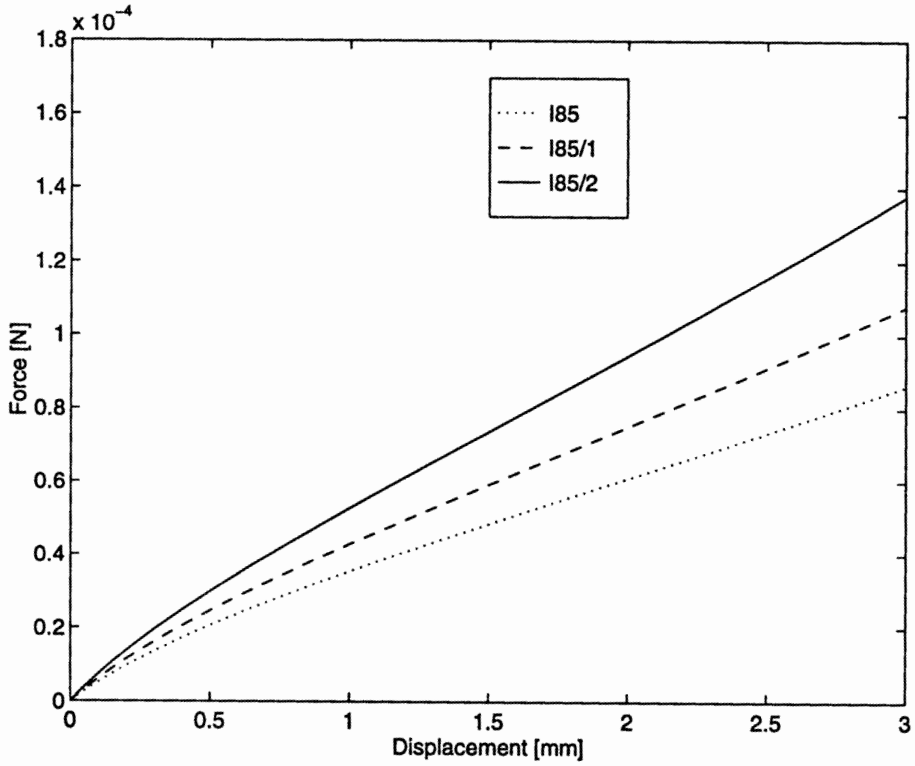

Figure 3-16: I85 series force-displacement

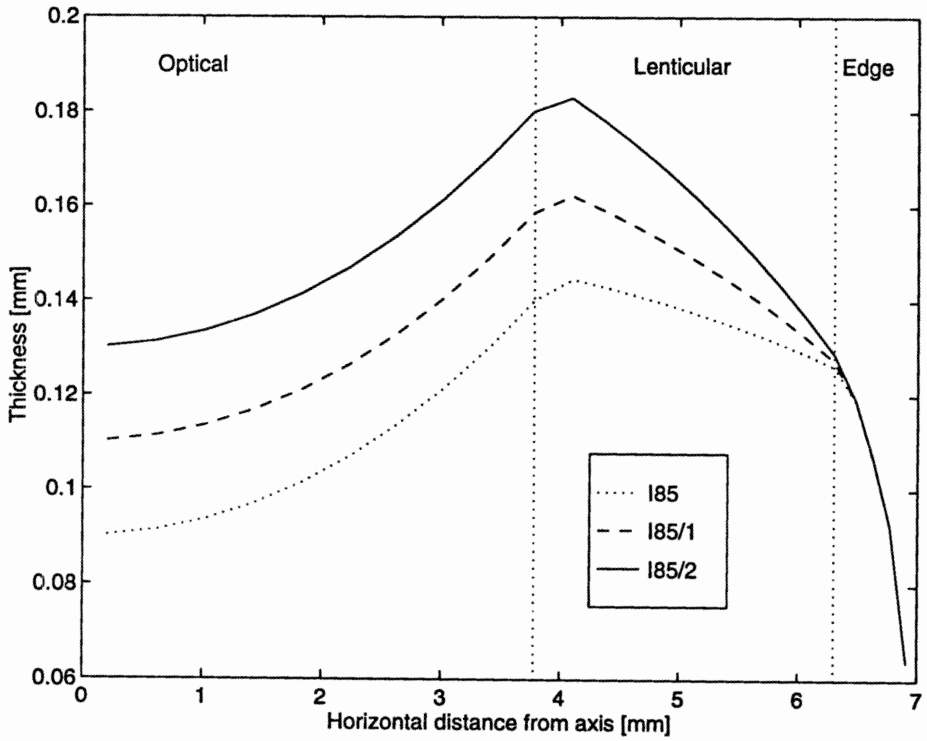

Figure 3-17: I85 series thickness profile

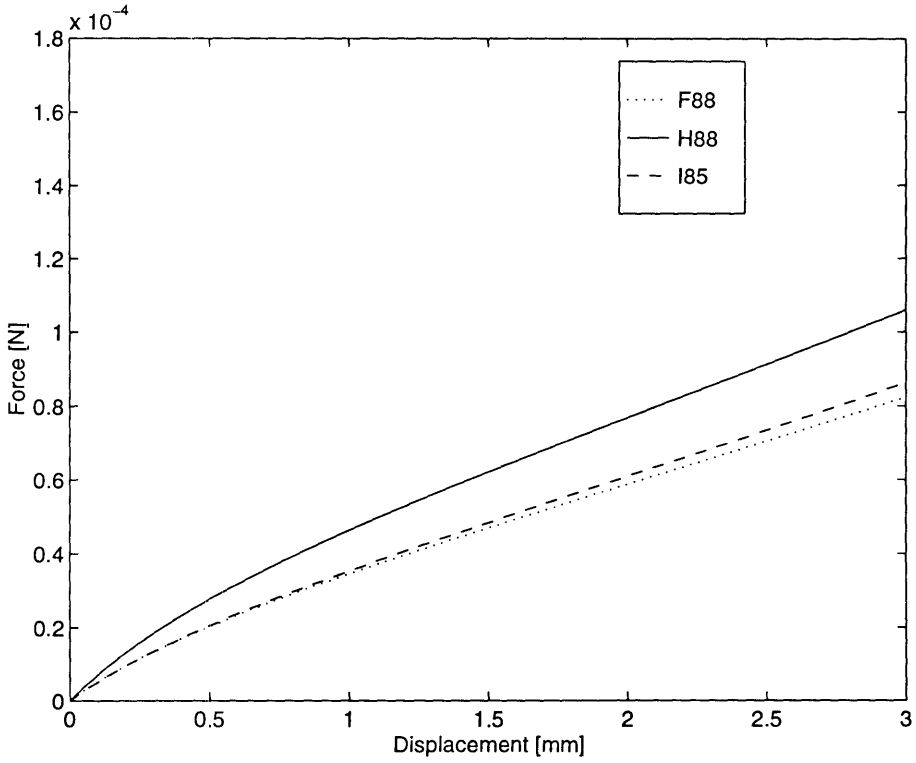

Figure 3-18: Force-displacement for F88, H88, and I85 lenses

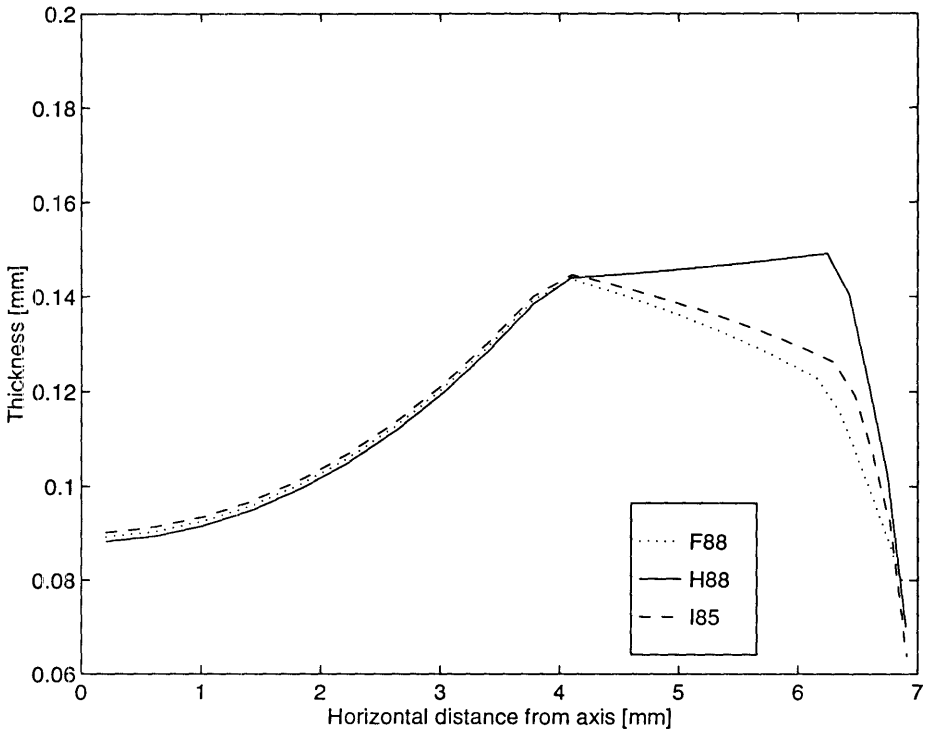

Figure 3-19: Thickness profile of F88, H88, and I85 lenses

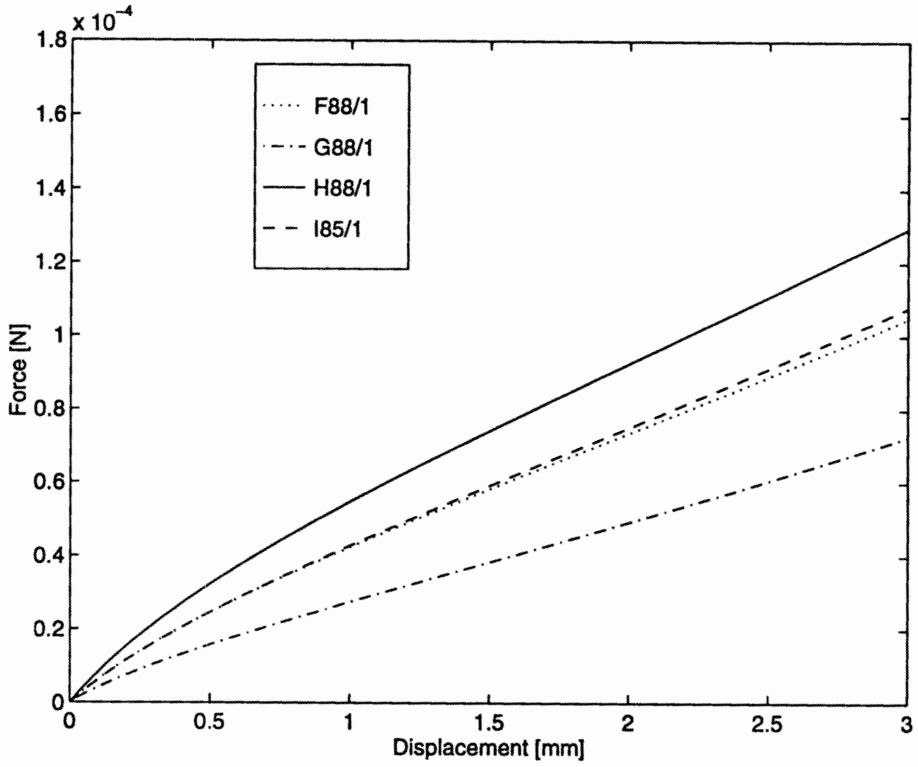

Figure 3-20: Force-displacement of "/1" series lenses

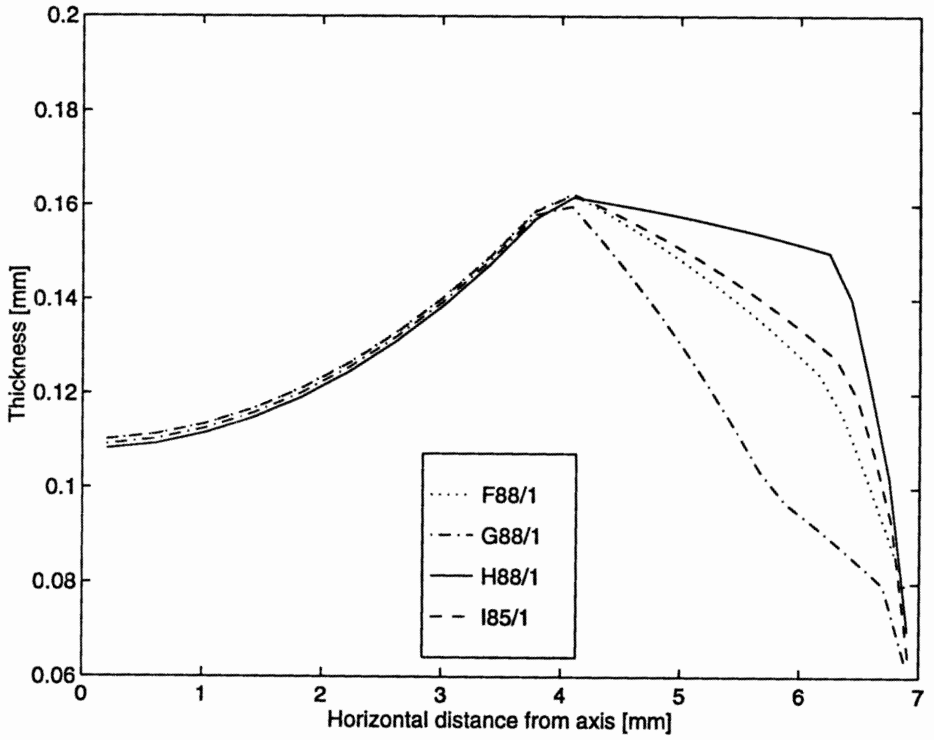

Figure 3-21: Thickness profile of "/1" series lenses

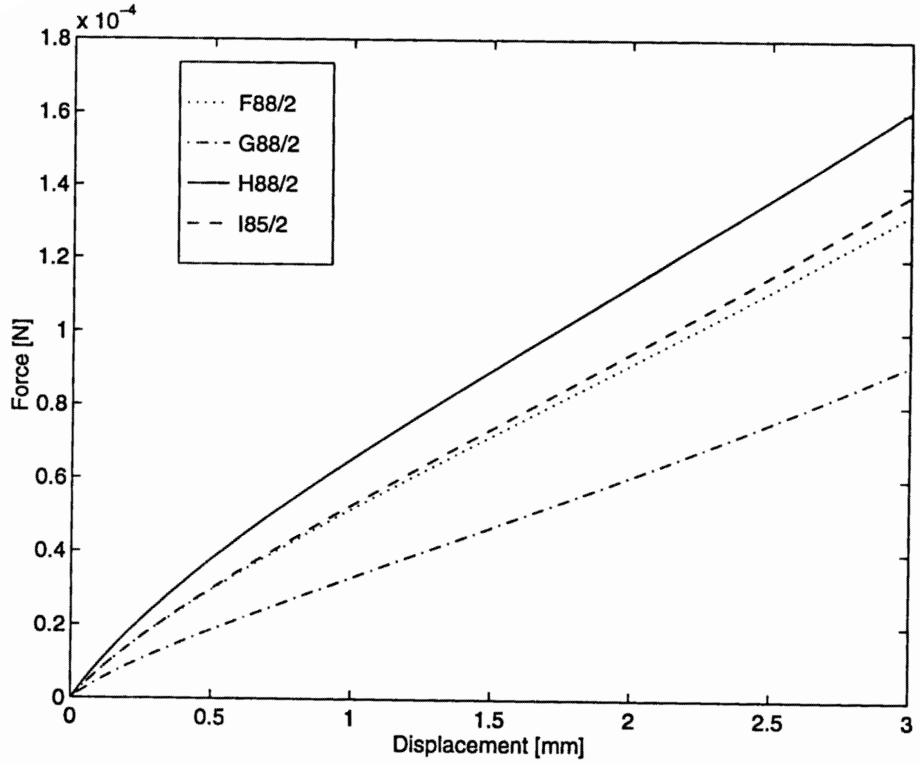

Figure 3-22: Force-displacement of "/2" series lenses

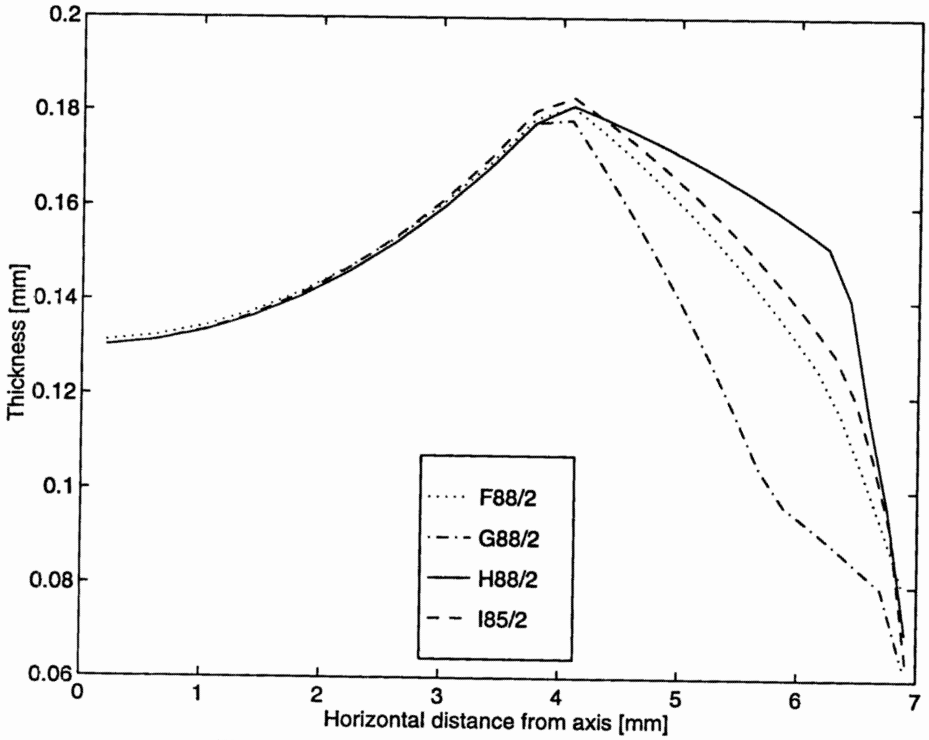

Figure 3-23: Thickness profile of "/2" series lenses

3.4 Results of Simulations with Uniform Thickness Lens Blanks

The stiffness response of the uniform thickness lens blank simulations are shown in Figures 3-24 and 3-25. Figure 3-24 shows the force-displacement behavior of five lens blanks with a basecurve radius of 8.5mm and a thickness that varied between 0.08 and 0.13mm. Each curve starts with an initial slope, which gives the lens stiffness at very small initial deflection, and then softens to a second constant slope after about 1.5mm displacement. This second slope is the lens stiffness at the final stage of deflection. It was found that both these initial and the final stiffnesses scale as the lens thickness cubed, as expected from shell theory. The change in shape as the displacement is increased is a result of the change in curvature of the shell during pinching. Figure 3-26 shows the final and initial lens stiffnesses plotted against thickness, along with two curves proportional to the cube of the thickness. The proportionality constant for each curve was determined by performing a least-squares fit of an equation of the form stiffness $= At^3$, to the measured initial and final lens stiffnesses. This relationship of stiffness to thickness is the same as that in beam and plate theory, where the member stiffness varies with thickness cubed.

Figure 3-25 shows the results of simulations using three blanks whose thickness was 0.09mm and whose radii of curvature varied from 8.5 - 8.8mm. This graph demonstrates that this magnitude of variation in basecurve radius has little effect on the lenses' force-displacement behavior.

3.5 Results of Simulations with Step-Variable Thickness Lens Blanks

Figure 3-27 shows the force-displacement responses of blanks that had a radius of curvature of 8.5mm and a thickness that varied between regions. In each blank, one region was assigned a thickness of 0.125mm, while the thickness of other two regions

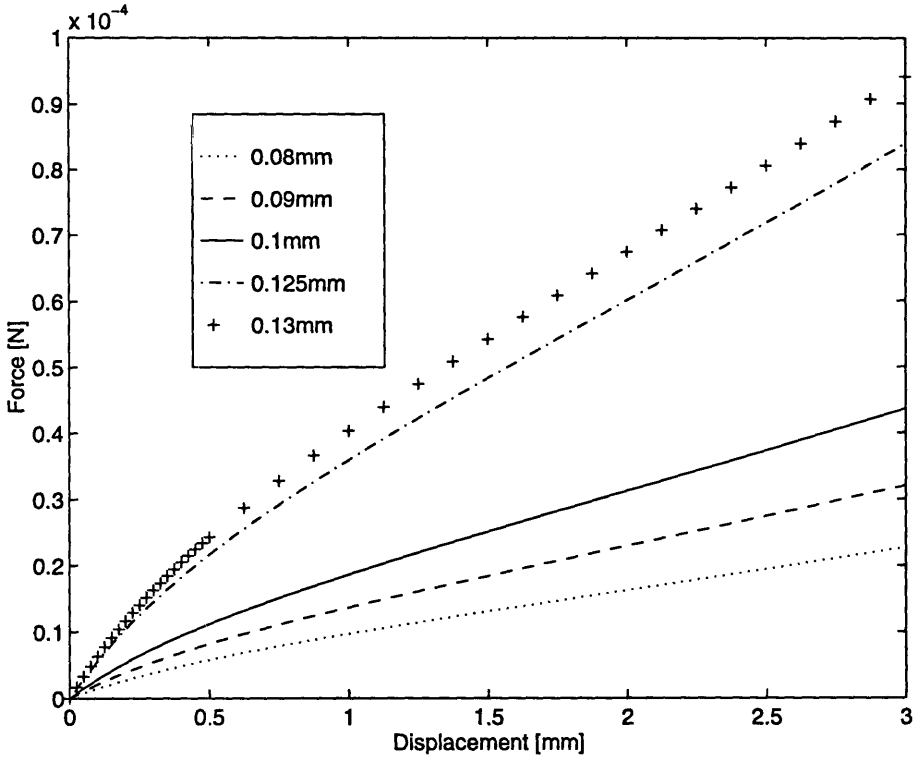

Figure 3-24: Force-displacement of 8.5mm radius blanks of varying thickness

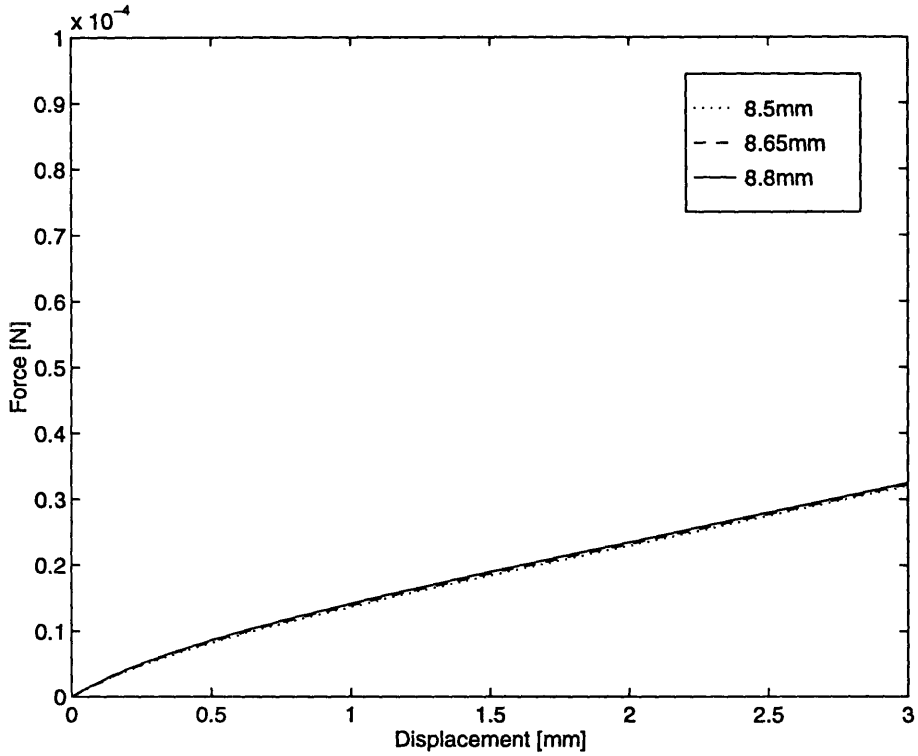

Figure 3-25: Force-displacement of 0.09mm thickness of varying basecurve radius

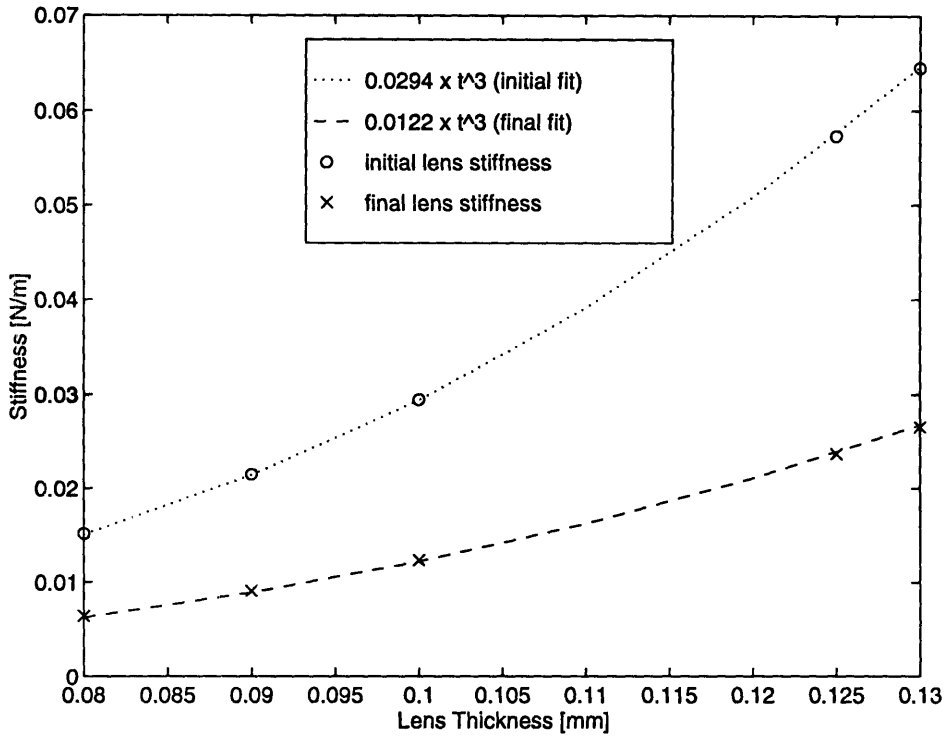

Figure 3-26: Stiffness vs. thickness of constant-thickness blanks

was set to 0.1mm. The results of simulations in which all three lens regions were 0.1mm and 0.125mm thick are also shown for reference. As one would expect, all three blanks with a single 0.125mm thick section had stiffnesses that fell between those of the 0.1mm and 0.125mm uniform blanks. In addition, the stiffness response was different for each of the three variable-thickness blanks. The initial and final stiffnesses of these five blanks is given in Table 3.1. Table 3.1 also gives the ratio of the initial and final stiffness of each blank to the corresponding stiffness of the 0.1mm constant thickness blank (columns 4 and 5) The magnitude of the ratios in columns 4 and 5 correspond to the relative influences of the three lens regions on the initial and final lens stiffnesses. These ratios show that the final stiffness response is most strongly influenced by the thickness of the lenticular region, followed by that of the edge region, and finally, that of the optical region. The sensitivity of the initial stiffness to lens region thickness follows the same trend, with the lenticular region thickness being most influential, followed by those of the edge and optical regions, respectively. However, the relative influences of the edge and lenticular region on stiffness response is more nearly equal for the initial response than for the final

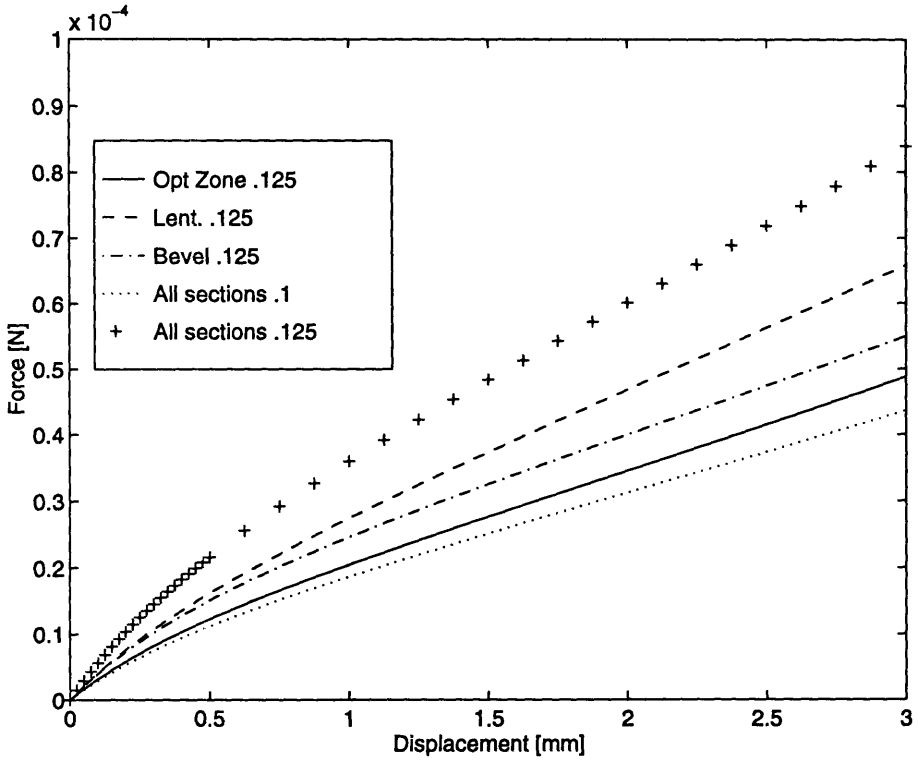

Figure 3-27: Force-displacement of blanks with step variable thickness

response.

If it is assumed that the stiffness behavior of a lens blank of nonuniform thickness scales like that of a uniform thickness blank, i.e. that the initial and final force-displacement slopes are proportional to the thickness cubed, then it is possible to calculate an effective uniform thickness for a blank with varying actual thickness. The dotted and dashed lines shown in Figure 3-26, which fit the initial and final

Blank	Initial Stiffness [N/m]	Final Stiffness [N/m]	Initial/ Initial$_{t=0.1}$	Final/ Final$_{t=0.1}$
0.1mm const. thickness	0.029446	0.012340	1.00	1.00
optical zone 0.125mm	0.032331	0.014090	1.098	1.142
lenticular zone 0.125mm	0.041916	0.018969	1.423	1.537
edge zone 0.125mm	0.040573	0.014895	1.378	1.207
0.125mm const. thickness	0.057355	0.023711	1.948	1.922

Table 3.1: Initial and Final stiffnesses of variable-thickness blanks

stiffnesses of the constant thickness blanks, are described by the equations:

$$\text{initial stiffness} = 0.0294t^3 \tag{3.1}$$

$$\text{final stiffness} = 0.0122t^3 \tag{3.2}$$

where t is the lens thickness. Two values for effective constant thicknesses can be calculated for each variable-thickness blank by inserting the measured initial and final stiffnesses for each blank into equations 3.1 and 3.2 and solving for t. The effective thicknesses obtained by this process are plotted in Figure 3-28. The vertical position of the data points is equal to the actual initial and final stiffnesses measured for each of the blanks. (Initial stiffnesses are plotted on the dotted line, and final stiffnesses on the dashed line.) The horizontal position of points of the dotted line is the effective thickness calculated with equation 3.1, while the position of the points on the dashed line gives the effective thickness calculated with equation 3.2. The calculated effective thicknesses illustrate the same effects shown by the stiffness responses given in Table 3.1. The large stiffening effect of the lenticular region illustrated above is shown in Figure 3-28 by the fact that the effective thicknesses was greatest for the blank with a thicker lenticular region, both when the initial and final stiffnesses were used as an indicator. Likewise, the small effect on both final and initial stiffness of the optical zone is illustrated by the low effective thicknesses calculated for the blank with a thicker optical region.

In addition, the relative influence on initial and final stiffness response of the three lens regions corresponds to the difference in effective thicknesses calculated for each lens with equations 3.1 and 3.2. For example, the effective thickness of the blank with a thicker edge zone is greater when calculated with equation 3.1 than with equation 3.2, demonstrating that the edge region has a stronger influence on the initial response of the lens than on its final response. The opposite trend is seen for the blanks with thicker optical and lenticular regions, which have greater effective thicknesses when the final lens stiffness is used as an indicator. This shows that the optical and lenticular regions play a relatively more important role in determining

final rather than initial stiffness.

Effective thicknesses were also calculated for some actual lens geometries. (F88/1, G88/1, H88/1, and H88/2) The measured initial and final stiffnesses of these lenses are plotted against their effective thicknesses in Figure 3-29. The same trends observed in the step variable thickness blanks are present in the actual geometries. Figure 3-21 illustrated that the F88/1, G88/1, and H88/1 thickness profiles differ only in the lenticular and edge regions. As with the blanks that were thicker in these regions, the real lenses show increasing effective thickness and increasing influence on the final and initial slopes as the thickness of the lenticular and edge regions increases. A comparison of the H88/1 and H88/2 geometries in Figure 3-29 also illustrates similar trends. The H88/2 lens demonstrated a stiffer response both at the initial and final deformations. (See Figure 3-14) Figure 3-15 shows that the these two lenses differ in thickness only in their optical and lenticular regions. Since the simulations of the step variable thickness blanks demonstrated that the lenticular region thickness had much greater influence on stiffness than that of the optical zone, it is reasonable to assume that most of the additional stiffness of the H88/2 lens is due to its thicker lenticular region.

3.6 Conclusions of Lens Flexibility Simulations

The simulations performed illustrate several characteristics of the relationship of lens geometry to flexibility and also of the stiffness response of lenses in general.

First, all lens and blank geometries tested yielded the same basic force-displacement response: one that was relatively stiff at the very early stages of displacement, and that softened to a significantly more compliant response at greater deflection. This characteristic is due to the large geometry change the lens undergoes during deflection. The change in stiffness demonstrates that as the lens shape changes, the mechanism for carrying load also changes.

The shifting of load-carrying during the deformation is related to the second general characteristic observed in the simulations - that the relative influence on stiffness

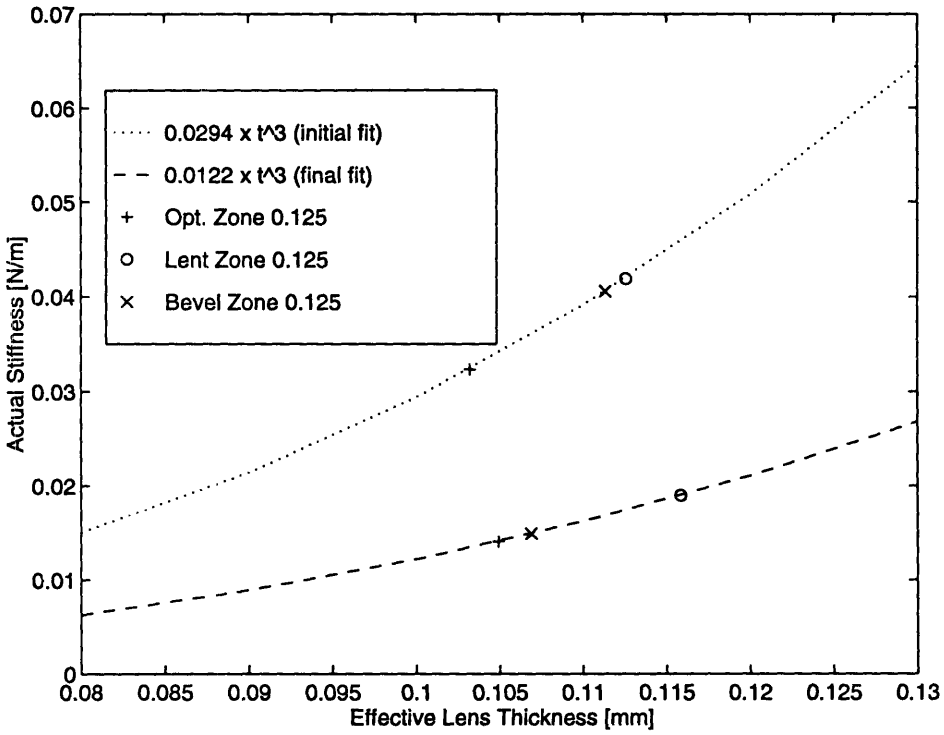

Figure 3-28: Stiffness vs. thickness of blanks with step variable thickness

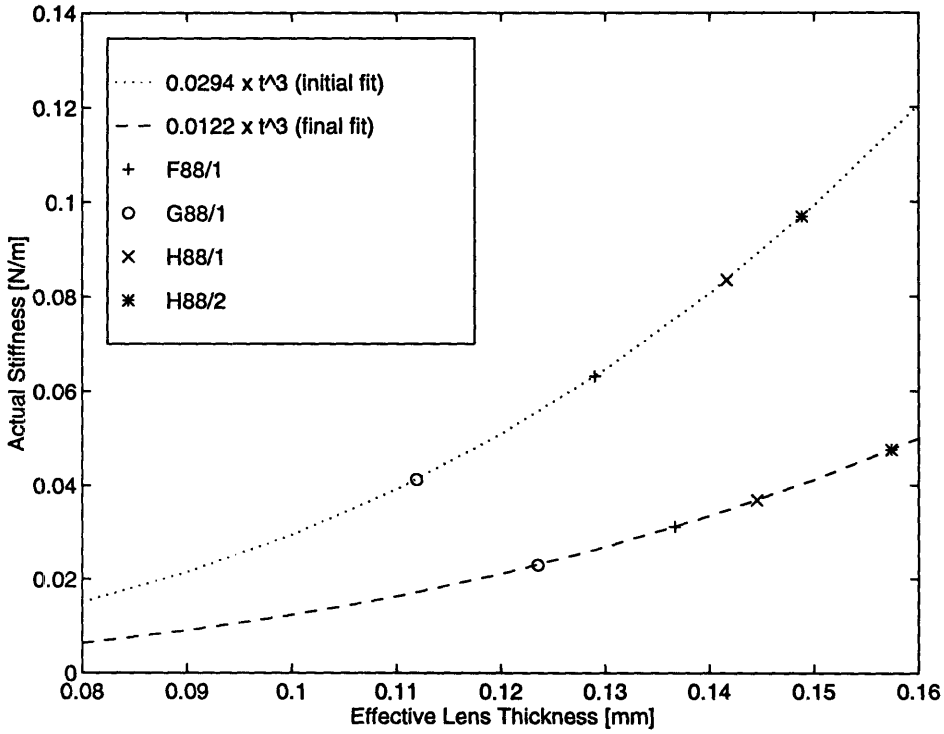

Figure 3-29: Stiffness vs. thickness of F88/1, G88/1, H88/1, and H88/2 lens geometries

of the different lens regions changes as the deformation progresses. This behavior was illustrated by the fact that the effective constant thickness of the variable thickness blanks was different when the calculation was based on the blanks' initial and final stiffnesses. In particular, the results showed that the thickness of the edge zone had relatively more influence on the initial stiffness than on the final stiffness.

A third lens stiffness characteristic illustrated by the simulations is that variation in the radius of curvature over the range tested had relatively little influence on lens stiffness when compared to the influence due to the thickness variation tested.

A final property that the simulations demonstrated is that the initial and final stiffnesses of a constant thickness lens vary with the cube of thickness, as would be predicted by linear beam or plate theory.

While the above characteristics do not directly predict how a lens will fit and move on the eye, or how comfortable a particular lens will be to wear, they do provide information about the mechanical response of a lens, which could be correlated to its behavior once it is placed on the eye. Such correlations between fit and flexibility could then be used to establish a range of stiffness responses that are characteristic of comfortable lenses. Lens designers could use simulations similar to the ones performed in this chapter to compare the stiffness responses of proposed new lens designs to the characteristic stiffnesses of comfortable lenses. This type of evaluation could be performed very early in the design process, and would provide a quantitative indication of the likely comfort and fit of a new lens design.

Chapter 4

Modeling of Lens Fit on the Eye

In the previous chapter, the stiffness properties of isolated lenses as a function of geometry were examined. In this chapter, the question of how lenses behave as part of a system that includes the eye and tears as well as the contact lens is considered. The goal of this investigation is to provide information about the mechanical response of the system as a whole that can be used to further determine the role of lens geometry in lens comfort and fit on the eye.

Experimental work on lens fit on the eye has been performed by Fatt [2], Fatt and Chaston [3], and Martin and Holden [6] to measure the pressure distribution in the tear layer under a contact lens that is in static equilibrium on the eye. Experiments conducted by both groups consisted of placing contact lenses of varying geometries and material properties on rigid model eyes and then measuring the fluid pressure in the tear layer underneath the lenses. Fatt used three different spherical eye models with radii of curvature of 7.5, 7.7, and 7.9mm. [2] Each had a 1mm diameter hole drilled in the surface at the center of the cornea for pressure measurement. The lenses were centered over this hole, so measured pressure would be representative of that at the center of the cornea. Four lenses made of silicone rubber were tested. The lenses had varying basecurve radius, (7.3 - 7.6mm) diameter (10.7 - 12.5mm) and thickness (0.15 - 0.29mm.) (See Table 4.1 for a list of lens geometries tested by Fatt) The stiffness of the lens material was not indicated. Each lens was placed onto the eye and smoothed down to conform to the eye shape using fingers or a moist

Lens #	Basecurve [mm]	Diameter [mm]	Thickness[mm]
1	7.60	12.5	0.29
2	7.30	10.9	0.20
3	7.40	10.7	0.20
4	7.54	10.9	0.15

Table 4.1: Lens blank geometries used in the experimental study by Fatt

tissue. Fatt found that when the radius of curvature of the lens was smaller than that of the cornea, (i.e. when the lens had a steep bearing[1]) a negative (pulling) pressure was induced on the eye at the center of the cornea. This pressure remained for approximately 1 minute after the lens was smoothed onto the eye. The magnitude of the pressure was found to vary linearly with the difference in radii of curvature of the lens and cornea. The greatest negative pressure measured at the center of the eye was -3.92×10^{-4}MPa when the lens radius of curvature was 0.6mm smaller than that of the cornea. Fatt also found that when the lens bearing was 0.1mm flat, no measurable negative pressure was induced at the eye center. It was not indicated if a positive pressure was measured in this case. Fatt did not attempt to find any relationship between induced pressure and lens thickness.

In an earlier study, Fatt and Chaston [3] measured induced pressure under hydrogel lenses. No relationship between bearing and pressure was reported. However, it was found that when a lens with a constant 6.5mm radius of curvature was placed on a spherical model eye with radius of curvature of 7.5mm (lens bearing is 1mm steep), a negative pressure was induced under the lens of -4.9×10^{-5}MPa. This value is approximately 10 times smaller than the pressure measured under a silicone lens that had an even less steep bearing (0.6mm steep.) The much greater magnitude of induced pressure under the silicone lens was attributed to its much stiffer modulus, though no specific values were given for the stiffness of either the rubber or the

[1]The bearing of a lens is the difference between the curvature of the inner surface of the lens and the curvature of the cornea. Authors use different conventions for positive and negative bearing, therefore, in this thesis, bearing will be referred to as "steep," when the radius of curvature of the lens is smaller than that of the eye, or "flat," when the radius of curvature of the lens is greater than that of the eye.

hydrogel.

The experiments performed by Martin and Holden [6] were similar to those of Fatt and Fatt and Chaston. Martin and Holden used a single eye model with corneal radius of curvature of 7.8mm, and diameter of 12.9mm, and a scleral radius of curvature of 12.0mm. Lenses were placed on the eye, and a force was applied normal to the lens that was approximately equivalent to the pressure applied by the eyelid during a blink. The force was removed after approximately 60 seconds. Tear pressure was measured at four stations at different distances from the center of the eye both during and after the force application.

The lenses used in these experiments were hydrogel lenses of two different moduli (25kPa and 0.16MPa.) The lenses had constant thickness that ranged from 0.06 - 0.31mm and radius of curvature that ranged from 7.39 to 9.22mm (bearing range: 0.41mm steep to 1.42mm flat)

Like Fatt, Martin and Holden found a negative induced pressure under the lenses at the center of the eye. They found that the magnitude of the central pressure increased with increasing lens thickness and with material modulus. They also found that lenses with a steeper bearing induced greater negative central pressures. In addition, it was found that the magnitude of the pressure was greatest at the center of the lens, and became less negative at the edge of the cornea (at approximately 6.5mm from the central axis.) The difference between the magnitudes of central and edge pressures was greatest for the most steeply fit lenses. The lenses with a flatter bearing yielded a much more constant spatial pressure distribution. Like Fatt, Martin and Holden did not report the measurement of any positive pressures in the tear layer under the lenses.

A model was also proposed by Jenkins and Shimbo [5] to predict the tear fluid pressure under a lens as a function of lens geometry and modulus, and eye geometry. Jenkins and Shimbo assumed small lens deformations and linear elastic, incompressible material behavior. (Poisson ratio=0.5) They also considered only in-plane membrane forces. The tear pressure distribution for three different lenses placed on an eye of realistic geometry were calculated. The cornea geometry used for the model was

elliptical and had a diameter of 12mm, and a central radius of curvature of 7.8mm. The ratio of the length of the major axis to the minor axis was 1:0.77. The sclera modeled was spherical with a radius of 13mm. The lenses modeled had a central base curve radius of curvature of 9.2, 8.4, and 7.7mm, and all had a common center thickness of 0.07mm.

The predicted tear pressures under the three lenses was positive at the center of the lens, became negative near the cornea/sclera junction, and then became positive again near the lens edge.

Jenkins and Shimbo also modeled the eye and lens geometry used by Fatt and Chaston in the experiment described above with a hydrogel lens. The pressure distribution predicted by the model was negative at the lens center, became positive at approximately 5.31mm from the central axis, and became increasingly positive as the lens edge was approached. Jenkins and Shimbo determined that in order for their predicted central pressure to match that measured by Fatt and Chaston, the material modulus would have to be 0.0298MPa.

In both the experimental and analytical modeling work described above, pressure in the tear layer under a lens was the only measure of lens fit considered. In the simulations described below, the pressure at the eye surface will be examined, and, in addition, the internal stress state of lenses in their deformed configurations on the eye will also be observed. These two parameters are related in that, in general, higher internal lens stress will tend to induce greater eye surface pressures. However, the internal stress state provides additional information about how the loads caused by deformation are carried by the lens, which will aid in understanding the relationships between lens geometry characteristics and lens fit.

In this chapter, issues pertaining to the numerical modeling of fit on the eye are first discussed. Due to the complexity of actual lens geometries and also to the nature of lens deformation when conforming to the eye, the finite element method is used to model the fit of a lens on the eye. Next, a set of simulations with various lens geometries is described, followed by the results of these simulations and the conclusions that can be drawn from them.

4.1 Lens Fit Modeling Issues

To capture the main characteristics of this problem, it was necessary to model the lens, the eye, and the contact behavior between them. It was also necessary to determine whether to include the effects of the tear layer in the simulations, and if so, how to model the tear layer itself and its interactions with the lens and the eye.

4.1.1 Eye Model

Although the eye is a flexible, multilayered structure, for the simulations described here, it was modeled as a single surface since the stiffness of the eye is many times greater than that of the lenses under consideration. [7] One model eye geometry used is shown in Figure 4-1. It is axisymmetric and consists of three tangent circular arcs which represent the cornea, the sclera (white part of the eye), and the junction between the two (the limbus.) The radii of curvature of the three arcs are representative of a typical eye geometry. [7] Throughout these simulations, the same basic three circle surface representation of the eye geometry was used. The radius of curvature of the cornea ranged from 7.8 to 7.87mm, and its diameter was approximately 6.2mm. Various geometries for the limbus were tested that ranged from a 3mm circle to a straight line. The outer edge of the curve used to define the limbus was approximately 6.8mm from the central axis. The geometry of the sclera was not varied, and was equal to that of a circular arc of 12mm radius whose center lay on the central axis 13.51mm below the center of the cornea surface.

4.1.2 Lens Model

The lens material was modeled as described earlier in the lens flexibility study to be a linear elastic, nearly incompressible solid (E = 2MPa, Poisson ratio=0.49.) Axisymmetric 8-node hybrid elements (parabolic displacement interpolation and linear pressure interpolation) were used. These elements provide accurate pressure calculation for incompressible solids. The lens mesh used is shown in Figure 4-2. It is more refined than meshes previously used, with two rows of 46 elements each. The finer

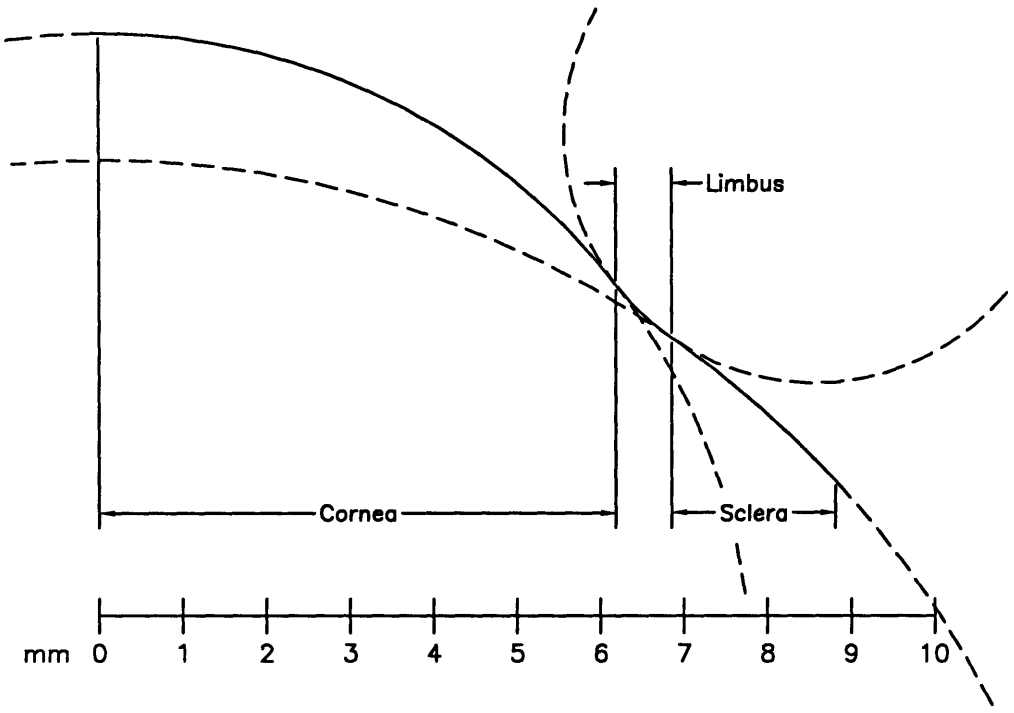

Figure 4-1: Geometry of the eye model

mesh was used for two purposes. The first was to provide a more accurate internal stress approximation. The additional row of elements was helpful in this regard, since much of the stress would be caused by bending of the lens as it conforms to the eye and would therefore vary dramatically through the lens thickness. The second reason for mesh refinement was to accommodate the shape distortion necessary for the lens to conform to the eye. This is especially important at the outer edge where the lens must bend back and up in order to fit onto the sclera. The lens cross section was that of the I85/1 lens given in the previous chapter. This geometry was used for all the simulations used to explore the modeling issues described below.

4.1.3 Tear Model

The tear layer was by far the most difficult part of the system to model. While it is clear that the tear layer provides the surface tension bridge between the eye and the lens needed to conform the lens to the eye, the importance of the tear layer in

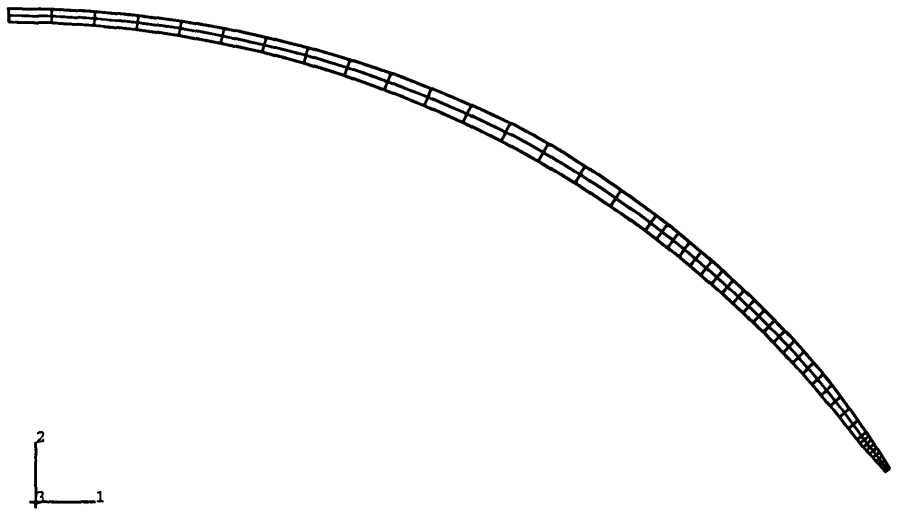

Figure 4-2: I85/1 lens mesh used for placement simulations

the mechanics of lens fit is not clear beyond this point. Therefore, the question of modeling or not modeling the tear layer must be addressed. The influence of the tear layer was investigated by several models with various assumptions of the tear behavior as discussed below. The results of one successful model are then later compared to simpler models which did not include a tear layer.

Nature of the Tear Several models of the tear layer were investigated. In reality, the tear is a thin layer of liquid floating on the surface of the eye. i.e. it is essentially incompressible and confined only by the surface tension attraction with the eye. These two characteristics lead to two important mechanical responses: 1) The tear is subject to large displacements and strains. The tear's thin geometry contributes to this effect, resulting in large tangential flow due to through-thickness compression. 2) Since the tear is unconfined, it can provide no resistance to applied pressures, which can cause computational difficulties. These characteristics forced us to explore many issues in modeling the tear.

The first issue encountered was the question of how to translate the physical tear into a usable finite element model. The first approach used was to model the tear as a layer of incompressible fluid approximately 0.07mm thick surrounded by a thin

sheath. (See Figure 4-3.) The sheath was necessary to enclose the fluid. The liquid was modeled with 2-node linear fluid elements (F2D2) that lined the inside of the sheath. The fluid elements defined the boundary of a volume of incompressible fluid that could support a uniform hydrostatic pressure. Modeling the tear layer with a single volume of liquid would not capture pressure variations within the fluid, however, this model was an initial attempt at using the fluid/sheath modeling technique, and was designed to to evaluate the feasibility of the technique. If the results of this first attempt had proved promising, the simple sheath would have been replaced by a multichambered structure that would allow varying pressures to develop in the tear layer. The sheath was constructed of axisymmetric, 3-node parabolic shell elements (SAX3.) The sheath material was modeled as linear elastic with a modulus of 20MPa, and as highly compressible with a Poisson ratio of 0.01. The thickness of the sheath was set to 0.001mm, which is 70 times smaller than the initial thickness of the fluid volume.

It was hypothesized that the shell elements would be thin enough to have negligible effect on the stiffness of the system, and that the hydrostatic pressure of the fluid would dominate the response. However, the behavior of the sheath did come into play. As the lens was placed on the tear, the shell was subjected to compressive stress which caused local buckling instabilities in the sheath. (See Figure 4-4. The displacements shown have been magnified by a factor of 10, and the sheath does not actually penetrate the cornea.) This wrinkling also influenced the interface pressure measurements between the lens and the tear, resulting in causing artificial pressure variations. The lens/tear interface pressure measured as the lens just began to contact the tear layer is shown in Figure 4-5. Although the wrinkling behavior currently rules out this model, we also note the realistic thickening of the tear layer in the limbus region. These results suggest that future work should further pursue this fluid/sheath tear layer representation, with a focus on better sheath modeling.

The second modeling approach attempted was to model the tear as an incompressible solid, similar to the material model for the lens, except with a much lower shear modulus. In order to allow for large displacements that occur in the real tear,

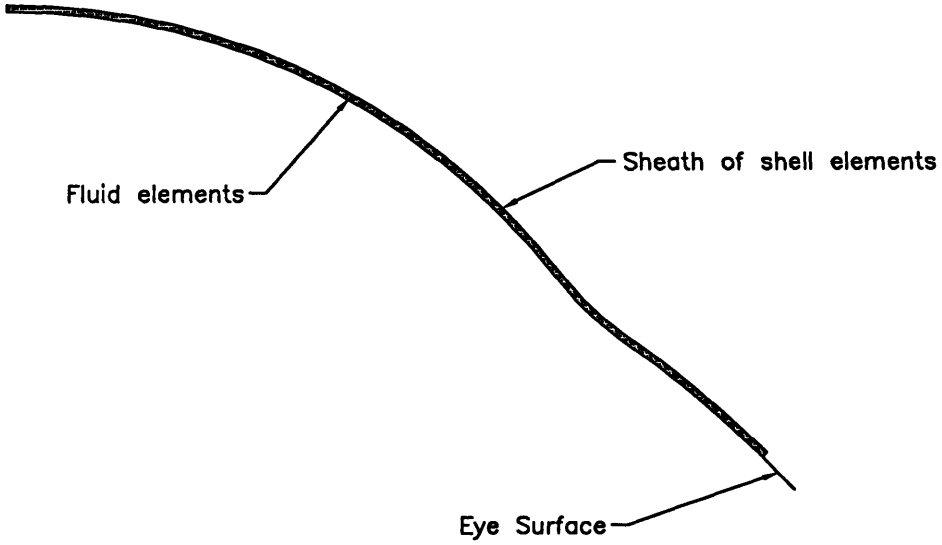

Figure 4-3: Model of tear as a thin sheath surrounding an incompressible liquid

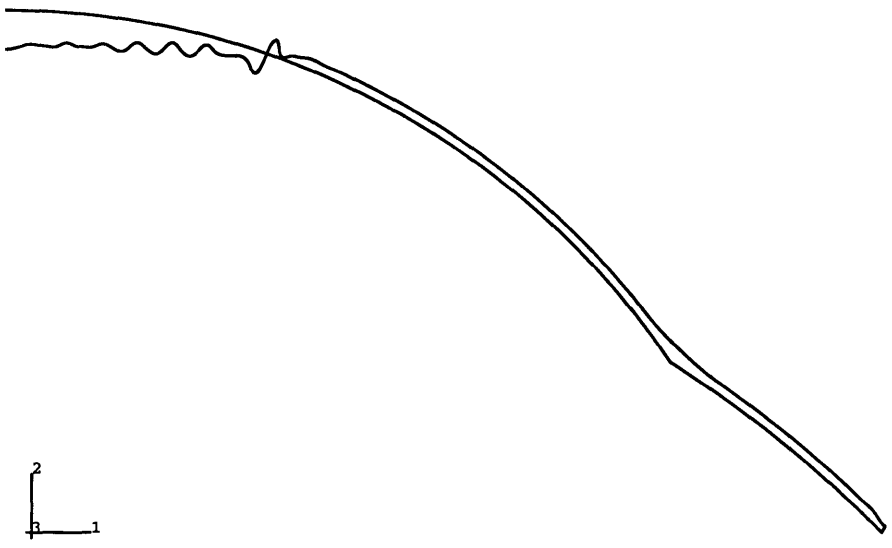

Figure 4-4: Buckling of the sheath as the lens is lowered onto the tear. The displacement shown has been magnified by a factor of 10

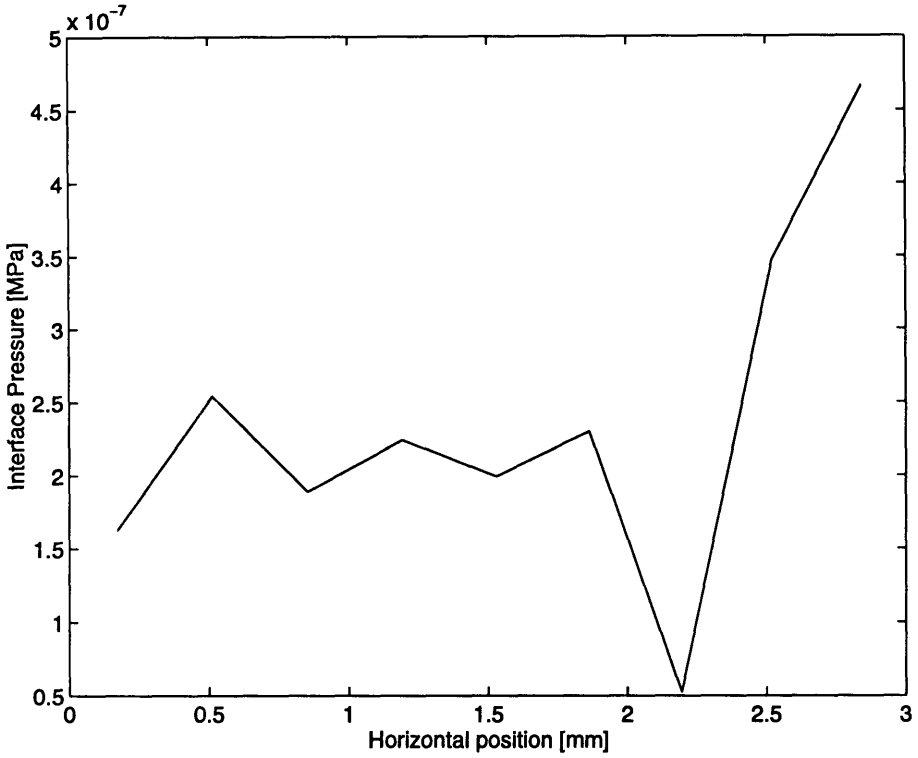

Figure 4-5: Interface pressure between lens and sheath near center of lens

the tear was assigned a modulus of 0.001MPa, while that of the lens was set to 2MPa. Therefore, equal stress in the lens and tear would cause much greater strains in the tear. A Poisson ratio of 0.49 was assigned to the tear to capture the its essentially incompressible behavior. Different types of solid elements were tested in the tear layer, and each produced different results. The element types tested for use in the tear layer and the corresponding results produced will be discussed further below.

Tear Geometry Another modeling issue considered was the geometry of the tear layer. On a real eye, the shape of the tear layer can change dramatically when a contact lens is placed on the eye. When no contact lens is present, the tear shape is governed by surface tension which causes the tear to spread into a relatively uniform thin layer over the eye surface. A contact lens introduces pressure variations in the tear layer which act to redistribute the tears, driving the fluid towards regions of lower pressure. The resulting thickness distribution of the tear layer is one that acts to fill in the gaps between the back surface of the lens and the eye. This is especially noticeable at the cornea/sclera junction, where the eye becomes flatter, and where

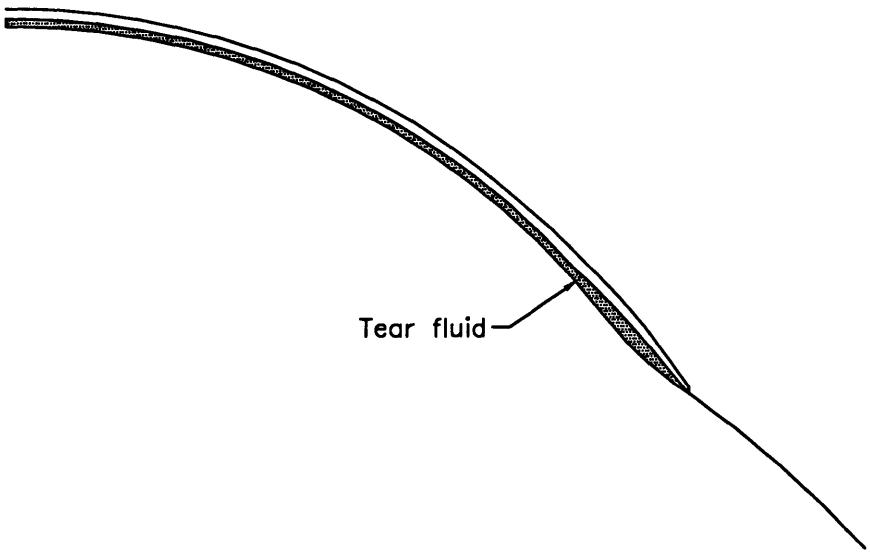

Figure 4-6: Thickening of tear layer at cornea/sclera junction to relieve hydrostatic tension

the lens must bend backwards to conform to the eye shape. Tears tend to well up in the depression, relieving the high negative pressure caused by the large bending moment in the lens at this point. [4] (see Figure 4-6) It was important that the finite element model capture this shape-changing behavior of the real tear.

One tear geometry explored was a uniform layer attached to the back surface of the lens - in effect creating a two-material lens. Figure 4-7 shows a 10μm tear attached to the lens, where 10μm was chosen since this is a typical tear thickness specified in the literature. A blow-up of the edge of the lens is shown so that the tear layer can be seen more clearly. The tear layer was much more compliant than the lens, and acted as a bumper between the lens and the eye, absorbing pressure variations by deforming. A computational advantage of this geometry was that it possessed only one contact surface pair - between the tear layer and the eye. Axisymmetric, 3-node parabolic rigid surface interface elements (IRS22A) were placed on the entire lower surface of the tear layer to monitor contact between the tear and the eye surface.

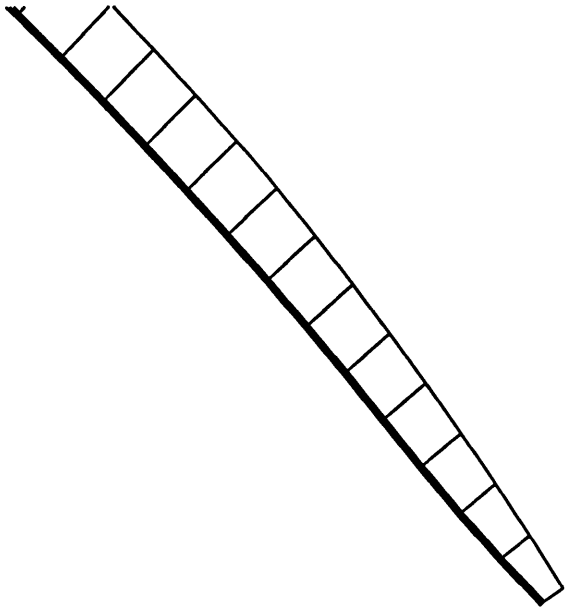

Figure 4-7: Solid tear attached to underside of lens

Because the eye was defined as a rigid surface, the interface elements could monitor contact between the tear and any point on the eye surface even as individual points on the tear surface slid along on the eye. Several thicknesses for the lens-attached tear layers were tested but it was found that no uniform tear thickness could adequately accommodate the gap size and pressure variation along the entire lens radius. If the tear was thin, it served well near the lens center, but did not have enough volume to fill in the depression at the cornea/sclera junction. If the tear was thick, high pressures developed at the center of the tear layer. Since the tear could not compress, the central material had to move tangentially outward, causing large shear stresses that would not be present in a real tear. Using an attached tear with varying thickness was then considered, however, designing a successful tear thickness distribution would require knowing beforehand the final shape of the lens on the eye. This is difficult due to the large bending deflections the lens undergoes during placement. In addition, this method would require creating a new tear layer for each lens geometry tested, limiting the usefulness of the method as a design tool.

The next tear geometry investigated was a free solid tear layer. The tear's initial thickness was uniform, and its lower surface coincided with the shape of the eye. However, the nodes of the tear layer were not fixed on the eye, as the previously

described tear layer was fixed to the lens, but was free to slide radially along the eye surface to accommodate pressure variations without developing significant internal shear stresses. This geometry was computationally more expensive than the previous one, because it involved two contact surface pairs: eye/tear and tear/lens. In addition, the tear/lens pair involved contact between two deformable bodies. Unlike rigid surface interface elements, which can monitor contact with any point on a rigid surface, interface elements for use between two deformable bodies can only monitor contact between two specified regions on each body. Since the tear would slide along the surface of the lens, it was not sufficient to monitor contact only between predetermined points on the tear and the lens. Therefore, a different kind of contact modeling which could monitor contact between arbitrary points on two surface was used. This interface modeling technique will be described in the next section.

An advantage of the free tear geometry was that it had an initial shape independent of lens geometry, just as a real tear does. Various initial tear layer thicknesses were tested, (10-50 μm) and reasonable results were obtained with the 50μm layer. It was found that computational difficulties arose with thinner tear layers, and also that convergence in the tear layer depended on the type of element used. Both of these issues will be discussed further below.

Interface Characteristics The behavior of the model would depend strongly on the characteristics of the interfaces between the two contact surfaces (eye/tear and tear/lens.) There were two primary requirements for the interface behavior. The first arose from the large displacements that occur in the lens and tear as the lens is placed onto the eye. This large geometry change made it necessary to be able to monitor contact between large regions on two surfaces, since the surfaces would shift position with respect to one another while in contact. As mentioned above, this could be accomplished with deformable body/rigid surface interface elements. These interface elements were placed on the deformable body at every point where contact with the rigid surface was expected to occur. Each element would monitor contact between the small region of the deformable body to which it was attached, and the entire rigid

surface. Therefore, when only one independent deformable body was modeled, which was the case when the tear layer was attached to the underside of the lens, it was possible to monitor contact between the tear and the eye by covering the entire lower surface of the tear with rigid surface interface elements.

However, when interaction between more than one deformable body was modeled, using interface elements to monitor contact between the two bodies was not adequate. Such interface elements can only determine if contact has been established between two pre-specified elements - one located on each body. Therefore, when the tear layer was modeled as a free body separate from the lens and the eye, contact between the three entities was monitored by establishing contact surface pairs. Contact surfaces were defined as sets of adjacent element faces (for example, the lowermost surfaces of the lower layer of lens elements.) Contact was then monitored between pairs of contact surfaces. For example, contact between the entire upper surface of the tear and the entire lower surface of the lens was monitored.

The second required interface characteristic was that the interface be able to support normal tensile stress, which had been shown experimentally to exist in the tear layer. This behavior was modeled by specifying a "no separation" condition on both the eye/tear and tear/lens surface contact pairs. This definition requires assigning one surface in each contact pair to be designated as "master" and the other as "slave." The no separation condition specifies that once a given node on the slave surface has established contact with the master surface, it must remain in contact with some point on the master surface. (See Figure 4-8) However, the reverse is not true - master nodes can leave the slave surface (by sliding off the edge of a surface, for example.) The no separation interface behavior permits sliding between the surfaces, allowing relief of interface shear stresses, but it prevents separation in the normal direction, supporting normal tensile stresses at the interface. The no separation interface behavior could be used with the rigid surface interface elements described above, however, the master and slave designations are not required.

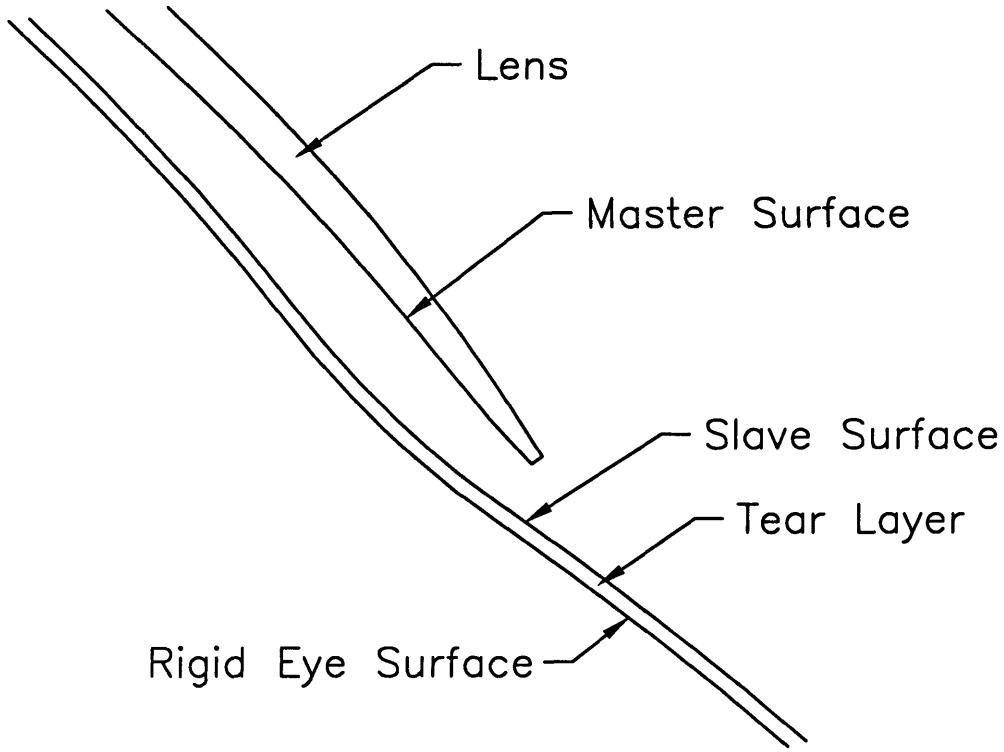

Figure 4-8: Master (lower surface of lens) and slave (upper surface of tear) surfaces. Once contact is established between the two surfaces, nodes of the slave surface may not separate from the master surface.

4.1.4 Loading History

The goal in loading the model was straightforward - to place the lens onto the tear layer, which was covering the eye, and then to release all prescribed displacements and/or forces and allow the tear/lens system to reach equilibrium. The no separation interface condition would then require the tear and lens to remain on the eye once the external constraints were removed. However, the large difference in elastic modulus of the tear and the lens and the presence of two large surface contact interfaces demanded careful attention to the prescribed loading conditions. Two primary issues arose in specifying the loading. The first was to ensure that contact was established at every node on both the upper and lower tear surfaces. If contact were not complete, "bubbles" could form at unconnected points during equilibration. It was found that even though the initial position of the lower tear surface coincided with the eye surface, not all tear nodes were initially in contact with the eye. Therefore, it was necessary to perform the preliminary loading steps of displacing the upper layer of the tear downward by a small amount (approximately 1/2 the initial tear layer thickness), raising it back to its original position, and then releasing displacement conditions on the tear.

Establishing contact between the lens and tear was a more difficult problem. It was not possible to simply prescribe uniform vertical displacements on the entire lens because the initial separation between the lens and tear varied along the profile. It was also not possible to simply measure the initial vertical distance between the lens and the tear and then to prescribe this varying vertical displacement at the points along the lens profile. As the lens was moved downward, it also extended radially, in the process, changing the amount of vertical displacement necessary to make contact with the tear.

A seemingly simpler approach was to press the lens down onto the tear by applying a pressure to the upper surface of the lens. This technique would not require knowing the necessary vertical displacements of each point on the lens. However, this approach was unsuccessful due to the large difference in the lens' and tear's elastic moduli and

the large amount of bending of the lens necessary to make it match the tear shape. When pressure was applied, the central portion of the lens would contact the tear first. As the pressure was increased, the force was transmitted through the lens and acted to compress the central portion of the tear, rather than to bend the lens. This phenomenon is similar to applying force to two springs in series. The springs will stretch in a ratio proportional to their relative compliances. If one spring is much more compliant than the other, it will undergo great extension, while the stiffer spring will remain relatively undeformed. Very large strains developed in the central part of the tear long before the entire lens had contacted the tear, resulting in numerical singularities which prevented the simulation from reaching a solution. This problem occurred even when pressure was only applied to the outer portion of the lens.

These results demonstrated that it was necessary to prescribe displacements on the lens rather than forces in order to bring the lens and tear into contact. The method arrived at was to specify lens displacements step by step: to move a single lens node until contact with the tear was established, then to examine the newly displaced mesh, and then to repeat the process with another node, iterating at each step to determine how much displacement was required in that step. Typically, imposed displacements from earlier steps were held fixed as other displacements were imposed. Figure 4-9 illustrates a typical progression of this process. While this method was successful, it is cumbersome and must be repeated to some extent with each new lens and/or tear geometry.

Once contact was established at all points at the tear/eye and the lens/tear interfaces, the second phase of loading - allowing the lens and tear to equilibrate - still had to be performed. Several difficulties arose during this process.

In a first attempt at unloading, all prescribed displacements were simply removed in a single step. This resulted in the lens edge "digging in" to the tear. (See Figure 4-10) The penetration of the lens into the tear surface is one of the characteristics of the master/slave contact pair relationship described above. Penetration of the slave surface by the master surface is permitted, but the reverse is not true.[2] The digging

[2]A simulation was performed in which the master/slave designations of the tear/lens interface

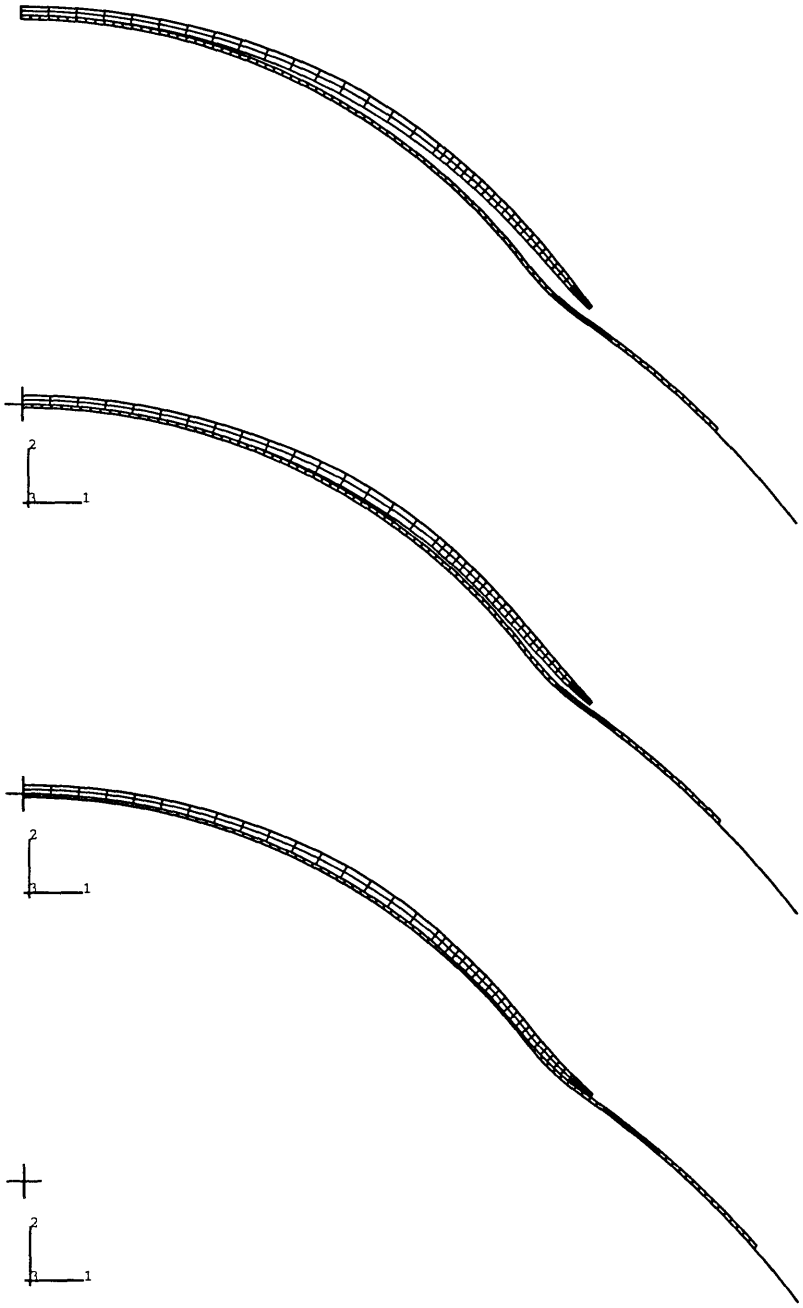

Figure 4-9: Step by step procedure for placing lens on tear

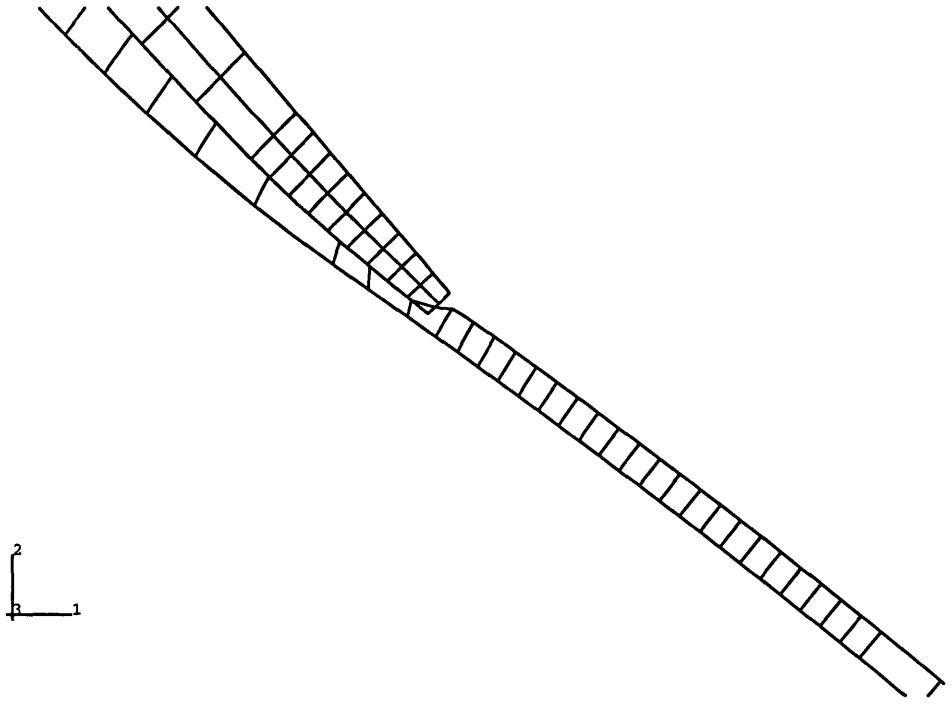

Figure 4-10: Digging into the tear by the lens when all displacements were released simultaneously

in of the lens caused the tear to become caught on the edge of the lens, which could prevent it from sliding inward in response to the negative pressure induced by the relaxing lens.

In order to prevent the digging in of the lens, a simulation was attempted in which the edge of the lens was held up while all other prescribed lens displacements were released. The lens edge was then released in a second step. This method produced the result shown in Figure 4-11. The tear layer slid inwards in response to the hydrostatic tension developed near the cornea/sclera junction. In the process, many points on the lens surface became detached from the tear. This release was permitted because the lens surfaces was the master of the pair. Note that no tear nodes separated from the master surface, they simply moved to another location on the surface.

The third modeling approach was to establish a redundant contact pair in which the tear surface was designated as master and the lower surface of the edge of the lens as slave. (See Figure 4-12) This second lens/tear contact pair was introduced in order to resolve the problems that occurred in the previous two release attempts. The

were reversed, but in this case, numerical singularities arose that prevented placement of the lens onto the tear.

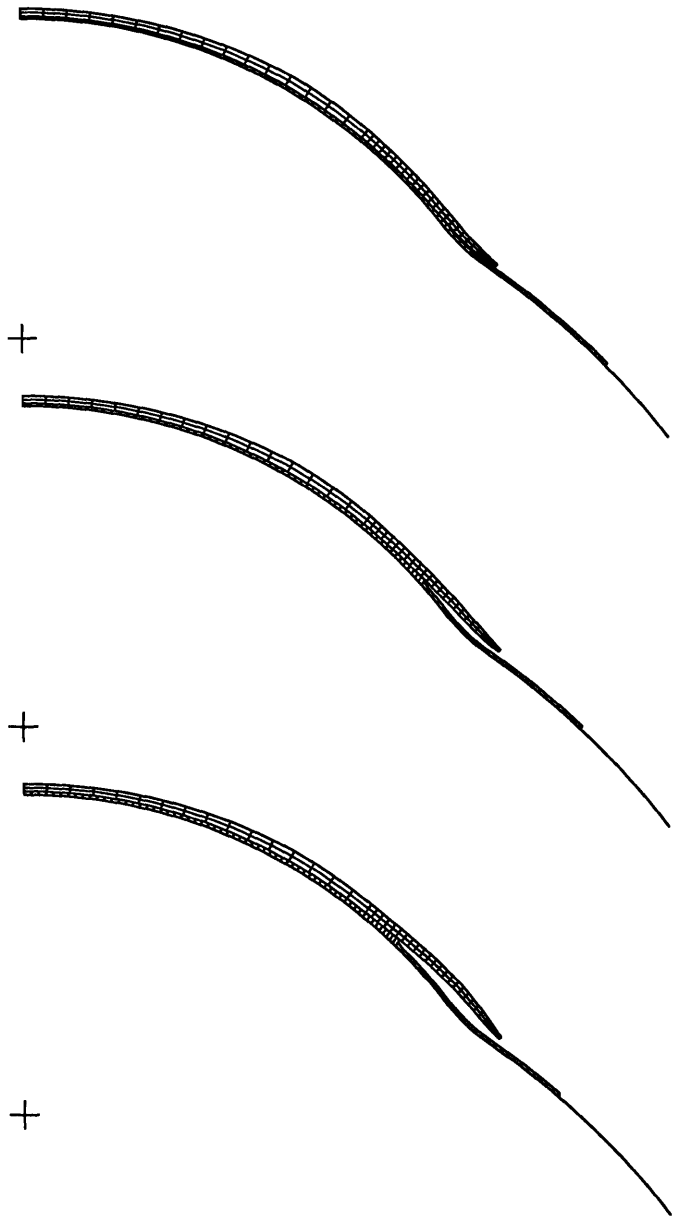

Figure 4-11: Separation of the tear from lens when lens displacements were released before tear/lens contact was established at lens edge.

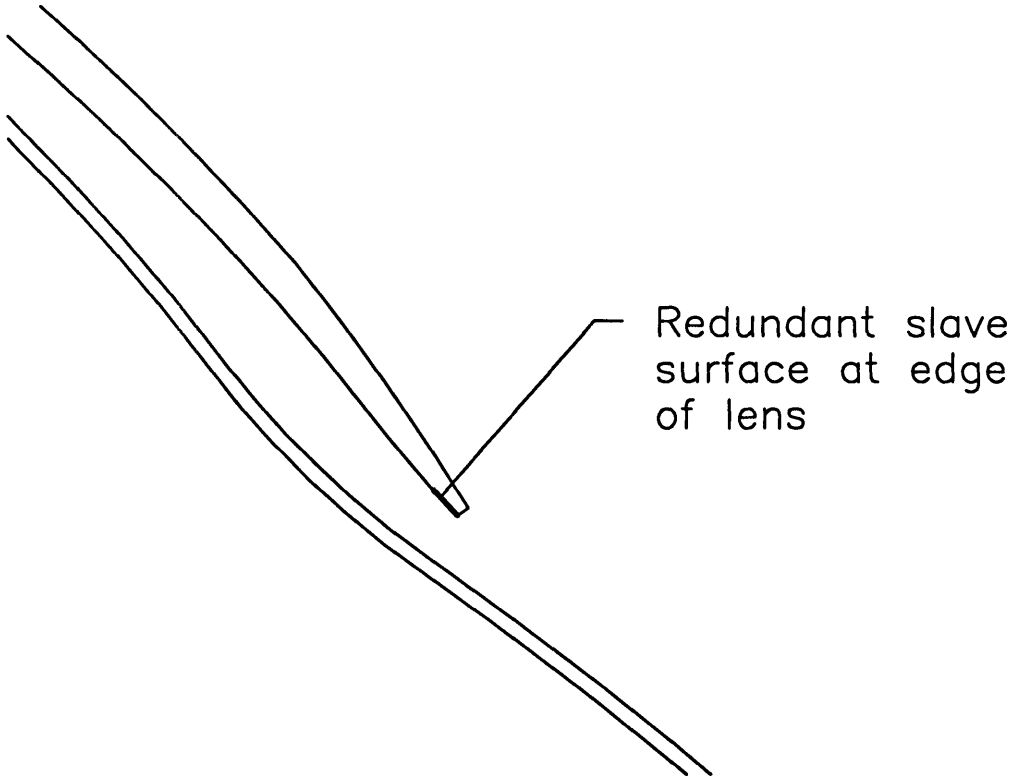

Figure 4-12: Position of redundant surfaces introduced to prevent digging-in and tear/lens separation

digging in by the lens that appeared in the first case would be prevented by the fact that the slave nodes on the edge of the lens would not be able to penetrate the tear master surface. The sliding of the tear in the second case would also be prevented because the slave nodes on the lens would not be permitted to separated from the tear, keeping the two bodies in contact.

The establishment of a redundant surface did solve both these problems. However, during equilibration a region of high hydrostatic tension arose in the tear layer near the cornea/sclera junction (the lightest shading shown in Figure 4-13.) A solution was reached for the I85/1 lens geometry provided that: 1) the tear layer was thick (50μm) and 2) the displacement interpolation elements were used in the tear layer rather than hybrid displacement/pressure interpolation elements. The displaced mesh of the lens in equilibrium on the 50μm tear layer is shown in Figure 4-14. A plot of the tear/eye interface pressure distribution obtained from this simulation is shown in Figure 4-15, and the thickness distribution of the tear layer is shown in Figure 4-16.

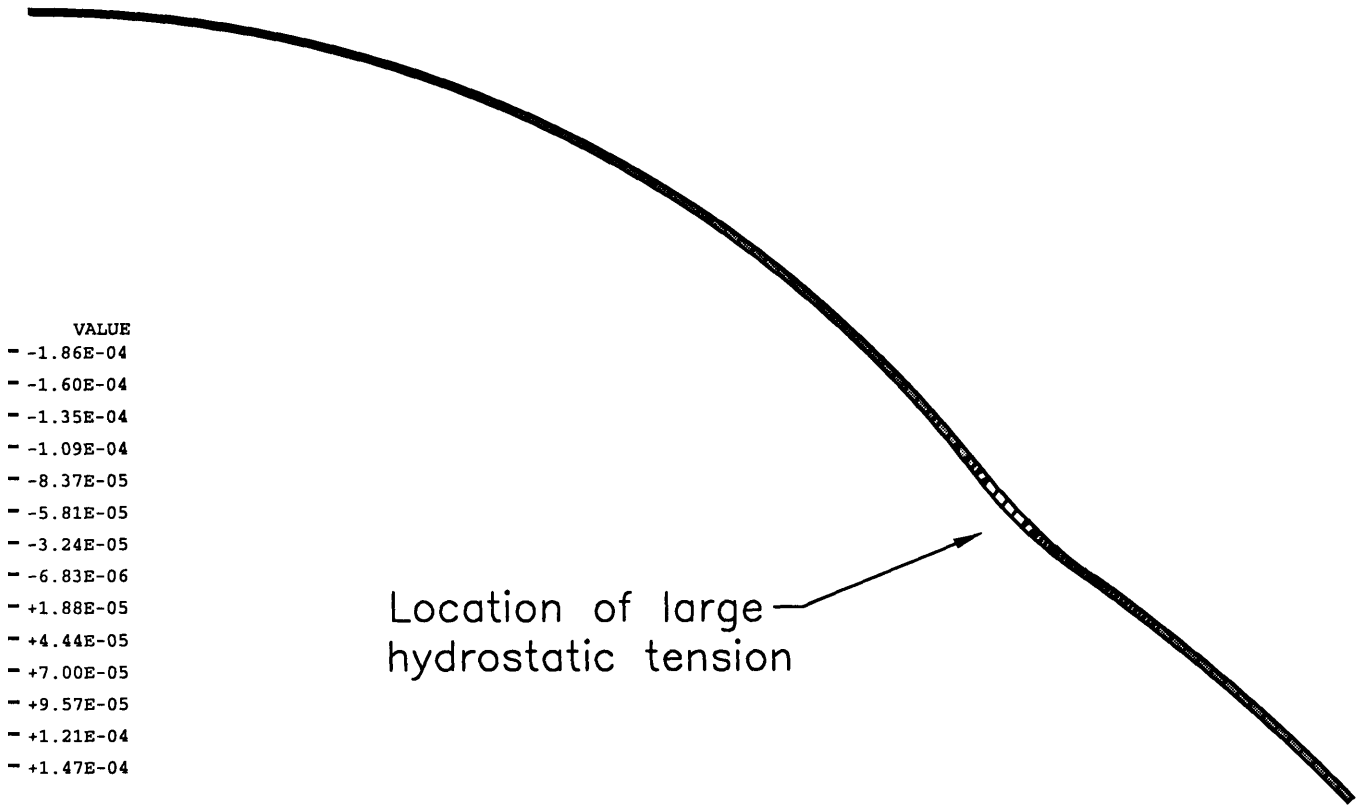

Figure 4-13: Large hydrostatic tension in tear layer at equilibrium state

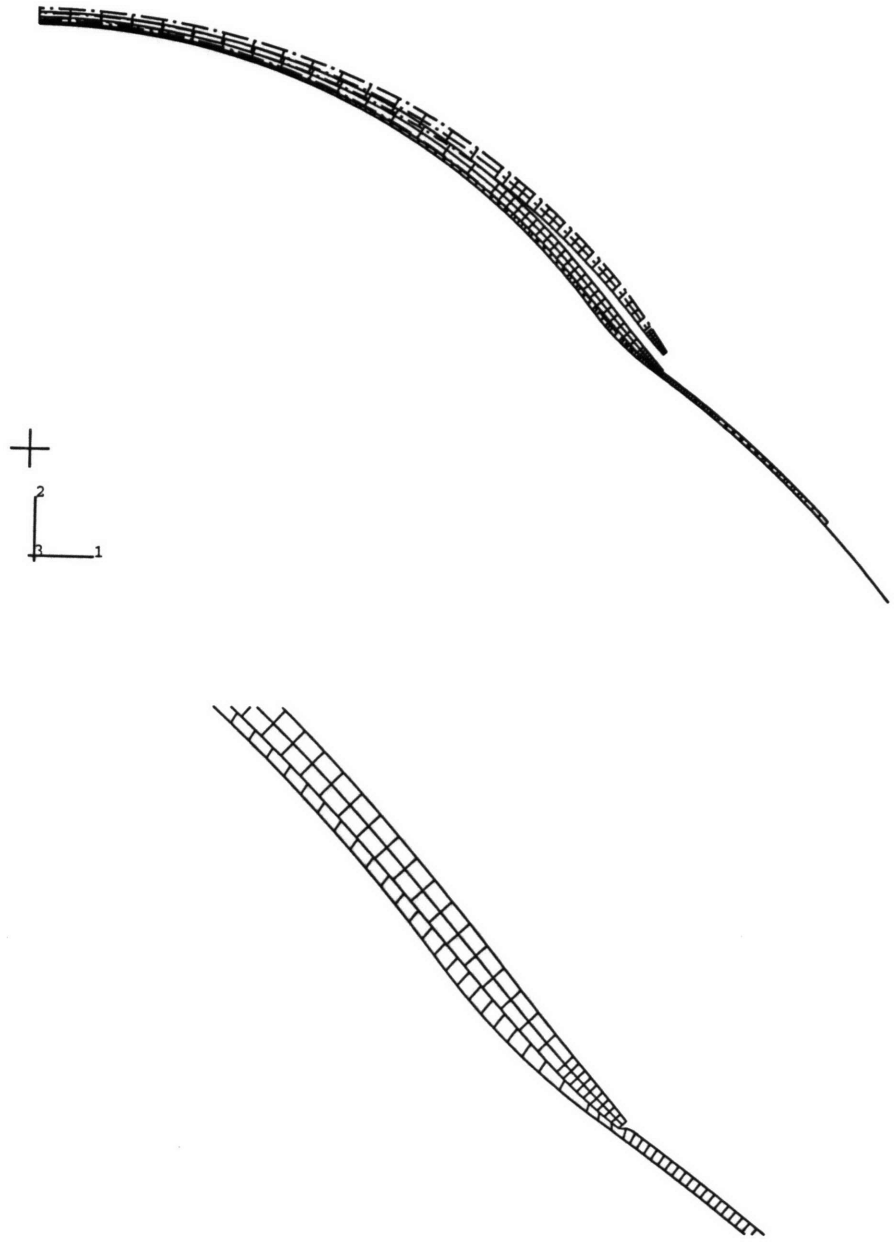

Figure 4-14: Lens in equilibrium on 50μm tear layer. The lower figure shows an enlargement of the cornea/sclera junction region, and the upper figure includes the undeformed lens mesh.

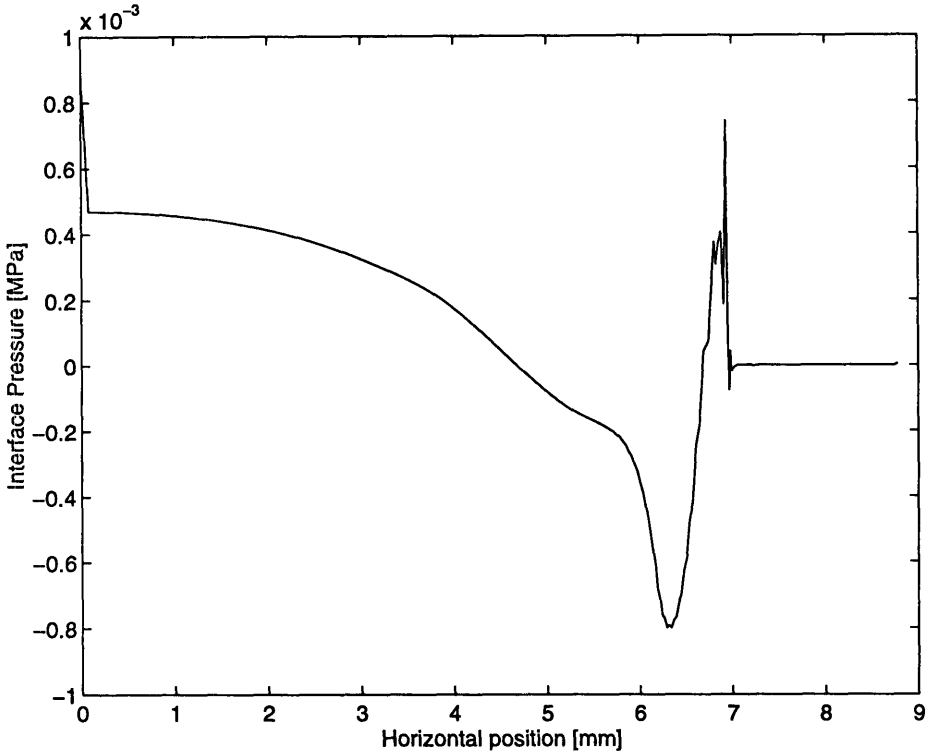

Figure 4-15: Pressure Distribution at tear/eye interface for lens in equilibrium on 50μm tear layer

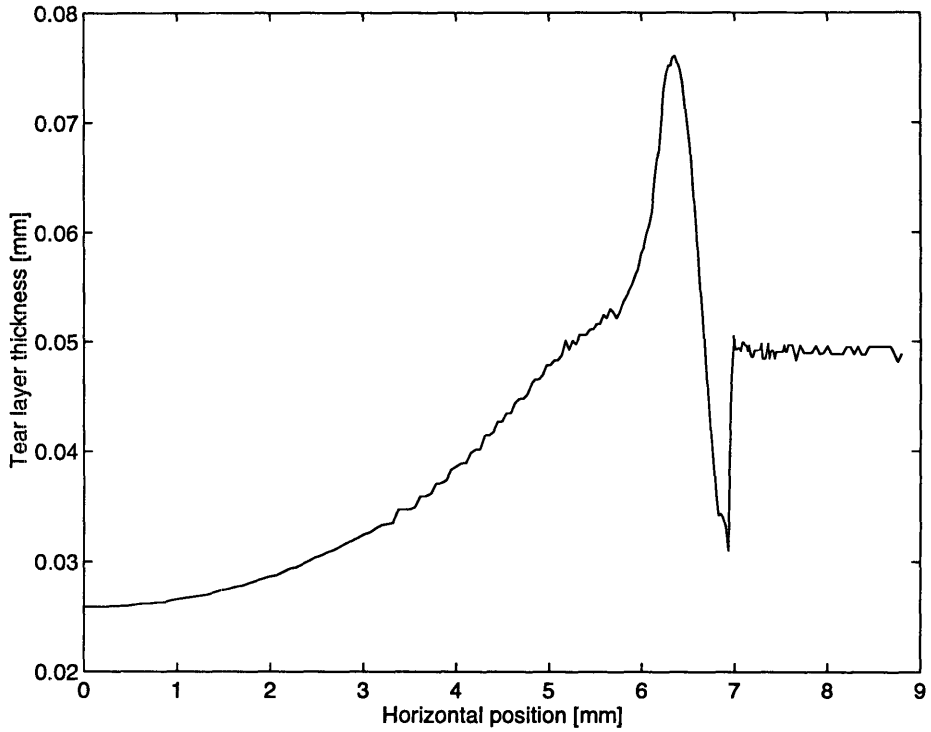

Figure 4-16: Tear layer thickness distribution when lens was in equilibrium on 50μm tear layer

4.1.5 Tear Layer Element type

As stated above, convergence of the solution depended on the type of element used in the tear layer. Three different element types were tested for use in the tear layer: an 8-node element, (quadratic displacement interpolation, no explicit independent pressure interpolation) an 8-node hybrid element, (quadratic displacement interpolation, linear pressure interpolation) and a 4-node element (linear displacement interpolation, constant pressure assigned to all integration points within element.) When the tear was composed of 8-node elements, a solution could be reached only with the thickest (50μm) tear layer tested. When thinner tear layers were used (20, 10μm) the mesh would lock, preventing further steps from being taken. When the 8-node hybrid element was used in the tear layer, completion of the loading process was always possible, however, the model would not converge to a solution during the unloading (equilibration) process. This was the case for all tear layer thicknesses tested. (10, 20, 50μm) The 4-node element behaved similarly to the 8-node hybrid element. It caused no mesh locking, but the models failed to converge during release of the imposed displacements on the lens. In addition, the solution provided by the 4-node element was very similar to that yielded by the 8-node hybrid element up to the point of completion of both models.

4.1.6 Summary of Tear Modeling Issues

Table 4.2 provides a summary of the tear modeling issues discussed in the previous sections.

At the end of tear experimentation with the tear layer, the loading procedure arrived at was difficult to implement, and provided a result only in a single simulation. The sensitivity of the method was likely to make it prone to failure in certain cases. e.g. if a stiffer lens were tested that would induce greater hydrostatic tension in the tear layer. Another approach was attempted that was much more reliable and easier to implement.

Aspect	Options	Problems
nature of tear	sheath/fluid	sheath buckling
	incompressible solid	
tear geometry	attached to lens	high shear stresses
	free	multiple contact surfaces
interface behavior	interface elements	can only be used for rigid surface contact
	contact surface pairs with no separation condition	penetration of master into slave, separation separation of slave from master
loading	all displacements prescribed in one step	cannot determine necessary displacements
	apply pressure to lens	excessive tear strain
	step-by-step displacement	tedious to implement
unloading	remove all displacements simultaneously	digging into tear by lens
	remove all but edge displacements	sliding in of tear
	introduce redundant contact surface	large hydrostatic tension in tear
element type	8-node	mesh locking with thinner tears convergence only with thick tear
	8-node hybrid	no convergence achieved
	4-node	

Table 4.2: Summary of tear modeling issues

4.1.7 A Test: No Tear Layer

Due to the numerical difficulties involved when modeling the tear layer, simulations were performed without a tear layer, and the internal lens stresses and interface pressures obtained were compared to those obtained when a tear layer was used. If the results were similar, the no tear method would be a very attractive alternative to the difficult and unreliable modeling approach described above.

Simulations performed without a tear are much easier to implement than those that include the tear for several reasons. First, no-tear simulations involve a single contact pair - between a deformable body and a rigid surface - which is relatively easy contact to monitor. In addition, the problems of digging in and sliding apart illustrated above are automatically eliminated. A second simplification is that the no tear simulation involves only one material with a single modulus, preventing the problems caused by the large difference in modulus between the lens and tear. Therefore, pressure rather than displacement can be prescribed in order to deform the lens onto the eye. Also, the large hydrostatic tension developed in the tear due to the relaxation of the much stiffer lens is eliminated.

Eye Geometries One difficulty with not using a tear layer is that the lens must conform to the shape of the eye rather than to the shape of the tear on the eye. Figure 4-14 illustrates that the tear wells up at the cornea-sclera junction, effectively smoothing out the shape of the eye at this point. Stresses in the lens shown in Figure 4-14 are lower than they would be if the lens matched the eye shape exactly.

In order to compensate for the loss of this smoothing effect, a modified eye shape was used for the no tear simulations. Four eye geometries were tested. (See Figure 4-17) The first was the same as the eye used in the simulations with the tear layer described earlier. It had a corneal radius of curvature of 7.8mm, and a scleral radius of curvature of 12mm. The radius of the circle at the cornea/sclera junction was 3mm. For the second geometry, the radius of the cornea and sclera were unchanged, but the radius of the circle at the cornea/sclera junction was increased to 8mm. For the third geometry, the circle was flattened to a straight line. For the fourth geometry,

a different approach was taken. The final tear thickness distribution obtained in the simulation with the 50μm tear layer was measured along the eye profile. This thickness distribution was then normalized and smoothed and added to the original eye shape, in order to obtain the fourth eye geometry.

A series of simulations was performed in which the I85/1 lens tested in the previous chapter was placed on the four different eye geometries without a tear layer present. A no separation condition was specified at the lens/eye interface. Contact was established at the tear/eye interface by applying a large pressure (0.05MPa) to the upper surface of the lens. This pressure was then removed, and the lens was allowed to come to equilibrium on the eye. The initial and the final equilibrium position of the lens on eye geometry 4 is shown in Figure 4-18. The final configuration was typical for all simulations with all four eye geometries tested. The internal stress distributions and lens/eye interface pressures for the four no-tear cases were compared to those obtained when the 50μm tear layer was included.

The internal stresses obtained are shown in Figures 4-19 to 4-24. All stress directions are oriented with respect to the elements: the 1 direction points tangentially along the curve of the eye, the 2 direction points through the lens thickness, and the 3 direction points circumferentially around the lens (out of the plane of the paper.) All reported stresses are the values calculated at the integration point located at the center of the element. The position given on the horizontal axis in Figures 4-19 to 4-24 is the perpendicular distance to the central axis. The vertical dotted lines mark the divisions between the three circular arcs used to construct eye1. (see Figure 4-1)

Figures 4-19 and 4-20 show the distribution of the lens normal stress in the 1 direction (S11) in both the upper and lower layer of lens elements. The large increase in stress near 6.5mm is caused by the bending the lens experiences as it conforms to the eye at the cornea/sclera junction. Note that the stress peaks are compressive on the top of the lens and tensile on the lower lens surface due to bending.

The distribution of the S11 stress produced with the tear layer was most similar to those obtained with the eye geometries eye1, eye2, and eye4 when no tear layer was present. The magnitude of the peak stress obtained with eye2 most closely matches

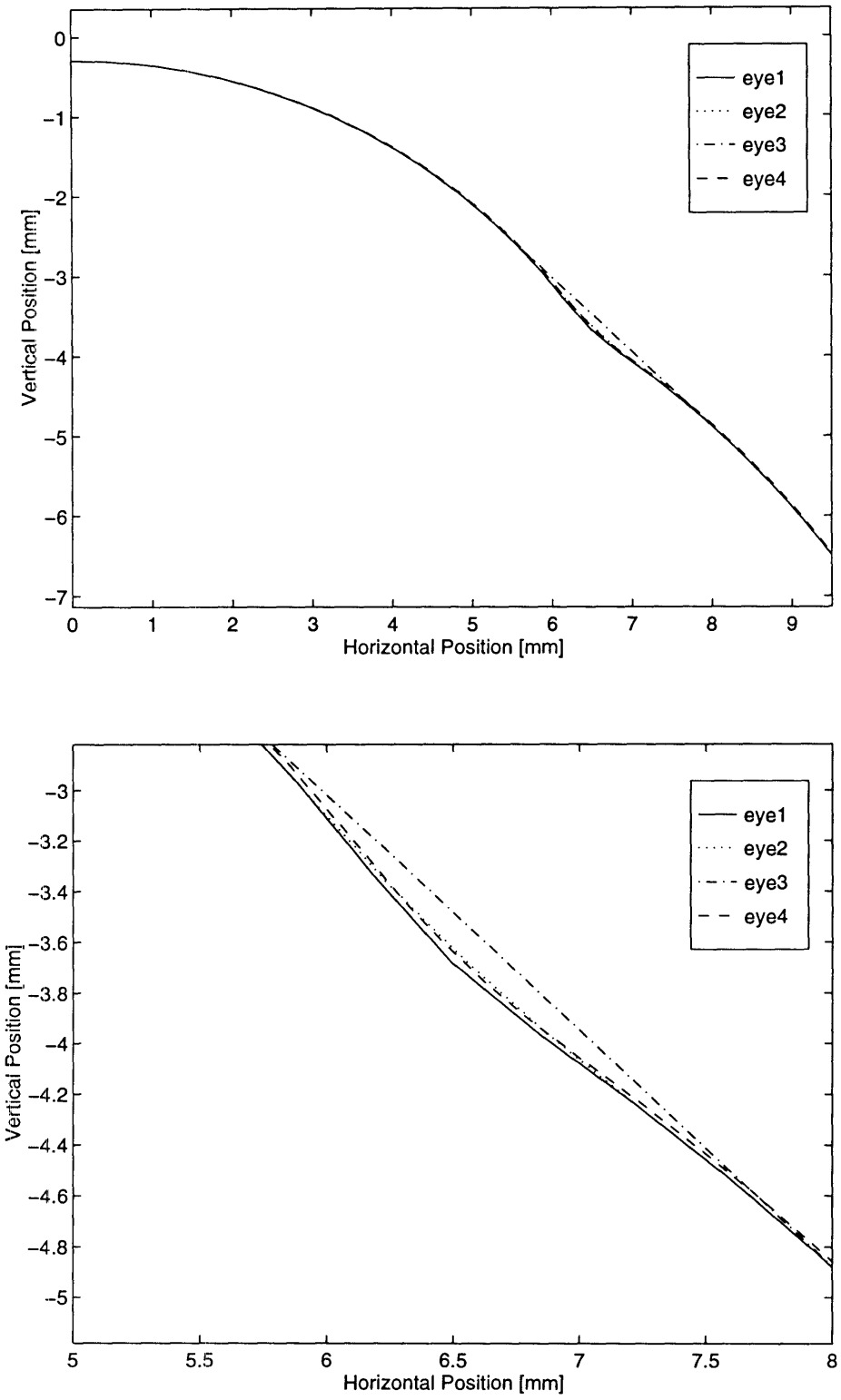

Figure 4-17: Four eye geometries tested for use in no-tear simulations. The lower plot shows a blow-up of the cornea/sclera junction zone.

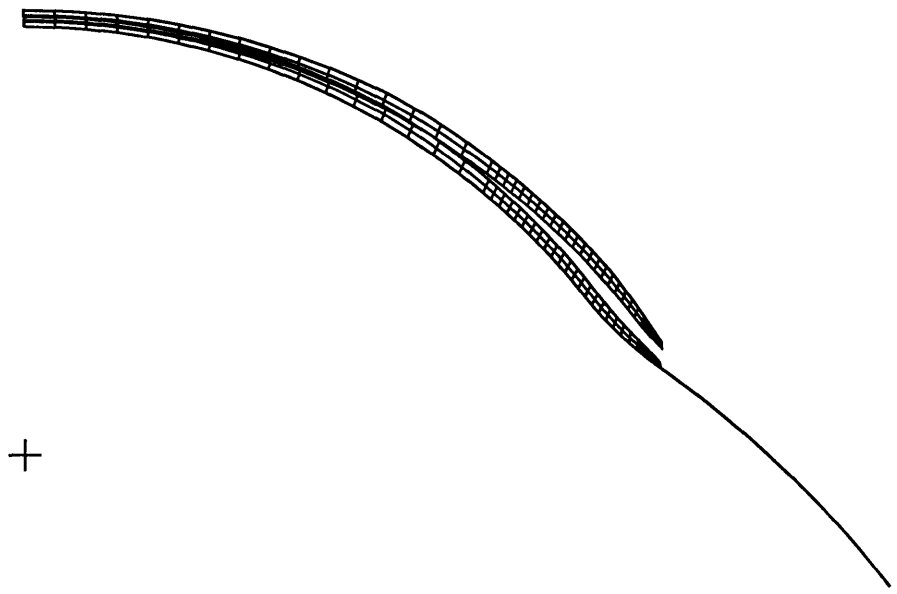

Figure 4-18: Initial and final configuration of lens I85/1 placed on eye geometry 4

that obtained with the tear layer, however, the position of the peak stress when the tear was present was most closely matched when eye1 and eye4 were used.

The through-thickness stress (S22) distributions obtained are shown in Figures 4-21 and 4-22. Note that the magnitude of this stress is very low, due to the thin shape of the lenses. Little distinction between eye geometries can be drawn from this distribution. However, the S22 stress distribution demonstrates a characteristic present in all the simulations performed without a tear , and absent in the one performed with the tear layer. The S22 distribution in all the no-tear cases contain large, oscillating spikes at the outer edge of the lens. These large stresses vary widely from one element to the next and are not a realistic representation of the through-thickness stress distribution, but rather demonstrate a numerical aberration due to the contact of the lens with a rigid boundary (the eye.) The S22 stress distribution in the lens tested with a tear also contains sharp jumps near the lens edge that are not present in reality, but the magnitude of these jumps is much lower than when no tear is present. This reduced magnitude of the stress jumps illustrates the tendency of the tear to smooth out the eye surface, and also to "cushion" the contact between the lens and the eye, resulting in a more uniform stress distribution within the lens.

The lens' S33 stress distributions are shown in Figure 4-23 and 4-24. For the stress

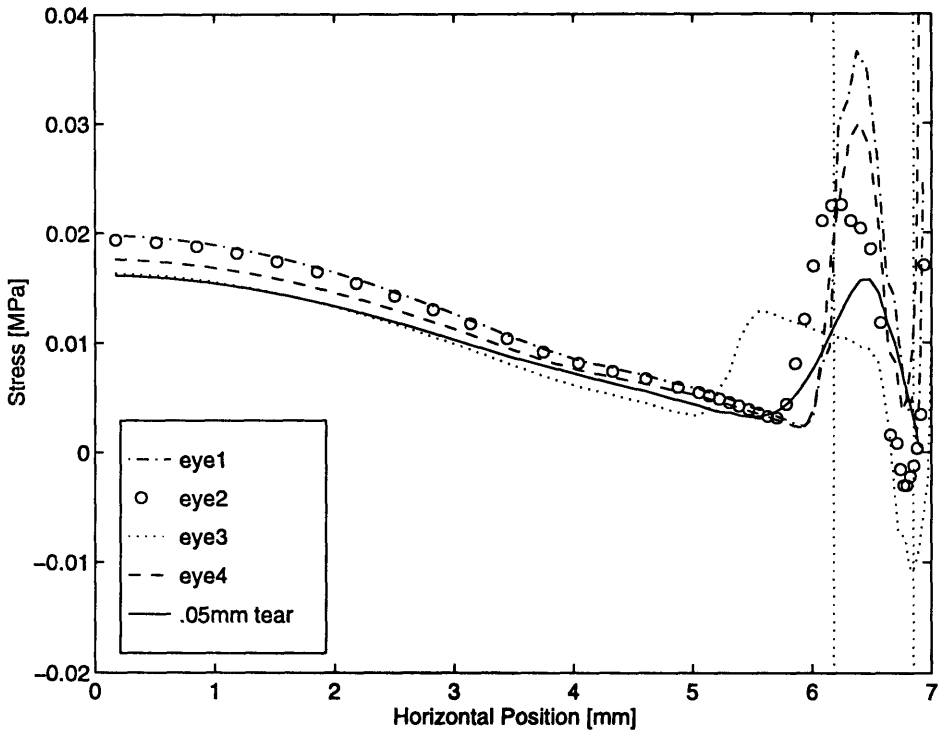

Figure 4-19: S11 stress distribution in lower layer of lens elements when lens is placed on 4 eye geometries with no tear, and when a 50μm tear layer is present

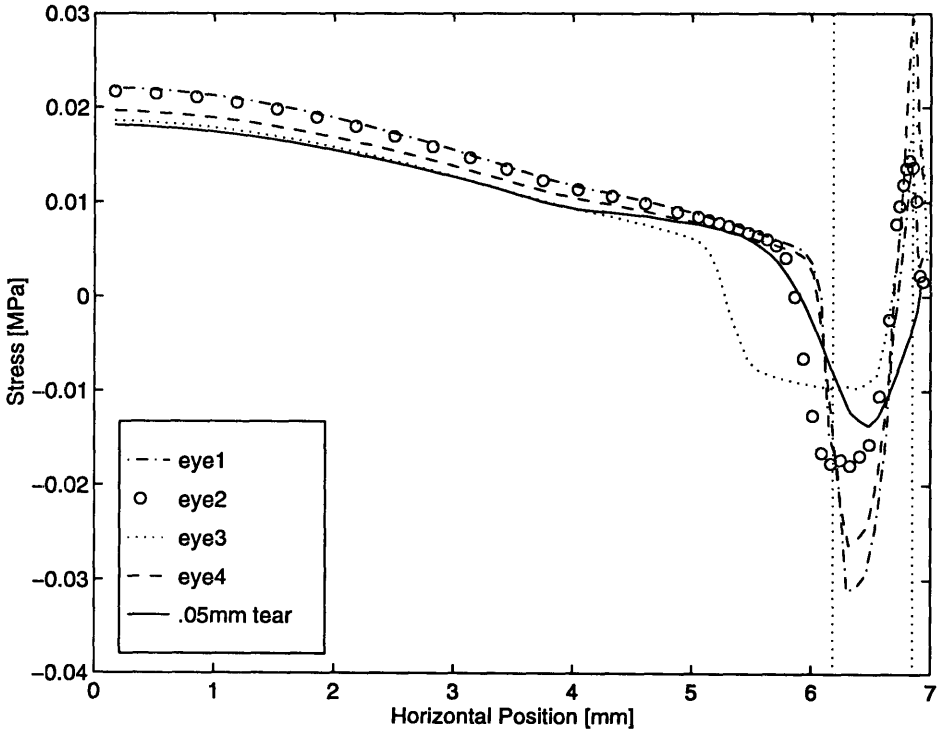

Figure 4-20: S11 stress distribution in upper layer of lens elements when lens is placed on 4 eye geometries with no tear, and when a 50μm tear layer is present

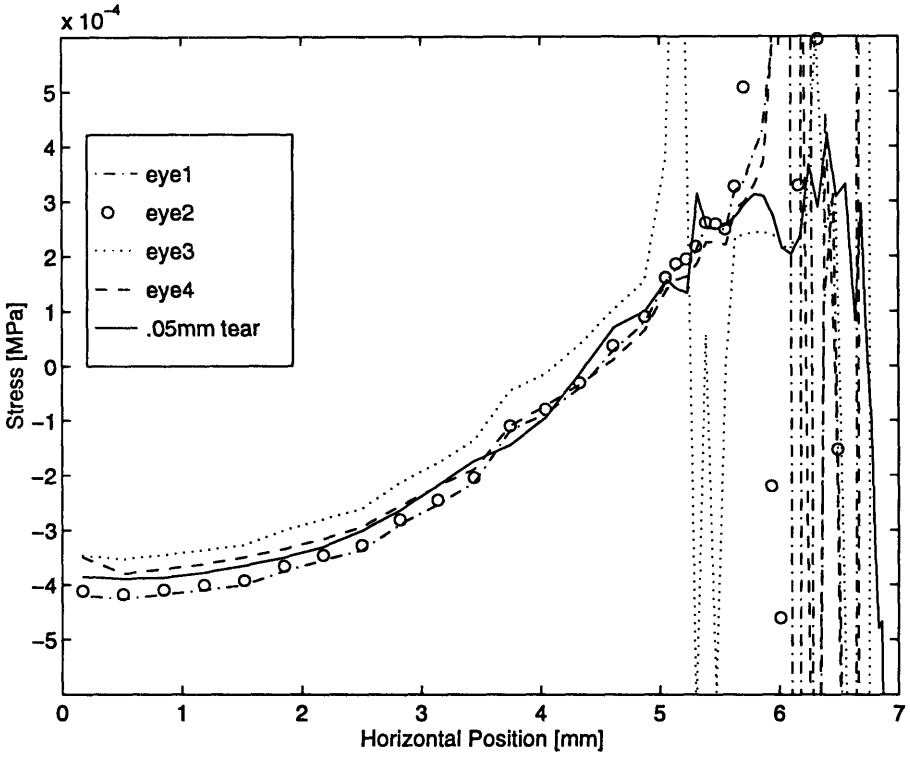

Figure 4-21: S22 stress distribution in lower layer of lens elements when lens is placed on 4 eye geometries with no tear, and when a 50μm tear layer is present

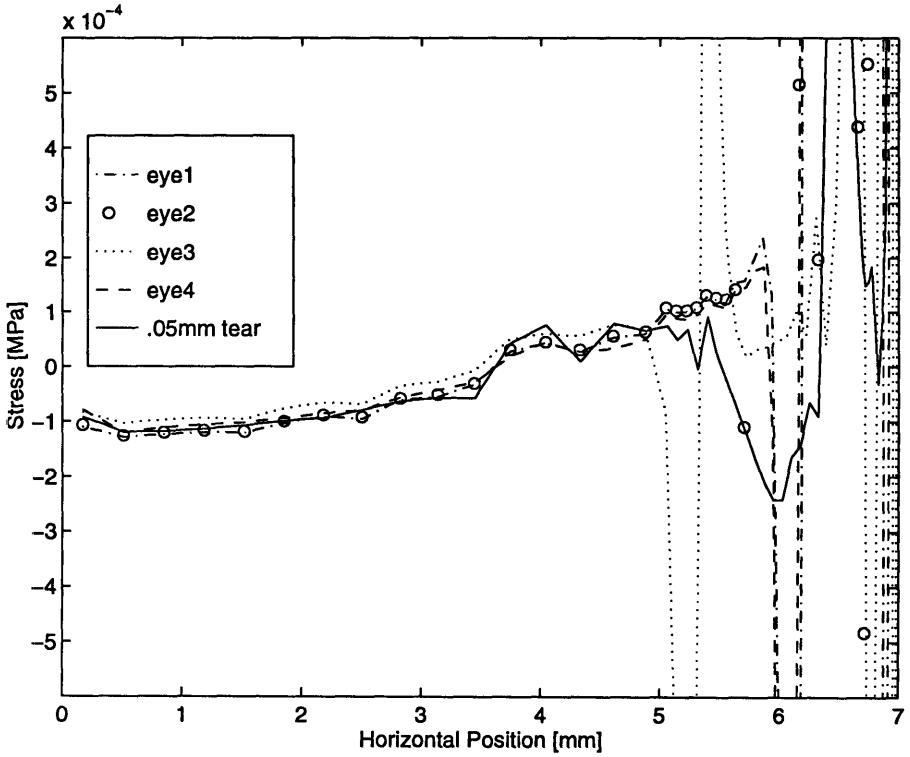

Figure 4-22: S22 stress distribution in upper layer of lens elements when lens is placed on 4 eye geometries with no tear, and when a 50μm tear layer is present

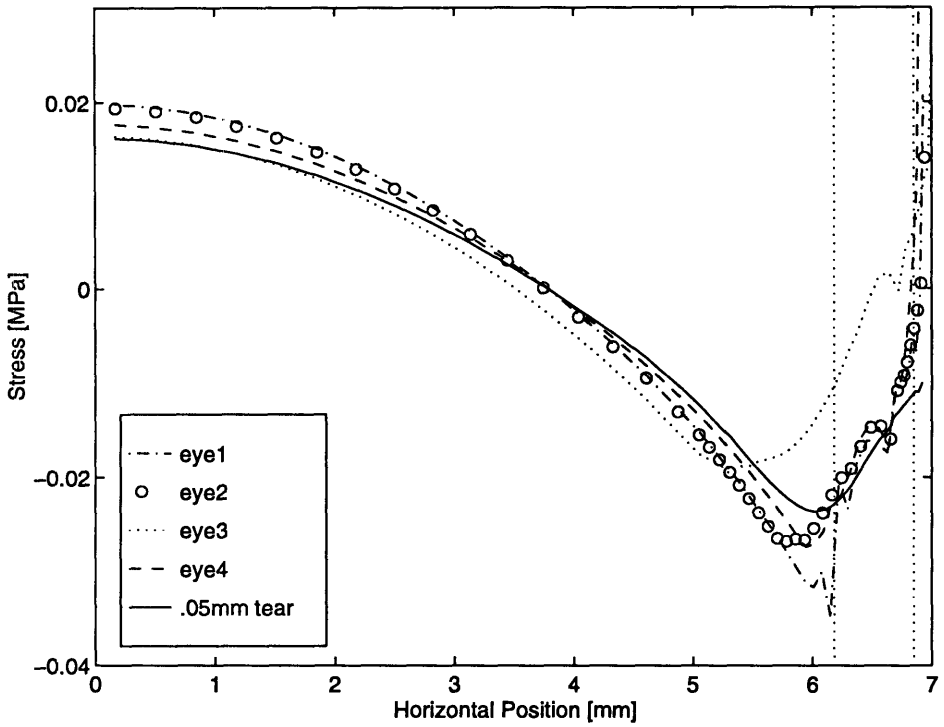

Figure 4-23: S33 stress distribution in lower layer of lens elements when lens is placed on 4 eye geometries with no tear, and when a 50μm tear layer is present

in this direction, very good correlation between the tear and no-tear cases is shown, especially for the eye1, eye2, and eye4. Again, the locations of the peak pressure near 6mm for eye1 and eye4 very closely match that of the tear-present case. However, the magnitude of stress for eye4 more closely matches that of the tear case, both at the center of the lens and near the edge.

Finally, the interface pressure at the lens/eye interface is shown in Figure 4-25. (For the case that includes the tear layer, the tear/eye interface pressure is plotted.) The interface pressure distribution is very smooth for the case that includes the tear layer, while those without the tear layer display oscillations about a mean value. As was the case in the S22 distributions, the oscillations vary at each node on the contact surface and are a result of modeling technique rather than of a physical phenomenon. Again, the smooth shape of the interface pressure distribution when the tear layer was present demonstrates the capacity of the tear to smooth out the numerical singularities that arise when no tear layer is used. This effect is very important at the lens edge, where large pressure gradients caused by the backwards bending of the lens

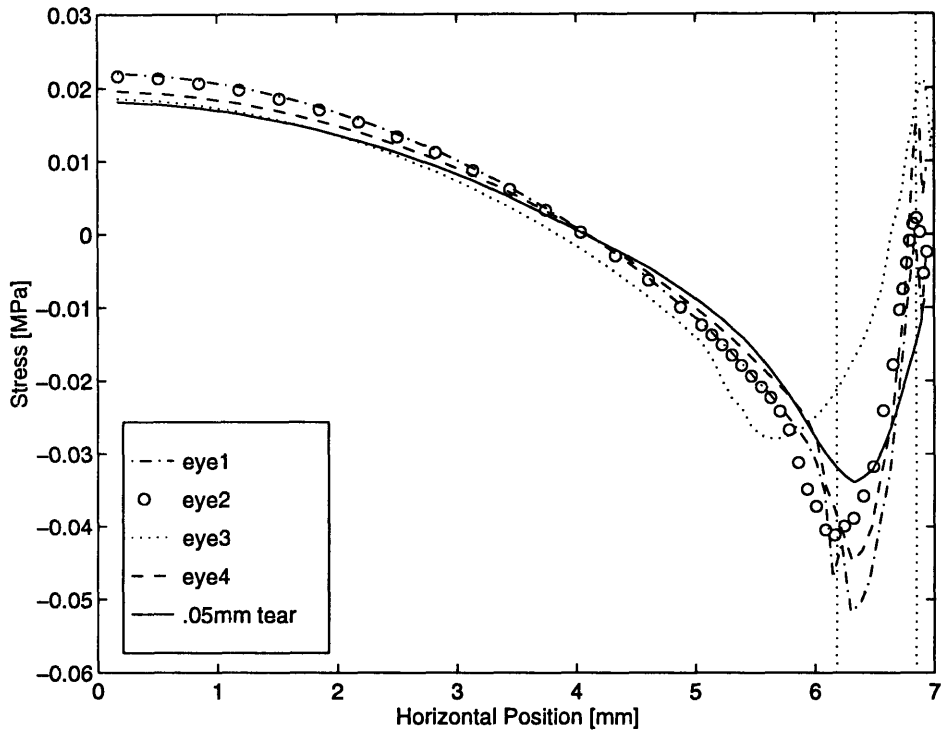

Figure 4-24: S33 stress distribution in upper layer of lens elements when lens is placed on 4 eye geometries with no tear, and when a 50μm tear layer is present

amplify the oscillations present in the interface pressure distributions of the no-tear cases.

A close similarity exists between the S33 and interface pressure distributions, especially at the center of the lens, where stresses in the lens are caused primarily by pressure. This resemblance is due to the thin, spherical shape of the lens, which causes it to behave much like a spherical pressure vessel. In such a vessel, the pressure, p, and hoop stress, $\sigma_{\theta\theta}$, are connected by the relation: $\sigma_{\theta\theta} = \frac{pr}{2t}$, where r is the radius of the vessel, and t is the wall thickness. As the edge of the lens is approached, bending begins to contribute significantly to the stress state in the lens, so the correlation between S33 and interface pressure is not as precise, but a general relationship between the two quantities can still be seen. The relationship between S33 and interface pressure is shown to hold well at the lens center in Figure 4-26 where both interface pressure the quantity $\frac{2tS33}{r}$ are plotted for the simulation that included a tear layer. The t used was the lens thickness along its profile, and r was taken to be constant and equal to the radius of curvature of the cornea. The difference between the two

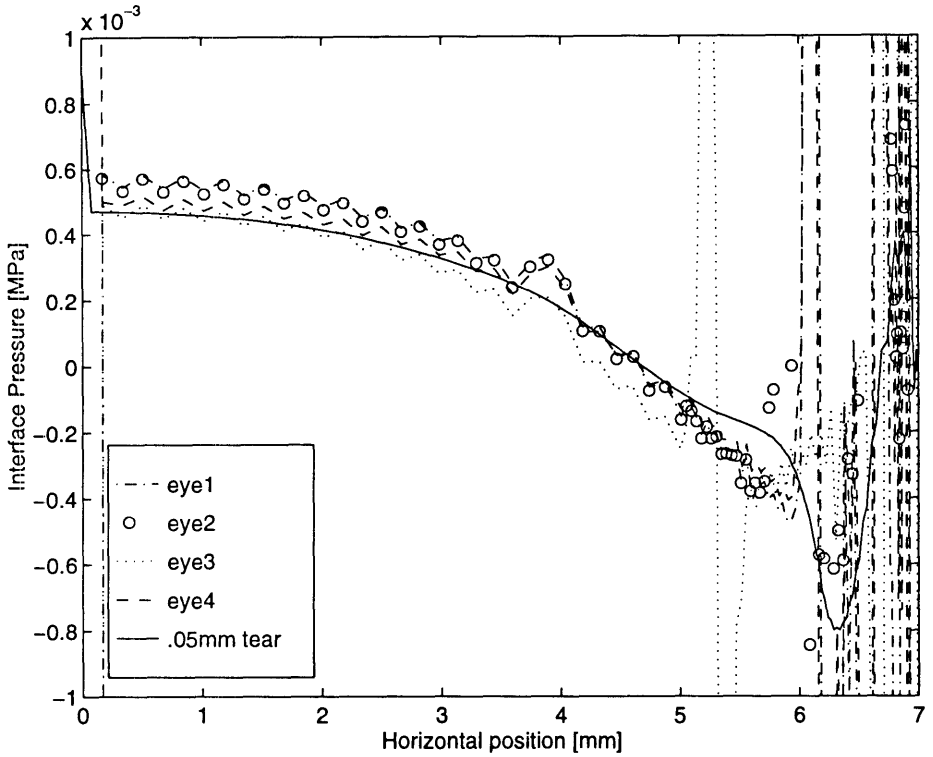

Figure 4-25: Lens/eye interface pressure distribution when lens is placed on 4 eye geometries with no tear, and when a 50μm tear layer is present

values of $\frac{2tS33}{r}$ calculated for the upper and lower element layers is greatest near the cornea/sclera junction, and is due to the effects of bending on S33 at this point. Interface pressure and $\frac{2tS33}{r}$ as calculated from S33 measured in the upper and lower element layers are also shown for the simulation when the lens is placed on eye4 without a tear layer in Figure 4-27. Again, the interface pressure and $\frac{2tS33}{r}$ agree very well, but the magnitude of $\frac{2tS33}{r}$ when calculated with the stress measured in the lower layer agrees more closely to that of the interface pressure.

The relationship between interface pressure and S33 provides a method for estimating interface pressure in cases when the direct measurement is unreadable, as is the case when no tear layer is used. In addition, the S33 distribution of the no-tear cases do not contain the artificial oscillations and singularities present in the corresponding interface pressure distributions. This is due to the fact that interface pressure is measured at the lens/eye interface, and is a measure of the forces acting directly along the eye surface normal. The difficulties of contact modeling can lead to artificial values and variations in the calculated interface pressure. In contrast, S33

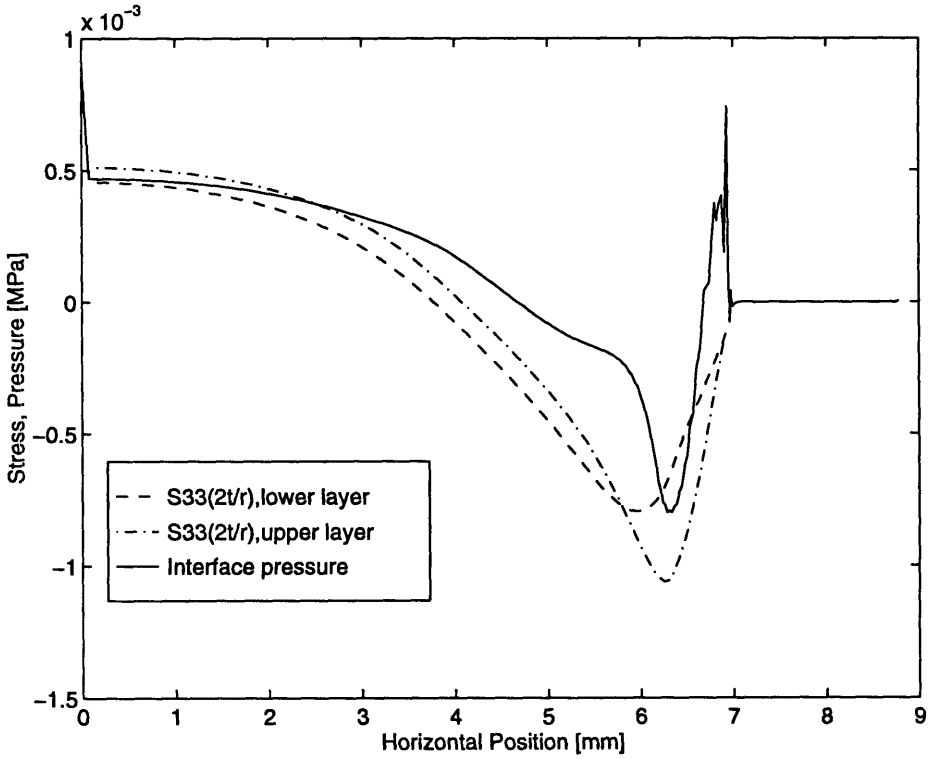

Figure 4-26: Interface pressure and $\frac{2tS33}{r}$ when lens is placed on the eye with a 50μm tear layer

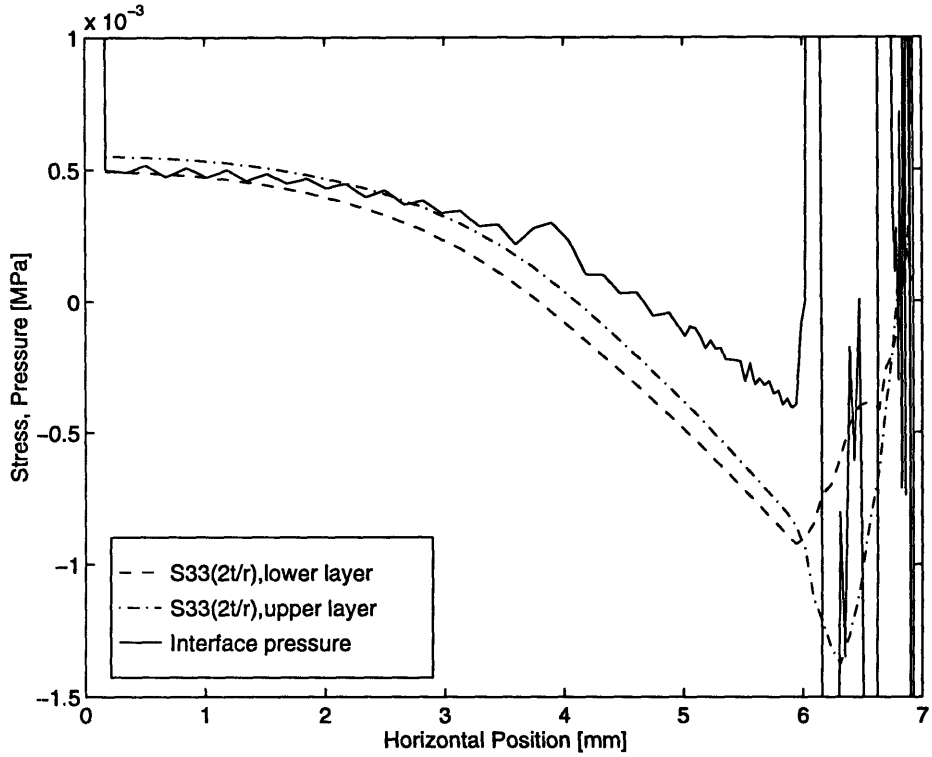

Figure 4-27: Interface pressure and $\frac{2tS33}{r}$ when lens is placed on eye4 without a tear layer

is calculated at integrations points within the element, and is directed circumferentially around the lens (perpendicular to the eye surface normal.) It is therefore less susceptible to numerical singularities caused by the lens/eye contact.

The above simulations illustrate that the tear layer has a significant effect on the internal stresses in the lens predicted by the finite element simulations. In general, the tear layer acts to reduce the magnitude of local peak stresses and to reduce stress gradients within the lens. This effect reflects the physical properties of a real tear. The pressures that would develop in a fluid layer beneath a real lens would act to redistribute stresses in the lens in such a way as to make the internal lens stresses more uniform. This is exactly what the simulated tear layer does.

In addition, the tear layer aids in the issue of accurately modeling the interface pressure at the eye surface. The low modulus of the tear layer relative to that of the lens allows the tear to conform to the eye surface under the pressure exerted by the lens more closely than the lens material could conform under the same pressure. This greater flexibility allows the tear to absorb the artificial interface pressure oscillations that arise when the lens is placed directly on the eye.

While the above simulations illustrate the important effects of the tear layer, they also demonstrate that the internal lens stress distributions obtained with simulations performed without a tear layer correspond very closely to those that arise in the lens when the tear layer is included in simulations. In addition, the close relationship between S33 and interface pressure distributions allow a good approximation of interface pressure to be obtained for simulations without a tear layer, even though the direct measurement of interface pressure for the no-tear simulations is highly distorted by modeling difficulties.

This close correspondence between stress and pressure information obtained with and without a tear layer demonstrates that modeling lens placement on the eye without a tear layer is a good alternative to models that include the tear layer. Given that the simulations performed with a tear layer were very unreliable in terms of converging to a solution, the no-tear modeling method was chosen as a means to compare the relative effects of lens geometry on lens fit. Of the four eye geometries tested

above without a tear layer, the stress and pressure distributions obtained with eye4 were judged to be the best approximation to those obtained when the tear layer was included. Therefore, the eye4 geometry was chosen to be the eye surface geometry used in subsequent simulations.

4.2 Lens Placement Simulations with Varying Lens Geometries

A number of simulations were performed, similar to the previous simulations, in which lenses of varying geometry were placed on a rigid eye without a tear layer. The purpose of these simulations was to determine the effects of various geometric characteristics such as thickness profile and basecurve radius on the internal stress distributions developed within the lens and also on the induced pressure distributions at the lens/eye interface.

4.2.1 Finite Element Model

A typical finite element model used in these simulations is shown in Figure 4-28. The eye was modeled as an axisymmetric rigid surface with the surface geometry of eye4. (See Figure 4-29) This eye geometry was used in all but one of the simulations, in which a spherical eye model was used instead.

The lens mesh used is the same as that described above in Section 4.2.1. It was composed of 92 8-node axisymmetric elements. The nodes on the central axis were constrained to remain on the axis, but were allowed vertical motion.

The lens material was modeled as linear elastic and nearly incompressible. (Poisson ratio=0.49) For most simulations, the elastic modulus was set to 2MPa, however, for the simulations with the lens blanks used in the Martin and Holden experiment, the modulus was set to 0.16 MPa to match the modulus of the experimentally tested lens material. Also, for a simulation of the Fatt and Chaston experiment, the lens modulus was set to 0.0298MPa to match the modulus calculated by Jenkins and

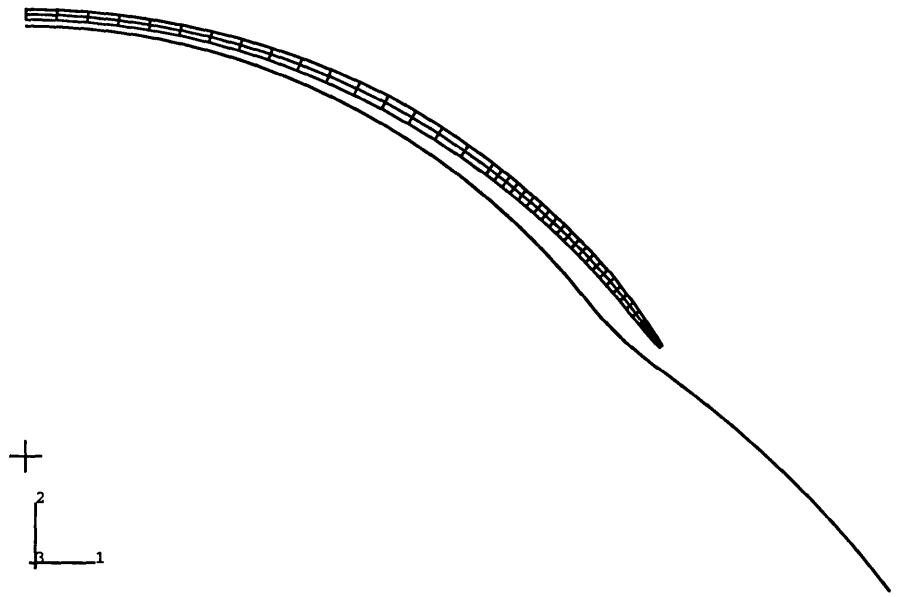

Figure 4-28: Typical finite element model for simulating the placement of various lens geometries on a rigid eye

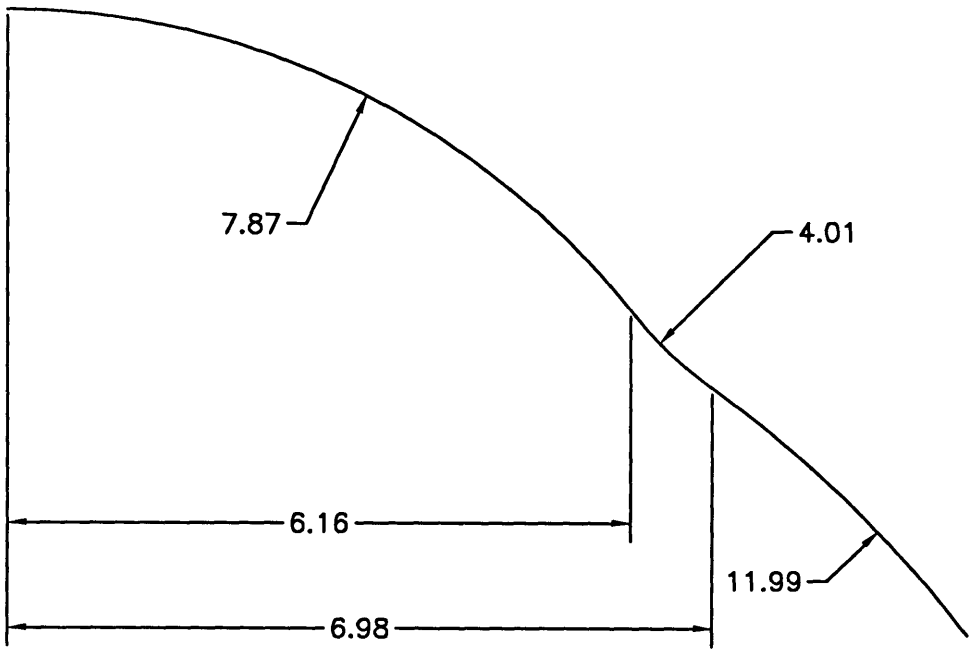

Figure 4-29: Geometry of the eye4 eye surface. All dimensions are in mm.

Shimbo.

The eye/lens interface was modeled with a no separation condition as described above. The lower lens surface was designated as slave, and the eye surface as master. Therefore, all lens nodes that established contact with the eye were required to remain in contact.

As before, the loading took place in two steps. First a 0.05MPa pressure was applied to the upper surface of the lens. Then, the pressure was removed and the lens allowed to equilibrate on the eye. For each simulations, it was verified that contact had been established between the eye surface and every node on the lower surface of the lens. Occasionally, a lens node would not be in contact with the eye after the initial pressure was applied. In this case, additional pressure was applied to the lens opposite the unconnected node, in order to establish lens/eye contact at all points.

4.2.2 Lens Geometries Modeled

A number of actual and blank lens geometries were modeled in lens placement simulations. First, the F88/1, G88/1, H88/1, and I85/1 geometries used in the flexibility simulations described in the previous chapter were modeled. These lenses all had the same central region thickness profile, but differing lenticular and edge region profiles. (See Figure 3-21 this is in the previous chapter) The F88/1, G88/1, and H88/1 lenses all had a basecurve radius of 8.8mm, (a bearing of 0.93mm steep) while the I85/1 lens had a basecurve radius of 8.5mm. (a bearing of 0.63mm steep)

Next, another group of actual lenses were modeled (labeled N83 and N85.) These lenses were similar to the F, G, H, and I lenses in that their upper surface was defined by three circular arcs of the optical, lenticular, and edge regions. However, the lower surfaces of the N83 and N85 lenses were also defined by three separate arcs rather than having a single basecurve radius. The three arcs that compose the lower surface are referred to as the Central Basecurve, the 2Basecurve, and the Bevel Zone. (See Figure 4-30)

For this group of lenses, four geometries were tested. The N83a, N83b, and N83c all had the same central thickness profile, but the thickness of their lenticular regions

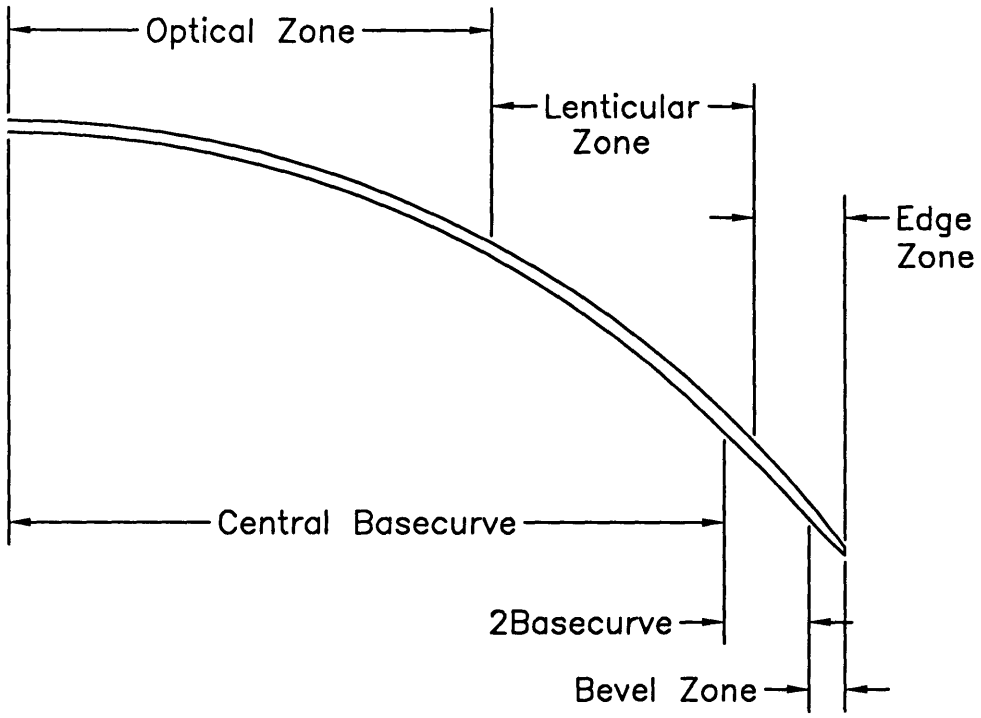

Figure 4-30: The six circular arcs that compose the N83 and N85 lenses.

differed slightly. (See Figure 4-31) The N85b was the fourth lens of this group tested. This lens had a very similar thickness profile to that of the N83b lens, (see Figure 4-31) but it had a slightly larger overall radius of curvature. (See Figure 4-32)

The third group of lens geometries tested was a set of blank geometries similar to the ones tested by Martin and Holden in the experiment described earlier. Martin and Holden tested lens blanks of three constant thicknesses (0.066, 0.16, and 0.31mm) and various constant radii of curvature (7.34 - 9.49mm.) The cornea of the model eye they used had a radius of curvature of 7.8mm. Therefore, the bearings of lenses tested ranged from 0.46mm flat to 1.69mm steep. Three geometries were chosen (M1, M2, and M3) for simulation that had a thickness of 0.16mm and a bearing equal to those of blanks actually tested by Martin and Holden. The corneal radius of curvature of the eye geometry used in these simulations is 7.87mm, so, while the bearings of the M1, M2, and M3 lenses match those of the lenses tested by Martin and Holden, the actual radii of curvature of these three blanks do not exactly match those of the blanks

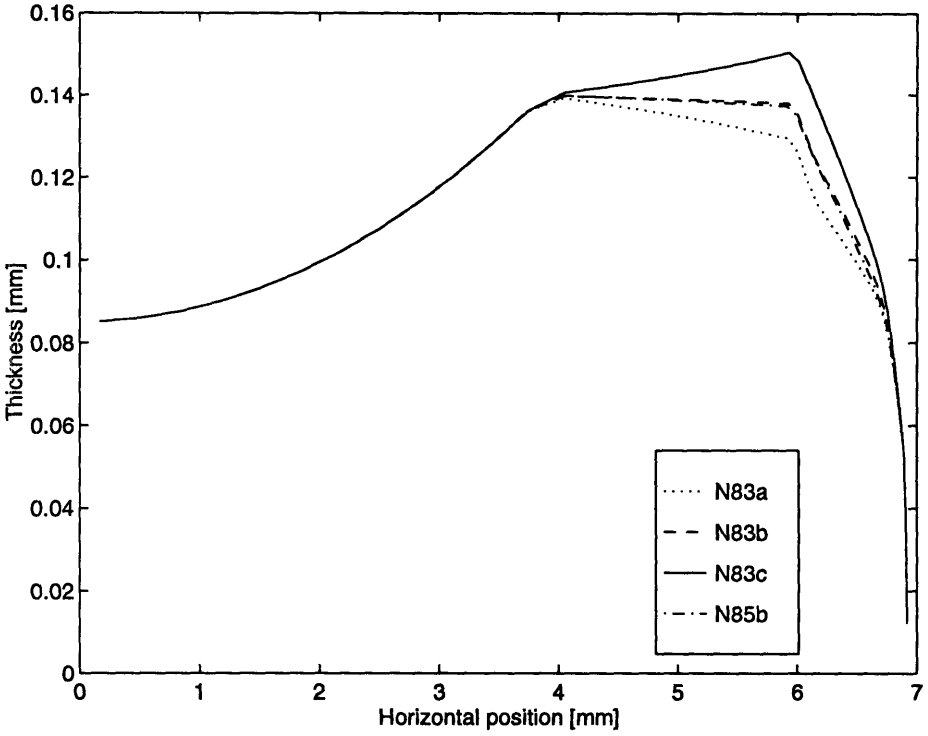

Figure 4-31: Thickness profiles of the N83a, N83b, N83c, and N85b lenses

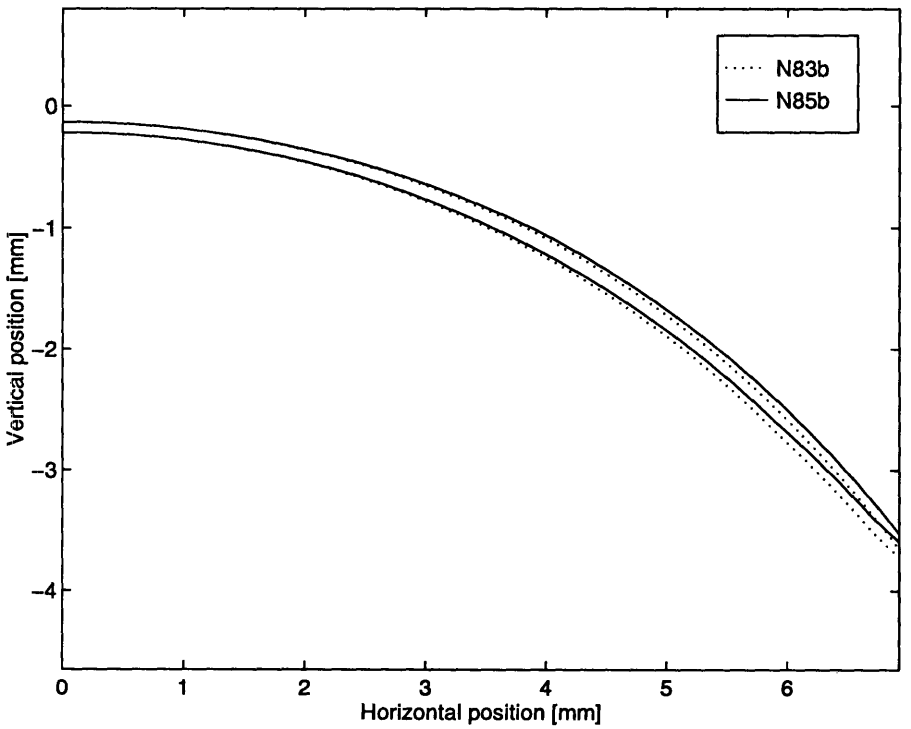

Figure 4-32: Cross sections of the N83b and N85b lenses

Blank	Thickness	Radius of Curvature	Bearing
M1	0.16mm	7.55mm	0.32mm steep
M2	0.16mm	7.84mm	0.03mm steep
M3	0.16mm	9.06mm	1.19mm flat
M4	0.066mm	7.55mm	0.32mm steep
M5	0.31mm	7.5mm	0.32mm steep

used in the Martin and Holden experiment. In order to study the effects of thickness independent of bearing, two additional geometries were simulated (M4 and M5) that had thicknesses equal to blanks actually tested (0.066 and 0.31mm) and bearings equal to that of blank geometry M1. (Martin and Holden did not test blanks with the geometries of blanks M4 and M5, but they did test blanks of thickness of 0.66 and 0.31mm with bearings slightly greater and less than the M4 and M5 bearing.) The diameter of all five blanks was 13.43mm, equal to the average diameter of the blanks used by Martin and Holden. The elastic modulus used was 0.16MPa, equal to the modulus of one set of lenses tested in the experiment. A list of the geometries of blanks M1 - M5 is listed in Table 4.2.2.

The final lens geometry tested was one used in the experiment by Fatt and Chaston and simulated by Jenkins and Shimbo. This lens had constant radius of curvature of 6.5mm and a thickness of 0.2mm. The modulus of the lens material was set to 0.0298MPa, the value used by Jenkins and Shimbo to obtain the same central lens/eye pressure measured by Fatt and Chaston. For this simulation, the eye surface was modeled as spherical with a radius of curvature of 7.5mm, to match the eye geometry used in the Fatt and Chaston experiment.

4.2.3 Results of Lens Placement Simulations

F88/1, G88/1, H88/1, and I85/1 lenses

The initial and final mesh configurations of the placement simulation of the G88/1 lens on eye geometry 4 is shown in Figure 4-33 This figure is typical for all the lenses in this group. The internal stress and interface pressure distributions obtained

with the F88/1, G88/1, H88/1 and I85/1 lens simulations are shown in Figures 4-34 to 4-39. As before, all stresses are oriented with respect to the individual elements, (1:tangential, 2:through-thickness, 3:circumferential) and all reported stresses are the values calculated at the integration point located at the center of the elements. The vertical dotted lines in the figures mark the endpoints of the three circular arcs to construct eye4.

The S11 stress distributions for the lower and upper layers of lens elements are shown in Figures 4-34 and 4-35. The bending at the cornea/sclera junction (at approximately 6mm) is evident in the S11 stress distributions for all four lenses, where the stress in the lower lens layer has a large tensile peak, and the stress in the upper surface has a large compressive peak. In contrast, at the center of the lenses, the magnitude of stress in the upper and lower element layers matches very closely within each lens, and the direction of stress is tensile in both layers. This indicates that the center of the lens is being stretched tangentially due to the contact pressure rather than being bent.

The differences in the S11 distributions of the four lenses reflect their geometric variations. For the F88/1, G88/1, and H88/1 lenses, which all have the same base curvature, the magnitude of S11 stress corresponds to the relative thickness of the lens' lenticular and edge regions. (See Figure reffigure in last chapter) The magnitude of stress is greatest for the H88/1 lens, which has the thickest profile, and least for the G88/1 lens, which has the thinnest profile, both in regions of tensile and compressive stress.

Figures 4-34 and 4-35 also show that the magnitude of S11 stress depends not only on lens thickness, but on lens curvature as well. Figure 3-21 illustrates that the thickness distribution of the F88/1 and I85/1 lenses is very similar. However, at the center of the lens, the magnitude of stress in the S11 direction is considerable lower for the I85/1 lens. This is due to the fact that the base curve of the I85/1 lens more closely matches the curvature of the cornea than the F88/1 lens and, therefore, less shape conformation is required for the I85/1 lens to fit the eye. (I85/1 basecurve=8.5mm, F88/1 basecurve=8.8mm, cornea radius of curvature=7.87mm) Recall that these two

lenses had very similar force-displacement behaviors in pinching. (See Figure 3-20)

Figures 4-34 and 4-35 also demonstrate that the relative influence of thickness and curvature on the S11 stress magnitude varies at different points in the lens. At the center of the lens, the S11 stress in the I85/1 lens is much lower than that in the other three lenses, even though the average thickness of the G88/1 lens is less than that of the I85/1 lens. This indicates that the curvature of the lens has a strong influence on the level of tensile stress developed at the lens center. However, at the cornea/sclera junction, where the S11 stress is predominantly caused by bending, the magnitude of the stress of all the lenses corresponds primarily to their lenticular zone thickness, with the G88/1 lens having the lowest magnitude, and the H88/1 having the greatest. The influence of curvature is only secondary at this point, and serves to differentiate between the F88/1 and I85/1 lenses, which have the same thickness profile. The magnitudes of stress of the four lenses at the cornea/sclera junction illustrates that when the stress is created by bending rather than stretching, the influence of thickness on stress magnitude increases relative to that of curvature. This result is expected, since stress in bending is related to the cube of the material thickness, while stress due to pressure is proportional to thickness. Therefore, as loading due to bending increases, the influence of thickness on stress should also increase.

The S33 stress distributions of the four lenses is shown in Figures 4-34 and 4-35. At the center of the lenses, the stress of all lenses closely matches the corresponding S11 stresses. This is expected, since at the very center of the lens, the tangential and circumferential directions are equivalent due to the axisymmetric geometry. Around 3.5mm, the S33 stress becomes compressive. This is due to the fact that all the lenses in this set are flatter than the cornea, and must contract circumferentially near the lens edge in order to conform to the shape of the eye. The maximum compressive stress is reached at the cornea/sclera junction, where the curvature of the eye changes. At this point, the magnitude of the compressive stress is greater on the upper layer of lens elements. This is due to the reverse in eye curvature at the junction, which causes the outer surface of the lens to compress more than the inner surface relative to their initial positions. A major difference between the S33 and S11 stresses at

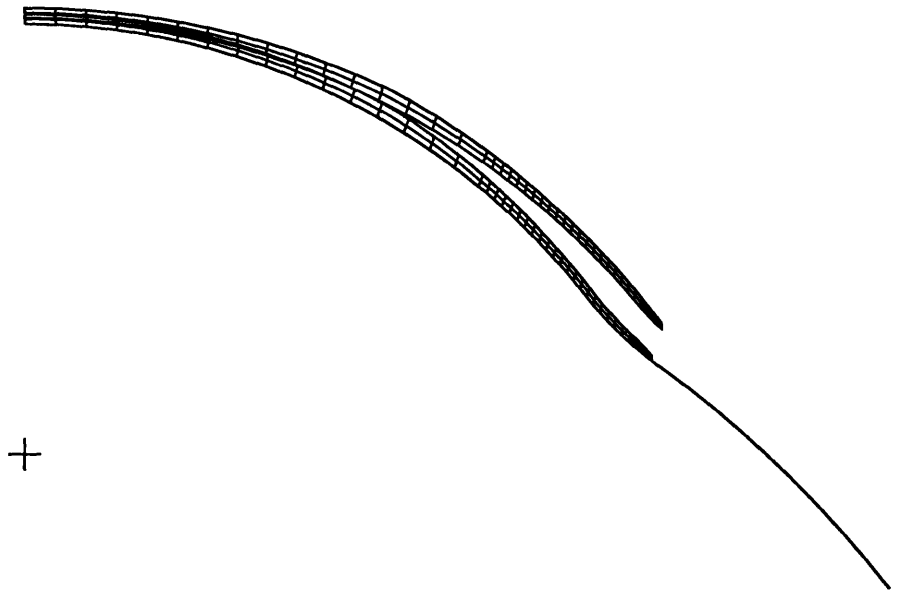

Figure 4-33: Initial and final configurations of G88/1 lens placed on eye with no tear layer

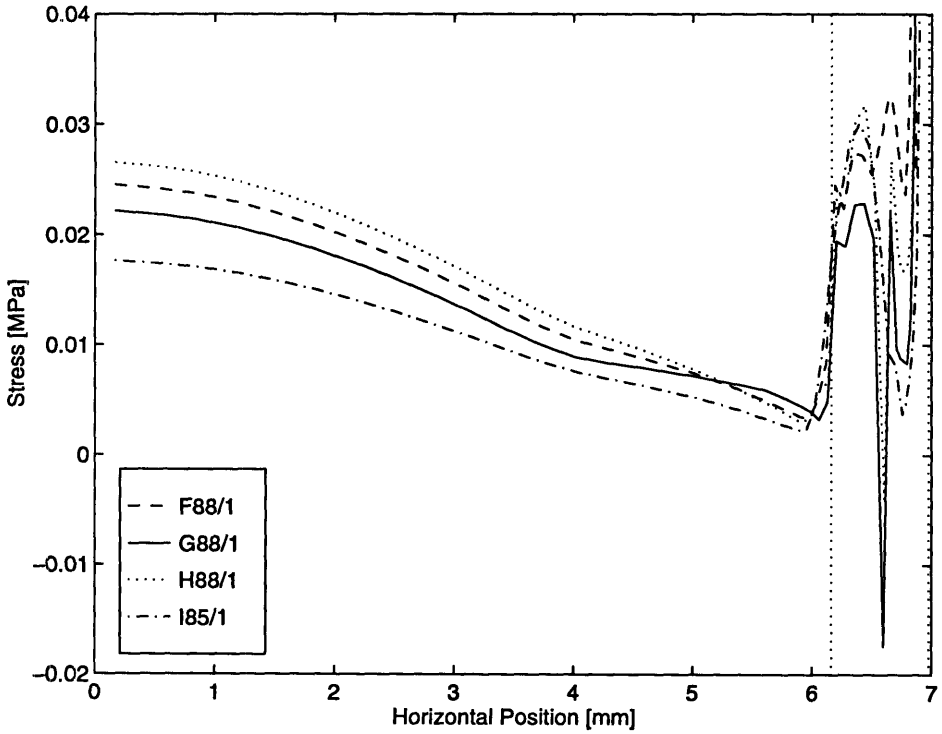

Figure 4-34: S11 stress distribution in lower layer of lens elements for F88/1, G88/1, H88/1, and I85/1 lens placement simulations

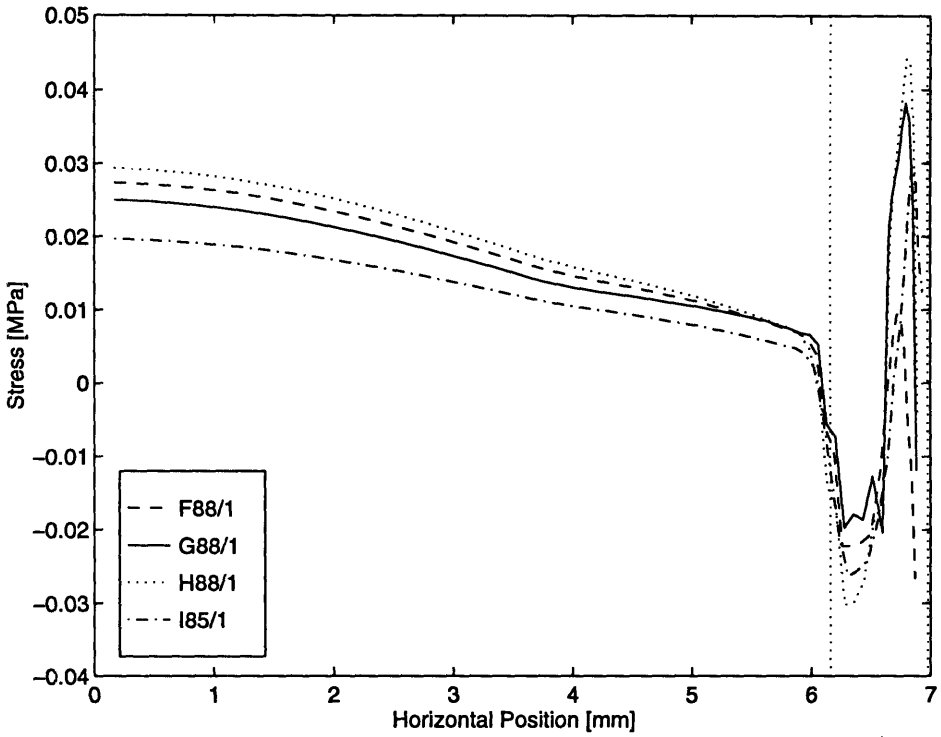

Figure 4-35: S11 stress distribution in upper layer of lens elements for F88/1, G88/1, H88/1, and I85/1 lens placement simulations

the cornea/sclera junction is that the S33 stresses are compressive in both layers of lens elements, while the S11 stresses were in opposite directions in the two layers. This is because the bending has only a Poisson effect on the circumferential stress, while it was a primary source of tangential stress. At the very edge of the lens (at approximately 6.8mm) the S33 stress becomes tensile as the lens must stretch circumferentially in order to fit onto the sclera, whose radius of curvature (12mm) is larger than that of the undeformed lenses ($\approx$ 8.6 mm.)

The S33 stress distributions also illustrate differences between the lens geometries. At the lens centers, the S33 stress behaves much like the S11 stress. For lenses of the same curvature (F88/1, G88/1, and H88/1) the magnitude of stress increases with increasing lens thickness. However, as with the S11 stress, the smaller curvature of the I85/1 lens causes it to have a lower central S33 stress than even the G88/1 lens, which has a thinner cross section. The four S33 stress distributions display a different trend at the cornea/sclera junction. The difference in thickness between the F88/1, G88/1, and H88/1 lenses has negligible effect on the magnitude of stress

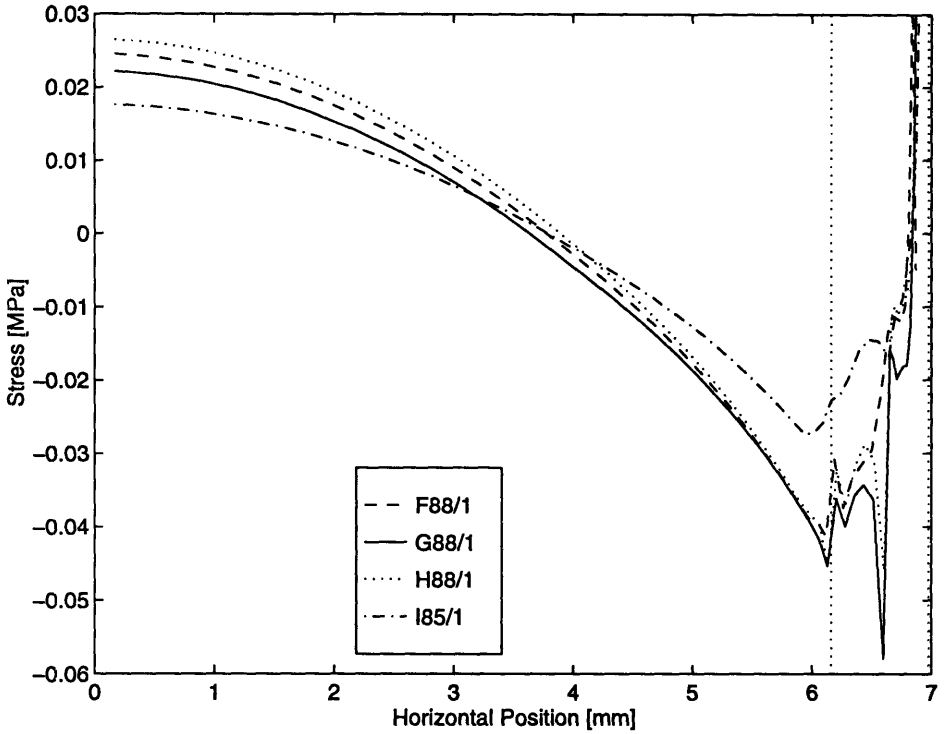

Figure 4-36: S33 stress distribution in lower layer of lens elements for F88/1, G88/1, H88/1, and I85/1 lens placement simulations

developed at this point, while the I85/1 lens has a much lower stress magnitude due to its smaller curvature. The relative magnitudes of the S33 stress between lenses at the cornea/sclera junction are very different than those of the S11 stress, where the thickness had a large effect on the magnitude of S11 stress in each lens. This difference is again due to the fact that S11 stress at the cornea/sclera junction was largely caused by bending, while the bending influence is much less on the S33 stress.

The interface pressure distributions for this group of lenses are shown in Figure 4-39, and the quantity $\frac{S33(2t)}{r}$ is shown in Figures 4-40 and 4-41. As in the previous section, r is taken as the radius of curvature of the cornea, and t as the lens thickness, which varies along the profile of each lens. These graphs illustrate that all four lenses apply a positive pressure to the center of the cornea, and exert a negative (tensile) pressure on the eye toward the lens edge. This pressure distribution corresponds to the flat bearing of all the lenses. In order to force the undeformed lenses to take on the smaller curvature of the cornea, it would be necessary to apply an upward force at the center of the lens, and an inward and downward force at the lens edge, a loading

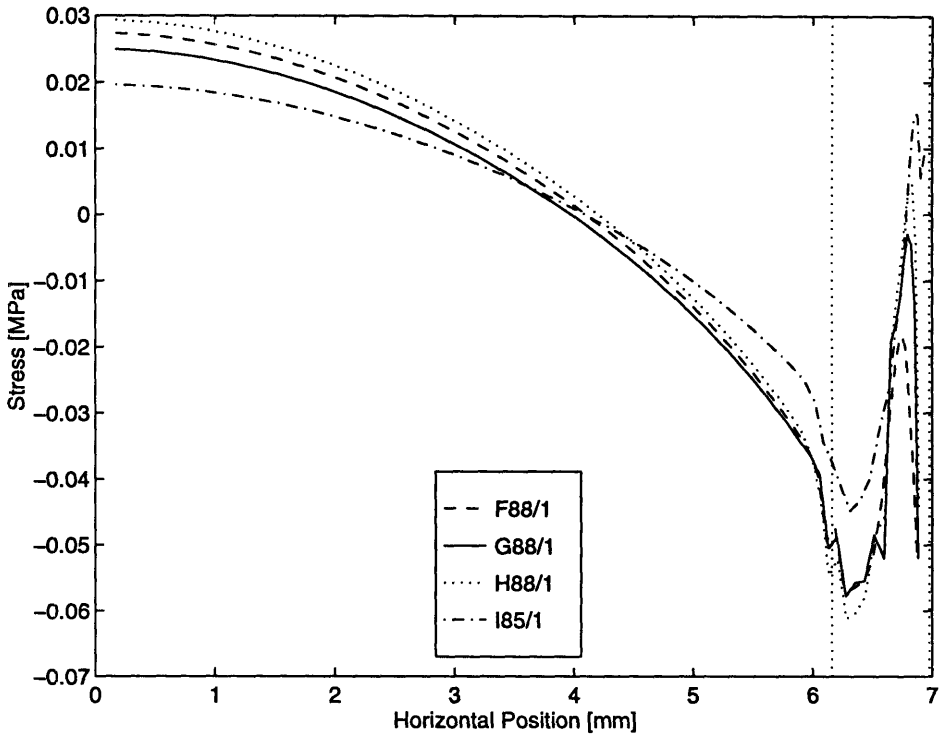

Figure 4-37: S33 stress distribution in upper layer of lens elements for F88/1, G88/1, H88/1, and I85/1 lens placement simulations

which agrees with the measured interface distributions. (See Figure 4-38a)

The differences in lens geometries are clearly reflected in both the interface pressure and $\frac{S33(2t)}{r}$ distributions at the center of the lenses. Again, the lowest pressure is applied by the I85/1 lens, due to its smaller curvature, and the pressure applied by the F88/1, G88/1, and H88/1 lenses increases with increasing thickness. The distinctions between effect of lens geometry becomes less clear near the edge of the lenses. In the interface pressure distribution, the values are unreadable beyond approximately 6mm, however, it appears that just before the spikes in pressure arise, the magnitudes of tensile pressure correspond roughly to lens thickness, with the thickest lens exerting the greatest tensile pressure. A much more clear separation between lenses exists in the $\frac{S33(2t)}{r}$ distributions near the lens edge, and the ordering of the pressure magnitude created by the four lenses is the same as it is at the lens centers. However, Figures 4-26 and 4-27 illustrate that near the lens edge, the equality between interface pressure and $\frac{S33(2t)}{r}$ breaks down, due to the increased contribution of bending near the edge region. Therefore, the magnitudes of $\frac{S33(2t)}{r}$ shown in Figures 4-40 and 4-41

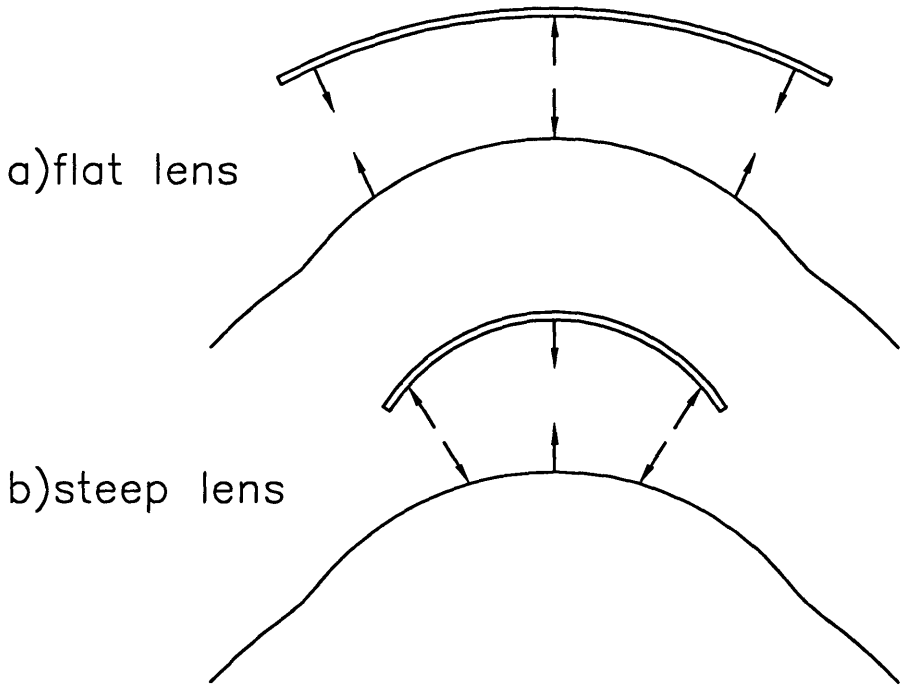

Figure 4-38: Free body diagram which illustrates the forces needed to cause lenses with flat (a) and steep (b) bearing to conform to the eye.

cannot be assumed to be accurate measures of interface pressure near the lens edges.

N series lenses

Figure 4-42 shows the typical initial and deformed mesh configurations obtained when an N series lens is placed on the eye without a tear layer. (The lens geometry shown in Figure 4-42 is N83b.) The S11, S33, interface pressure, and $\frac{S33(2t)}{r}$ distributions for the N83 and N85 set of lens geometries are shown in Figures 4-43 to 4-49. The thickness profiles of the four lenses modeled are given in Figure 4-31, and the cross sectional shapes of lenses N83b and N85b are shown in Figure 4-32.

The S11 stress distribution of the N series lenses (see Figures 4-43 and 4-44) are very similar to those of the previous lens group. The stress in tensile at the lens centers in both layers of elements, and has a tensile peak in the lower element layer and a compressive peak in the upper element layer near the cornea/sclera junction. However, the S11 distributions of the N series lenses contain a large spike in stress at approximately 5.8mm. This spike coincides with the beginning of the 2basecurve

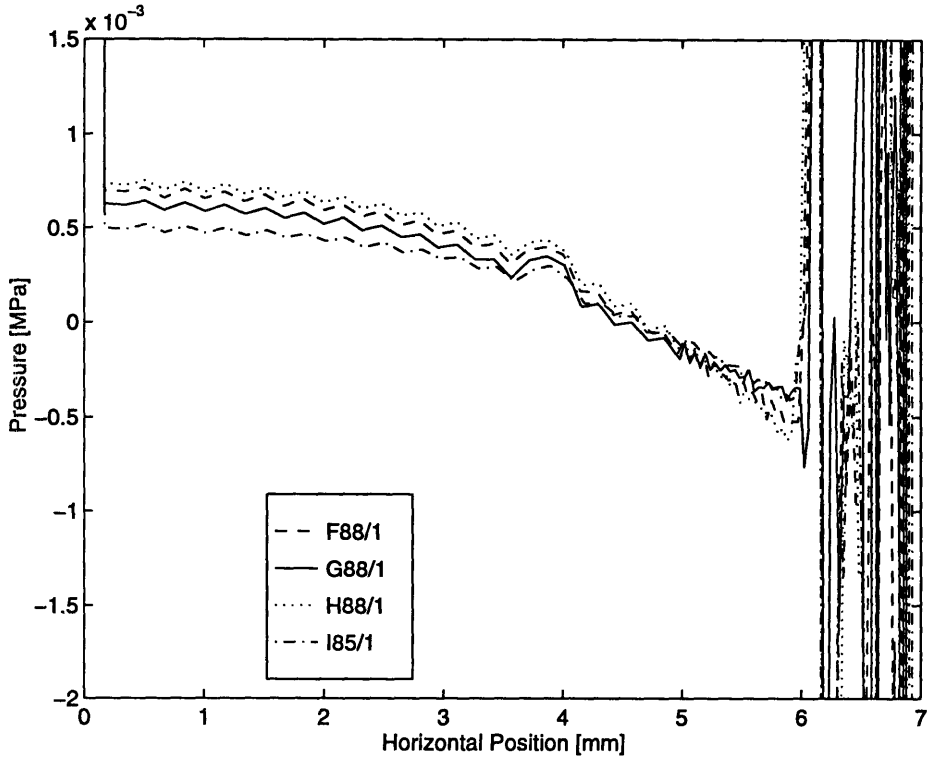

Figure 4-39: Interface pressure distributions for F88/1, G88/1, H88/1, and I85/1 lens placement simulations

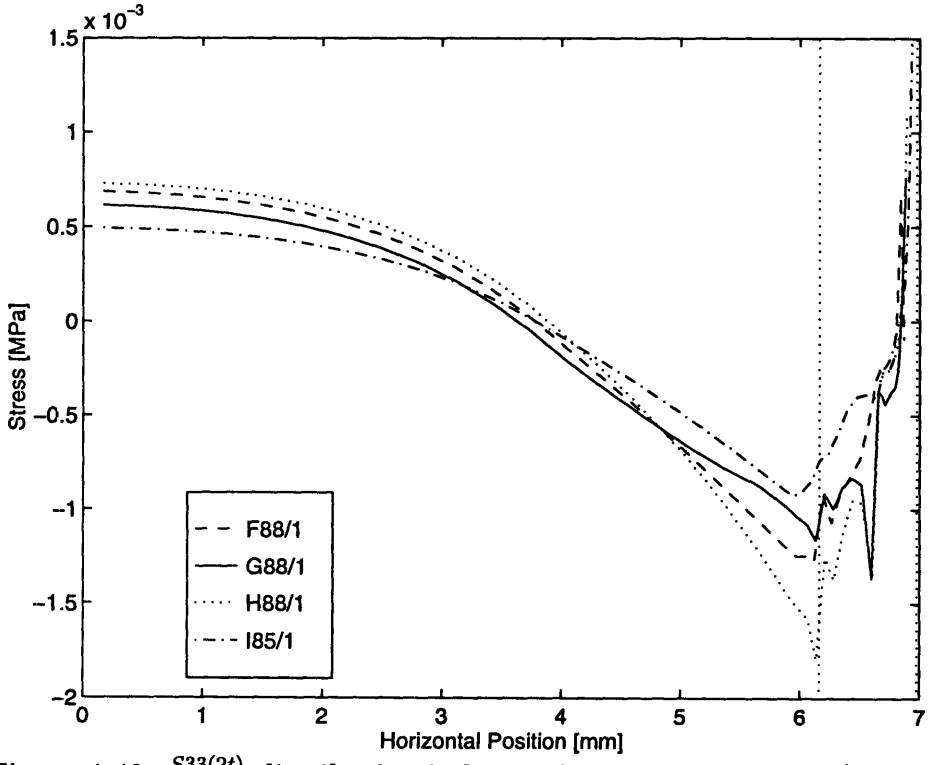

Figure 4-40: $\frac{S33(2t)}{r}$ distribution in lower element layer for F88/1, G88/1, H88/1, and I85/1 lens placement simulations

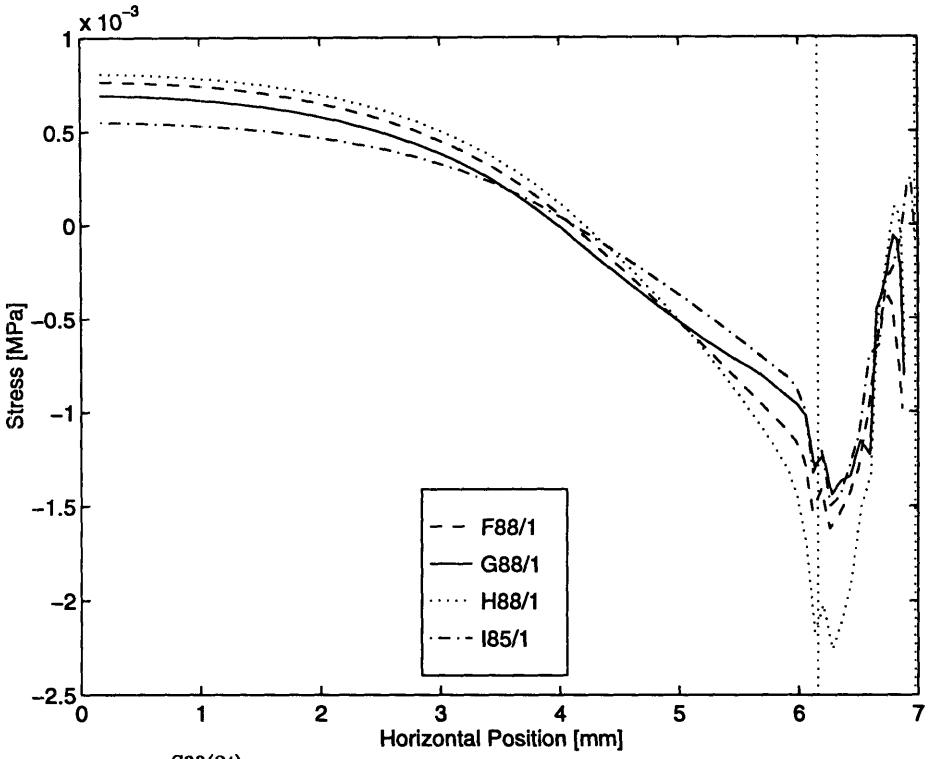

Figure 4-41: $\frac{S33(2t)}{r}$ distribution in upper element layer for F88/1, G88/1, H88/1, and I85/1 lens placement simulations

regions of the lenses. (see Figure 4-30) The spike was present in the stress distributions of all the N series lenses modeled, indicating that the change in basecurve at this point has some effect in the stress state in the lens. However, the severity of the effect in a real lens will be much less than predicted by the simulations because the sharp change in radius in this numerical model will not be able to be reproduced in an actual soft, hydrogel lens, and would be absorbed or cushioned by the tear layer.

A second general difference between the N series stress distributions and those of the F88, G88, H88, and I85 lenses is that there appears to be less large oscillation in the S11 and S33 stress distributions at the very edge of the lenses in the N series lenses than in the previous lens set examined. This difference seems to be due to the fact that the N series lenses do not reach as far onto the cornea/sclera junction as the other lenses did, and are therefore not as strongly influenced by the bending effects caused by the change of eye shape at this region.

The same relationships between lens geometry and S11 stress distribution observed in the previous set of lenses is also present in the N series lens stress distributions.

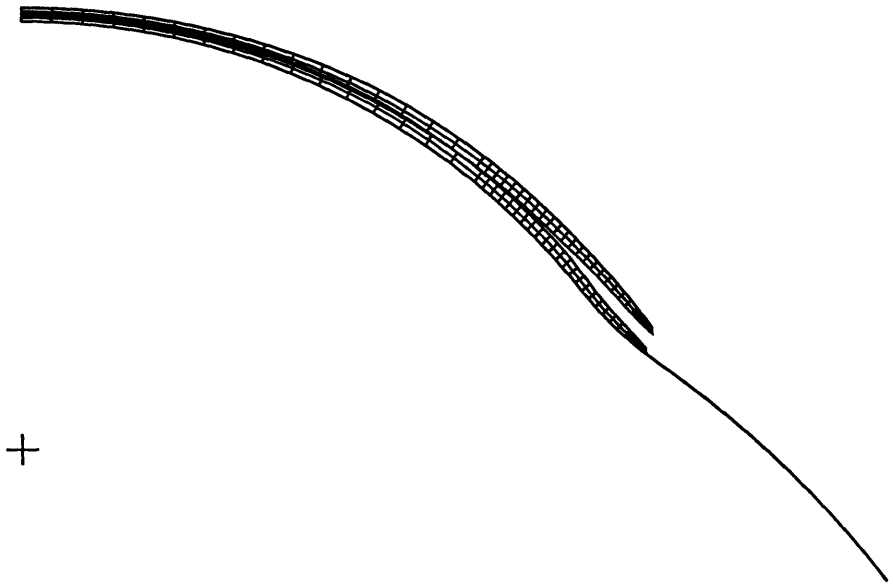

Figure 4-42: Initial and final configurations of N83b lens placed on eye with no tear layer

At the center of the lenses, the stress magnitude of the three N83 lenses (which share the same base curve geometry) is much less than that of the N85 lens (which has a flatter curvature.) Again, a closer match between the curvature of the lens and cornea results in a lower central S11 stress. Among the three N83 lenses, the magnitude of S11 stress at the lens center increases with increasing lens thickness. At the cornea/sclera junction, little difference exists in the magnitude of the lens' stress. The equivalence in stress at this point corresponds to the similarity of the lens' thickness profiles.

The S33 stress distributions of the N series lenses also correlates very well to those of the F,G,H, and I lenses. Like the previous set of geometries, the N lenses also have a flat bearing, and therefore display circumferential stress that is tensile at the center and compressive near the lens edge. The significant difference in the level of S33 stress between the N83 and N85 lenses again demonstrates a strong dependence of S33 stress magnitude on lens curvature, with lower stresses created in lenses more

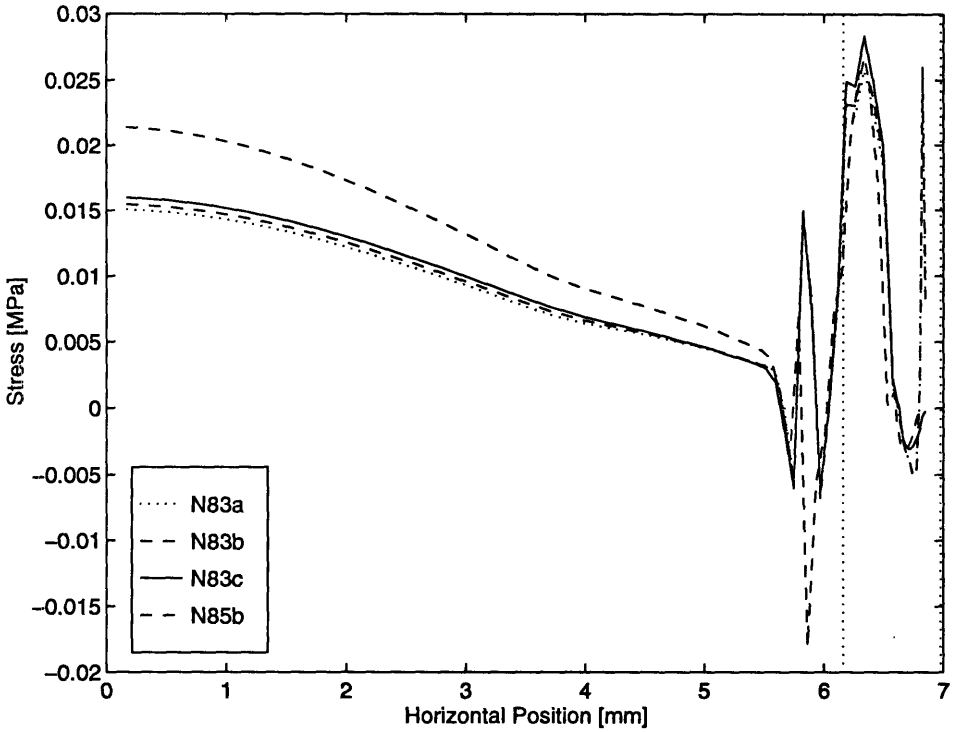

Figure 4-43: S11 stress distribution in lower layer of lens elements for N83a, N83b, N83c, and N85b lens placement simulations

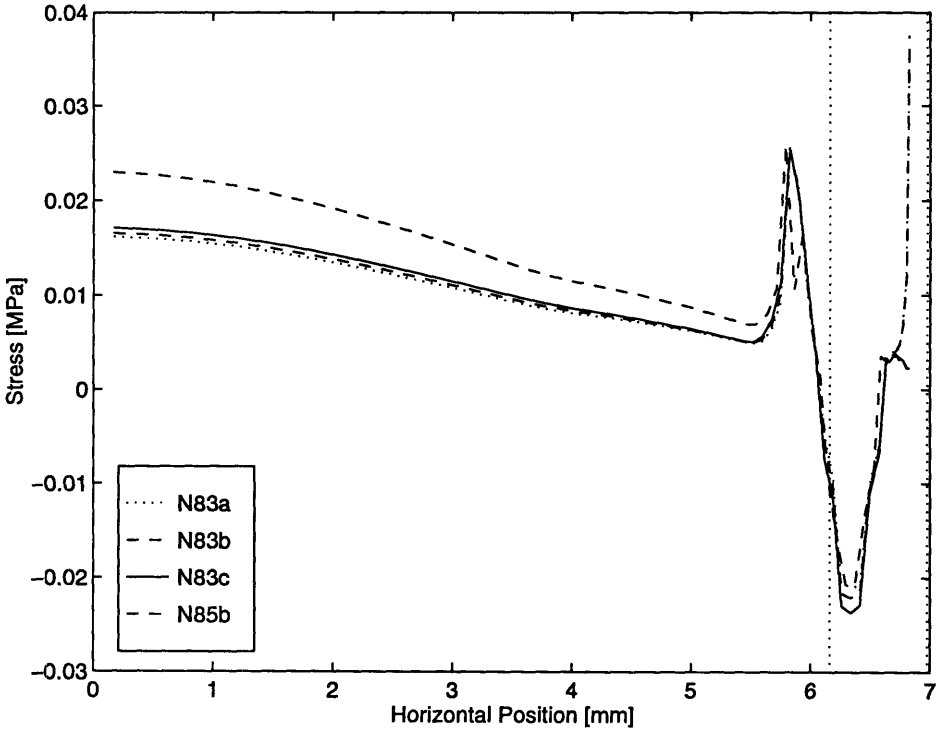

Figure 4-44: S11 stress distribution in upper layer of lens elements for N83a, N83b, N83c, and N85b lens placement simulations

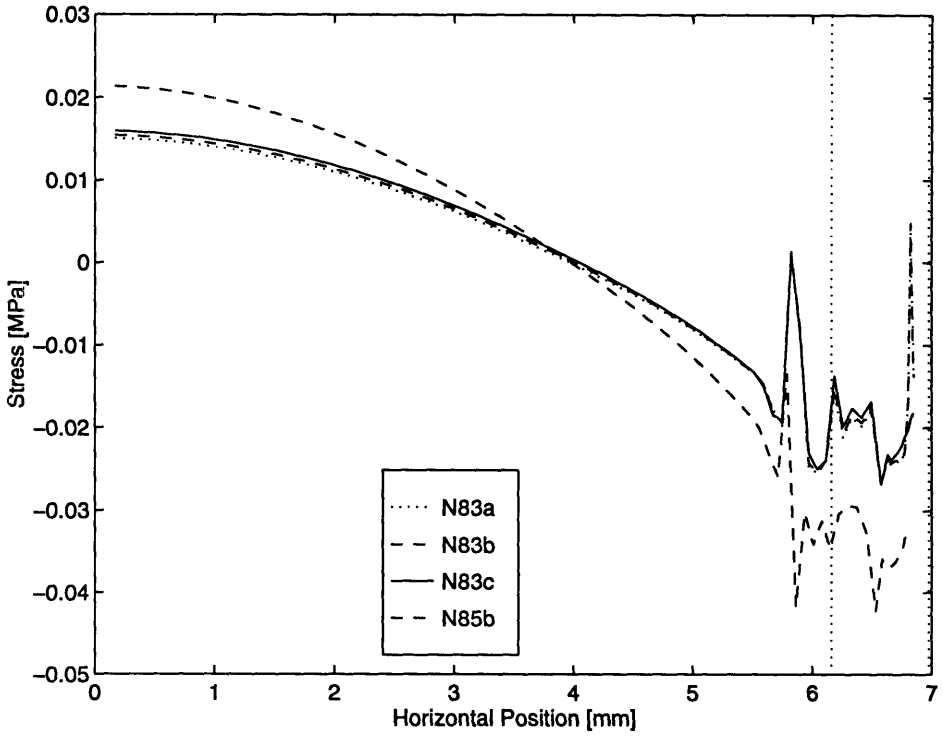

Figure 4-45: S33 stress distribution in lower layer of lens elements for N83a, N83b, N83c, and N85b lens placement simulations

closely fitted to the cornea. Note that the spike at 5.8mm in the S11 N series stress distributions is also present in the S33 stresses, however, the magnitude of the spike is smaller in the S33 distributions.

The interface pressure and $\frac{S33(2t)}{r}$ distributions for the N83 and N85 lenses are given in Figures 4-47, 4-48 and 4-49. As before, both quantities show a positive pressure applied to the eye by the center of the lenses, and a tensile pressure applied near the lens edges. There is a good match between the two quantities at the center of the lenses, where both show that the lenses of lower curvature exert a much lower positive pressure on the cornea than the flatter lens does. The small difference in thickness between the three N83 lenses is also reflected in both the interface pressure and $\frac{S33(2t)}{r}$ distributions, which show that at the center of the lenses, the highest pressure applied by the three lenses is caused by the thickest N83 lens.

The pressure distribution again contains large discontinuities at the lens edges, however, they begin slightly closer to the lens center for the N series lenses than for for F,G,H and I lenses. Just before the discontinuities occur, the pressure magnitude is

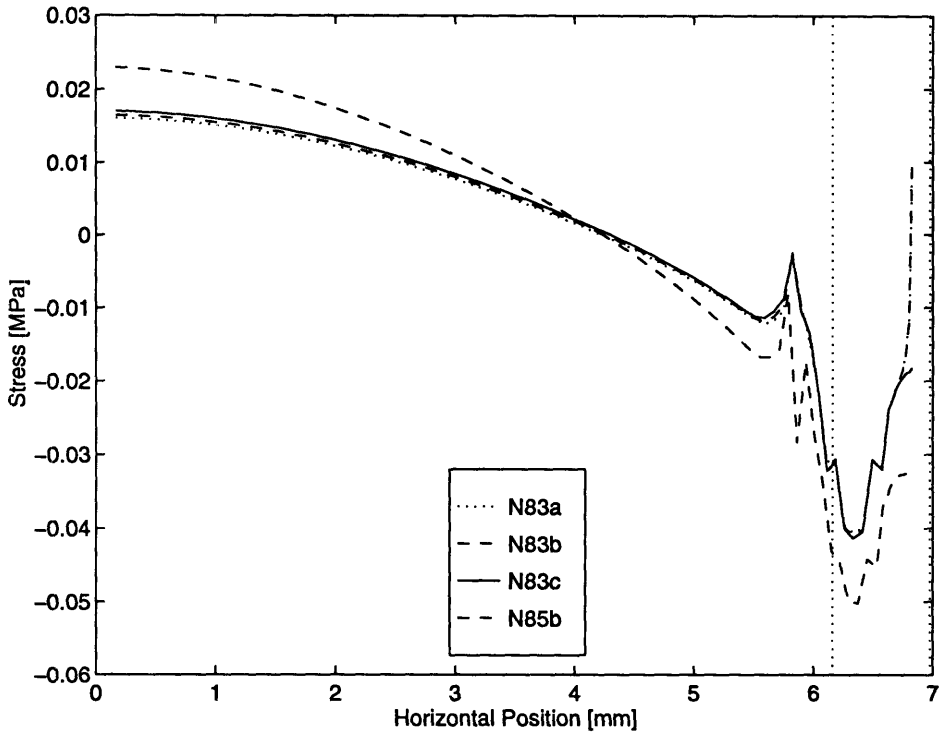

Figure 4-46: S33 stress distribution in upper layer of lens elements for N83a, N83b, N83c, and N85b lens placement simulations

higher for the N85 lens than for the N83 lenses, as was the case at the lens center. The $\frac{S33(2t)}{r}$ distribution for the lower element layer shows the same relationship as that of the previous lens set at the cornea/sclera junction, where the negative pressure generated by the N85 lens is noticeably greater than that generated by the N83 lenses. However, the difference in magnitude of the N85 lens is less pronounced when $\frac{S33(2t)}{r}$ was calculated on the upper element layer.

Martin and Holden lenses

The next set of geometries tested was the set of blanks whose thicknesses and bearings matched those used by Martin and Holden. The stress and pressure distributions obtained for these simulations are displayed in two sets of graphs. The first set compares blanks M1, M2, and M3, which have the same thickness but different bearings, and the second compares lenses M1, M4, and M5, which have the same bearing but different thicknesses.

The S11 stress distribution for blanks M1, M2, and M3 are shown in Figures 4-51

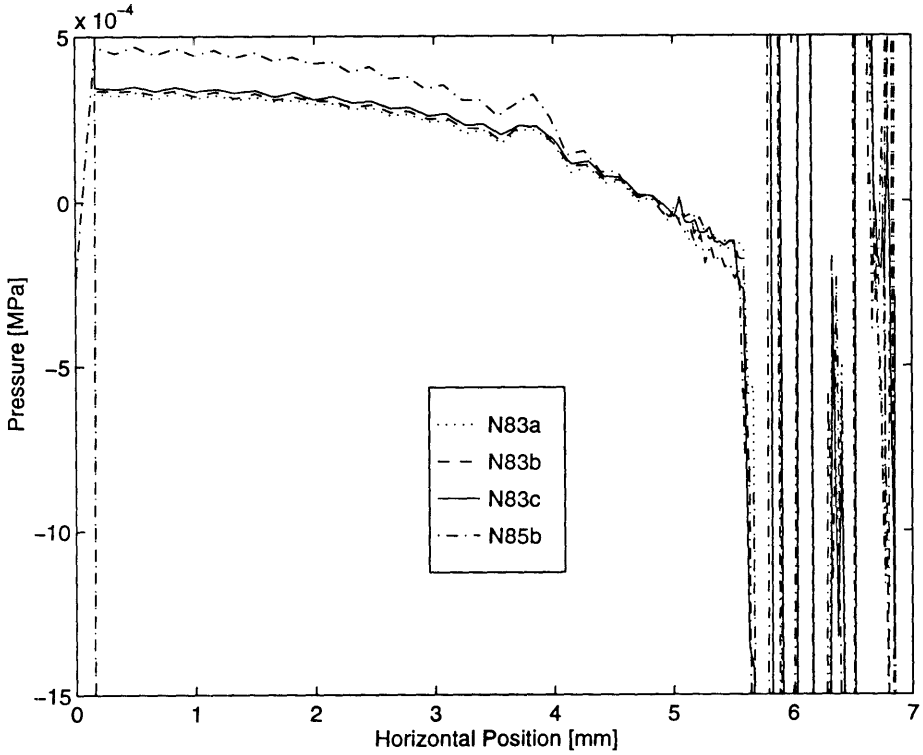

Figure 4-47: Interface pressure distributions for N83a, N83b, N83c, and N85b lens placement simulations

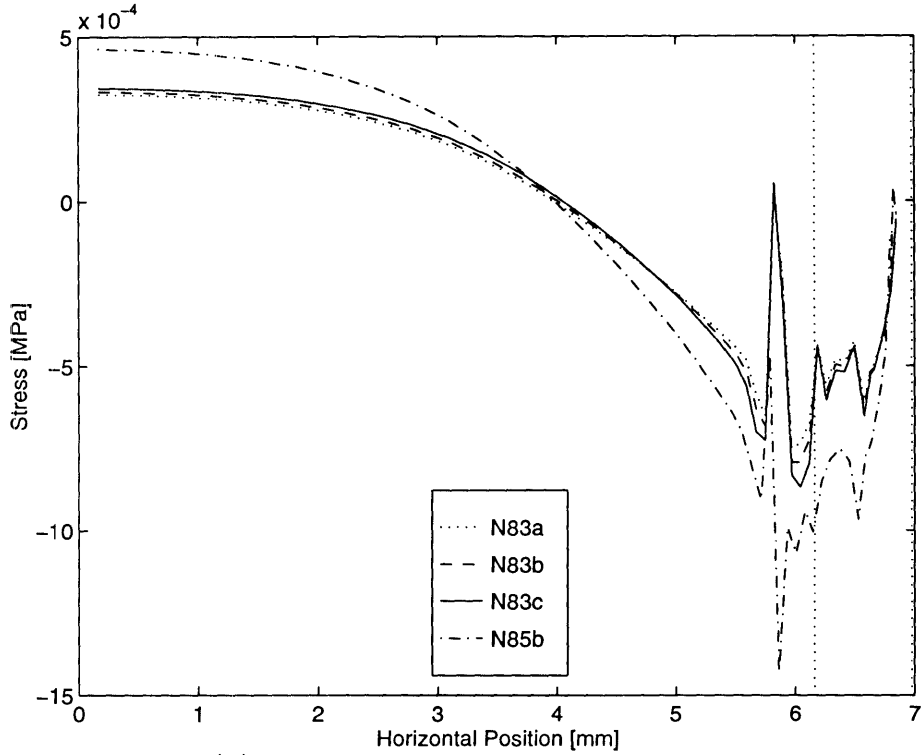

Figure 4-48: $\frac{S33(2t)}{r}$ distribution in lower element layer for N83a, N83b, N83c, and N85b lens placement simulations

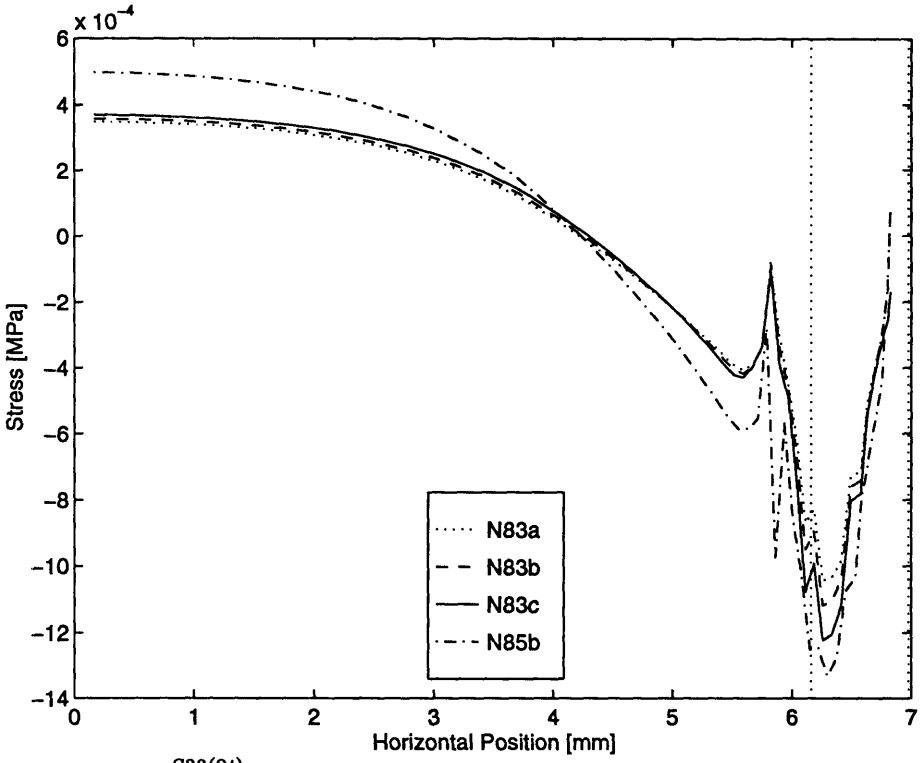

Figure 4-49: $\frac{S33(2t)}{r}$ distribution in upper element layer for N83a, N83b, N83c, and N85b lens placement simulations

and 4-52, and the simulation of the placement of blank M3 is illustrated in Figure 4-50. The three lenses show very different trends in S11 distribution. Lens M3, which has a flat bearing like the lenses in the previous two sets, has a S11 stress distribution similar to those of the previous lenses. It is tensile at the center, and decreases toward the lens edge. At the cornea/sclera junction, the S11 stress in the lower element layer becomes highly positive, and the stress in the upper element layer becomes highly negative. The M1 lens, which has in initial curvature smaller than that of the cornea, demonstrates the opposite trend in S11 stress at the center of the lens. The stress in both the upper and lower element layers is compressive, and after an initial increase in magnitude, becomes less negative toward the cornea/sclera junction. At the junction, the S11 distribution of blank M1 matches that of blank M3, becoming highly compressive in the upper element layer and highly tensile in the lower layer. Note that in the upper element layer of the M1 blank, the S11 stress becomes less compressive past the cornea/sclera junction. The M3 blank does not demonstrate this reduction in compressive stress because it does not reach beyond the beginning

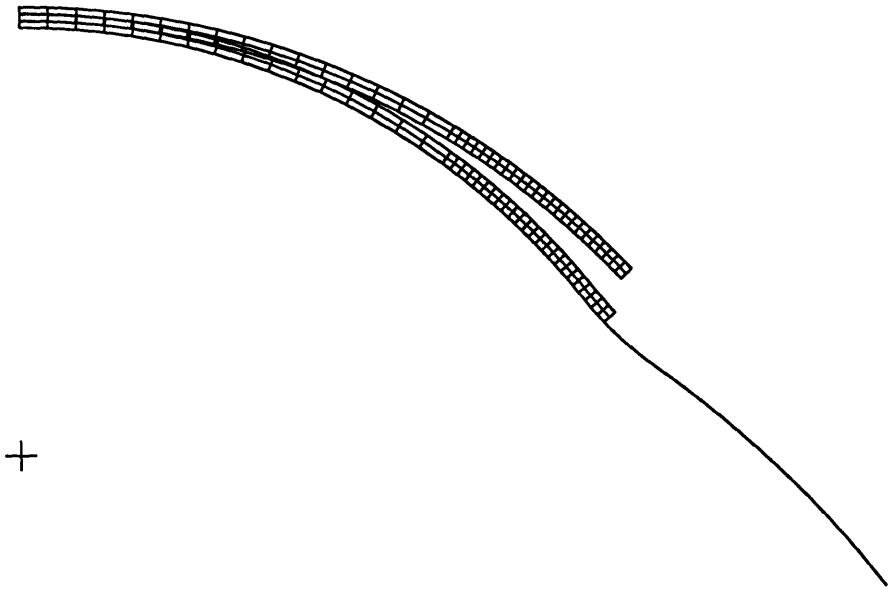

Figure 4-50: Initial and final configurations of Martin and Holden blank geometry M3 placed on eye with no tear layer

of the cornea/sclera junction. In the M2 blank, whose initial curvature is almost equal to that of the cornea, the magnitude of S11 stress is very low from the lens center to the beginning of the cornea/sclera junction. At the junction, the S11 distribution of the M2 lens demonstrates the same bending-induced S11 stress distribution present in the other two lenses.

The S33 stress distributions of the M1, M2, and M3 lenses also reflect their differences in bearing. (See Figures 4-53 and 4-54) The M3 lens has the same general S33 distribution of the other lenses with flat bearing. The stress in both element layers is tensile at the center and becomes compressive at the edge. The M1 lens demonstrates the opposite trend, with a compressive circumferential stress at the center, and a tensile stress at the edge. This circumferential stress distribution is compatible with its steep shape. At its center, the lens has too much material to fit smoothly on the cornea, so this material must contract during placement on the eye. At the edge, the circumference of the eye is greater than the initial circumference of the lens, so

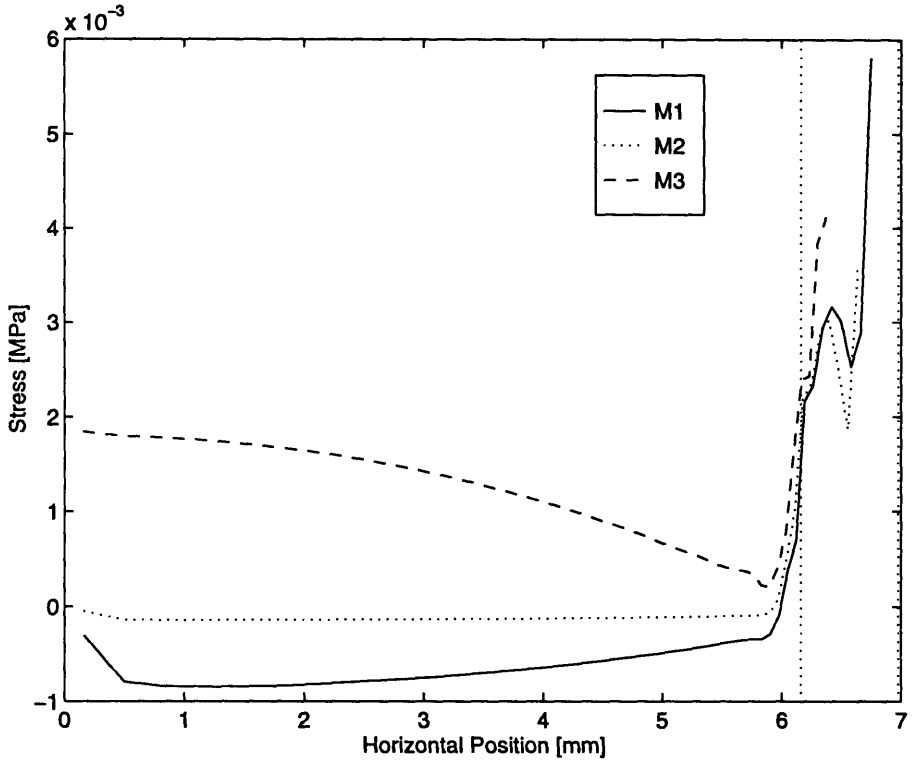

Figure 4-51: S11 stress distribution in lower layer of lens elements for M1, M2, and M3 lens placement simulations

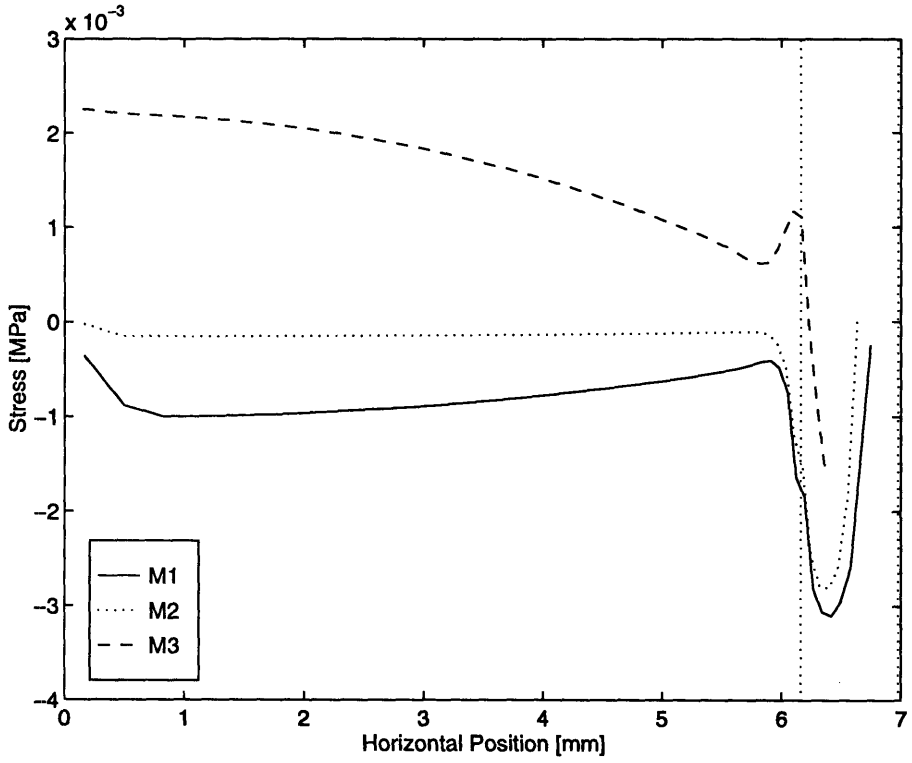

Figure 4-52: S11 stress distribution in upper layer of lens elements for M1, M2, and M3 lens placement simulations

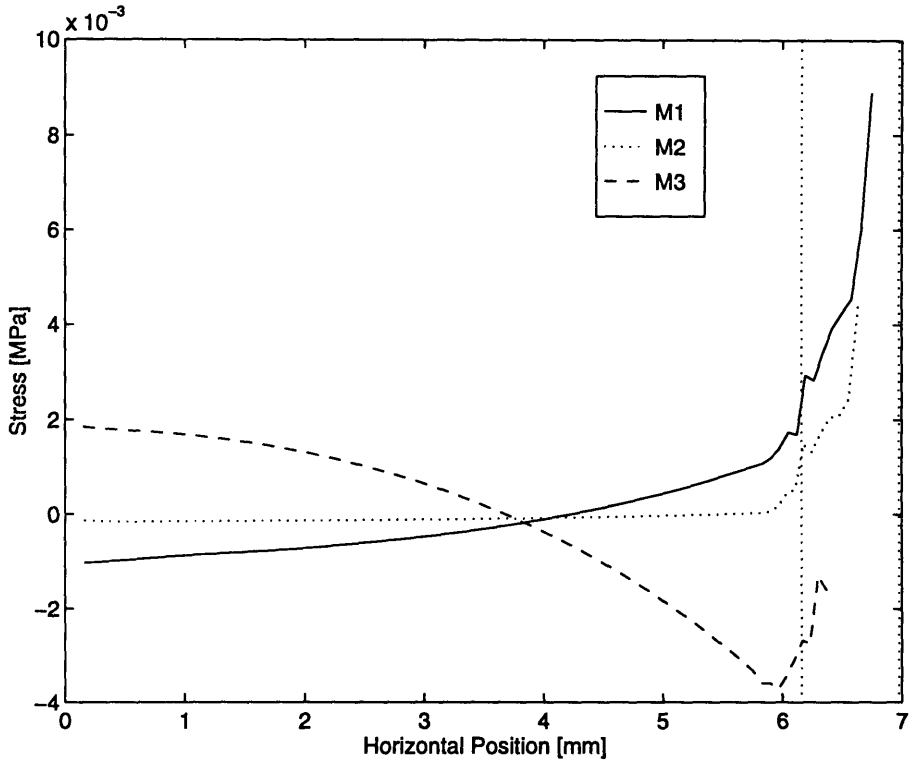

Figure 4-53: S33 stress distribution in lower layer of lens elements for M1, M2, and M3 lens placement simulations

the material at the edge must stretch circumferentially in order to fit on the cornea. The sharp upturn in S33 stress at approximately 6.2mm occurs where the eye begins to flatten, causing the outer material to stretch even more than it would have to if the curvature of the eye remained constant. Again, the M2 lens shows little internal S33 stress from the lens center to the cornea/sclera junction. This demonstrates that the lens has to deform very little in order to match the cornea shape. However, as in the M1 blank, the circumferential stress in the M2 blank increases sharply at the cornea/sclera junction, as the edge material stretches to accommodate the flatter eye shape at the junction.

The interface pressure and $\frac{S33(2t)}{r}$ distributions are shown in Figures 4-55, 4-56, and 4-57. The distributions of the M3 lens show that this lens applies positive pressure at the center of the eye, and tensile pressure near the edge, similar to the lenses of the two previous groups. The M1 lens demonstrates the opposite pressure distribution: it exerts a tensile pressure on the center of the eye, and a positive pressure at the edge. Unlike the lenses with a flat bearing, the steep M1 lens must be pulled downward

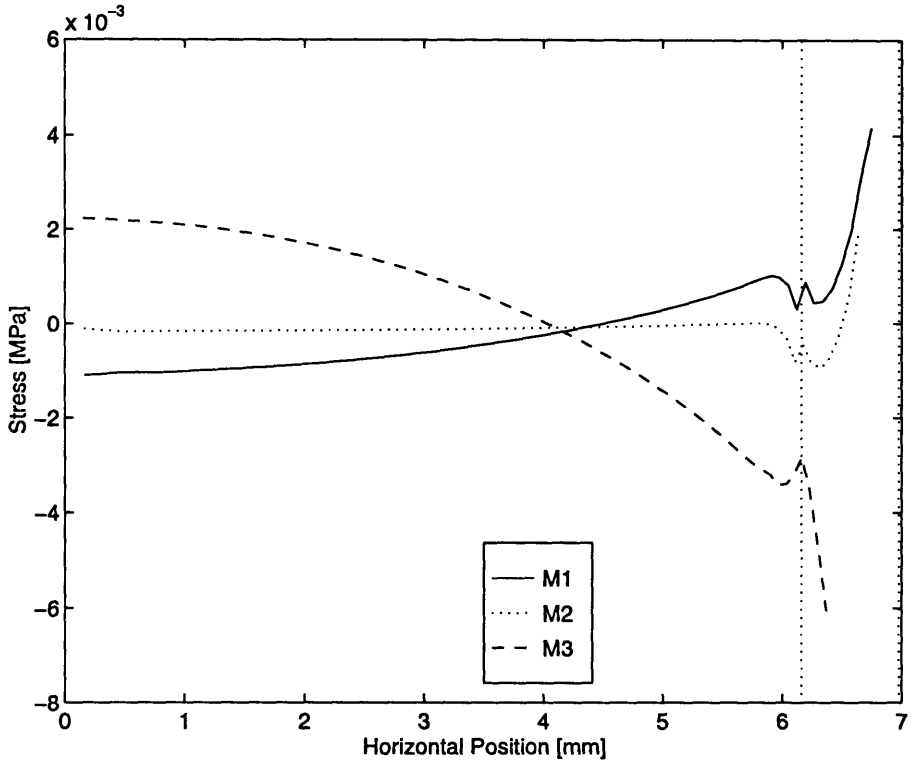

Figure 4-54: S33 stress distribution in upper layer of lens elements for M1, M2, and M3 lens placement simulations

toward the eye at the center, and pushed outward and upward at the edge in order to conform to the eye. (See Figure 4-38b) This difference accounts for the opposite shape of the M1 pressure distribution from that of the M3 lens. The M2 lens exerts very little pressure over most of the eye surface. However, at the cornea/sclera junction, first exerts a negative pressure at the beginning of the junction, where the lens must bend inward, and then a positive pressure at the outermost edge of the lens, where the lens must bend back onto the sclera. As stated above, the magnitude of the quantity $\frac{S33(2t)}{r}$ is probably not equal to the interface pressure near the lens edge, but it can be used to get a rough idea of the nature of the pressure variation.

The results of the second group Martin and Holden blanks are presented next. These lenses, M1, M4, and M5, all have the same steep bearing, but have three different thicknesses. (M1 thickness=0.16mm, M4 thickness=0.066mm, M5 thickness=0.31mm) The S11 stress distributions for these three blanks are shown in Figures 4-59 and 4-60, and the deformed and undeformed meshes of the simulation performed with blank M5 are shown in Figure 4-58. (The undeformed configuration is

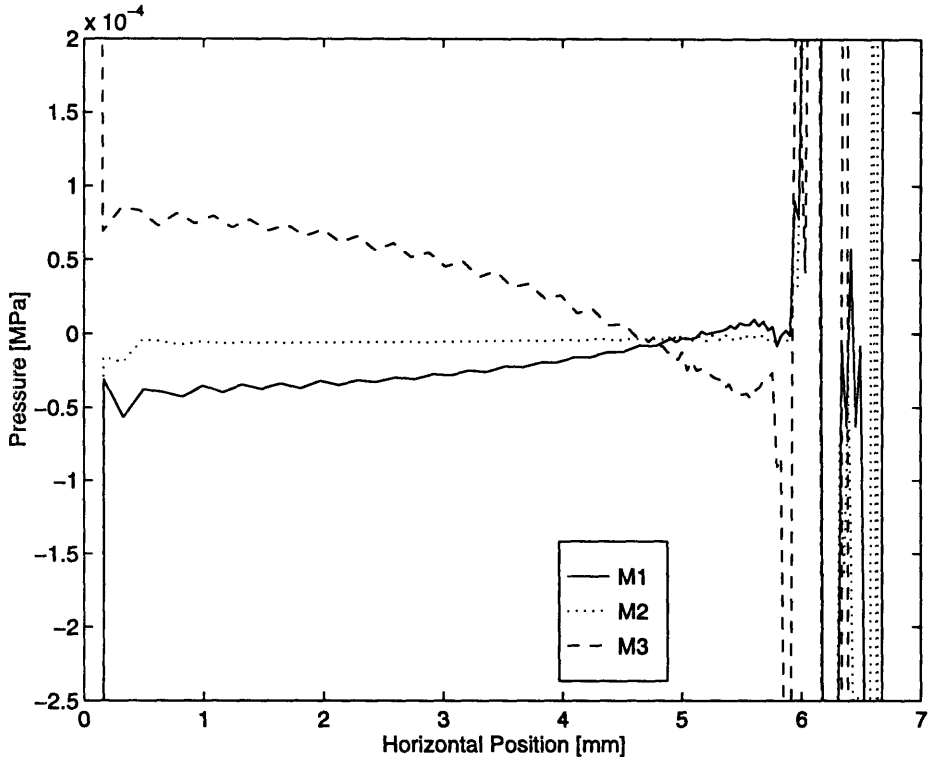

Figure 4-55: Interface pressure distributions for M1, M2, and M3 lens placement simulations

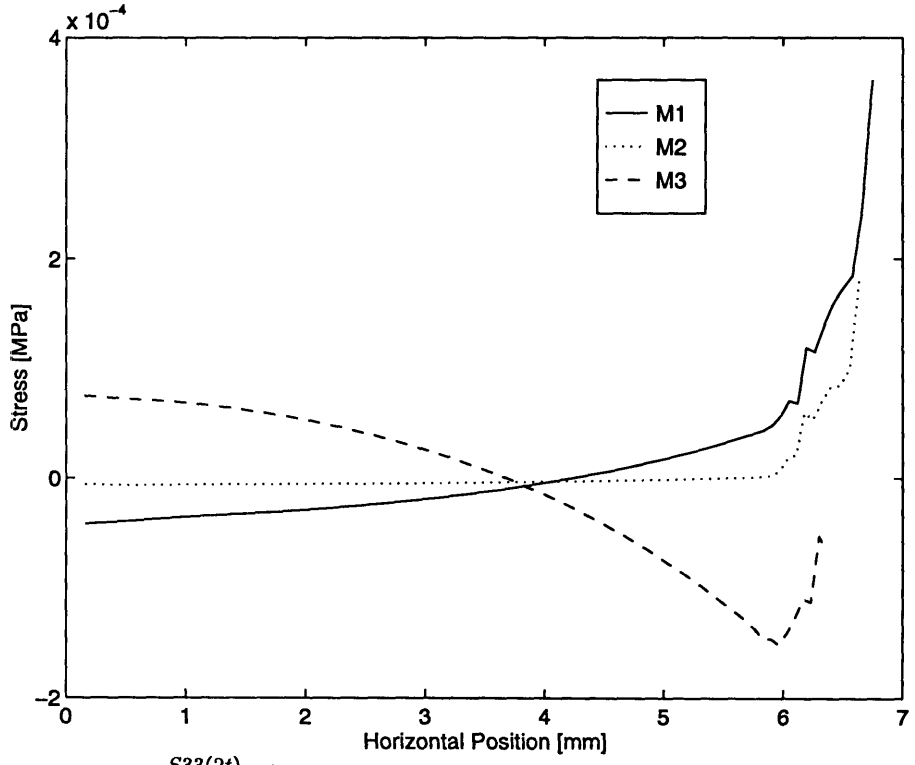

Figure 4-56: $\frac{S33(2t)}{r}$ distribution in lower element layer for M1, M2, and M3 lens placement simulations

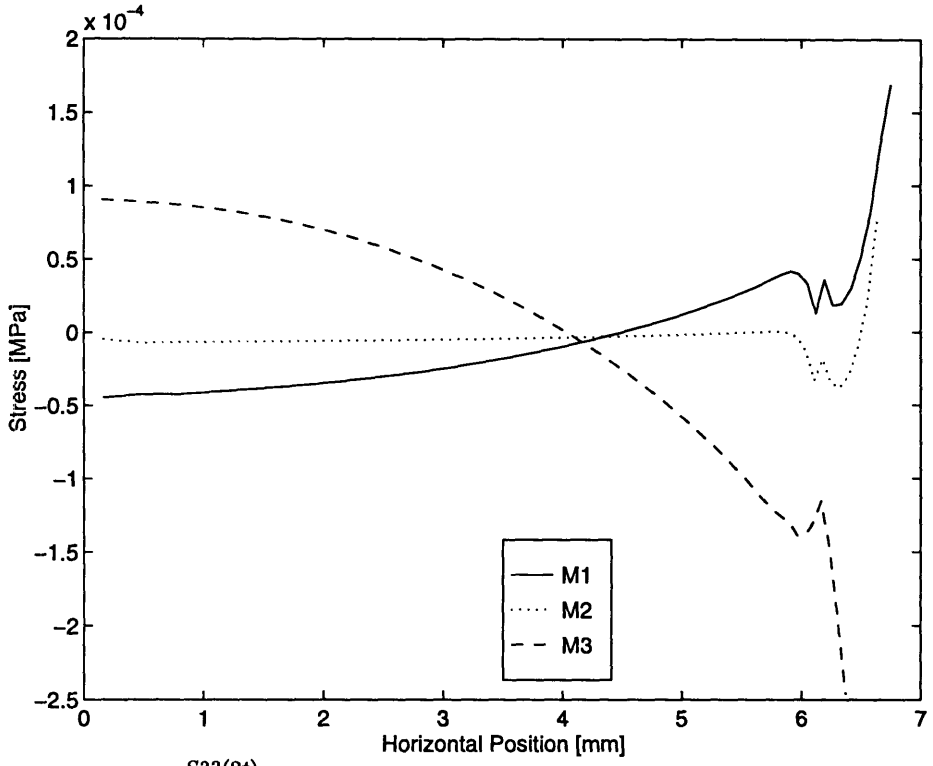

Figure 4-57: $\frac{S33(2t)}{r}$ distribution in upper element layer for M1, M2, and M3 lens placement simulations

drawn in dashed lines for clarity.) In both the upper and lower layers of elements, the S11 stress at the center of the lenses is compressive, and gradually decreases in magnitude toward the cornea/sclera junction, where the stress becomes highly compressive in the upper layer, and tensile in the lower layer.

The differences in thickness between the M1, M4, and M5 lenses have a very different effect on their S11 distributions than thickness differences did for the F88/1, G88/1, and H88/1 lenses and also for the N83a, b, and c lenses. In the first two sets of lenses tested, the magnitude of the S11 stress, both at the center of the lens and at the cornea/sclera junction, increased with increasing lens thickness. However, this is not the case for the M1, M4, and M5 lenses. At the very center of the lens, M4 has the greatest level of stress, though it has the thinnest cross section. The M5 blank, which has the thickest cross section, has the second greatest stress magnitude, and the M1 lens, with an intermediate thickness, has the lowest stress level at this point. Between approximately 1mm and 5mm, the magnitude of S11 stress for all three lens blanks is approximately equal, and at the cornea/sclera junction, the S11

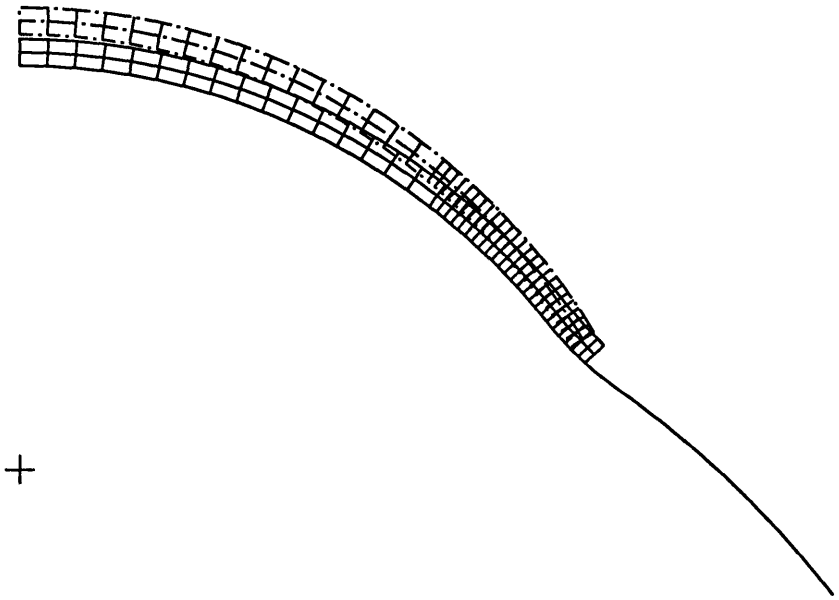

Figure 4-58: Initial and final configurations of Martin and Holden blank geometry M5 placed on eye with no tear layer

stress magnitudes of lenses M1 and M5 are nearly the same, while the S11 magnitude of the M4 blank is much lower.

The difference in stress and thickness relationship between the two actual lens sets and the set of M1, M4, M5 blank geometries could be due to two reasons. First, the actual lens geometries all had flat bearings, while the M1, M4 and M5 blanks all have a steep bearing. Figures 4-51 and 4-52 illustrate that the overall shape of the S11 distribution is very different for lenses with flat and steep bearings, indicating that flat and steep lenses support the stresses that develop during conformation to the eye in different ways. It is possible that for flat lenses, the lens thickness does not have the same relationship to S11 stress as it does for steep lenses.

A second major difference between the actual lens geometries and the M1, M4, and M5 blanks is the amount of thickness variation within each group. In actual lens geometries, the thickness variation between lenses was relatively small, and was confined to the lenticular and edge regions. The greatest amount of thickness differ-

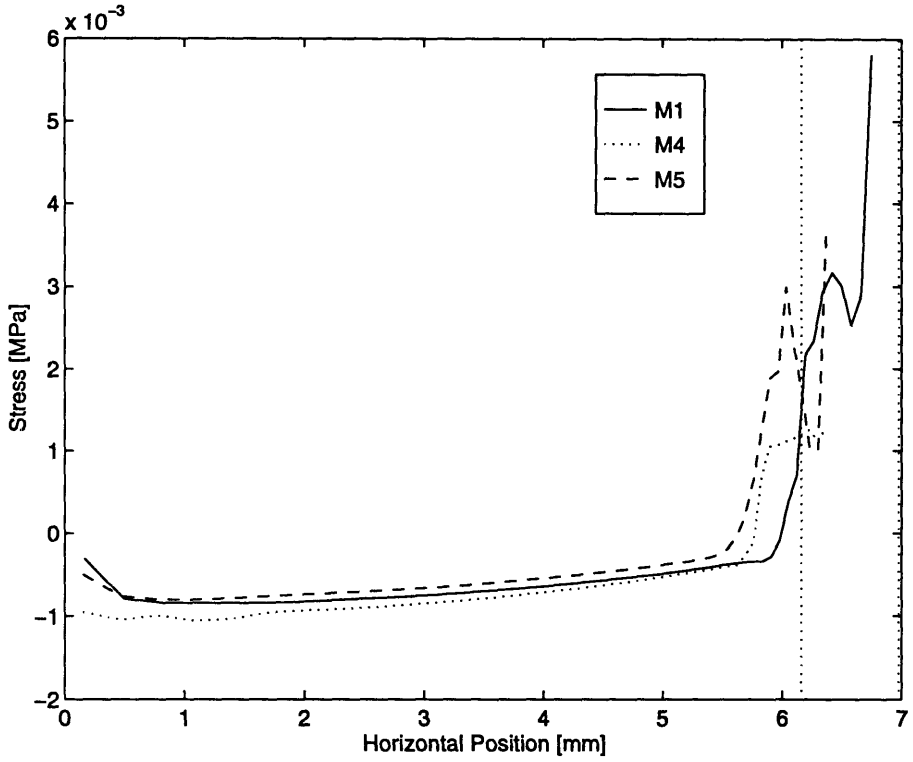

Figure 4-59: S11 stress distribution in lower layer of lens elements for M1, M4, and M5 lens placement simulations

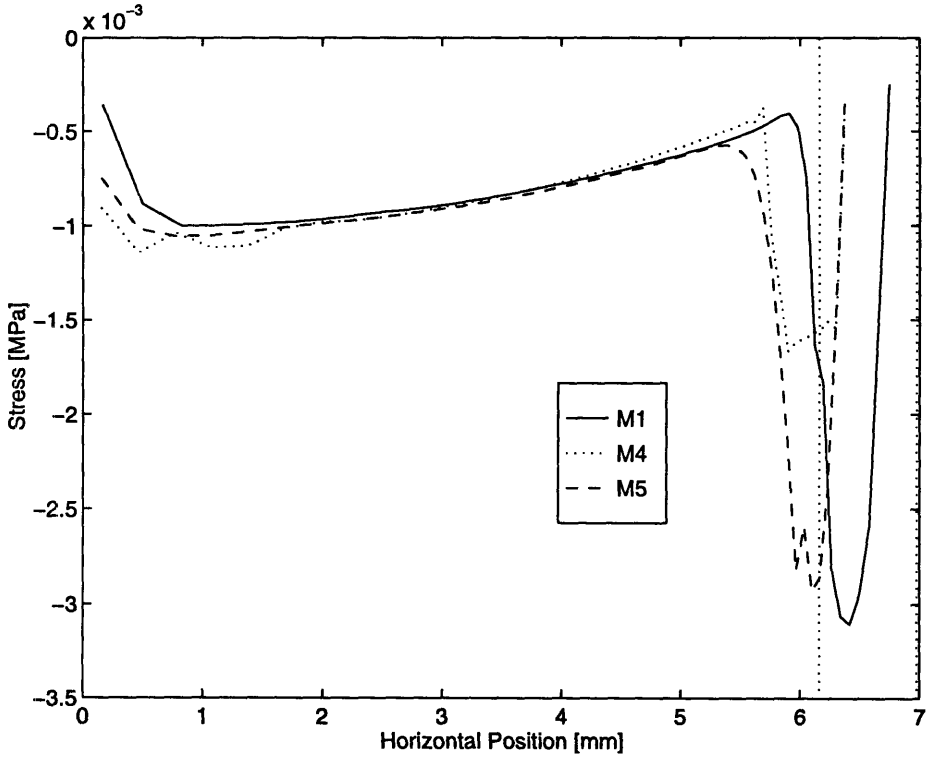

Figure 4-60: S11 stress distribution in upper layer of lens elements for M1, M4, and M5 lens placement simulations

ence between two lenses within a group was between the H88/1 and G88/1 lenses, whose thickness profiles differed at most by a factor of 1.6, which occurred only at one point. In contrast, the thickness of the M5 blank is greater than that of the M4 blank by a factor of 4.7, and it is thicker throughout the entire cross section, not just in the lenticular region. This large difference in thickness creates nonlinear geometric effects, which can result in very different lens responses. One such effect of the large thickness variation is a shifting of the point at which the S11 stress reflects the bending at the cornea/sclera junction. In lenses M4 and M5, the peak stress due to bending appeared closer to the center of the lens than it did for the M1 lens, even though all three lenses were placed on the same eye geometry.

The S33 stress distributions for the M1, M4, and M5 lenses also display very different relationships between stress and thickness than were observed for the actual lens geometries. (See Figures 4-61 and 4-62) In the real geometries, the magnitude of S33 stress at the lens center increased with increasing lens thickness. However, for the M1, M4, and M5 blanks, the magnitude of the S33 stress is very similar, both at the center of the lenses, and near the edges.

Finally, Figures 4-63, 4-64, and 4-65 show the interface pressure and $\frac{S33(2t)}{r}$ distributions for blanks M1, M4, and M5. At the center of the cornea, all three blanks exert a tensile pressure on the eye, and the magnitude of the pressure exerted increases with increasing lens thickness. The $\frac{S33(2t)}{r}$ distributions indicate that the lenses exert a positive pressure near the lens edge, the magnitude of which again increases with increasing lens thickness. In contrast to the S11 and S33 distributions, the interface pressure distributions of the M1, M4, and M5 blanks display a similar relationship to thickness as the pressure distributions of the actual lens geometries did. For both sets of real lenses, the interface pressure exerted by the lenses of equal bearing at the center of the cornea increased in magnitude as overall lens thickness increased, just at the interface pressures of the M1, M4, and M5 lenses did.

The results of the simulations with blank lens geometries similar to those used by Martin and Holden differ considerably from the results they obtained. As stated above, all the interface pressure distributions measured by Martin and Holden had

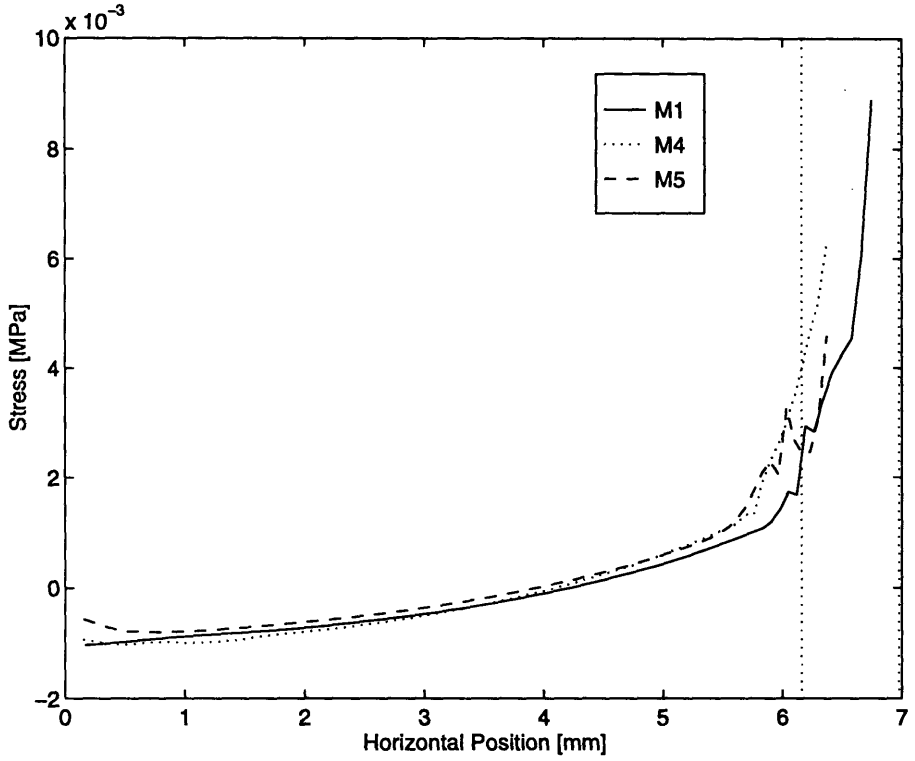

Figure 4-61: S33 stress distribution in lower layer of lens elements for M1, M4, and M5 lens placement simulations

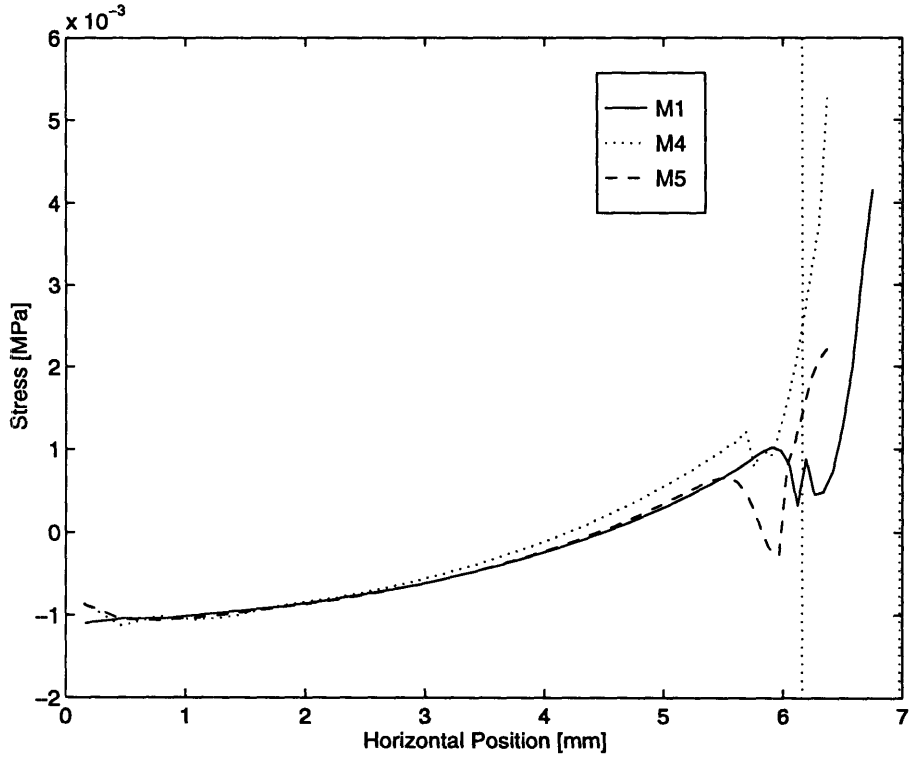

Figure 4-62: S33 stress distribution in upper layer of lens elements for M1, M4, and M5 lens placement simulations

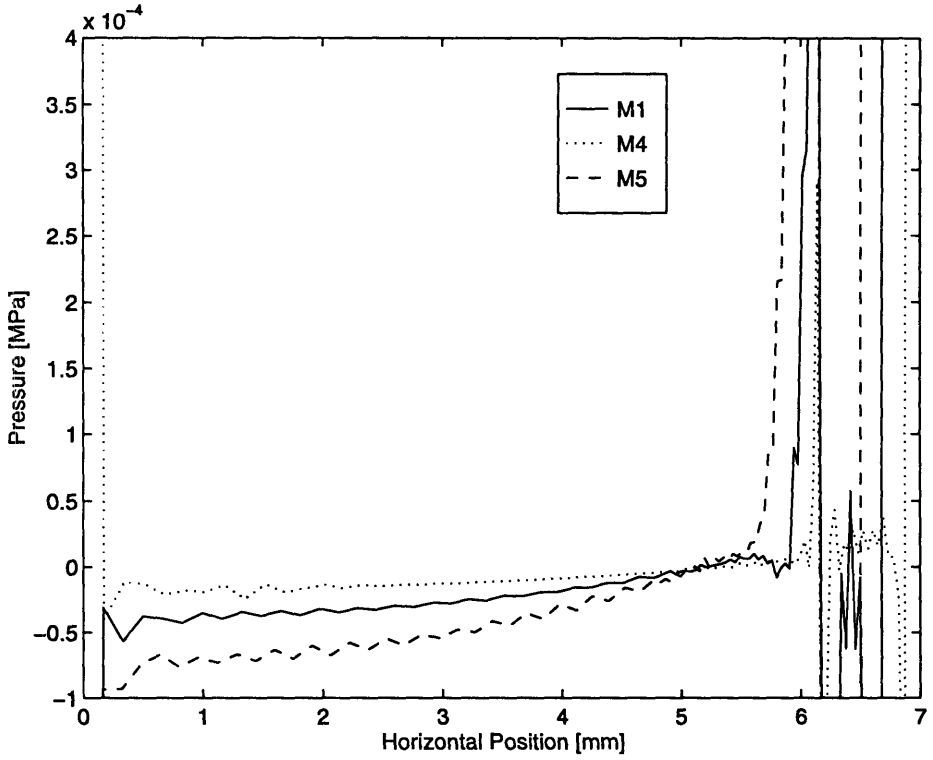

Figure 4-63: Interface pressure distributions for M1, M4, and M5 lens placement simulations

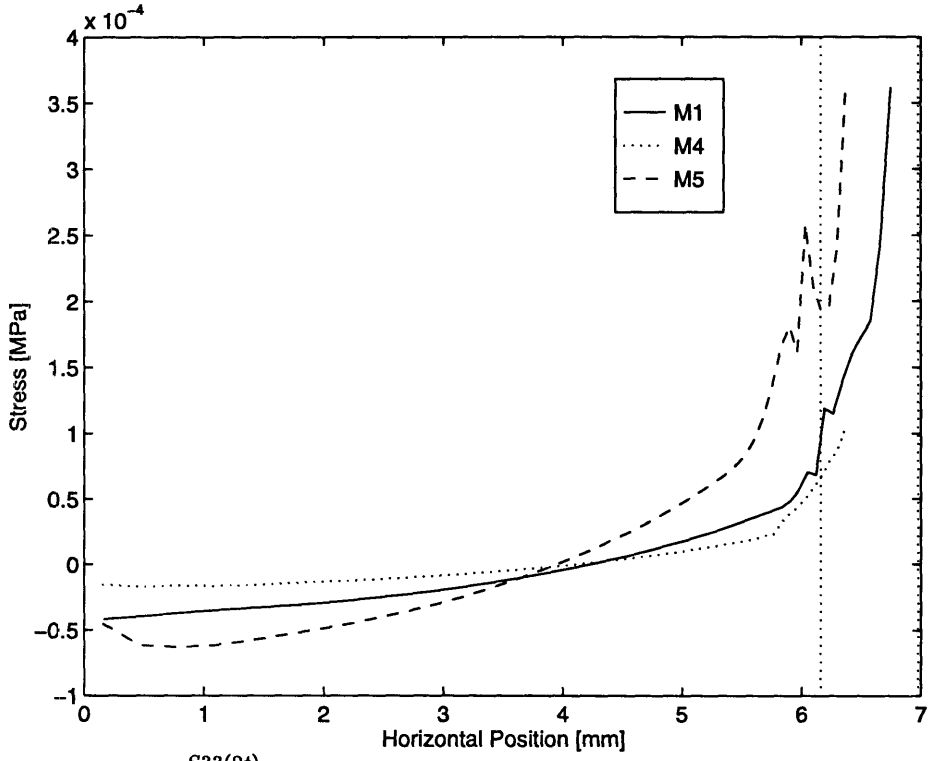

Figure 4-64: $\frac{S33(2t)}{r}$ distribution in lower element layer for M1, M4, and M5 lens placement simulations

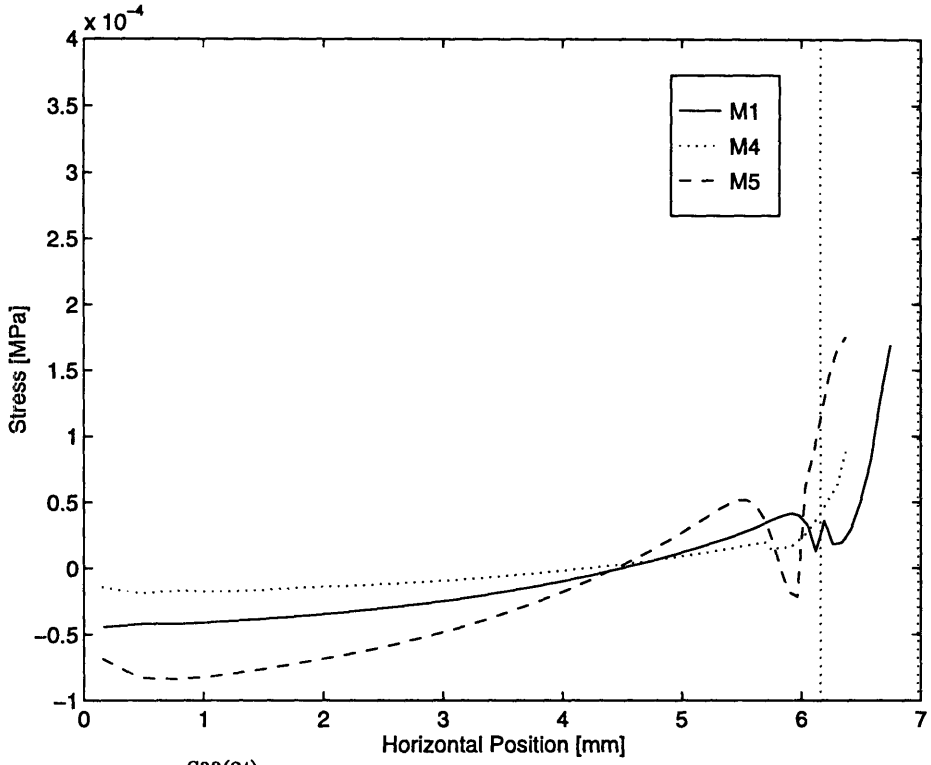

Figure 4-65: $\frac{S33(2t)}{r}$ distribution in upper element layer for M1, M4, and M5 lens placement simulations

basically the same shape: the pressure at the lens center was negative, and became monotonically less negative toward the lens edge. The magnitude of central pressure, and the difference between central and edge pressures varied with lens bearing and thickness. The approximate central and edge pressures measured by Martin and Holden for the five lens geometries simulated are given in Table 4.3. Also given in Table 4.3 are the values of central pressure obtained in the finite element simulations described above.

In general, the central pressures measured by Martin and Holden are approximately an order of magnitude greater than those predicted by the simulations. However, an even more significant difference between the simulated and experimentally measured pressures is the difference in the relationship between lens bearing and interface pressure shown by the experiments and simulations. For blanks M1, M2, and M3, Martin and Holden measured an interface pressure that was highly negative for the steeply-fitting lens, less negative for the closely-fitting lens, and nearly zero for the flat-fitting lens. In contrast, the simulations predict a negative central pressure for

Blank	Bearing	Experimental Central Pressure [Pa]	Experimental Edge Pressure [Pa]	Simulated Central Pressure [Pa]
M1	0.332mm steep	-460	-210	-50
M2	0.03mm steep	-290	-120	0
M3	1.19mm flat	0	-20	75
M4	0.32mm steep	-160	-70	-25
M5	0.32mm steep	-775	-245	-80

Table 4.3: Approximate interface pressures measured by Martin and Holden, and central interface pressures obtained in simulations

the steep-fitting lens, a nearly zero pressure for the close-fitting lens, and a positive pressure for the flat-fitting lens. Intuitively, the trends in the results of Martin and Holden do not make sense, especially the result that the lens whose geometry most closely matched that of the eye exerted a greater pressure on the eye than a lens that had to deform significantly in order to conform to the eye. These nonintuitive results suggest the need for further experimental studies, with special attention paid to the possibility of positive induced pressures being formed in the tear layer.

Fatt lenses

The final lens-placement simulation involved placing a steeply-fitting spherical lens (radius of curvature =6.5mm) onto a spherical eye (radius of curvature=7.5mm). The geometry of both the lens and the eye were equal to those used in the experiment described above by Fatt and Chaston.

The initial and deformed mesh configurations obtained when this simulation was performed are shown in Figure 4-66. Note that the eye geometry used in the Fatt experiments, and therefore, in this simulation, is quite different than the more realistic eye geometry used in previous simulations.

The S11 stress distributions measured in both element layers of the lens are shown in Figure 4-67. The S11 stress is compressive over nearly the entire lens, with the greatest stress magnitude occurring near the lens center. This S11 distribution does not contain the peak due to bending seen in the other S11 distributions because of

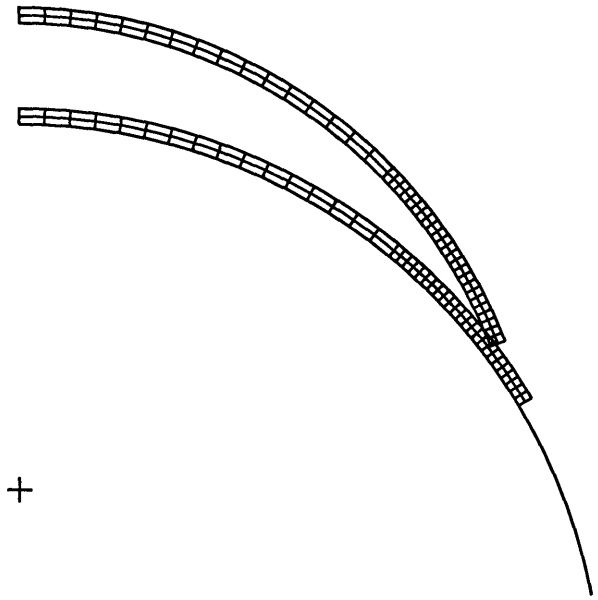

Figure 4-66: Initial and final configurations of Fatt lens geometry placed on spherical eye with no tear layer

the simple spherical geometry used in this simulation. However, differences in stress in the upper and lower element layers indicate the contribution of bending to the stress state.

The S33 stress distributions obtained are shown in Figure 4-68. Like the S33 stresses of other steeply-fitting lenses, the S33 stress shown in Figure 4-68 is compressive at the lens center, and tensile at the edge.

The interface pressure and $\frac{S33(2t)}{r}$ distributions are shown in Figure 4-69. Both quantities show a negative pressure applied by the lens at its center, and a positive pressure applied at the edge. The shape of the interface pressure distribution matches agrees very well with the interface pressure predicted by the analytical model of Jenkins and Shimbo. The magnitude of central pressure obtained in this simulation ($\approx$ -34Pa) also agrees with that predicted by their analytical model (-44.1Pa). In the simulation, the point of zero interface pressure occurred at approximately 4.7mm, compared to a value of 5.31mm predicted by the analytical model. Recall that the

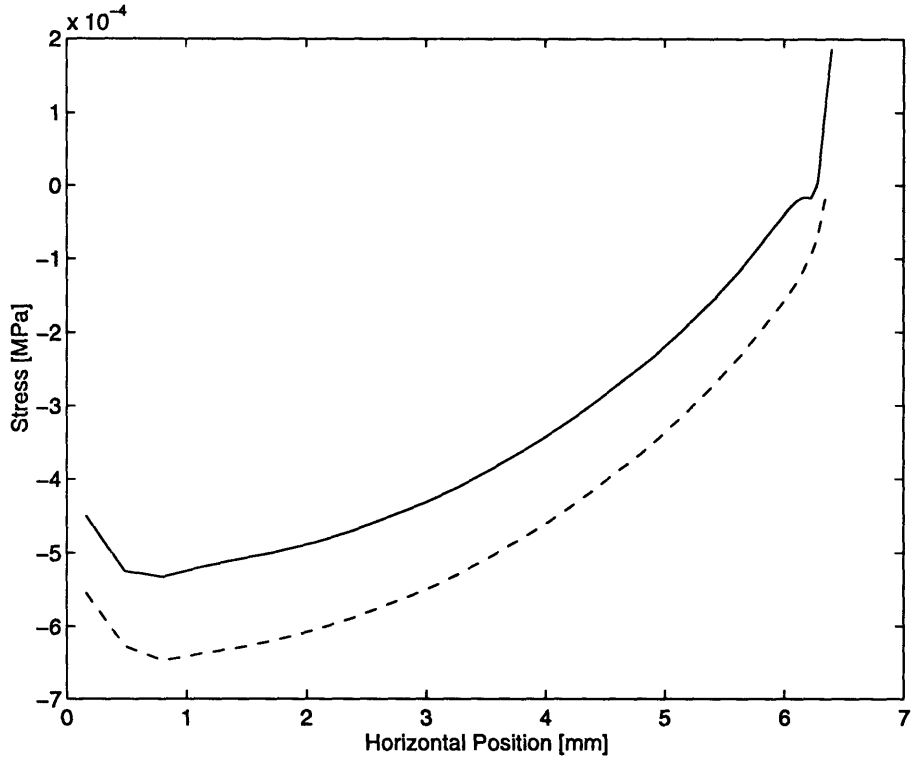

Figure 4-67: S11 stress distribution in lower and upper layer of lens elements for placement simulations of a spherical lens on a spherical eye

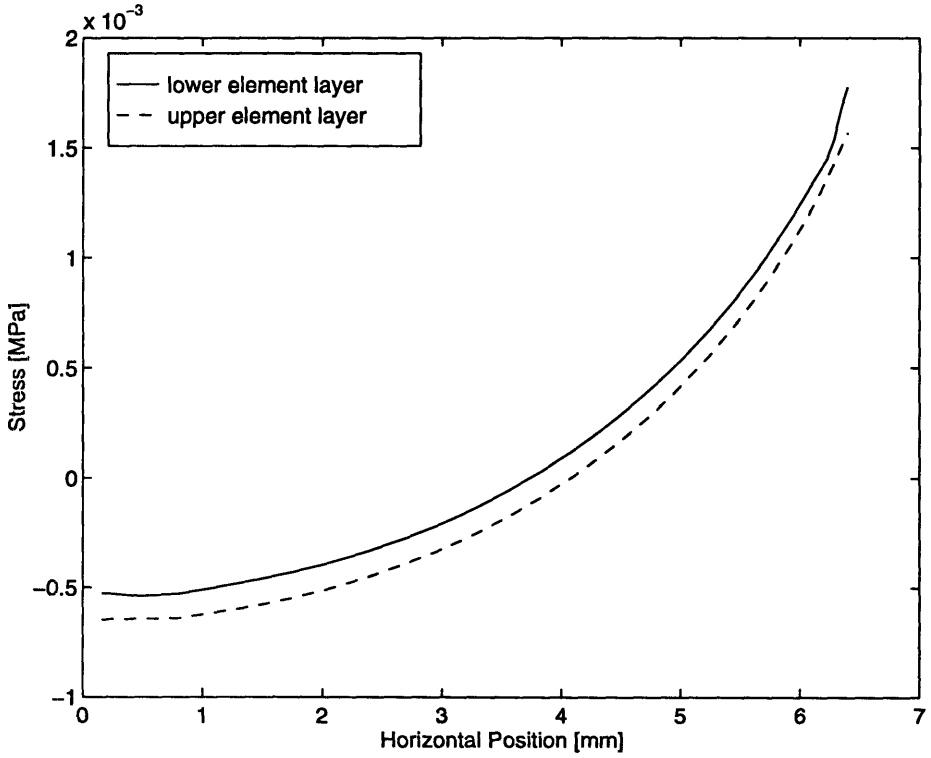

Figure 4-68: S33 stress distribution in lower and upper layer of lens elements for placement simulations of a spherical lens on a spherical eye

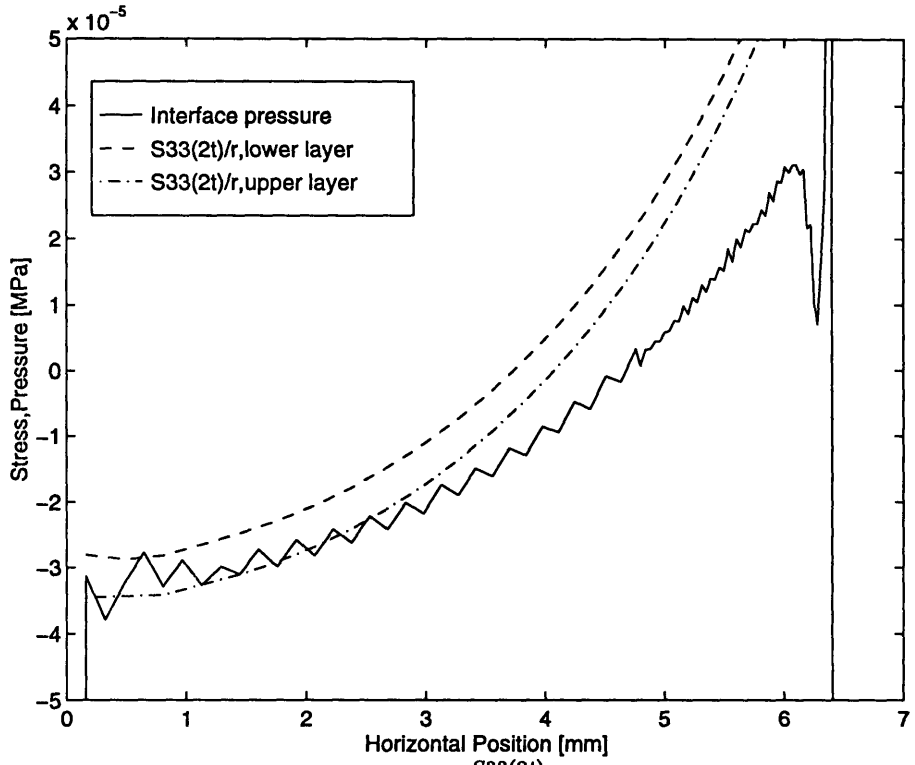

Figure 4-69: Interface pressure and $\frac{S33(2t)}{r}$ distributions for placement simulations of a spherical lens on a spherical eye

analytical model of Jenkins and Shimbo did not take into account large deformations or bending contributions.

4.3 Conclusions of Lens Placement Simulations

A number of issues concerning modeling of contact lens placement on the eye have been presented in this chapter. First, questions pertaining to modeling techniques were addressed, and then, one model was used to compare the fitting characteristics of lenses of varying geometries.

A primary focus of the modeling issues explored in this chapter was the question of how to model the tear layer. A number of separate aspects of modeling the tear were presented, (nature of the tear, tear geometry, interface characteristics, loading conditions, element type) and several modeling options for each issue were discussed. It was found that reasonable results were obtained by modeling the tear layer as a compliant, nearly incompressible solid body that was free to slide between the lens and the eye, but that was not permitted to separate from them. However, such a

model proved unreliable and difficult to implement.

The second primary modeling issue presented was the question of whether the information about lens fit obtained from simulations that did not include a tear layer was similar to the fit information obtained when a tear layer was included in the model. It was found that the presence of the tear layer had a significant effect on the internal lens stresses and interface pressures yielded by the simulations, by 1) reducing internal peak stresses and stress gradients, and 2) smoothing out numerical errors due to contact surface modeling. The significant effects of the tear layer demonstrated that it is an important component in the mechanics of lens fit, and that further work needs to be done to improve upon tear modeling techniques.

However, comparison of the tear and no tear simulations demonstrated that there was a strong correlation between the shapes of internal stress and interface pressure distributions performed with and without a tear layer. Therefore, it was determined that simulations performed without a tear layer were a useful alternative to those that included the tear.

Using the no tear model, a number of lens placement simulations were performed using both actual lens geometries and also blank lens shapes. In all the simulations, it was found that the tangential stress in the lenses varied consistently between the center and the edge of the lenses. At the lens centers, tangential stresses were relatively constant through the lens thickness, and were caused by in-plane tension or compression. However, near the cornea/sclera junction, tangential stresses were oppositely-directed on the upper and lower lens surfaces, indicating a significant amount of bending at this point, due to the conformation of the lens to the changing shape of the eye at the junction.

Geometric differences between lenses were also apparent in their corresponding stress and interface pressure distributions. It was found that the lens bearing had a significant effect on both S11 and S33 stresses and interface pressure levels, where greater stress and pressure magnitudes were caused by lenses whose curvatures were most different than that of the cornea. This relationship was true both at the center of the lens and also near the edge. In addition, the direction of the bearing (steep or flat)

played a strong role in determining the sign of the stresses and pressures measured. In general, flat lenses demonstrated positive tangential and circumferential stress and interface pressure at the center of the lens. Interface pressure near the lens edge was typically negative for flat lenses. The opposite trend was seen in steep lenses, which had negative values of S11 and S33 stress and interface pressure at the lens center, and positive values of interface pressure at the lens edges.

The opposite interface pressure distributions generated by flat and steep lenses is likely to have significant influence on how each type of lens feel and moves on the eye. Note that the only force holding the lens onto the eye is the tensile interface pressure, which, for flat lenses, is induced at the lens edge, and for steep lenses, is induced at the lens center. Therefore, the two types of lenses are held to the eye at completely different locations, and are therefore likely to have very different motion responses to the applied lid pressure. The comfort level of flat and steep lenses is also likely to vary widely. Due to the axisymmetric geometry of the eye, tensile pressure induced at the lens edge can act over a much larger surface area than centrally-located pressure. Therefore, the tensile pressure magnitude required to generate a given lens-retaining force will be smaller for pressures located at the lens edge than at the lens center. This is likely to cause flat lenses to be more comfortable to wear than steep lenses.

Lens thickness also influenced the stress and pressure measured in these simulations. As the lens centers, the magnitude of S11, S33 and interface pressure for various geometries increased with increasing lens thickness. Near the cornea/sclera junction, the effect of lens thickness was most apparent in the magnitude of S11 stress since, at the cornea/sclera junction, tangential stress is primarily caused by bending, and stress due to bending is related to the cube of the member thickness.

General results such as the relationship of bearing and lens thickness to interface pressure can be used to aid in lens design. For example, if certain requirements on interface pressure were established, such as the minimum total restraining force needed to hold the lens to the eye, or the maximum positive and negative local pressures that yield comfortable fit, it would be possible to modify such lens fitting parameters by appropriately adjusting the lens geometry characteristics that have the greatest

influence on each parameter. If, for example, the central interface pressure induced by a given lens were too high, but the pressure at the cornea/sclera junction were too low, the lens curvature could be modified to more closely match that of the cornea, in order to reduce the central pressure, and the thickness of the lenticular region could be increased to generate larger pressures near the lens edge. Such geometry modifications could be made iteratively, and the resulting lens shapes "tested" in simulations such as the ones performed in this chapter until the lens design produced the desired interface pressures and/or had the desired internal stress distribution. This lens could then be produced and tested on patients. In this way, information about relationships between lens geometry and fit characteristics could greatly reduce the time and cost of developing lens designs.

Chapter 5

Conclusions and Future Extensions of Contact Lens Processing and Design Modeling

In each of the three previous chapters, a basic issue pertaining to the processing or design of hydrogel contact lenses has been explored.

In Chapter 2, the problem of lens shape distortion due to crosslinking processing parameters was explored, and the effects of nonuniform swelling coefficient distribution and sequential crosslinking history were demonstrated. It was shown that when a change in lens volume on the order of 40% accompanied lens manufacturing process, (which is the case for lenses crosslinked to a rigid state and then hydrated) spatial variations in the expansion coefficient of $\pm 10\%$ would cause significant distortion of the final lens shape. This was true when the swelling coefficient distribution varied both through the lens thickness and tangentially along the lens. However, when the overall volume change that occurred during processing was small, (on the order of 7% for lenses crosslinked in an already hydrated state) shape distortion due to nonuniform material property distribution was slight.

In this set of simulations, the effect of initial lens geometry on final distorted shape was not studied. Further work could be performed to determine if there are certain geometry characteristics that make a lens more resistant to shape distortion

due to nonuniform swelling coefficient distribution. Another study might focus on compensating for uneven material property distribution in the initial mold shape. If, for example, it were found that it would be more feasible to adjust processing parameters so as to consistently produce certain patters of swelling coefficient distribution than it would be to consistently produce uniform swelling coefficient distribution, simulations could be performed "in reverse" to determine what initial mold shape would be needed to produce the correct final lens shape.

The simulations of a crosslinking process that occurs sequentially throughout a lens illustrated that such a process can result in large internal stresses and significant lens shape distortion, even when the overall volume change is small ($\approx 7\%$) A key characteristic of the hydrogel material modeled that leads to such large internal stresses and subsequent shape distortion is that volume change in the material occurs simultaneously with the formation of chemical crosslinks. The internal stresses develop as a result of the material attempting to contract while being restrained by the rigid mold. This suggests that a material that did not undergo volume change during crosslinking would not be susceptible to the shape distortion effects of sequential crosslinking.

The simulation of the sequential crosslinking of a cylindrical disk demonstrated how such simulations might be used in conjunction with laboratory experiments to evaluate the nature and extent of sequential crosslinking occurring in a processing method. The simulations illustrated that the distorted shapes of the blanks depended on both the initial blank geometry and on the pattern of crosslinking history. Therefore, by varying the geometry and crosslinking parameters in laboratory experiments, and comparing the distorted blank shapes to those obtained in simulations, it would be possible to obtain an approximation of the pattern of sequential crosslinking occurring during processing.

An extension of the sequential crosslinking modeling work might be to explore the curling-up phenomenon described earlier, in which lenses completely roll up upon removal from the mold. This type of behavior is due to an instability in the real lens that is not present in the finite element models used here. Therefore, in order to

study such a problem, it would be necessary to introduce random variations in the model lenses that could trigger instabilities, such as minor variations in the location of the mid surface of the lens.

The simulations performed in Chapter 3 demonstrated that the force-displacement response of lenses under pinching loading became stiffer as the overall lens thickness profile increased. In addition, it was shown that the shape of the response varied considerably over the range of loading. After a lens had undergone initial deformation, the force-displacement curve became very linear, and showed a stiffness response that was much more compliant than when the lens was undergoing its very early deformation. In contrast, at the very early stages of loading, the stiffness response varied rapidly, providing a very stiff initial response, and then quickly becoming more compliant. Another conclusion of this chapter was that the relative influence of various lens regions on lens stiffness changed as loading progressed. It was shown that at initial deformation, the thickness of the edge region had a large influence on the stiffness response, while at larger deformations, the thickness of the lenticular region had a relatively greater effect on lens stiffness.

Further work on the relationship of thickness profile to lens flexibility would probably focus on the effects of the edge region. The amount of deformation lenses experience when placed on the eye is similar in magnitude to that of the early part of the pinching loading simulated. Since the edge region was shown to be significant in determining the lens response during this early pinching deformation, it is likely that the edge region will also play a crucial role in determining the lens behavior during placement and motion on the eye, when the amount of lens deformation is relatively small. Another reason for focusing on the edge region in further studies is the demonstrated nonlinearity of the stiffness response at early pinching loading, when the edge region was shown to have significant influence. The rapid change in the early stiffness response indicates that the lens' load carrying mechanism was rapidly changing at this point, and further study to understand the influence of lens geometry on the way this change of load bearing occurs needs to be performed.

Additional work would also focus on correlating the flexibility response of lenses

to their fit, both to parameters obtained from simulations, such as interface pressure distribution and internal stress state, and also to experimental fitting parameters, such as comfort and amount of blink-induced motion. Such correlation of flexibility to fit would probably illustrate the need for different kinds of simulated testing. For example, the pinching simulations in Chapter 3 demonstrated that there was very little influence of lens bearing on stiffness in pinching, however, the lens placement simulations in Chapter 4 demonstrated a strong relationship between bearing and induced lens/eye interface pressure. Therefore, the measurement of a lens' force-displacement response in a pinch test does not in itself provide enough information to predict the pressure distribution the lens will generate on the eye. Other tests, such as an axisymmetric reverse bending, for example, are needed to more fully predict lens fit. The development and evaluation of such additional tests will be pursued.

In Chapter 4, many issues pertaining to the fit of contact lenses on the eye were explored. First, a number of modeling issues were discussed, which primarily focused on techniques for modeling the behavior of the tear layer and its interactions with the lens and the eye. Difficulties arose due to the incompressible and free-flowing nature of the tear, however, a model in which the tear was considered to be an incompressible, compliant solid, sliding freely between the lens and the eye yielded reasonable results. This model was not reliable enough to use for the simulation of placement of a large number of lens geometries. Therefore, simulations were performed without a tear layer. These no-tear simulations illustrated that the model tear layer had a significant effect in smoothing the stresses in the lens and the interface pressures, just as a real tear would, and, therefore, should be included when modeling lens/eye interactions. However, the stress and pressure distributions yielded by the no-tear simulations showed a good correlation to those obtained when the tear layer was modeled, indicating that simulations without a tear layer could provide a good approximation of the results that would be obtained with a tear layer.

When various lens geometries were tested in lens placement simulations, it was found that the lens bearing had a significant effect on both the magnitude and the direction of internal lens stress and lens/eye interface pressures. In general, lenses

whose curvature most closely matched that of the eye developed the lowest internal stresses and generated the lowest interface pressures. In addition, it was found that steep lenses induced a negative (tensile) central interface pressure, while flat lenses generated a positive interface pressure at the center of the lens. Lens thickness was also found to contribute to internal lens stress and interface pressure, with thicker lenses producing greater stresses and pressures. The effect of thickness was most noticeable at the cornea/sclera junction, where lenses must undergo significant bending in order to conform to the eye.

The results of lens placement simulations such as the ones performed can be applied directly to the development of new lens designs. A designer can simulate the placement of a proposed lens design, and evaluate fitting characteristics, such as interface pressure and internal stress state. Then, if modifications to lens fit are necessary, the designer can use the general relationships between lens fit parameters and specific lens geometric characteristics such as bearing and thickness profile to efficiently alter the lens design, appropriately adjusting the specific geometry characteristics that most strongly influence the fitting parameters of interest.

A number of extensions of work on the issues of lens fit will be explored. Due to the demonstrated importance of the tear layer, improved techniques for modeling it will be investigated. Of particular interest is the effect of the tear on the measured interface pressure distribution, since it is this pressure that contributes directly to the comfort of a contact lens on the eye.

A further extension of the lens fit modeling will be the modeling of lens motion induced by lid pressure during blinking. Such simulations will necessitate the use of a three-dimensional model. In addition, the material models of both the tear and the lens will need to be enhanced for dynamic simulations. Tear viscosity will need to be included, since viscous forces will be extremely important in the flow of the thin tear layer. The lens material will also need to be modified to include porosity characteristics. It has been shown that pressure gradients that develop within the lens material due to the flow of tear into and through the lens can contribute significantly to the forces that drive lens motion. [9]

Appendix A

Example Input Deck for Lens Placement Simulations

The following is the input deck used for the lens placement simulation of the I85/1 lens geometry which included a solid 50μm tear layer. The final deformed mesh configuration is shown in Figure 4-14.

```
*HEADING
placing I85/1 lens on solid, incompressible tear layer
**
*NODE,NSET=EYER
1000,0.,-5.
*NODE,NSET=TOPREF
2000,0.,1.
*NODE,NSET=BNODES
** bottom of lens nodes
401,0.,-0.22
402,0.169138,-0.221683
403,0.338209,-0.226731
404,0.507146,-0.235143
405,0.675882,-0.246914
406,0.84435,-0.262041
407,1.012484,-0.280517
408,1.180217,-0.302335
409,1.347483,-0.327486
410,1.514215,-0.355961
411,1.680348,-0.387748
```

412,1.845815,-0.422834
413,2.010551,-0.461206
414,2.174492,-0.502848
415,2.337571,-0.547744
416,2.499724,-0.595877
417,2.660887,-0.647226
418,2.820997,-0.701772
419,2.97999,-0.759494
420,3.137803,-0.820367
421,3.294373,-0.884369
422,3.449638,-0.951474
423,3.603538,-1.021655
424,3.75601,-1.094884
425,3.906995,-1.171133
426,4.056434,-1.250372
427,4.204265,-1.332568
428,4.350432,-1.417689
429,4.494876,-1.505703
430,4.637541,-1.596573
431,4.778368,-1.690263
432,4.917304,-1.786738
433,5.054292,-1.885958
434,5.099513,-1.919635
435,5.144509,-1.953611
436,5.189279,-1.987884
437,5.233821,-2.022454
438,5.278132,-2.057319
439,5.322211,-2.092477
440,5.366056,-2.127926
441,5.409665,-2.163665
442,5.453036,-2.199693
443,5.496166,-2.236008
444,5.539055,-2.272608
445,5.581701,-2.309492
446,5.6241,-2.346658
447,5.666253,-2.384104
448,5.708156,-2.421829
449,5.749807,-2.459831
450,5.791206,-2.498109
451,5.83235,-2.53666
452,5.873237,-2.575483
453,5.913866,-2.614577
454,5.954235,-2.65394
455,5.994341,-2.693569
456,6.034184,-2.733463

```
457,6.073762,-2.773621
458,6.113072,-2.814041
459,6.152113,-2.85472
460,6.190884,-2.895658
461,6.229382,-2.936852
462,6.267606,-2.9783
463,6.305554,-3.020001
464,6.343225,-3.061953
465,6.380616,-3.104153
466,6.417727,-3.146601
467,6.454556,-3.189294
468,6.4911,-3.23223
469,6.527359,-3.275408
470,6.563331,-3.318825
471,6.599014,-3.36248
472,6.634406,-3.406371
473,6.669507,-3.450496
474,6.704324,-3.494844
475,6.73948,-3.538924
476,6.751356,-3.553491
477,6.763309,-3.567994
478,6.775341,-3.582432
479,6.787449,-3.596806
480,6.799635,-3.611115
481,6.811897,-3.625358
482,6.824235,-3.639535
483,6.836649,-3.653646
484,6.849139,-3.66769
485,6.861704,-3.681667
486,6.874344,-3.695576
487,6.887058,-3.709417
488,6.899846,-3.72319
489,6.912707,-3.736894
490,6.925643,-3.750529
491,6.938651,-3.764095
492,6.951731,-3.77759
493,6.964884,-3.791015
*NODE,NSET=TNODES
** top of lens nodes
801,0.,-0.11
802,0.171754,-0.111619
803,0.343447,-0.116475
804,0.515017,-0.124566
805,0.686405,-0.13589
806,0.857549,-0.150443
```

807,1.028388,-0.168218
808,1.198862,-0.189211
809,1.36891,-0.213413
810,1.538471,-0.240817
811,1.707486,-0.271411
812,1.875894,-0.305186
813,2.043635,-0.342129
814,2.21065,-0.382228
815,2.37688,-0.425467
816,2.542265,-0.471832
817,2.706747,-0.521307
818,2.870267,-0.573872
819,3.032767,-0.629511
820,3.19419,-0.688203
821,3.354478,-0.749927
822,3.513573,-0.814661
823,3.671421,-0.882383
824,3.827964,-0.953068
825,3.983146,-1.026691
826,4.134419,-1.108011
827,4.283714,-1.192939
828,4.431266,-1.280862
829,4.577014,-1.371743
830,4.720898,-1.465547
831,4.862861,-1.562234
832,5.002844,-1.661766
833,5.14079,-1.764102
834,5.18631,-1.79883
835,5.231595,-1.833863
836,5.276644,-1.8692
837,5.321454,-1.904839
838,5.366023,-1.940779
839,5.41035,-1.977018
840,5.454432,-2.013554
841,5.498267,-2.050385
842,5.541853,-2.087511
843,5.585189,-2.124929
844,5.628272,-2.162637
845,5.6711,-2.200635
846,5.713672,-2.238919
847,5.755986,-2.277489
848,5.798039,-2.316343
849,5.83983,-2.355479
850,5.881357,-2.394895
851,5.922617,-2.434589

```
852,5.96361,-2.47456
853,6.004333,-2.514806
854,6.044785,-2.555324
855,6.084963,-2.596114
856,6.124866,-2.637173
857,6.164491,-2.6785
858,6.203838,-2.720092
859,6.242905,-2.761948
860,6.281688,-2.804065
861,6.320188,-2.846443
862,6.358402,-2.889078
863,6.396328,-2.93197
864,6.433965,-2.975115
865,6.470428,-3.019244
866,6.505923,-3.064169
867,6.541106,-3.109338
868,6.575975,-3.154749
869,6.61053,-3.200401
870,6.644767,-3.246291
871,6.678685,-3.292417
872,6.712284,-3.338777
873,6.74556,-3.385369
874,6.778513,-3.432189
875,6.811142,-3.479237
876,6.821945,-3.49497
877,6.832713,-3.510727
878,6.843444,-3.52651
879,6.854138,-3.542317
880,6.864796,-3.558148
881,6.875417,-3.574004
882,6.886002,-3.589885
883,6.89655,-3.60579
884,6.907061,-3.62172
885,6.917535,-3.637673
886,6.927973,-3.653651
887,6.938374,-3.669653
888,6.948738,-3.685678
889,6.959064,-3.701728
890,6.969354,-3.717801
891,6.979607,-3.733899
892,6.989822,-3.750019
893,7,-3.766164
*NODE,NSET=TEARBOT
2001,0,-0.29
2002,0.056771,-0.290207
```

2003,0.113539,-0.290826
2004,0.170301,-0.291859
2005,0.227054,-0.293305
2006,0.283795,-0.295164
2007,0.340521,-0.297437
2008,0.397229,-0.300121
2009,0.453915,-0.303219
2010,0.510578,-0.306729
2011,0.567214,-0.310651
2012,0.623819,-0.314986
2013,0.680392,-0.319732
2014,0.736929,-0.32489
2015,0.793426,-0.330459
2016,0.849882,-0.336439
2017,0.906292,-0.342831
2018,0.962655,-0.349632
2019,1.018966,-0.356844
2020,1.075224,-0.364465
2021,1.131424,-0.372495
2022,1.187565,-0.380935
2023,1.243642,-0.389782
2024,1.299654,-0.399038
2025,1.355597,-0.408701
2026,1.411468,-0.418771
2027,1.467265,-0.429247
2028,1.522983,-0.440129
2029,1.578621,-0.451417
2030,1.634175,-0.463109
2031,1.689643,-0.475205
2032,1.745021,-0.487704
2033,1.800307,-0.500606
2034,1.855498,-0.513911
2035,1.91059,-0.527616
2036,1.965581,-0.541723
2037,2.020468,-0.556229
2038,2.075247,-0.571134
2039,2.129917,-0.586437
2040,2.184474,-0.602138
2041,2.238915,-0.618236
2042,2.293238,-0.634729
2043,2.347439,-0.651618
2044,2.401516,-0.6689
2045,2.455466,-0.686576
2046,2.509285,-0.704644
2047,2.562972,-0.723103

2048,2.616523,-0.741952
2049,2.669935,-0.761191
2050,2.723206,-0.780817
2051,2.776332,-0.800831
2052,2.829312,-0.821232
2053,2.882141,-0.842017
2054,2.934818,-0.863186
2055,2.98734,-0.884738
2056,3.039703,-0.906672
2057,3.091905,-0.928986
2058,3.143943,-0.951679
2059,3.195815,-0.974751
2060,3.247518,-0.9982
2061,3.299048,-1.022024
2062,3.350404,-1.046223
2063,3.401582,-1.070795
2064,3.45258,-1.095739
2065,3.503395,-1.121053
2066,3.554024,-1.146736
2067,3.604466,-1.172788
2068,3.654716,-1.199205
2069,3.704773,-1.225988
2070,3.754633,-1.253134
2071,3.804295,-1.280643
2072,3.853755,-1.308512
2073,3.90301,-1.336741
2074,3.95206,-1.365327
2075,4.000899,-1.39427
2076,4.049527,-1.423567
2077,4.09794,-1.453217
2078,4.146136,-1.483219
2079,4.194113,-1.513571
2080,4.241867,-1.544271
2081,4.289397,-1.575319
2082,4.336699,-1.606711
2083,4.383772,-1.638446
2084,4.430612,-1.670524
2085,4.477218,-1.702941
2086,4.523587,-1.735697
2087,4.569716,-1.76879
2088,4.615602,-1.802217
2089,4.661245,-1.835977
2090,4.70664,-1.870069
2091,4.751786,-1.90449
2092,4.79668,-1.939239

2093,4.841321,-1.974314
2094,4.885704,-2.009713
2095,4.929829,-2.045434
2096,4.973693,-2.081475
2097,5.017293,-2.117834
2098,5.060628,-2.15451
2099,5.103694,-2.1915
2100,5.14649,-2.228803
2101,5.189014,-2.266416
2102,5.231262,-2.304337
2103,5.273234,-2.342565
2104,5.314926,-2.381098
2105,5.356336,-2.419933
2106,5.397463,-2.459068
2107,5.438304,-2.498502
2108,5.478857,-2.538232
2109,5.519119,-2.578256
2110,5.559089,-2.618572
2111,5.598765,-2.659178
2112,5.638144,-2.700071
2113,5.677224,-2.74125
2114,5.716004,-2.782713
2115,5.754481,-2.824456
2116,5.792653,-2.866479
2117,5.830518,-2.908778
2118,5.868074,-2.951352
2119,5.905319,-2.994197
2120,5.942252,-3.037313
2121,5.97887,-3.080697
2122,6.015171,-3.124346
2123,6.051153,-3.168258
2124,6.086815,-3.21243
2125,6.122154,-3.256861
2126,6.157169,-3.301548
2127,6.191896,-3.34646
2128,6.227143,-3.390963
2129,6.263226,-3.434791
2130,6.300132,-3.477929
2131,6.337848,-3.52036
2132,6.37636,-3.562071
2133,6.415654,-3.603045
2134,6.455716,-3.643268
2135,6.496533,-3.682726
2136,6.510304,-3.695706
2137,6.524156,-3.708599

2138,6.538089,-3.721404
2139,6.552102,-3.734122
2140,6.566196,-3.74675
2141,6.580369,-3.75929
2142,6.594621,-3.771739
2143,6.608951,-3.784099
2144,6.623359,-3.796368
2145,6.637843,-3.808546
2146,6.652405,-3.820632
2147,6.667042,-3.832626
2148,6.681755,-3.844528
2149,6.696542,-3.856336
2150,6.711404,-3.868051
2151,6.726339,-3.879672
2152,6.741347,-3.891199
2153,6.756428,-3.902631
2154,6.77158,-3.913967
2155,6.786804,-3.925208
2156,6.802098,-3.936352
2157,6.817463,-3.947399
2158,6.832896,-3.95835
2159,6.848399,-3.969203
2160,6.86393,-3.980015
2161,6.879443,-3.990852
2162,6.89494,-4.001713
2163,6.91042,-4.012598
2164,6.925882,-4.023508
2165,6.941327,-4.034442
2166,6.956755,-4.045401
2167,6.972166,-4.056383
2168,6.987559,-4.067391
2169,7.002935,-4.078422
2170,7.018294,-4.089478
2171,7.033635,-4.100557
2172,7.048958,-4.111661
2173,7.064264,-4.12279
2174,7.079553,-4.133942
2175,7.094824,-4.145118
2176,7.110077,-4.156319
2177,7.125313,-4.167543
2178,7.14053,-4.178792
2179,7.15573,-4.190064
2180,7.170913,-4.201361
2181,7.186077,-4.212681
2182,7.201224,-4.224025

```
2183,7.216352,-4.235394
2184,7.26163,-4.269641
2185,7.306746,-4.304102
2186,7.351698,-4.338776
2187,7.396486,-4.373663
2188,7.441108,-4.408761
2189,7.485563,-4.44407
2190,7.529851,-4.479589
2191,7.57397,-4.515316
2192,7.61792,-4.551253
2193,7.661699,-4.587396
2194,7.705307,-4.623747
2195,7.748743,-4.660303
2196,7.792005,-4.697064
2197,7.835092,-4.73403
2198,7.878004,-4.771199
2199,7.92074,-4.808571
2200,7.963299,-4.846144
2201,8.005679,-4.883919
2202,8.04788,-4.921893
2203,8.089901,-4.960067
2204,8.131741,-4.998439
2205,8.173399,-5.037008
2206,8.214874,-5.075774
2207,8.256166,-5.114736
2208,8.297272,-5.153893
2209,8.338193,-5.193244
2210,8.378927,-5.232788
2211,8.419473,-5.272524
2212,8.459831,-5.312452
2213,8.5,-5.35257
*NODE,NSET=TEARTOP
3001,0,-0.24
3002,0.05699,-0.240207
3003,0.113976,-0.240827
3004,0.170957,-0.241862
3005,0.227929,-0.24331
3006,0.284888,-0.245171
3007,0.341833,-0.247446
3008,0.398759,-0.250135
3009,0.455665,-0.253236
3010,0.512546,-0.256751
3011,0.569401,-0.260678
3012,0.626225,-0.265018
3013,0.683017,-0.269771
```

3014,0.739772,-0.274935
3015,0.796489,-0.280512
3016,0.853163,-0.2865
3017,0.909793,-0.292899
3018,0.966375,-0.29971
3019,1.022905,-0.306931
3020,1.079382,-0.314562
3021,1.135802,-0.322603
3022,1.192162,-0.331054
3023,1.248459,-0.339913
3024,1.304691,-0.349181
3025,1.360853,-0.358857
3026,1.416944,-0.36894
3027,1.47296,-0.37943
3028,1.528899,-0.390327
3029,1.584757,-0.401629
3030,1.640531,-0.413337
3031,1.696219,-0.425449
3032,1.751818,-0.437965
3033,1.807324,-0.450885
3034,1.862735,-0.464207
3035,1.918048,-0.477931
3036,1.97326,-0.492056
3037,2.028368,-0.506582
3038,2.083368,-0.521508
3039,2.138259,-0.536832
3040,2.193038,-0.552554
3041,2.247701,-0.568674
3042,2.302245,-0.58519
3043,2.356668,-0.602102
3044,2.410967,-0.619408
3045,2.465138,-0.637108
3046,2.51918,-0.655201
3047,2.573089,-0.673686
3048,2.626862,-0.692562
3049,2.680497,-0.711827
3050,2.733991,-0.731481
3051,2.78734,-0.751524
3052,2.840543,-0.771953
3053,2.893596,-0.792767
3054,2.946496,-0.813967
3055,2.999241,-0.835549
3056,3.051828,-0.857515
3057,3.104254,-0.879861
3058,3.156517,-0.902587

3059,3.208613,-0.925692
3060,3.26054,-0.949175
3061,3.312295,-0.973034
3062,3.363876,-0.997269
3063,3.415279,-1.021877
3064,3.466503,-1.046857
3065,3.517543,-1.072209
3066,3.568399,-1.097931
3067,3.619066,-1.124021
3068,3.669542,-1.150478
3069,3.719825,-1.177302
3070,3.769912,-1.204489
3071,3.8198,-1.232039
3072,3.869487,-1.259951
3073,3.91897,-1.288223
3074,3.968247,-1.316853
3075,4.017314,-1.345841
3076,4.06617,-1.375183
3077,4.114811,-1.40488
3078,4.163235,-1.434929
3079,4.21144,-1.465329
3080,4.259423,-1.496078
3081,4.307182,-1.527174
3082,4.354713,-1.558616
3083,4.402015,-1.590403
3084,4.449085,-1.622532
3085,4.495921,-1.655002
3086,4.542519,-1.687811
3087,4.588878,-1.720958
3088,4.634995,-1.75444
3089,4.680868,-1.788256
3090,4.726494,-1.822405
3091,4.771871,-1.856883
3092,4.816997,-1.891691
3093,4.861869,-1.926825
3094,4.906484,-1.962283
3095,4.950841,-1.998065
3096,4.994937,-2.034168
3097,5.03877,-2.07059
3098,5.082337,-2.107329
3099,5.125636,-2.144383
3100,5.168665,-2.181751
3101,5.211422,-2.219431
3102,5.253904,-2.257419
3103,5.296109,-2.295716

3104,5.338035,-2.334317
3105,5.379679,-2.373222
3106,5.42104,-2.412428
3107,5.462116,-2.451934
3108,5.502903,-2.491736
3109,5.5434,-2.531834
3110,5.583606,-2.572224
3111,5.623517,-2.612906
3112,5.663131,-2.653876
3113,5.702447,-2.695133
3114,5.741463,-2.736673
3115,5.780176,-2.778497
3116,5.818584,-2.8206
3117,5.856686,-2.86298
3118,5.894478,-2.905637
3119,5.931961,-2.948566
3120,5.96913,-2.991767
3121,6.005985,-3.035236
3122,6.042524,-3.078971
3123,6.078744,-3.122971
3124,6.114643,-3.167233
3125,6.150221,-3.211754
3126,6.185474,-3.256532
3127,6.220401,-3.301565
3128,6.255522,-3.346445
3129,6.291502,-3.390641
3130,6.328329,-3.434133
3131,6.365988,-3.476906
3132,6.404467,-3.518943
3133,6.443751,-3.560229
3134,6.483825,-3.600749
3135,6.524675,-3.640487
3136,6.538461,-3.653557
3137,6.552331,-3.666537
3138,6.566284,-3.679428
3139,6.580321,-3.692229
3140,6.594439,-3.704939
3141,6.608638,-3.717559
3142,6.622919,-3.730086
3143,6.63728,-3.742521
3144,6.651721,-3.754864
3145,6.666241,-3.767113
3146,6.68084,-3.779268
3147,6.695516,-3.791329
3148,6.71027,-3.803296

3149,6.725101,-3.815167
3150,6.740008,-3.826942
3151,6.75499,-3.838621
3152,6.770047,-3.850204
3153,6.785179,-3.861689
3154,6.800384,-3.873077
3155,6.815662,-3.884366
3156,6.831012,-3.895557
3157,6.846435,-3.906649
3158,6.861928,-3.917641
3159,6.877492,-3.928533
3160,6.893082,-3.939388
3161,6.908655,-3.950267
3162,6.924211,-3.961171
3163,6.93975,-3.972099
3164,6.955271,-3.983051
3165,6.970775,-3.994029
3166,6.986262,-4.00503
3167,7.001731,-4.016056
3168,7.017183,-4.027106
3169,7.032618,-4.038181
3170,7.048035,-4.04928
3171,7.063435,-4.060403
3172,7.078817,-4.071551
3173,7.094181,-4.082723
3174,7.109528,-4.093919
3175,7.124857,-4.105139
3176,7.140168,-4.116383
3177,7.155462,-4.127652
3178,7.170738,-4.138944
3179,7.185996,-4.150261
3180,7.201236,-4.161602
3181,7.216459,-4.172966
3182,7.231663,-4.184355
3183,7.246849,-4.195768
3184,7.2923,-4.230149
3185,7.337588,-4.264745
3186,7.382712,-4.299555
3187,7.427671,-4.334577
3188,7.472463,-4.369812
3189,7.517089,-4.405259
3190,7.561546,-4.440916
3191,7.605834,-4.476783
3192,7.649952,-4.512859
3193,7.693899,-4.549143

```
3194,7.737673,-4.585634
3195,7.781275,-4.622333
3196,7.824703,-4.659237
3197,7.867955,-4.696346
3198,7.911032,-4.733659
3199,7.953932,-4.771176
3200,7.996653,-4.808895
3201,8.039196,-4.846815
3202,8.081559,-4.884937
3203,8.123742,-4.923258
3204,8.165742,-4.961778
3205,8.20756,-5.000497
3206,8.249194,-5.039413
3207,8.290644,-5.078525
3208,8.331909,-5.117833
3209,8.372987,-5.157336
3210,8.413877,-5.197033
3211,8.45458,-5.236922
3212,8.495093,-5.277004
3213,8.535417,-5.317276
*NFILL,NSET=LENSNODE
BNODES,TNODES,4,100
*NFILL,NSET=TEARNODE
TEARBOT,TEARTOP,2,500
*ELEMENT,TYPE=CAX8,ELSET=MATEL
1,401,403,603,601,402,503,602,501
*ELGEN,ELSET=MATEL
1,46,2,1,2,200,100
**1,40,2,1
*ELEMENT,TYPE=CAX8,ELSET=TEAREL
401,2001,2003,3003,3001,2002,2503,3002,2501
*ELGEN,ELSET=TEAREL
401,106,2,1
*ORIENTATION,NAME=ONE,DEFINITION=OFFSET TO NODES,SYSTEM=RECTANGULAR
2,4
3,0.
*SOLID SECTION,ELSET=MATEL,MATERIAL=POLY,ORIENTATION=ONE
*SOLID SECTION,ELSET=TEAREL,MATERIAL=TEARS,ORIENTATION=ONE
***SOLID SECTION,ELSET=LIDEL,MATERIAL=LID
*MATERIAL,NAME=POLY
*ELASTIC
2.,.49
*MATERIAL,NAME=TEARS
*ELASTIC
.001,.49
```

```
*RIGID SURFACE,TYPE=SEGMENTS,NAME=EYE,REF NODE=1000
** this is the smoothed  eye4
START,0,-0.29
CIRCL,0.475621,-0.304515,0,-8.09
CIRCL,0.949473,-0.348004,0,-8.09
CIRCL,1.41979,-0.420307,0,-8.09
CIRCL,1.884824,-0.521153,0,-8.09
CIRCL,2.342843,-0.650169,0,-8.09
CIRCL,2.792143,-0.806873,0,-8.09
CIRCL,3.231051,-0.990682,0,-8.09
CIRCL,3.657934,-1.200913,0,-8.09
CIRCL,4.071204,-1.436783,0,-8.09
CIRCL,4.469322,-1.697414,0,-8.09
CIRCL,4.850807,-1.981835,0,-8.09
CIRCL,5.214238,-2.28899,0,-8.09
CIRCL,5.558264,-2.617734,0,-8.09
CIRCL,5.881604,-2.966844,0,-8.09
CIRCL,6.183055,-3.33502,0,-8.09
CIRCL,6.491525,-3.677964,8.56115266,-1.50618157
CIRCL,6.848922,-3.969567,8.56115266,-1.50618157
CIRCL,7.220864,-4.238791,0.,-13.8231
CIRCL,7.582234,-4.522047,0.,-13.8231
CIRCL,7.932503,-4.81892,0.,-13.8231
CIRCL,8.271158,-5.128975,0.,-13.8231
CIRCL,8.597705,-5.451759,0.,-13.8231
CIRCL,8.911664,-5.786799,0.,-13.8231
CIRCL,9.212576,-6.133605,0.,-13.8231
CIRCL,9.5,-6.491668,0.,-13.8231
*ELSET,ELSET=LENSBOT,GENERATE
1,46,1
*ELSET,ELSET=TMASTER,GEN
468,491,1
*ELSET,ELSET=LSLAVE
44,45,46
*SURFACE DEFINITION,NAME=LENSBOT,TRIM=NO
LENSBOT,S1
46,S2
*SURFACE DEFINITION,NAME=LSLAVE
LSLAVE,S1
*SURFACE DEFINITION,NAME=LBOTC,TRIM=NO
1,S1
*SURFACE DEFINITION,NAME=TEARTOP,TRIM=YES
TEAREL,S3
*SURFACE DEFINITION,NAME=TTOPC,TRIM=YES
401,S3
```

```
*SURFACE DEFINITION,NAME=TMASTER
TMASTER,S3
*CONTACT PAIR,INTERACTION=NS
TEARTOP,LENSBOT
*CONTACT PAIR,INTERACTION=LENSTEAR
LSLAVE,TMASTER
*SURFACE DEFINITION,NAME=TEARBOT,TRIM=YES
TEAREL,S1
*CONTACT PAIR,INTERACTION=NS
TEARBOT,EYE
*SURFACE INTERACTION,NAME=LENSTEAR
*FRICTION
0.
*SURFACE BEHAVIOR,SOFTENED
5e-4,1e-5
*SURFACE INTERACTION,NAME=NS
*FRICTION
0.
*SURFACE BEHAVIOR,NO SEPARATION
**
*BOUNDARY
2001,1
2501,1
3001,1
401,1
501,1
601,1
701,1
801,1
1000,1,6
*NSET,NSET=LOADED
3001,3045,3081
3113,3191
***
******* step 1 lower top tear surface
*STEP,NLGEOM,INC=100
*STATIC
.05,1.,1e-10,.5
*BOUNDARY
TEARTOP,2,2,-.003
TEARTOP,1,1,0.
*NODE PRINT,FREQ=0
*EL PRINT,FREQ=0
*CONTACT PRINT,FREQ=0
*PRINT,FREQ=0
```

```
*ENDSTEP
**
********* step 2 release tear surface displacements
*STEP,NLGEOM,INC=100
*STATIC
.05,1.,1e-10,.5
*BOUNDARY,OP=NEW
2001,1
2501,1
3001,1
401,1
501,1
601,1
701,1
801,1
1000,1,6
*NODE PRINT,FREQ=0
*EL PRINT,FREQ=0
*CONTACT PRINT,FREQ=100,MASTER=EYE,SLAVE=TEARBOT
*PRINT,FREQ=0
*ENDSTEP
**
******** step 3 lower some lens nodes
*STEP,NLGEOM,INC=100
*STATIC
.05,1.,1e-10,.5
*BOUNDARY,OP=NEW
2001,1
2501,1
3001,1
401,1
501,1
601,1
701,1
801,1
1000,1,6
**
640,2,2,-.1907
640,1,1,-.067658
671,1,1,-.1
671,2,2,-.257
693,1,1,-.015
693,2,2,-.187
628,2,2,-.125
*NODE PRINT,FREQ=0
```

```
*EL PRINT,FREQ=0
*CONTACT PRINT,FREQ=0
*PRINT,FREQ=0
*ENDSTEP
********** step 4 lower additional lens nodes
*STEP,NLGEOM,INC=100
*STATIC
.05,1.,1e-10,.5
*BOUNDARY
665,2,2,-.26
*NODE PRINT,FREQ=0
*EL PRINT,FREQ=0
*CONTACT PRINT,FREQ=100,MASTER=LENSBOT,SLAVE=TEARTOP
*PRINT,FREQ=0
*ENDSTEP
**
********** step 5 lower additional lens nodes
*STEP,NLGEOM,INC=100
*STATIC
.05,1.,1e-10,.5
*BOUNDARY
**665,2,2,-.26
**667,2,2,-.27
667,1,1,-.12
*EL PRINT,FREQ=0
*CONTACT PRINT,FREQ=100,MASTER=LENSBOT,SLAVE=TEARTOP
*ENDSTEP
**
********** step 6 release imposed lens node displacements
*STEP,NLGEOM,INC=100
*STATIC
.001,1.,1e-10,.1
*CONTROLS,ANALYSIS=DISCONTINUOUS
*CONTROLS,PARAMETERS=TIME INCREMENTATION
** 1 ,2 ,3 ,4 ,5 ,6 ,7 ,8 ,9 ,10
     ,15,  ,25,2 ,  ,25,20
     ,.2,.2,  ,.2
*BOUNDARY,OP=NEW
2001,1
2501,1
3001,1
401,1
501,1
601,1
701,1
```

```
801,1
1000,1,6
*NODE PRINT,FREQ=100,NSET=TEARBOT
COORD
*NODE PRINT,FREQ=100,NSET=TEARTOP
COORD
*NODE PRINT,FREQ=100,NSET=BNODES
COORD
*EL PRINT,FREQ=100
S,MISES,PRESS
*CONTACT PRINT,FREQ=100
*PRINT,FREQ=0
*RESTART,WRITE,FREQ=1,OVERLAY
*ENDSTEP
```

Bibliography

[1] Bruno A. Boley and Jerome H. Weiner. *Theory of Thermal Stresses*, pages 429–430. Robert E. Krieger Publishing Company, 1960.

[2] Irving Fatt. Negative pressure under silicone rubber contact lenses. *Contacto*, January 1979.

[3] Irving Fatt and Jennifer Chaston. Negative pressure under a soft contact lens. *The Optician*, 172, 1976.

[4] October 1994. Private conversation with Dr. Peter Hagman.

[5] J. T. Jenkins and M. Shimbo. The distribution of pressure behind a soft contact lens. *Journal of Biomechanical Engineering*, 106, February 1984.

[6] D. K. Martin and B. A. Holden. Forces developed beneath hydrogel contact lenses due to squeeze pressure. *Phys. Med. Biol.*, 30(6), 1986.

[7] Donald Keith Martin. *Studies on the Mechanics of Hydrogel Contact Lenses and Biophysical Aspects of the Anterior Eye.* PhD thesis, University of New South Wales, 1985.

[8] A. R. Plepys and R. J. Farris. Evolution of residual stresses in three-dimensionally constrained epoxy resins. *Polymer*, 31, October 1990.

[9] Peter E. Raad and Adrian S. Sabau. Dynamics of a gas permeable contact lens during blinking. Accepted for publication in ASME Journal of Applied Mechanics, 1995.

[10] Yves Termonia. Molecular model for the mechanical properties of elastomers. 3. networks cross-linked in a state of strain. *Macromolecules*, 23(7), 1990.

[11] Menas S. Vratsanos and Richard J. Farris. Network mechanical properties of amine-cured epoxies. *Polymer Engineering and Science*, 29(12), June 1989.

[12] W.H. Wittrick. Stability of a bimetallic disk. *Quarterly Journal of Mechanics and Applied Math*, 6, 1953. Part 1.

[13] Graeme Young, Brien Holden, and Geoff Cooke. Influence of soft contact lens design on clinical performance. *Optometry & Vision Science*, 70(5), 1993.